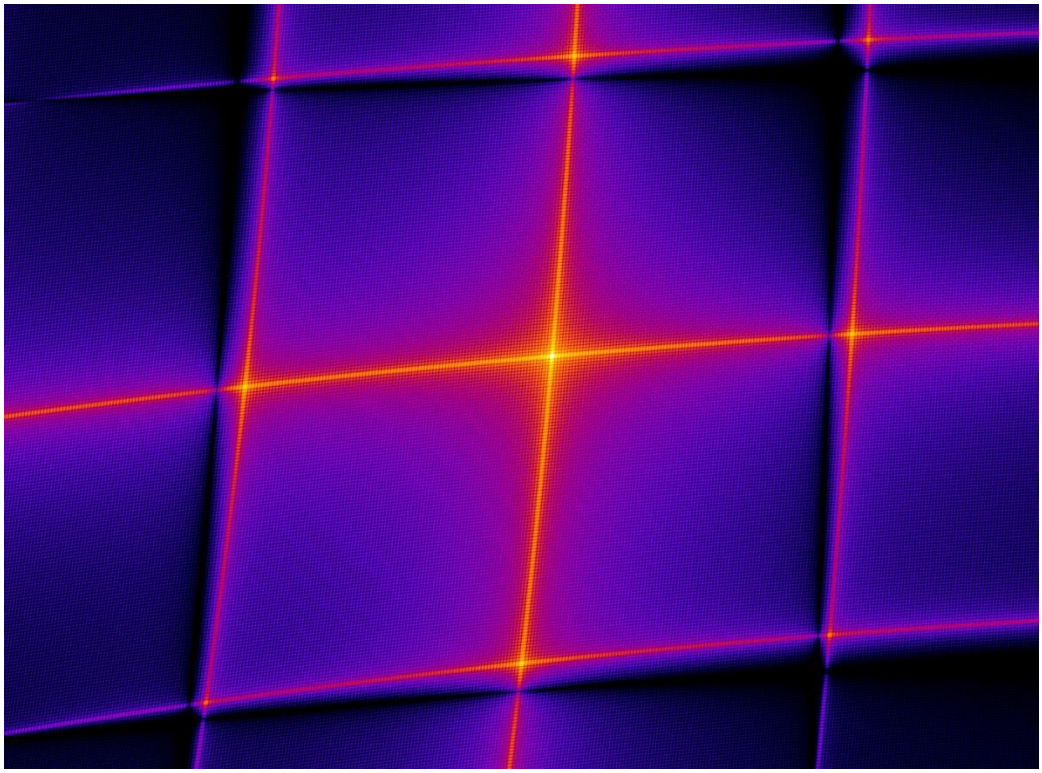

Development and cost-effective implementation of a structured illumination microscope and an optical projection tomography setup

PhD Thesis

Mario Lachetta | 22.10.2021

Printed on aging resistant paper °° ISO 9706

Development and cost-effective implementation of a structured illumination microscope and an optical projection tomography setup

PhD Thesis

To obtain the degree of

Doktor der Naturwissenschaften (Dr. rer. nat.)

Author:
Mario Lachetta

Bielefeld University

Department of Physics

Bielefeld, 22.10.2021

Reviewers:

- Prof. Dr. Thomas Huser
- Prof. Dr. Andreas Hütten

Contents

1 Introduction

Most humans perceive their environment primarily visually. Therefore, it is not surprising that a significant part of science and engineering is concerned with the development and application of visualization techniques [1]. Human eyes provide a spatial resolution of about one arc second, which corresponds to about 0.03 mm at a distance of 10 cm (minimum visual range) and serve to visualize the surroundings. In order to be able to resolve more details than possible with the human eye, technical aids such as magnifying glasses and microscopes are needed. Since magnifying glasses reach their limits in practical use for magnifying very small objects, the first light microscopes were developed in the 17th century by arranging lenses cleverly [2–5]. With help of the first light microscopes, it was possible to discover cells, the fundamental structure of a biological unit that underlies all known organisms [6]. Today's light microscopes are further developments of those devices. In addition to better optics, they use modern light sources (LEDs and lasers instead of sunlight) and digital detectors (e.g. camera chips) [7].

The field of modern light microscopy, especially fluorescence microscopy, offers the possibility to investigate biological structures and processes on different length scales and with different complexities [1]. The techniques presented in the course of this thesis are intended to complement the tools and methods used in biological and biomedical research. With the super-resolution and mesoscopic imaging systems developed in this thesis, images of subcellular dynamics [8] and the anatomical structure of human liver have already been successfully obtained [9].

Typically, light microscopy, including the fluorescence microscopy which is presented in this thesis, is employed with light in the visible to near-infrared spectrum (400 nm to 800 nm). Due to its wave nature and the related diffraction effects, there is a fundamental resolution limit for optical imaging systems such as microscopes. In general, this depends on the wavelength of the light, the aperture angle of objective lens, and the refractive index of the medium between the objective lens and the sample. This limit was first formulated by Ernst Abbe in 1873 and is known as the Abbe limit [10]. Microscopes optimized for high resolution typically achieve resolutions of about 200 nm in the lateral direction [11]. The Abbe limit is of physical origin and therefore even applies to the technical and optical highest quality lens-based microscopes.

Due to continuous development, various methods for contrast generation (including: bright/dark field, phase contrast, polarization, fluorescence) are available in light microscopes nowadays [12]. Fluorescence microscopy is used to generate specific contrasts for biomolecules. Samples can be stained with fluorescent molecules called

fluorophores, which are functionalized to bind specifically to the biomolecules of interest. Noncovalent binding can be achieved by specific chemical structures of fluorophores or by using specific antibodies. Another possibility, i.e., labeling with fluorescent proteins, is typically accomplished genetically. A fusion of gene sequences coding for the desired target covalently bind to a fluorescent protein, is introduced into the target cell or organisms (Nobel Prize in Chemistry 2008 [13]). In opposition to other contrast mechanisms, this enables the targeted observation of specific structures and is therefore superior for answering biomedical questions. For this reason, fluorescence microscopy has become a standard technique used in biomedical research. Both, in vitro and in vivo, fluorescence microscopy is used to answer biomedical questions [14]. The structures imaged range from pieces of tissue to individual cells and viruses [15–18]. Typically, standard wide-field or confocal (laser scanning) fluorescence microscopes are used to image biomedical samples [19].

In addition to (fluorescence) light microscopy, electron microscopy (EM), focused ion beam microscopy (FIB) and atomic force microscopy (AFM) have also established themselves as imaging methods [12,20–22]. While they provide structural information at very high spatial resolution, they lack the specificity offered by fluorescent labelling. For this reason, EM, FIB and AFM are often combined with fluorescence microscopy to form the field of correlative microscopy. In this way, specificity and very high resolution can be combined in a roundabout way [23–25].

Super-resolution microscopy

Unfortunately, the length scale of many biological processes and subcellular structures is well below the Abbe limit [26,27]. The Abbe limit, however, makes it impossible to obtain information below this fundamental physical resolution limit by only using optical imaging. Nevertheless, there is a set of methods that can resolve structures below the Abbe limit without violating it. These methods are based on either shifting spatial sample information into the time domain and/or introducing pre-known information about the sample or illumination. These methods are collectively referred to as super-resolution microscopy (or optical nanoscopy) and represent a wide-ranging interdisciplinary field of research [28]. For the successful development of the broadly applicable methods to overcome the Abbe limit, the Nobel Prize in Chemistry was awarded in 2014 "for the development of super-resolved fluorescence microscopy" [29]. The methods STED (stimulated emission depletion) [30] and SMLM (single molecule localization microscopy) [31,32] considered by the Nobel Prize are today, along with SIM (structured illumination microscopy) [33,34], among the three best-known representations of super-resolution microscopy [28,35–37]. Each of these methods uses a different concept to overcome the Abbe limit.

STED belongs to the superordinate concept RESOLFT (reversible saturable optical fluorescence transitions), which uses deterministic switchable fluorophores [38]. Specifically for STED, the focus of the excitation laser scanning over the sample is enclosed by a second donut-shaped depletion laser that suppresses the fluorescence, reducing the effective excitation volume for the fluorescence to about 50 nm in diameter in typical biological applications [28,39,40]. The superordinate concept SMLM uses the concept of stochastically switchable (blinking) fluorophores [41]. To be more precisely, the intensity distribution (point spread function) of individual blinking fluorescence molecules (point emitters) is fitted using appropriate functions [32]. From these fits, the position of the fluorescent molecules can be determined with a resolution down to tens of nanometers [32,42]. The field of SMLM includes, among others, the established methods PALM (photo-activatable localization microscopy) [43], STORM (stochastic optical reconstruction microscopy) [44] and dSTORM (direct stochastic optical reconstruction microscopy) [45,46]. STED and SMLM have in common that usable additional information about the sample, more precisely about the switchable fluorescent response of the sample, is known and can ultimately be converted into a gain in resolution.

SIM uses the concept of structured and varying illumination. Illuminating the sample with spatially structured light patterns shifts high frequency information (small structures) in frequency space (Fourier domain) to lower frequencies (larger structures). This allows information, that would actually be below the Abbe limit to be collected by the microscope [33,34]. The most common implementation of SIM, introduced by Gustafsson and Heintzmann [33,47] uses sinusoidal intensity distributions and their harmonics. In this case, 9 or 15 raw images with different phases and angles of the sinusoidal pattern are needed to directly extract the high frequency information and shift them back to their originally high frequency position in frequency domain [33,34,48]. The images reconstructed in this way achieve resolutions of about 100 nm [28].

The three concepts, respectively their methods (RESOLFT, SMLM and SIM) just presented, form a kind of foundation for super-resolution microscopy. In addition, there is a great variety of other methods (GSD, MINFLUX, SOFI, nonlinear SIM, …) that also enable super-resolution. In general, these are derived from one or more of the fundamental methods or the concepts behind them [49–59].

Regardless of the concept and the specific method, more time is required to acquire a super-resolution image compared to conventional microscopy methods. Either because the sample has to be scanned pointwise (STED) or because several raw image acquisitions are needed to reconstruct one super-resolved image (SMLM and SIM).

Thus, the additional spatial resolution is ultimately achieved at the expense of temporal resolution.

Depending on the application, the choice of the right super-resolution technique is essential. There often is a trade-off between temporal and spatial resolution, while SMLM and STED allow particularly high resolutions, they are not or only conditionally suitable for the investigation of living cells [60]. The main reason for this, is the comparatively slow acquisition speed and the need for relatively high excitation intensities, which often result in cell death or fluorophore bleaching [60,61]. SIM does not achieve the particularly high resolutions of SMLM and STED, but it allows the acquisition of several super-resolution images per second. Depending on the system, it is possible to achieve up to 60 super-resolved frames per second with SIM [8,62–64]. For this reason, SIM is the super-resolution technique, which is particularly suitable for the study of living cells [60,65].

Mesoscopic optical projection tomography

In addition to the drive of super-resolution microscopy for higher resolutions in biological applications, there is an area of research moving in a different direction. The field of microscopic imaging enables the observation of biological structures and processes on comparatively small length scales and sample sizes. The corresponding counterpart for large biological organisms, such as the human body, is macroscopic imaging. Its best known representatives, X-ray computed tomography (CT) [66,67] and magnetic resonance imaging (MRI) [68], are mostly associated with medical diagnostics and researches [69–72]. The area between microscopic and macroscopic imaging is called mesoscopy or mesoscopic imaging. As with macroscopic procedures, mesoscopy is concerned with obtaining three-dimensional volumetric images. This provides an advantage to the mostly section-based approaches of microscopy because rarer events or anomalies are more likely to be observed due to the much larger volume viewed. In addition, three-dimensional tracing of anatomical structures, e.g. of blood vessels, is possible.

Optical projection tomography (OPT) is a technique that allows mesoscopic imaging of centimeter-sized samples, such as (human) tissues, rodent organs, and rodent embryos [9,73–76]. It is the optical equivalent of computed tomography [76]. The images acquired by an OPT setup, are projections of the sample from different viewing angles. These are then reconstructed into virtual cross-sections through the sample, which is known as filtered back-projection. In this way, complete three-dimensional images of samples are obtained without the need of being cut up. Despite the comparatively large samples, optical projection tomography can achieve resolutions of tens of micrometers down to 7 µm [77]. To ensure the required transparency of the samples, they are usually clarified by using organic solvents [73,78]. Depending on the application, either

absorption or fluorescence can be used as contrast mechanisms, providing the invaluable benefit of specificity in optical projection tomography as well.

Main contributions to optical nanoscopy and mesoscopy of this thesis

The research presented here pertains to the implementation of microscope systems, more specifically, to the still growing field of developing bespoke microscope systems and the efforts in *democratizing* fluorescence microscopy [79–84]. Although many high-end optical imaging systems (microscopes) are commercially available today (from well-known optic manufacturers such as Zeiss, Olympus, Leica, and Nikon), custom-made systems are often needed to answer individual biomedical questions and to meet specific requirements. In addition, the high purchase and operating costs for commercial devices are a hurdle for individual research groups or small facilities, which require cost-effective alternatives [80–83]. All cost-efficient custom-made optical systems developed within the scope of this thesis are described holistically and in detail. Likewise, the software developed for simulations, imaging, or post-processing is open-source and freely available on GitHub. This should enable other scientists to easily reproduce the presented systems and/or to further evolve them for their specific application.

In the beginning of this thesis, the relevant theoretical background of light and fluorescence microscopy is introduced (section 2.1). Among other things, the imaging process of optical systems, resolution limits and fluorescence will be discussed. Subsequently, the concepts of super-resolution microscopy will be presented by introducing three prominently used super-resolution techniques, named STED, SMLM and SIM (section 2.2). However, the focus is primarily on SIM, as it is the particularly relevant technique for this thesis. The theoretical basics are concluded with an introduction to mesoscopic imaging via OPT (section 2.3). Both, the peculiarities of acquiring projections (raw data) and the reconstruction by means of filtered back-projection are explained on that note.

In section 3 the implementation and further development of a SIM microscope is described. The special feature of this microscope is the generation of illumination patterns by a digital micromirror device (DMD). These are of great interest due to their small structure-size, low costs, and extremely high speed. DMDs belong to the generic term of spatial light modulators (SLMs), which act as robust and fast electronically controllable diffraction gratings in SIM microscopes [85]. Commonly, ferroelectric liquid crystal on silicon (FLCoS) are used as SLMs to realize fast custom-made SLM-based SIM microscopes [62,63,86–89]. DMDs, in contrast to FLCoSs, exhibit the so-called blazed grating effect (BGE) due to their jagged surface structure [90,91]. It is responsible for asymmetric intensity distribution in the diffraction pattern and therefore ultimately for

poor modulation depths of the structured illumination in the sample. The BGE becomes particularly problematic when it comes to more than one color channel.

Within the scope of this thesis, a mathematical-physical model for the theoretical investigation of the BGE was evolved and transferred into a framework for the simulation of DMDs with coherent light [92]. The simulation results could be verified and confirmed by measurements in the laboratory. Based on these, a fast (60 super-resolved fps), compact and cost-efficient DMD-SIM microscope with one color channel could be built, and put into operation [8]. Due to further developments of the simulations and the evaluation of their results, the DMD-SIM microscope could be successfully extended to two colors in the next step. If necessary, this can even be extended to three colors in the future. The functionality, quality, and the achieved super resolution below the Abbe limit of the DMD-SIM microscope, both with one and two color channels, was successfully demonstrated by various measurements on artificial reference samples and biological samples (cells). For the operation of the DMD-SIM microscope the open-source software fairSIM-VIGOR was further developed and applied [63,93].

In section 4, imaging of mesoscopic samples (rodent organs and human tissues) with optical projection tomography (OPT) is presented. Since OPT systems are not commercially available, a fluorescence OPT setup was built and put into operation. It is based on a setup originally developed by David Nguyen [74] and differs primarily in the choice of another high-resolution 20 megapixel camera. The system can measure samples up to 17.5 mm in diameter. Depending on the sample size, the acquired projections and reconstructed cross sections can reach resolutions down to 10 µm. Also, for the fluorescence OPT setup, the functionality and quality were proven by measurements of artificial reference samples and biological samples (mouse organs). The first biomedical relevant data was acquired from human liver tissue, which allows the three-dimensional tracing of blood vessels and bile ducts. These could be compared with light sheet data from the same sample [9]. Beyond this thesis and the work of the author, the fluorescence OPT setup is in constant development and application. For example, the setup has been extended to include mesoscopic light sheet illumination and has been used to investigate human nasal polyps and mouse embryos.

Sections 3 and 4 represent the scientific work related to this thesis and are built around five publications (3 as first author [8,64,92], 2 as contributions [9,63]) in which the author of this thesis was significantly involved (see Section B).

2 Theoretical background

The general idea of light microscopy is the study of small (biological) structures. Photons from the visible or near-infrared range of the electromagnetic spectrum serve as carriers of the information of the object being observed. The unavoidable diffraction effects are essential for understanding the achievable resolution (Abbe limit) and the image formation using optical systems such as microscopes.

In order to understand the concepts and methods used later in this thesis, it is first necessary to go into the theoretical background of microscopy. Starting with the basics of light and fluorescence microscopy, it goes on to super-resolution methods with a special focus on structured illumination microscopy and ends with an introduction to optical projection tomography.

2.1 Basics of light and fluorescence microscopy

A fundamental understanding of the optical imaging process in microscopes is important before delving into the concepts of advanced microscopy techniques. The introduction to conventional light and fluorescence microscopy with fundamental considerations of resolution limits and image formation prepares for the understanding of optical projection tomography and super-resolution methods, especially structured illumination microscopy.

2.1.1 Conventional light microscopy

The aim of microscopes is to observe objects with a certain magnification. Simple lenses already offer an easy way to do this. If you place an object with the object size G at a distance g (object distance) from a lens with a focal length f, a real image of the object with the image size B is formed at the image distance b. (see Figure 1) The magnification results from the ratio of B to G and of b to g:

$$M = \frac{B}{G} = \frac{b}{g} \tag{1}$$

From geometrical optics, the application of the ray theorem results in the lens equation, which describes the relationship between b, g and f:

$$\frac{1}{b} + \frac{1}{g} = \frac{1}{f} \tag{2}$$

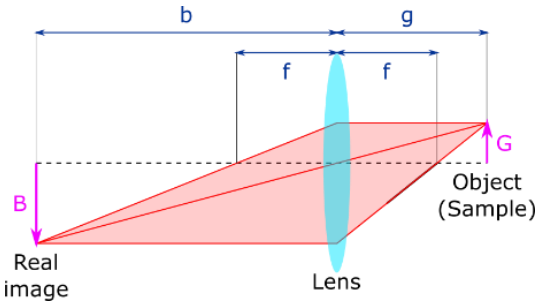

Figure 1: Image formation by a single convex lens

The lens with focal length $f \geq 0$ images the object G on the right at distance g onto the left side at distance b as real image B.

Modern microscopes are usually built with so-called infinity optics (see Figure 2). The first lens (objective lens) is positioned at its focal distance from the object or sample. This means that the image distance b is infinite. With the help of the second lens (tube lens), the image can be focused from infinity onto a camera chip. Instead of a camera chip, a third lens (eyepiece) can also be used to view the sample with the eye. Objective lenses, tube lenses and eyepieces usually do not consist of a single lens, but of a lens system of several lenses. This serves to correct aberrations (imaging errors). In the context of this section, however, it is sufficient to consider these as a single thin lens. The ratio of the focal lengths of the objective and tube lenses determine the magnification:

$$M = \frac{f_{tub}}{f_{obj}} \tag{3}$$

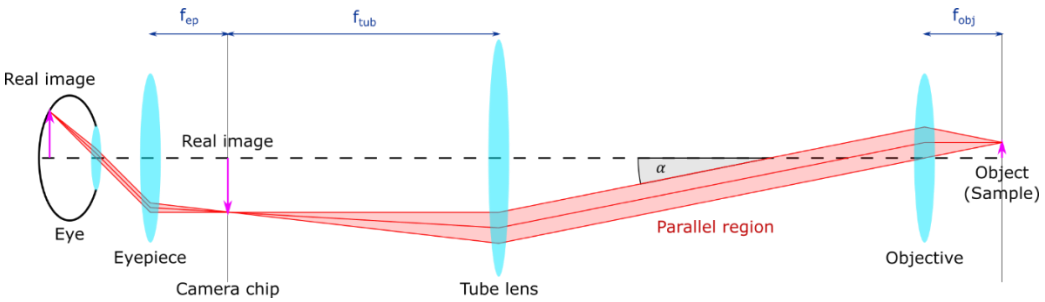

Figure 2: Infinity optics

The light emanating from the object/sample in the focal plane is collected by the objective lens and transmitted as a parallel beam at the angle α. The tube lens collects the parallel beams again and focuses them in its focal plane. A camera chip can be used to acquire the image created at this point. Optionally, instead of the camera chip, an eyepiece can be placed behind the focal plane of the tube lens at its focal length to allow the image to be viewed by eye.

In terms of ray optics, each point in the object and image plane can be assigned a parallel ray bundle between the objective and the tube lens. The angle of incidence or angle of emergence of the rays is related to the position in the object and image plane.

$$\frac{G}{f_{Obj}} = \tan(\alpha) \quad \text{and} \quad \frac{B}{f_{Tub}} = \tan(\alpha) \tag{4}$$

2.1.2 Resolution and its limits

If a point-like light source (e.g. a fluorescence molecule of a few nanometers in size) is transmitted through an optical system, its image is not point, but an extended structure. This is due to the wave nature of light and the associated diffraction effects, which smear the light distribution of each point source into an Airy disk. This intensity distribution is called the point spread function (PSF, see Figure 3).

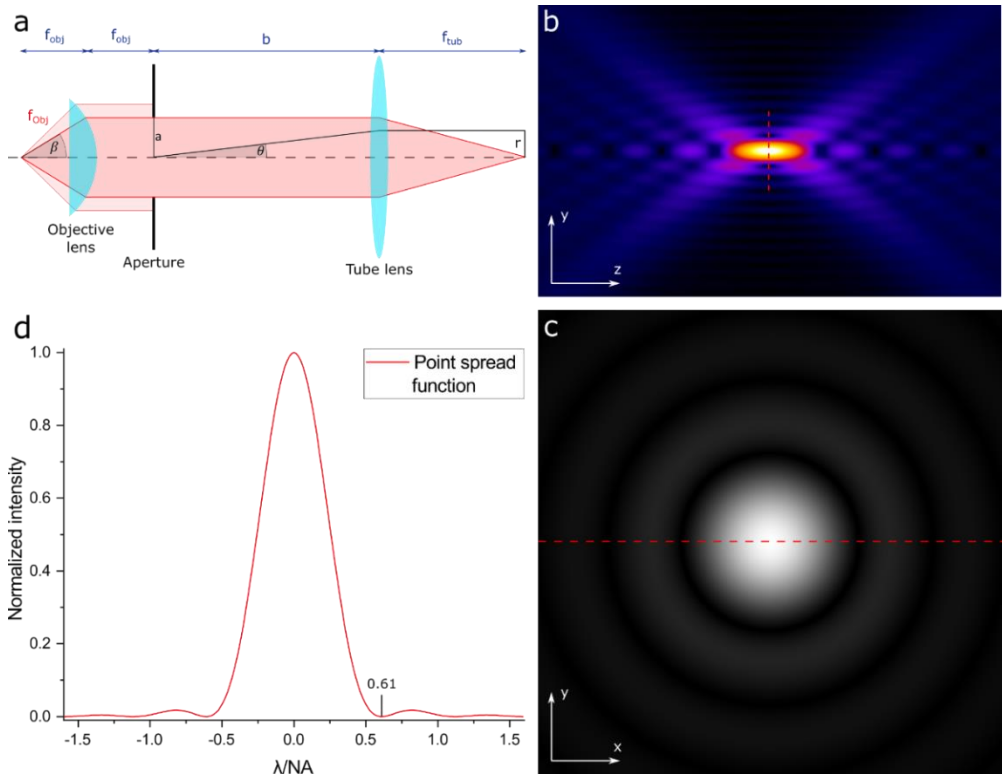

Figure 3:Point spread function

(a) Schematic representation of a simple infinity optics microscope with a circular aperture diaphragm in the back focal plane of the objective lens. β is the maximum opening angle of the objective, a corresponds to the radius of the aperture diaphragm, θ and r indicate the observation angle and observation radius. (b) yz-cross-section through the center of a PSF [94]. (c) xy-cross-section through the center of a PSF. (d) Intensity distribution of a lateral radial cross-section through the center of a PSF. For better visibility of the side maxima of the PSF, (b) and (c) are shown with a gamma correction of 0.5.

To derive the PSF from the wave propagation of light, we consider a point light source which is located on the optical axis in the front focal plane of an idealized objective lens (fulfilling Abbe's sine condition [95]). The spherical waves with wavelength λ emitted by the point light source are collimated by the objective lens. The maximum (half) opening angle β under which an objective lens can collect light is closely related to the size of the aperture of the objective lens in the back focal plane. Often the size of the aperture is limited by the diameter or the mount of the objective lens. The collimated planar wavefronts of the light collected by the objective lens are diffracted at the aperture. The resulting intensity distribution can be calculated in the far field (Fraunhofer approximation) via the absolute square of the Fourier transformation of the circular aperture diaphragm with radius a as a function of the viewing angle θ [96]:

$$PSF(\theta) = PSF_{max} \cdot \left(2 \frac{J_1\left(\frac{2\pi a}{\lambda}\sin(\theta)\right)}{\frac{2\pi a}{\lambda}\sin(\theta)} \right)^2 \quad \text{with} \quad PSF_{max} = \left(\frac{\pi a^2}{\lambda b}\right)^2 \tag{5}$$

J_1 is the first order Bessel function of the first kind. The highest intensity PSF_{max} is observed in the center ($r = 0$). If the angle-dependent diffraction image is imaged with the aid of a lens (tube lens), the observation angles θ can be transferred to distances r in the image plain (e.g. on a camera chip). With sufficient distance between the back focal plane of the objective and the tube lens, the small-angle approximation ($sin(\theta) \approx tan(\theta) = r/b$) is fulfilled. For the intensity distribution in the image plane (e.g. on a camera chip) it follows:

$$PSF(r) = PSF_{max} \cdot \left(2 \frac{J_1\left(\frac{2\pi a}{\lambda}\frac{r}{b}\right)}{\frac{2\pi a}{\lambda}\frac{r}{b}} \right)^2 \tag{6}$$

If both, the point light source and the camera chip, are within the focal distance of the objective and the tube lens, the two-dimensional description of the PSF in the xy-plane is sufficient. If the point light source is above or below the focal plane of the lens, the third spatial dimension (z) must also be taken into account. There are several models for approximating optical systems that can be used to calculate three-dimensional PSFs [94].

For the characterization of objective lenses and optical systems, not the previously used (half) aperture angle β is usually used, but the numerical aperture NA. This additionally considers the refractive index n of the immersion medium between the objective and the sample (air, water, immersion oil), whereby the effective opening angle of the objective can be increased. In case there are different media with relevant thickness (more than a few nanometers) between objective lens and sample (e.g. air and glass),

the lowest refractive index applies. The NA decisively determines the width of the point spread function and thus also the resolution of optical systems and microscopes.

$$NA = n \cdot \sin(\beta) \tag{7}$$

The answer to the question at what distance two incoherent point light sources can be distinguished from each other has become established as one of the common methods for determining the resolution of an optical system. However, since this distance is not clearly defined, two frequently mentioned criteria have become popular. The Sparrow criterion (Figure 4a) describes the distance from which a minimum is formed in the center of the superimposed intensity profile of the imaged point light sources [97]. The Rayleigh criterion (Figure 4c) is defined by the distance at which the maximum of the PSF of one imaged point light source is located in the minimum of the other [98].

$$d_{Sparrow} = \frac{0.47\,\lambda}{NA} \qquad d_{Rayleigh} = \frac{0.61\,\lambda}{NA} \tag{8}$$

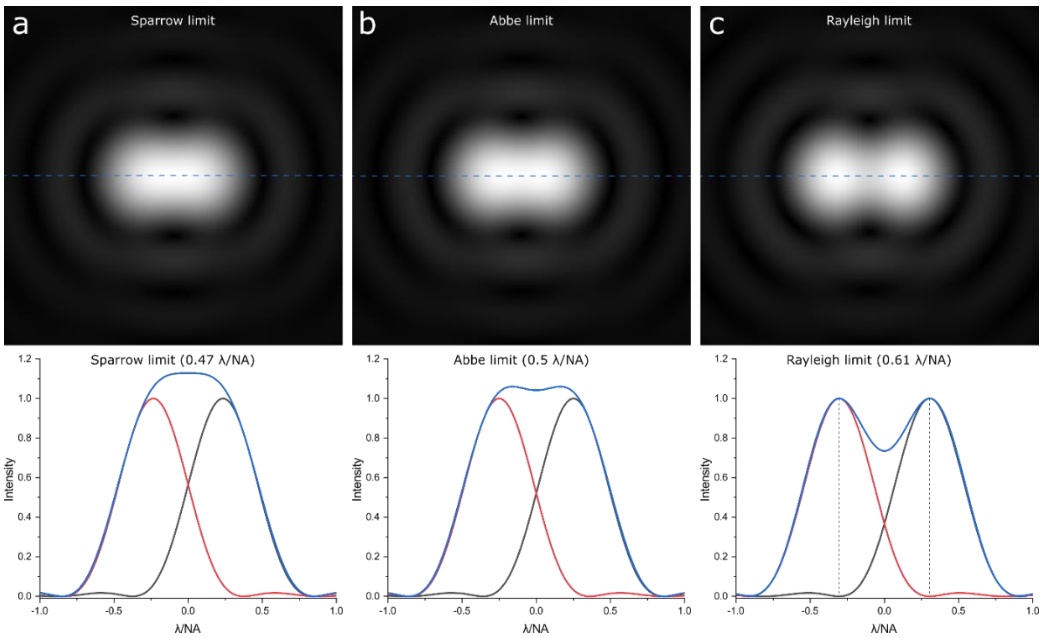

Figure 4: Resolution limits in comparison

Top: Two-point light sources image by an optical system at a distance of $d_{Sparrow}$ (a), d_{Abbe} (b) and $d_{Rayleigh}$ (c) are shown with a gamma correction of 0.5. Bottom: The intensity distribution of the cross-sections through the center of the corresponding images. The red and black graphs each represent a single PSF, while the blue graph indicates the superposition of the two PSFs. The dotted vertical lines in (c) indicate that the main maximum of each PSF lies in the first minimum of the other.

Ernst Karl Abbe chose a different approach to determine the resolution of optical systems. If one tries to observe a coherently exposed grating structure through an optical system, it can only be imaged if at least the zeroth and one of the two first orders of diffraction can be collected by the optical system [10].

$$|\beta_0| \leq \beta_{obj} \qquad |\beta_1| \leq \beta_{obj} \tag{9}$$

As shown in Figure 5, we consider an optical grating with grating constant d. This is exposed to coherent light of wavelength λ along the optical axis (angle of incidence $\gamma = 0$). For the angle of emergence β_m of the m[th] diffraction order applies [99]:

$$\sin(\beta_m) + \sin(\gamma) = \frac{m\lambda}{nd} \tag{10}$$

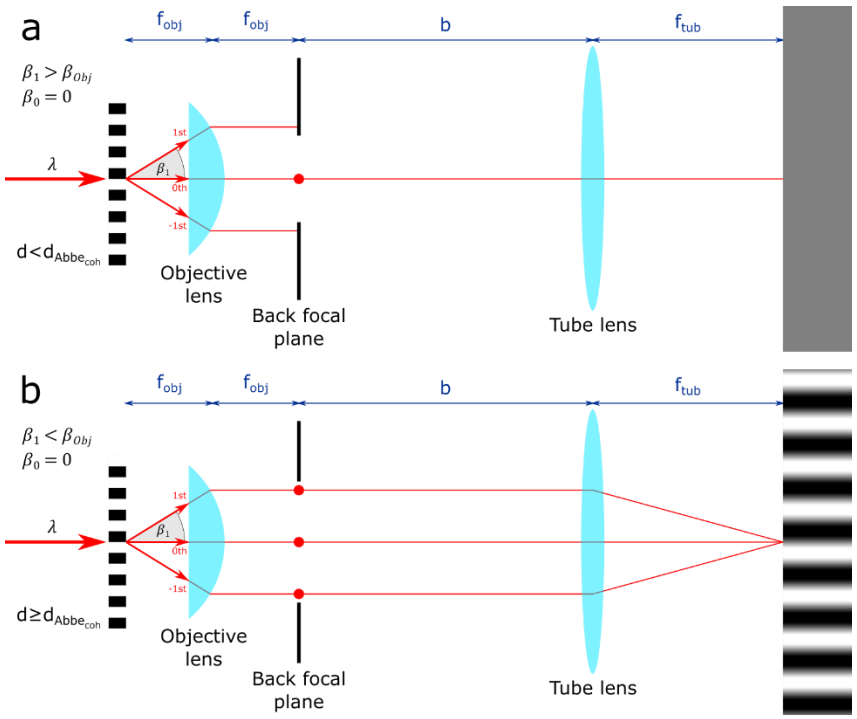

Figure 5: Coherent Abbe limit

Coherent light of wavelength λ falls parallel to the optical axis on a grating located in the focal plane of the objective lens. The diffraction orders collected by the objective lens are parallelised. In case (a), the grating constant is $d > d_{Abbe_{coh}}$, so that only the zeroth order is transmitted, resulting in no image on the screen. In case (b), the grating constant is $d \leq d_{Abbe_{coh}}$ the zeroth and the two first diffraction orders are transmitted, with the result that the grating is imaged on the screen as a sinusoidal structure.

For $m = 1$ and $\gamma = 0$ eq. (10) follows:

$$d = \frac{\lambda}{n \cdot \sin(\beta_1)} \geq \frac{\lambda}{n \cdot \sin(\beta_{obj})} = \frac{\lambda}{NA} \tag{11}$$

The limiting case $\beta_1 = \beta_{obj}$ eq. (11) leads to the coherent Abbe limit:

$$d_{Abbe_{coh}} = \frac{\lambda}{NA} \tag{12}$$

As shown in Figure 6, if the optical grating is exposed at an angle γ, the angle of incidence is always equal to the angle of emergence for the zeroth order of diffraction.

$$\beta_0 = -\gamma \tag{13}$$

In order for the zeroth diffraction order to be acquired by the optical system, the exposure angle γ must not exceed half the aperture angle of the lens.

$$|\beta_0| = \gamma \leq \beta_{obj} \tag{14}$$

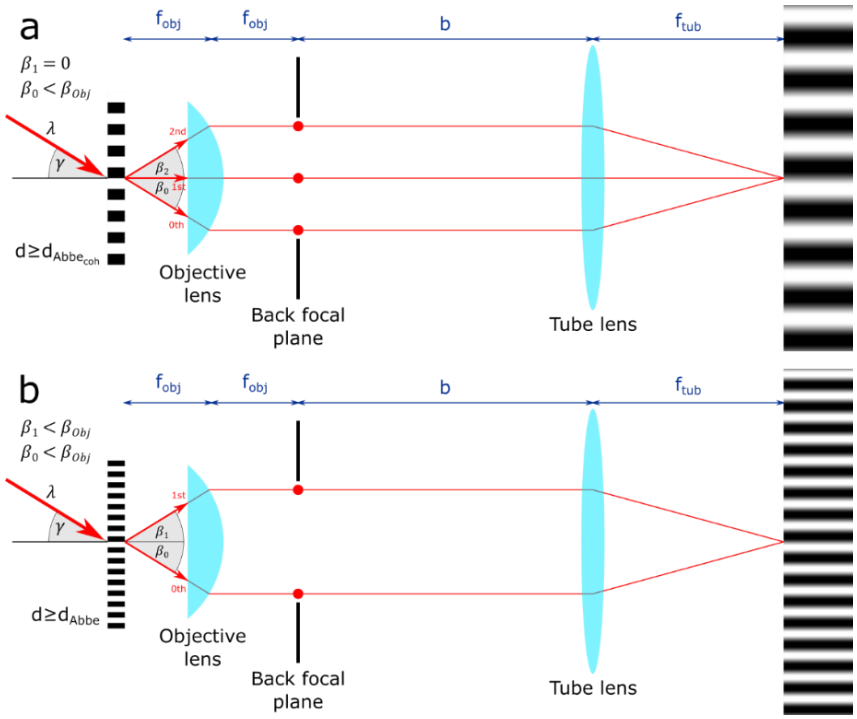

Figure 6: Coherent Abbe limit with angle of incidence

Coherent light of wavelength λ falls at the maximum opening angle of the objective $\gamma = \beta_{obj}$ on a grating which is in the focal plane. In case (a) the grating constant is $d \geq d_{Abbe_{coh}}$, so that the zeroth, one first and one second diffraction order are transmitted. In case (b), the grating constant is exemplarily $d \geq d_{Abbe}$, so that the zeroth and one of the first diffraction orders are transmitted. In both cases, the grating is imaged as a sinusoidal structure.

The following relation results from eq. (10) for the first diffraction order:

$$d = \frac{\lambda}{n \cdot (\sin(\beta_1) + \sin(\gamma))} \geq \frac{\lambda}{n \cdot \left(\sin\left(\beta_{obj}\right) + \sin\left(\beta_{obj}\right)\right)} = \frac{\lambda}{2NA} \tag{15}$$

The limiting case $\beta_1 = \beta_{obj}$ and $\gamma = \beta_{obj}$ leads to what is generally known as Abbe limit (Figure 4b) [10]:

$$d_{Abbe} = \frac{\lambda}{2NA} \tag{16}$$

This limit applies not only to coherent exposure but also to incoherent exposure. As shown in Figure 7, one way to model incoherent light is to have coherent light coming from all directions. The relationships shown above apply to each of these directions. Based on eq. (15), each angle of incidence γ_i produces an image with the resolution:

$$d_i = \frac{\lambda}{n \cdot \left(\sin\left(\beta_{obj}\right) + \sin(\gamma_i)\right)} \tag{17}$$

Summing up all these images, we get the image that is imaged by the optical system with incoherent light. We assume that the numerical aperture (effective opening angle) of our exposure $NA_{condenser}$ is at least equal to that of the lens.

$$n \cdot \sin(\gamma_{max}) = NA_{condenser} \geq NA_{obj} \tag{18}$$

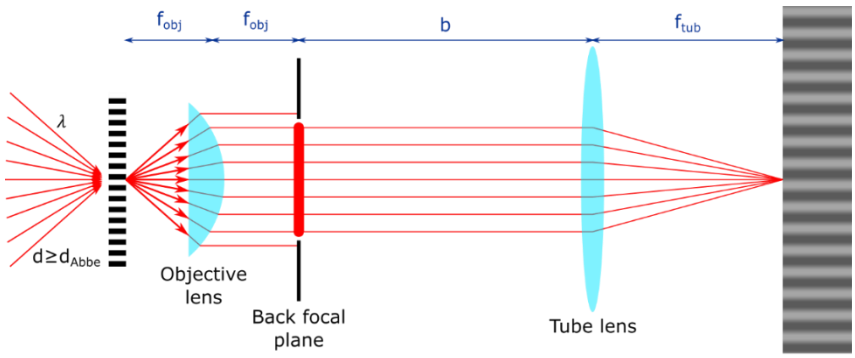

Figure 7: Incoherent Abbe limit

Incoherent light is modelled as coherent light of wavelength λ from all directions ($-\beta_{obj} \leq \gamma \geq \beta_{obj}$) and exposes a grating located in the focal plane. The grating constant is $d \geq d_{Abbe}$. All angles of incidence for which the zeroth and one of the first diffraction orders is transmitted contribute to the contrast of the image as a sinusoidal pattern.

In this case, all angles of incidence $-\beta_{obj} \leq \gamma_i \leq \beta_{obj}$ contribute to the image and thus also to the resolution. From eq. (17), this leads to:

$$\begin{aligned} d_{Abbe_{incoh}} &= \min\left(d_i = \frac{\lambda}{n \cdot \left(\sin\left(\beta_{obj}\right) + \sin(\gamma_i)\right)}\right) \\ &= \frac{\lambda}{NA + NA_{condenser}} = \frac{\lambda}{2NA} = d_{Abbe} \end{aligned} \tag{19}$$

For decreasing structure-sizes, however, the achievable contrast decreases more and more until it finally falls to zero for d_{Abbe} [65]. Figure 8 serves as a comparison between a coherent and incoherent image with a diffraction-limited optical system.

Which of the three resolution criteria presented is the supposedly correct one remains controversial to this day. In the further course of this thesis, the (incoherent) Abbe limit (eq. (16)) will be considered as the one resolution limit. The argumentation based on structures (gratings) with grating constants and the associated spatial frequencies $k = 1/d$ is more appropriate in the context of this thesis than the argumentation about point light sources. In addition, all microscopy images shown in this document are subject to incoherent image formation.

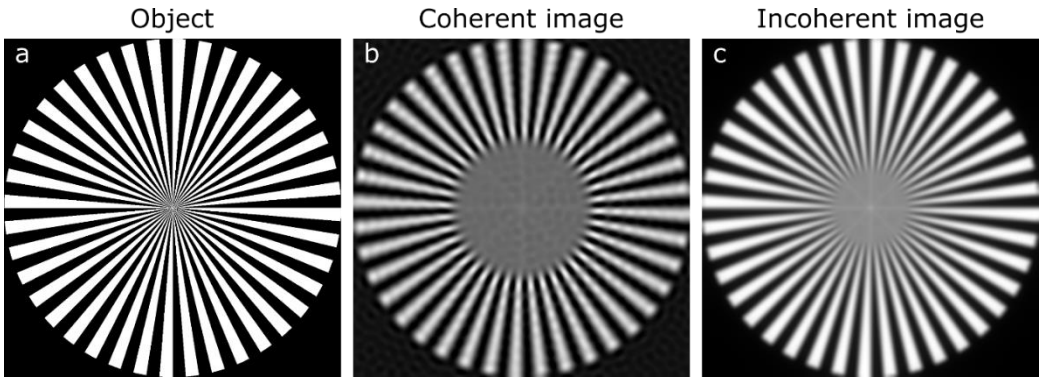

Figure 8: Comparison of coherent and incoherent images

Simulated image of the test object (a) through a diffraction-limited optical system with coherent (b) and incoherent (c) illumination incident parallel to the optical axis ($\gamma = 0$). While the contrast in the coherent image decreases abruptly with decreasing structure-sizes, the contrast in the incoherent image decreases gradually.

2.1.3 Optical transfer function and image formation

The so-called optical transfer function (OTF) indicates how well an optical system can map the spatial frequencies k of an object. For the idealised coherent case, with angle of illumination $\gamma = 0$, the OTF is constant 1 for spatial frequencies whose absolute value is below the coherent abbe limit, otherwise 0 [96]:

$$OTF_{coh}(k) = \begin{cases} 1 & if \quad |k| < \dfrac{1}{d_{Abbe_{coh}}} = \dfrac{NA}{\lambda} \\ 0 & if \quad |k| > \dfrac{1}{d_{Abbe_{coh}}} = \dfrac{NA}{\lambda} \end{cases} \tag{20}$$

In general, the incoherent OTF of an optical system can be calculated by the Fourier transform of the PSF or by autocorrelating the back focal plane aperture of the objective lens. The Fourier transform of the PSF of an idealized optical system (eq. (5) & (6)) yields the corresponding incoherent OTF [96]:

$$\begin{aligned} OTF_{incoh}(k) &= \mathcal{F}\big(PSF(r)\big) = \widetilde{PSF}(k) \\ &= \frac{2}{\pi}\left(\arccos\left(\left|\frac{k}{k_{max}}\right|\right) - \left|\frac{k}{k_{max}}\right|\sqrt{1-\left(\frac{k}{k_{max}}\right)^2}\right) \end{aligned} \tag{21}$$

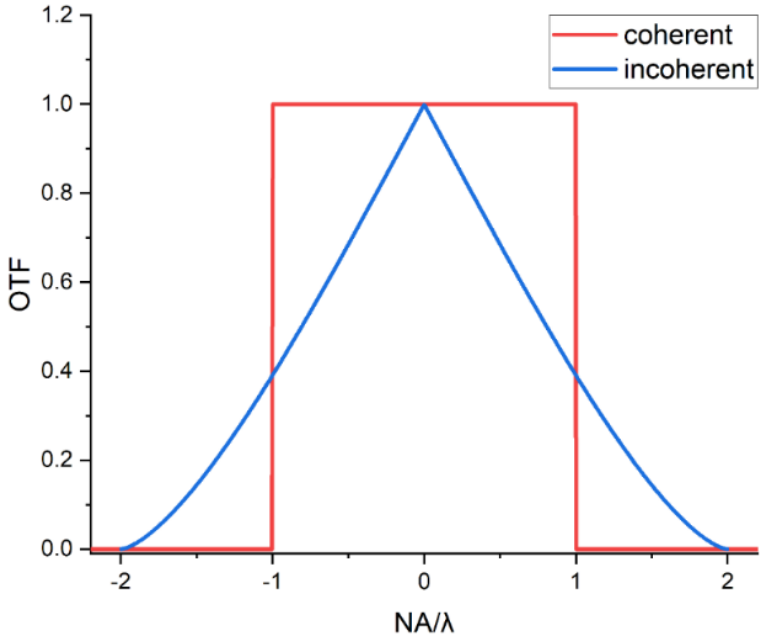

Figure 9: Coherent and incoherent OTF

Representation of an idealized coherent (red) and incoherent (blue) OTF of an optical system.

In general, the OTF is a complex-valued function that can be divided into the modulation transfer function (MTF) and phase transfer function (PhTF). The MTF corresponds to the amplitude and the PhTF to the phase. OTF and MTF are often used synonymously in microscopy, typically using the term OTF also when referring (only) the amplitude (MTF) and explicitly stating when the phase component (PhTF) is of interest.

$$OTF(k) = MTF(k) \cdot e^{i \cdot PhTF(k)} \tag{22}$$

The shape of the incoherent OTF (see Figure 9) also clarifies why the contrast in the incoherent case continues to decrease with increasing spatial frequency up to the Abbe limit. In frequency space, the frequency of the Abbe limit is called the cut-off frequency:

$$k_{max} = \frac{1}{d_{Abbe}} = \frac{2NA}{\lambda} \tag{23}$$

Mathematically, the formation of the image $D(\vec{r})$ in the spatial domain $\vec{r}$ can be described as a convolution (convolution operator: $*$) of the sample $S(\vec{r})$ (including illumination $I(\vec{r})$) with the point spread function $PSF(\vec{r})$:

$$D(\vec{r}) = [S(\vec{r}) \cdot I(\vec{r})] * PSF(\vec{r}) \tag{24}$$

In Fourier space $\vec{k}$ (frequency domain) we get:

$$\mathcal{F}\big(D(\vec{r})\big) = \widetilde{D}\big(\vec{k}\big) = \big[\tilde{S}\big(\vec{k}\big) * \tilde{I}\big(\vec{k}\big)\big] \cdot \widetilde{PSF}\big(\vec{k}\big) = \big[\tilde{S}\big(\vec{k}\big) * \tilde{I}\big(\vec{k}\big)\big] \cdot OTF\big(\vec{k}\big) \tag{25}$$

Using the convolution theorem for Dirac delta functions $\delta(\vec{k} - \vec{a})$,

$$\tilde{S}\big(\vec{k}\big) * \tilde{I}\big(\vec{k}\big) = const \cdot \mathcal{F}\big(S(\vec{r}) \cdot I(\vec{r})\big) \qquad \tilde{S}\big(\vec{k}\big) * \delta\big(\vec{k} - \vec{a}\big) = \tilde{S}\big(\vec{k} - \vec{a}\big) \tag{26}$$

we obtain, for spatially constant illumination $I(\vec{r}) = I_0$:

$$\widetilde{D}\big(\vec{k}\big) = \big[\tilde{S}\big(\vec{k}\big) * \delta\big(\vec{k}\big) \cdot I_0\big] \cdot OTF\big(\vec{k}\big) = I_0 \cdot \tilde{S}\big(\vec{k}\big) \cdot OTF\big(\vec{k}\big) \tag{27}$$

Equation (24) in the spatial domain and (27) in the frequency domain are equivalent in their meaning. The description in Fourier space, however, has certain advantages that make procedures such as deconvolution and super-resolved SIM microscopy possible (section 2.1.5 & 2.2.3). Figure 10 illustrates the formation of the image in spatial and frequency domain.

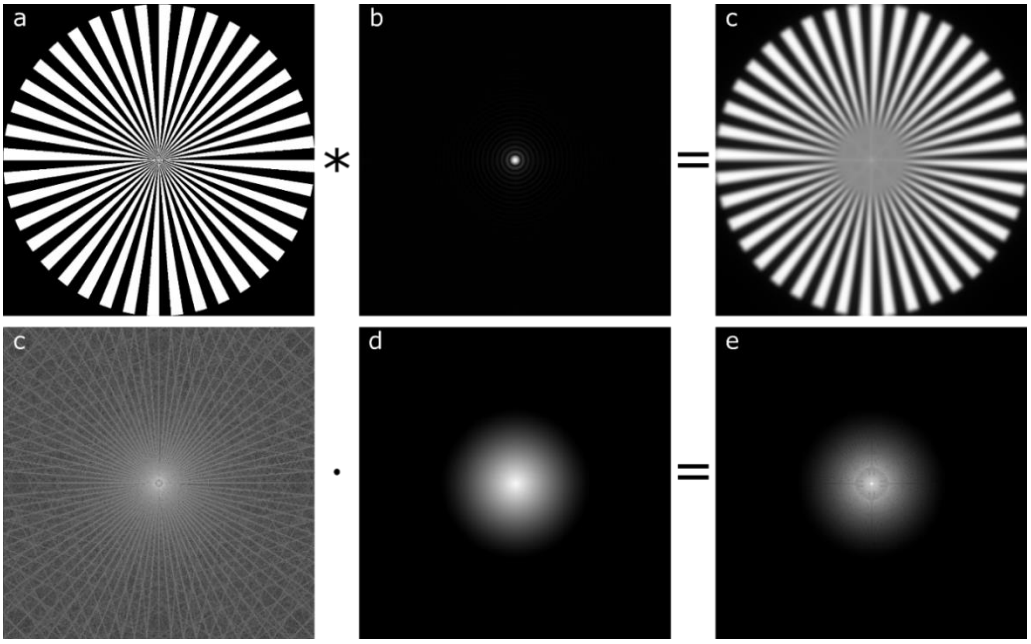

Figure 10: Image formation in spatial and frequency domain

With spatially constant exposure, the formation of an image (c) can be described mathematically in spatial domain as the convolution of the sample (a) with the PSF (b). Equivalently, in frequency domain the Fourier transform of the image (e) can be described as multiplication of the Fourier transform of the sample (c) with the (incoherent) OTF (d). The Fourier transform and its inverse enable the change between spatial and frequency domain.

So far, we have only considered two-dimensional OTFs from the focal plane of an optical system. Outside the focus ($z \neq 0$), the image formation can still be described by equations (24) and (27), as long as a three-dimensional OTF (see Figure 11) is considered. This is also obtained by the Fourier transformation of the three-dimensional PSF (see 2.1.2). Three-dimensional OTFs usually have the so-called missing cone. This describes the disappearance of the OTF near $k_r = 0$ for $k_z \neq 0$. This means that low frequencies (coarse structures) can be poorly resolved along the optical axis (z). This "missing cone problem" manifests itself in practice as a background or out-of-focus signal.

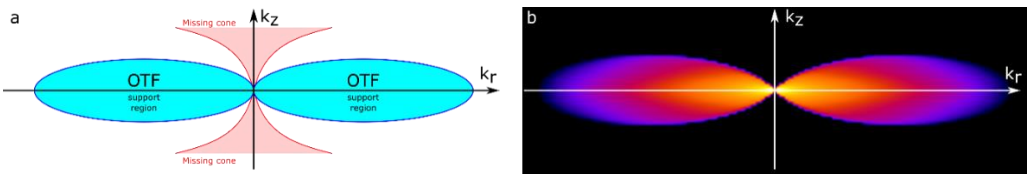

Figure 11: Three dimensional OTF

(a) Schematic representation of the scope of a three-dimensional OTF (blue) and the missing cone (red). (b) Exemplary representation of a real OTF [100].

2.1.4 Fluorescence microscopy

For a long time, microscopy was limited to unspecific contrast generation with methods such as bright-field, dark-field, polarization, and phase-contrast microscopy. It was not until the development of fluorescence microscopy that it became possible to specifically obtain a strong contrast of the desired structures in biological samples [101].

Fluorescence

The discovery and first description of fluorescence goes back to George Gabriel Stokes in 1852 [102]. Fluorescent molecules (fluorophores) are usually described using the Born-Oppenheimer approximation and the Franck-Condon principle. The change of state of the electrons (approx. $10^{-15}\ s$) compared to the nuclei (approx. $10^{-13}\ s$) can be assumed to be instantaneous [101]. This results in the so-called Jablonski diagrams, which visually describe the electronic energy levels and the possible transitions (see Figure 12a). A distinction is made between the singlet states S with spin multiplicity one, which is important for fluorescence, and the triplet states T with spin multiplicity three, which is important for phosphorescence. The energy of a photon results from the Planck constant h and its frequency ν, which can be determined from the speed of light c and the wavelength λ.

$$E = h\nu = \frac{hc}{\lambda} \tag{28}$$

Through the absorption of a photon λ_{abs}, valence electrons can be brought from the singlet ground state S_0 into one of the vibrational levels v_{0-m} of the excited singlet states S_{1-n} [101]. Due to radiation less vibrational relaxation, however, the higher vibrational levels have a comparatively short lifetime, so that the electron is in the lowest vibrational level v_0 of the excited state S_{1-n} after approx. $10^{-12}\ s$ [103,104]. If the electron is not in the first excited state, but in a higher one, it can reach the S_1 state by means of internal conversion. After a lifetime of approx. $10^{-8}\ s$ [101], a fluorescence photon λ_{fl} is emitted during the transition from $S_1 v_0$ to a vibrational level v_{0-m} of the singlet ground state S_0.

In the case of strong spin-orbit coupling, an actually spin-forbidden transition from an excited singlet state to a triplet state and finally to T_1 is possible through so-called inter-system crossing [101]. Since the transition from T_1 to S_0 is also spin-forbidden, the lifetime in T_1 can last from a few microseconds to one second after excitation [105]. During the transition from $T_1 v_0$ to a vibronic level v_{0-m} of the singlet ground state S_0, a phosphorescence photon λ_{ph} is emitted [103,104,106].

There are three rules for fluorescence, which do not apply without exception and therefore serve more as a guideline for understanding fluorescence:

- **Kasha's rule**: Due to the very short lifetime (approx. $10^{-12}\ s$) of higher ($v \neq v_0$) vibronic states, fluorescence transitions usually take place from the lowest vibronic level ($v = v_0$) of the first excited singlet state. Therefore, the wavelength of the exciting photon has no effect on the wavelength of the fluorescence [107].
- **Mirror image rule**: Due to the Franck-Condon principle, the absorption and emission spectra of fluorophores often exhibit mirror symmetry to each other (see Figure 12b) [101,106].
- **Stokes shift**: Due to the radiation less transitions between the absorption and emission of a photon, the energy of the emitted photons is smaller than that of the absorbed photons. As a result, the wavelength of the emission is red-shifted compared to the absorption, $\lambda_{fl} \geq \lambda_{abs}$ (see Figure 12b) [102,106].

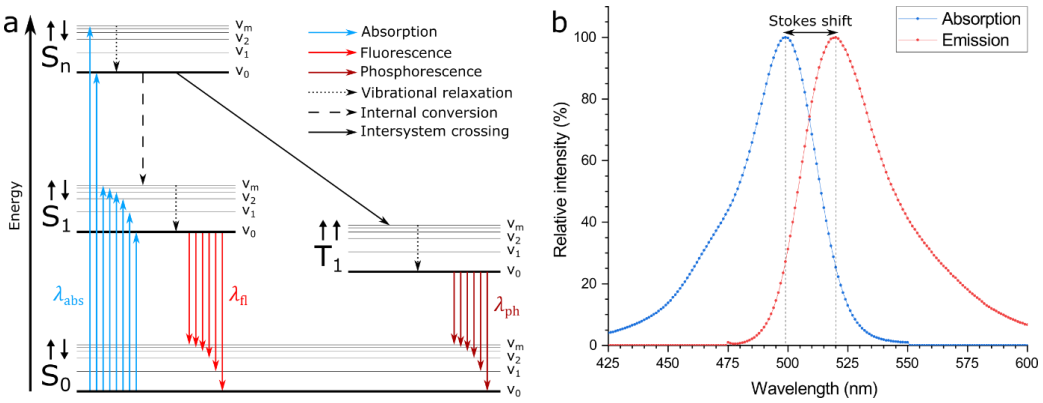

Figure 12: Jablonski diagram & absorption and emission spectrum of fluorophores

(a) The Jablonksi diagram illustrates the possible transitions of valence electrons in fluorescent molecules. Upon interaction with a photon λ_{abs}, the molecule can be brought from the electronic singlet ground state S_0v_0 to the first excited singlet state S_1v_{0-m}. Due to radiationless vibrational relaxation, the electron is in the vibrational ground state S_1v_0 shortly afterwards (Kasha's rule). If the molecule is excited into a higher singlet state S_n, it can also reach S_1 by internal conversion. With strong spin-orbit coupling, the actually spin forbitten transition from S_n to the triplet state T_1 is possible through intersystem crossing. The emission of a photon λ_{fl} during the transition from S_1v_0 to S_0v_{0-m} is called fluorescence. Phosphorescence describes the emission of photons λ_{ph} during the transition from T_1v_0 to S_0v_{0-m}. Due to the energy dissipation of the non-radiative transitions before the fluorescence and phosphorescence transition, the wavelength of the emitted photons is greater than that of the absorbed ones (Stokes shift). (b) Absorption and emission spectrum using the example of Alexa Fluor 488. An almost mirror-symmetrical shape of the two spectra is recognizable (mirror rule). The wavelength difference between the maxima of the absorption and emission illustrates the Stokes shift.

Equivalent to radioactive decay, the fluorescence process can be described by an exponential decay law [99]. The number of excited fluorophores N at time t results from the number of excited fluorophores N_0 at time $t = 0$ and the mean lifetime of excitation τ.

$$N(t) = N_0 \cdot e^{-t/\tau} \tag{29}$$

The emission of a photon by an excited fluorophore is (usually) an independent stochastic process, meaning the time of each emission is random and not influenced by other emissions. Thus, the phase information of the absorbed (possibly coherent) photons cannot be obtained. Therefore, fluorescence can be considered incoherent. Consequently, the resolution limit for fluorescence microscopy is the (incoherent) Abbe limit from eq. (16).

Biological structures are fluorescent themselves (autofluorescence) due to the nature of cellular structures and components. For example, amino acids such as tryptophane, tyrosine and phenylalanine in high concentration can lead to significant autofluorescence in proteins. These can be observed in a fluorescence microscope without further preparation (staining). Nevertheless, autofluorescence is usually very weak. However, if desired structures require visualization, strong stable efficient fluorophores should be added to the molecule of interest. The staining then also provides the necessary specificity. Depending on the fluorophore, these are functionalized either directly or with the help of tags such as antibodies or small structures with affinity to the desired molecules [101]. Fluorophores can reach the molecule of interest through diffusion in a medium containing the target. These can stain the desired structures through non-covalent interactions or covalently bound after induced chemical reactions. Another important possibility for fluorescent staining is the genetic engineering of the gene coding for of the desired target protein to a gene coding for a fluorescent protein of choice, such as eGFP (enhanced green fluorescent protein) [108]. The resulting chimeric gene expresses the protein of interest fused to a fluorescent protein. Due to its great importance in the research applications in biology, especially cell biology, the Nobel Prize in Chemistry was awarded in 2008 for the discovery, further development, and application of GFP [13]. If the fluorophores used have weak signal, the autofluorescence, which is actually weak, may be strong enough to cause undesirable non-specific (background) signal.

With the longer exposure, one often observes a bleaching of the fluorophores. The reason for this is usually the reaction of a fluorophore in the triplet state with molecular oxygen O_2. The reaction product is usually not fluorescent and therefore bleached. Fluorophores that bleach comparatively little are called photostable. If the application permits, these should be used primarily for fluorescent labelling.

As of today, there is a wide range of fluorophores with different properties [109,110]. Especially for advanced techniques, it is sometimes necessary that the fluorophores can be made to blink [111], or that they can be specifically switched off (quenching) [101].

Wide-field fluorescence microscope

Modern standard widefield microscope essentially consists of four components: A light source, an objective lens, a tube lens, and a camera. Fluorescence microscopes additionally have a special component, a dichroic mirror. these reflect or transmit light depending on the wavelength and are available in various configurations [112]. For example, a simple dichroic mirror could reflect all wavelengths below 500 nm and transmit all above. Thus, thanks to the Stokes shift, the light of excitation (usually lasers or LEDs, e.g. a 488 nm laser) can be separated from that of fluorescence (e.g. from Alexa Fluor 488, Figure 12b). This makes it possible to use the objective lens for both illumination and detection (see Figure 13) [101,103,106].

Wide-field fluorescence microscopes can be operated in different illumination configurations depending on how the excitation light is shone into the objective. If it is focused in the center of the back focal plane, the result is a collimated transmitted light illumination known as epi-illumination (Figure 13b). This allows structures to be acquired anywhere in the field of view, but comparatively much unwanted background signal is obtained from outside the focal plane.

The further out the focus is created in the back focal plane, the larger the angle Θ at which the excitation light falls into the sample. When Θ becomes so large that total internal reflection occurs at the interface between the cover glass with refractive index n_1 and the sample with refractive index n_2 (eq.(30), $\Theta \geq \Theta_{TIRF}$), light no longer propagates into the sample (Figure 13c). To achieve this, two technical conditions have to be fulfilled: The objective lens must support a sufficiently large opening angle Θ (so-called TIRF objectives), and the refractive index of the immersion medium between the objective lens and the sample must be greater than that of the sample.

$$\Theta_{TIRF} = \arcsin\left(\frac{n_2}{n_1}\right) \tag{30}$$

On the sample side, an evanescent electromagnetic field of the excitation light is formed at the interface, which decreases exponentially with distance and penetrates about 100nm deep into the sample [113]. This TIRF (total internal reflection fluorescence) exposure excites only fluorophores within this evanescent field and is therefore particularly well suited for imaging structures within the sample that are very close to the coverslip (bottom). Background signal is practically non-existent here, since only fluorophores within the focal plane are excited [114].

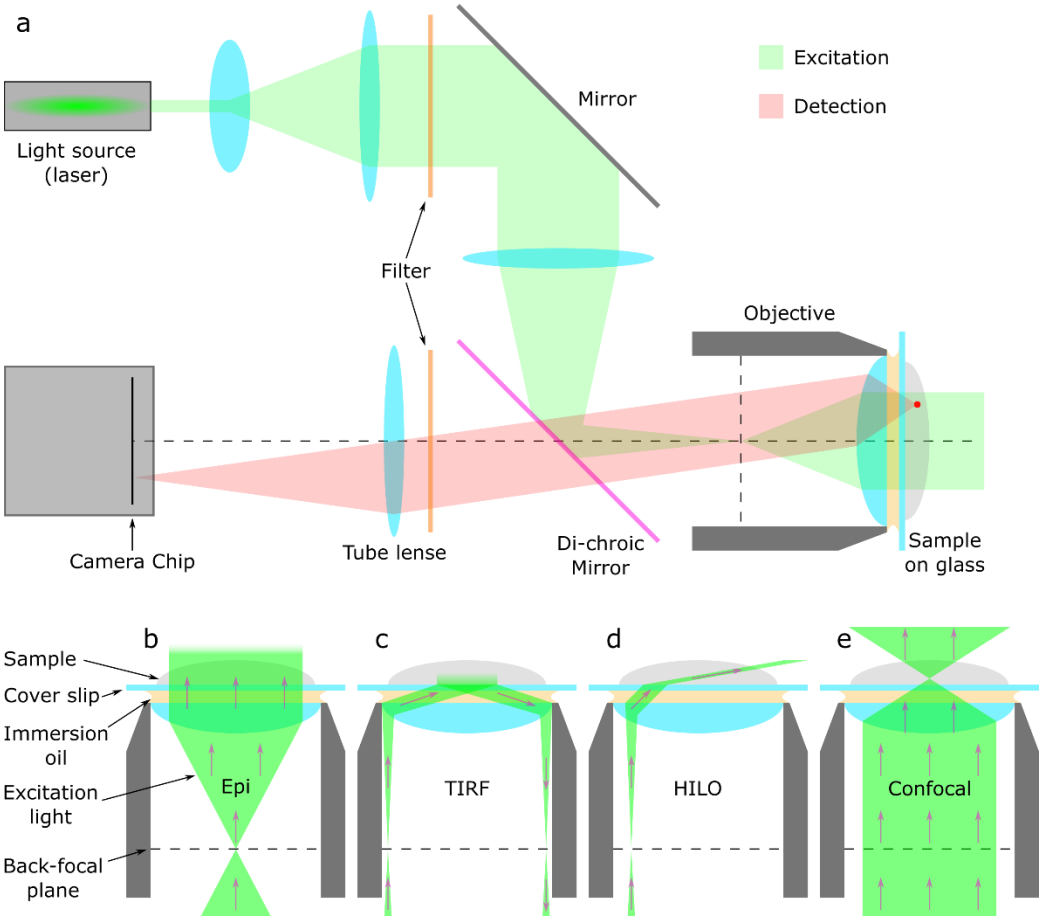

Figure 13: Wide-field fluorescence microscope and illumination configurations

(a) Schematic representation of a wide-field fluorescence microscope. The excitation light from the light source (laser) is expanded by a telescope and, if necessary, purified by an excitation filter. After redirection by a mirror, the light is focused by means of a lens via the reflection at the dichroic mirror into the center of the back focal plane of the objective (epi-illumination). The collimated fluorescence light collected by the objective is transmitted through the dichroic mirror and cleaned up by a detection filter before being focused through the tube lens onto the camera chip. (b) Schematic representation of epi-illumination. The excitation light is focused into the center of the back focal plane of the objective lens, flooding the sample with collimated excitation light. (c) Schematic representation of TIRF illumination. The excitation light is focused very far out in the back focal plane, so that total internal reflection occurs at the interface between the coverslip and the sample. Fluorophores are excited only very close to the coverslip within the sample (about 100 nm) by an evanescent field. (d) Schematic representation of the HILO illumination. The excitation light is focused outside in the back focal plane, but in such a way that there is no total internal reflection, but a slightly oblique excitation light sheet inside the sample. (e) Schematic representation of the illumination in a confocal laser scanning microscope (CLSM). The collimated excitation light is shone into the back focal plane of the objective, causing it to be focused in the focal plane in the sample (diffraction limited). Scanning mirrors can be used to vary the angle of incidence in the back focal plane, allowing scanning of the focus over the sample.

If the advantages of TIRF illumination are not to be used close to the cover glass, but rather deeper in the sample, HILO (highly inclined and laminated optical sheet) exposure is a compromise (Figure 13d) [115]. The focus in the back focal plane is off-center, similar to TIRF illumination. The angle Θ at which the sample is exposed remains smaller than in TIRF exposure ($\Theta \leq \Theta_{TIRF}$). As a result, a slightly oblique excitation light sheet is formed in the sample, which produces less background signal compared to wide-field illumination.

Another possibility of illumination is offered by light sheet fluorescence microscopy (LSFM) or single plane illumination microscopy (SPIM) [116,117]. Here, a thin (a few micrometers thick) light sheet is usually shone into the sample perpendicular to the detection objective. The simplest way to generate this is to focus an expanded collimated laser beam along one direction using a cylindrical lens. Since the fluorophores are excited only within the thin light sheet, light sheet images have a very low amount of out-of-focus signal and allow better sectioning (z-resolution) than wide-field images. For the same reason, photobleaching and phototoxicity of the whole sample is significantly reduced.

Light sources

While the first microscopes used the sun as a light source, today various artificial light sources can be used for illumination. The first representative for this were incandescent lamps. These heat a filament by means of electric current, so incoherent omnidirectional blackbody radiation (up to 3400 K in halogen lamps [118]) is emitted by them. Since it is blackbody radiation, i.e., approximately white light with a very broad spectrum, incandescent lamps are not very suitable for fluorescence excitation. Spectral filtering can be used to obtain a narrow enough portion of the spectrum for fluorescence excitation, but then a large part of the light output is lost.

The successor to incandescent lamps were gas-discharge lamps. Here, a gas in a transparent cylinder is ionized by means of an electric discharge. The transitions of the electronic energy levels of the atoms or molecules of the ionized gas yields an incoherent omnidirectional emission at specific spectral lines emitted by the lamp. Appropriate splitting and/or filtering of those spectral lines results in nearly monochromatic light. This is well suited for fluorescence excitation, particularly because the visible emission spectrum (especially 405 nm, 436 nm, 546 nm, and 578 nm [119]) of mercury vapor lamps is compatible for excitation of various fluorophores.

Nowadays, modern microscopes that do not require a coherent light source mainly use **LEDs** (light-emitting diodes). A Nobel Prize in Physics was awarded in 2014 "for the invention of efficient blue light-emitting diodes which has enabled bright and energy-saving white light sources" [120], which greatly enhanced the applicability of LEDs for

scientific and general lighting applications by greatly enhancing the available spectrum. LEDs are based on semiconductor diodes whose band gap corresponds to the spectral energy of the desired light. The incoherent and for most applications monochromatic (20nm typical spectral width) light is emitted omnidirectionally, but in contrast to incandescent lamps and gas discharge lamps, it can easily be given a direction with the help of appropriate optics due to the comparatively small luminous surface. LEDs are efficient, cost-effective and have a high light output. For this reason, they are widely used not only in microscopy but have replaced most other forms of illumination in everyday life.

Lasers (Light Amplification by Stimulated Emission of Radiation) are the go-to light source as soon as the microscopy technique used requires or benefits from a coherent light source. The principle of operation of lasers is based on the pumping medium (gas, solid crystal or semiconductor), which has a multi-level system, pumped by an (external) energy source (e.g. an LED), so that a population invasion occurs. The pumping medium is usually surrounded by two mirrors (one fully reflective, the other partially reflective) aligned parallel to each other, forming an optical resonator (cavity). Stimulated emission triggers an avalanche effect, whereby the atoms or molecules of the pump medium emit photons coherently (same wavelength, phase and direction). The optical resonator further enhances this effect.

Diode lasers are often used in microscopes and are nowadays available in many wavelengths. Diode lasers use an LED semiconductor as pump medium, which requires a more complex band structure than for ordinary LEDs. Due to the dimensions of the LED semiconductor, the size of the optical resonator is correspondingly small here, resulting in lower coherence lengths of the emitted laser light. However, for most microscopy applications, even a low coherence length is usually still sufficient. Diode lasers are comparatively inexpensive and enable very high output powers (up to 1 W and more). An important feature that distinguishes diode lasers from gas or solid-state lasers is the possibility of tuning the lasing wavelength via the diode temperature. The main reason for this is the temperature dependence of the refractive index of the semiconductor and the length of the laser cavity.

Diode lasers can furthermore be used to pump a solid-state crystal. This leads to the term **DPSS** (diode pumped solid state) lasers. These then have the lasing wavelength of the solid-state crystal and a much larger coherence length than pure diode lasers. DPSS lasers are usually spectrally cleaned to ensure that no light from the pumping diode laser leaks out.

Detectors

Wide-field fluorescence microscopes typically use semiconductor-based camera chips as detectors. These consist of a two-dimensional pixel array of light-sensitive photodiodes that convert incident photons of the visible spectrum into electrical charges using the internal photoelectric effect.

The basis of the square pixels is a (usually positively) doped semiconductor (e.g. silicon). Above this is an insulating layer (e.g. silicon dioxide). The top layer of each pixel is an electrode made of an optically transparent and conductive material (e.g. polycrystalline silicon) [121]. By applying a (positive) voltage to the electrode, a potential well for the minority charge carriers (electrons) is formed in the top of the semiconductor. Incident photons, whose energy is greater than that of the bandgap of the semiconductor, can lift electrons from the valence band to the conduction band in the depletion region via the internal photoelectric effect, creating an electron-hole pair. The released minority carriers (electrons) accumulate in the potential well of the pixel, while the majority carriers (holes) flow away into the interior of the semiconductor. The number of carriers in the potential well is proportional to the amount of photons interacted, as long as the potential well is not full. Nowadays there are two dominant types of camera chips (CCD and CMOS) [122], which differ primarily in the process of reading out the charge carriers (hereinafter electrons) collected in the pixels.

CCD (charged-coupled device) chips have one readout amplifier. Each pixel is therefore read out via the same electronics. By switching electric fields, the electrons of each pixel are shifted one line down. At the bottom is a non-light-sensitive shift register. From the shift register, the electrons of each pixel are shifted one by one into the readout amplifier, where they are finally amplified and counted with the help of an analog-to-digital converter [123]. CCD cameras have a comparatively low dark current, which results in a good signal-to-noise ratio. Therefore, they are particularly well suited for images with few photons (1 to 5) per pixel. If the chip is exposed during the readout process, so-called rolling readout effects occur, which can, however, be avoided by shifting the electrons to a light-insensitive duplicate of the chip that is subsequently read out (frame-transfer camera). If a pixel is overexposed (potential well overfilled), electrons can get stuck during shifting, causing so-called blooming as an artifact. Due to the low speed of CCD chips, they are not well suited for observing fast dynamics [124].

An **emCCD** (electron multiplying charged coupled device) chip is a CCD chip with an additional electron multiplication register. There, the electrons are amplified with the help of high voltages. This makes it possible to detect even single photons, but then the noise of the readout electronics increases significantly [125].

CMOS (complementary metal-oxide semiconductor) chips are active pixel sensors (APS) in which each pixel has three transistors. Two of these transistors are used for electronic communication with the readout electronics via a row and column matrix. Each column of the chip has its own readout amplifier and analog-digital converter, so that they can be read out in parallel. For this purpose, each pixel is connected row by row to the readout amplifier responsible for each column. During this process, the electrons do not leave their pixel, which is why a reset of the pixels, after the readout, is necessary before the next acquisition. By switching the third transistor of a pixel, the electrons in the potential well can flow away. CMOS chips allow high frame rates compared to CCD chips. Since each pixel has its own transistors and each column its own amplifier and analog-to-digital converter, inhomogeneities occur in the images due to the respective manufacturing tolerances. However, these can be measured and corrected in the camera's firmware or software. High-quality CMOS cameras calibrated in this way are known as sCMOS (scientific CMOS) and are characterized by high speed, low noise, homogeneity, wide dynamic range (grayscale) and high quantum efficiency (probability of detecting a photon).

Wide-field fluorescence microscopes can be operated with both CCD and (s)CMOS chips [126]. While in the past, CCD and emCCD camera systems outperformed CMOS sensors, as of today, advances in CMOS design and manufacturing techniques have made them the preferred technology for most scientific and commercial imaging applications.

Every camera has a certain amount of unwanted **noise**. There are three main causes of noise (shot, read-out and dark current), which can vary in severity depending on the camera. Shot noise, also called Poisson noise, is caused by the statistical nature of the detection process. Since each photon is detected only with a certain probability (quantum efficiency), the number N of detected photons has an uncertainty of $\sqrt{N}$ if $N \gg 1$. The read-out noise arises from the electronics of the read-out process and can be reduced by the quality of the corresponding components (amplifier, analog-digital converter). The mainly thermally induced dark current noise is based on the tunneling of electrons into or out of the potential well and can be reduced by cooling the camera chip. Read-out noise and dark current are influenced by the camera sensor, and for example, better sensor designs, and temperature control (cooling) can improve these factors. However, shot noise is a fundamental effect of light quantization, and cannot be improved upon by technical development. As of today, when using a high quality sCMOS sensor, the dominating noise contribution is shot noise.

The **Nyquist-Shannon sampling theorem** states that a spatial (or temporal) signal must be sampled at twice its maximum frequency (band limit) to fully reconstruct it [127,128]. Thus, for use as detectors in microscopes, the size of the pixels projected into the sample should be at most half the resolution limit (eq. (16)). This results in a projected

pixel size of at most a (eq. (31)). By considering the quadratic nature of the pixels, an additional factor $\sqrt{2}$ might be considered for the diagonal. The adjustment of the projected pixel size can be realized by choosing a tube lens with a corresponding focal length depending on the focal length of the objective [122].

$$a = \frac{d_{Abbe}}{2} = \frac{\lambda}{4 \cdot NA} \tag{31}$$

At this point it should be mentioned that the Nyquist-Shannon sampling theorem actually only applies to point sampling. Strictly speaking, the value of a camera pixel is the integrated signal over its square area. In addition, when imaging incoherently (as in fluorescence microscopy), frequencies close to the cut-off frequency (eq. (23)) are very strongly attenuated, which in turn suppresses aliasing artifacts. Thus, it is often viewed as an acceptable compromise if the projected pixel size is approximately equal and not strictly smaller than half the Abbe limit.

Confocal laser scanning microscopes

Confocal laser scanning microscopes (CLSM), in contrast to the classic wide-field microscope, do not illuminate the entire field of view simultaneously, but with a focused laser beam. The laser focus is created by shining collimated light into the back focal plane (see Figure 13e). The illumination volume is diffraction limited and therefore has the intensity distribution of a point spread function (PSF). Since only one point is illuminated, it is sufficient to use a point detector such as a photomultiplier tube (PMT). To acquire a two-dimensional (or three-dimensional) image, the laser focus is scanned over the sample using two scanning mirrors (one each for the x and y directions) synchronized with the detector [19,99].

Common scanning microscopes are very slow compared to wide-field microscopes. The acquisition speed varies depending on the scanning speed, the desired resolution, and the field of view. Typically, only a few frames per second (fps) are possible. At high scanning speeds, very high local intensities are required to excite the fluorescence, which is technically difficult to realize and can damage the biological sample [19,99].

By inserting a pinhole in the intermediate image plane in front of the detector, a large part of the out-of-focus signal can be blocked, while signal within the focus is hardly blocked [129]. In addition, there is a gain in resolution the smaller the pinhole is closed. With an infinitesimally small opening, the theoretical cut-off frequency doubles, which cannot be achieved in practice due to the very strong attenuation of high frequencies that are lost in the noise. In addition, with a closed pinhole, no more light reaches the

detector, so no image can be acquired [130]. Because both the excitation volume and the detection of the fluorescence are diffraction limited, the effective PSF is the product of the PSF for excitation $PSF_{ex}(\vec{r})$ and the PSF for detection $PSF_{det}(\vec{r})$:

$$D(\vec{r}) = [S(\vec{r}) \cdot I(\vec{r})] * \left(PSF_{ex}(\vec{r}) \cdot PSF_{det}(\vec{r})\right) \approx [S(\vec{r}) \cdot I(\vec{r})] * PSF^2(\vec{r}) \qquad (32)$$

Neglecting the Stokes shift between excitation and detection, the effective PSF can be taken as the square of the actual PSF. This effective PSF is narrower, which is why the effective optical transfer function (OTF) becomes wider, and generally leads to a gain in contrast and resolution. If the PSF is approximated by a Gaussian bell curve and squared, this results in a reduced half-width by a factor of $\sqrt{2}$ for an infinitesimally small pinhole [19], which is often mentioned as a resolution criterion for confocal (and similar) microscopes:

$$d_{conf} = \frac{d_{Abbe}}{\sqrt{2}} = \frac{\lambda}{2\sqrt{2} \cdot NA} \qquad (33)$$

In practice, this maximum resolution is not achieved with classical confocal microscopes, since the aperture in the detection must be completely closed for this purpose and thus all signal is blocked before detection [130]. Modern systems based on the confocal approach are known under the generic term ISM (image scanning microscopy). They often use small camera chips, with few pixels (e.g. 32 concentrically arranged pixels), instead of a point detector with a pinhole. This allows the pinhole to be digitally adjusted, solving the closed aperture problem. Ultimately, however, such systems must always make tradeoffs between background reduction, effective resolution gain, signal-to-noise ratio, and speed.

Whether confocal or ISM microscopes are considered super-resolution is ultimately a matter of definition. They achieve resolutions just beyond the Abbe limit but are still diffraction limited. Their strengths lie primarily in high-contrast and low-background images and are therefore standard equipment in many laboratories alongside wide-field fluorescence microscopes.

2.1.5 Deconvolution

Based on eq. (24), we know that the formation of an image in a microscope can be described as a convolution of the sample (multiplied by the illumination) with the point spread function (PSF). The (fluorescent) emission $E(\vec{r})$ of the sample can be understood as multiplication of the sample by the exposure. Considering the noise of the detector (camera) a noise term $n(\vec{r})$ must be added:

$$D(\vec{r}) = [S(\vec{r}) \cdot I(\vec{r})] * PSF(\vec{r}) + n(\vec{r}) = E(\vec{r}) * PSF(\vec{r}) + n(\vec{r}) \tag{34}$$

In frequency space, the result is therefore:

$$\tilde{D}(\vec{k}) = \tilde{E}(\vec{k}) \cdot OTF(\vec{k}) + \tilde{n}(\vec{k}) \tag{35}$$

The idea behind deconvolution is to get a better smoothed or sharper image by undoing the convolution operation [131]. It should be noted that for the ranges where the OTF is zero (above the cut-off frequency eq. (23)) no information is detected and therefore cannot be recovered without further assumptions. This means that deconvolution generally does not provide an increase in resolution but can only increase the contrast of attenuated signals [131]. Nowadays, a wide range of algorithms are available [132]. A popular approach for the estimation $A(\vec{r})$ of the real signal $E(\vec{r})$ is done by the convolution of the measured signal $D(\vec{r})$ with a filter function $F(\vec{r})$:

$$A(\vec{r}) = D(\vec{r}) * F(\vec{r}) \quad \leftrightarrow \quad \tilde{A}(\vec{k}) = \tilde{D}(\vec{k}) \cdot \tilde{F}(\vec{k}) \tag{36}$$

For most methods, the three-dimensional PSF (or OTF in frequency space) is elementary for deconvolution. Ideally, one measures this for the particular microscope with which the image was acquired. Often, however, it is not possible to measure the PSF or it requires a lot of effort. In this case, various models (e.g. the Born-Wolf Model) are available to estimate the PSF [94,131,133].

An intuitive but at the same time naive choice of $F(\vec{r})$ is to simply invert the convolution by dividing the OTF in frequency space:

$$\tilde{F}_{inv}(\vec{k}) = \frac{1}{OTF(\vec{k})} \tag{37}$$

This leads to:

$$\tilde{A}(\vec{k}) = \frac{\tilde{D}(\vec{k})}{OTF(\vec{k})} = \tilde{E}(\vec{k}) + \frac{\tilde{n}(\vec{k})}{OTF(\vec{k})} \tag{38}$$

With this approach, the noise is amplified very strongly, since the noise usually has high frequencies and especially at these frequencies the OTF is very small and thus the noise term grows disproportionately.

Wiener deconvolution

A cleverer variant is the Wiener deconvolution, also called Wiener filter. In contrast to eq. (37), it is also suitable for filtering images with a poor signal-to-noise ratio. The original idea of the associated filter function is based on minimizing the mean square deviation between $E(\vec{r})$ and $A(\vec{r})$ and ultimately leads to [134]:

$$\begin{aligned}\tilde{F}_{wiener}(\vec{k}) &= \frac{1}{OTF(\vec{k})} \cdot \frac{\left|OTF(\vec{k})\right|^2}{\left|OTF(\vec{k})\right|^2 + \frac{\tilde{n}(\vec{k})}{P(\vec{k})}} \\ &= \frac{1}{OTF(\vec{k})} \cdot \frac{\left|OTF(\vec{k})\right|^2}{\left|OTF(\vec{k})\right|^2 + \frac{1}{SNR(\vec{k})}}\end{aligned} \tag{39}$$

With $P(\vec{k})$ as power spectral density and $SNR(\vec{k}) = P(\vec{k})/\tilde{n}(\vec{k})$ as frequency-dependent signal-to-noise ratio. Without noise or when the signal-to-noise ratio is very high, the Wiener filter simplifies to division by the OTF, as eq. (37). Since the signal-to-noise ratio is mostly unknown, this value must be estimated by an appropriate parameter in practical applications.

Richardson-Lucy deconvolution

Using the maximum likelihood approach with a Poisson distribution for the noise [135] yields the iterative Richardson-Lucy deconvolution [136,137]:

$$A_{n+1}(\vec{r}) = A_n(\vec{r}) \cdot \left(\frac{D(\vec{r})}{A_n(\vec{r}) * PSF(\vec{r})} * PSF^*(\vec{r}) \right) \tag{40}$$

With $PSF^*(\vec{r})$ as the flipped PSF (mirrored at the origin). The assumption of Poisson noise is legitimate especially when the dominant noise is shot noise. However, acquisitions with other noise distributions (e.g. Gaussian distribution) can also be filtered using Richardson-Lucy deconvolution.

2.2 Super-resolution microscopy

The field of super-resolution microscopy, also known as optical nanoscopy, encompasses, with more or less sharp delineation, all those microscopy techniques that enable spatial resolutions below the Abbe limit. Depending on the method and effort, resolutions down to a few nanometers are possible [28,36,138].

First of all, however, it must be emphasized again at this point that the Abbe limit is physically fundamental. Even with the highest quality components (objective, camera, ...) spatial frequencies above the cut-off frequency eq. (23) are attenuated to zero. Therefore, the information reaching the camera is always band-limited. Thus, no structures below the Abbe limit can be resolved with a single acquisition. In abstract terms, super-resolution microscopy is based on converting spatial sample information into temporal information. Therefore, many techniques require more than a single image of the sample to decode the temporal information back into spatial information. From eq. (24), it is known that the PSF is convolved not only with the sample, but with the product of the sample and illumination. By introducing additional information about the illumination or the fluorescent response of the sample (and often its deterministic or stochastic variation over multiple acquisitions), additional information about the sample can be obtained [60].

In 2014, the Nobel Prize in Chemistry for the development of super-resolved fluorescence microscopy was awarded [29] to Eric Betzig [139,140], Stefan W. Hell [30,57,141] and William E. Moerner [142,143]. Due to the continuous development of super-resolution techniques, diverse methods are available today [144]. These can be classified into three basic techniques: SMLM, STED, and SIM. Each approach brings its strengths and weaknesses, which is why different methods are suitable depending on the application [28]. In most cases, compromises must be made between imaging speed, resolution, and observation time due to bleaching of fluorophores or degradation of the biological sample (cell death). Each method or microscope requires specific conditions. Accordingly, super-resolution measurements are often associated with high costs, special know-how, adaptations of the microscope, and/or special sample preparation. In addition, not all methods are live-cell compatible and some require fluorophores with special properties, such as nonlinearity or blinking [36,60].

2.2.1 Stimulated emission depletion

STED (stimulated emission depletion) microscopy is based on confocal microscopes (see section 2.1.4) [19]. The idea of the method was developed in 1994 by Stefan W. Hell and Jan Wichmann [30]. The first experimental realization was achieved in 1999 by Thomas Klar and Stefan W. Hell [145]. By using the donut-shaped STED beam, the linear response of the sample to light is modified. Specifically, the STED beam causes excited fluorophores to transition from the $S_1 v_0$ level to a high vibrational level v_m of the ground state S_0 with a probability that depends on the STED intensity. As a result, these fluorophores are no longer available for fluorescence and are effectively turned off. With sufficient intensity, the usual fluorescence can even be completely suppressed [146]. The STED wavelength is chosen as short as possible so that the transition from $S_1 v_0$ to $S_0 v_m$ is favored. However, care must be taken to ensure that the STED wavelength is sufficiently red-shifted relative to the excitation wavelength to avoid re-excitation of the fluorophores [147]. The use of a high quality optical long pass filter with a steep slope just above the STED wavelength ensures that only the fluorescence photons and not the STED photons are detected.

The donut-shaped STED beam is shaped using a special phase mask and positioned so that the excitation focus of the confocal microscope is in the center, at the minimum, of the donut. In order for the scanning mirrors to allow scanning of the sample for both the excitation and STED beams, it is necessary for the two beams to have been superimposed beforehand with extremely precise alignment. Only ultrashort (picosecond) pulsed lasers are suitable as light sources for the STED beam so that the required local STED intensities can be achieved. The STED pulse is irradiated immediately after excitation to deplete the excited fluorophores in the STED donut. This reduces the effective excitation volume in the center of the STED donut, which ultimately results as a narrowing of the point spread function (PSF). Since the size of the STED donut is diffraction limited, it cannot be reduced arbitrarily. Nevertheless, the effective excitation volume and thus the PSF can be reduced by increasing the intensity of the STED donut [30,148]. The STED resolution results from an additional STED term in the denominator of the Abbe limit:

$$d_{STED} = \frac{d_{Abbe}}{\sqrt{1 + I_{STED}/I_{sat}}} = \frac{\lambda}{2NA \cdot \sqrt{1 + I_{STED}/I_{sat}}} \tag{41}$$

Here, I_{sat} corresponds to the fluorophore-specific saturation intensity at which the probability of a fluorescence process has dropped to $\sim 1/e$ [149]. By increasing maximal focal intensity I_{STED}, infinite resolution can theoretically be achieved [150]. However, in practice, technical hurdles exist that limit I_{STED} and biological samples are damaged or destroyed at such high intensities. Typically, resolutions of 120 nm to 60 nm are

achieved with commercial STED microscopes [28]. With custom-made STED microscopes optimized for the specific biological application, resolutions below 50 nm can be achieved [39,40]. By artificial preparation with carbon dots, even resolutions of 30 nm could be achieved [151]. The highest resolution of 2.4 nm could be achieved when studying non-biological nitrogen vacancies in diamonds [152].

Since STED is based on confocal microscopes, this method has a low acquisition speed. In addition, a compromise must be made between the achievable resolution and live cell compatibility, due to photo-toxicity. Once the very complicated STED microscope with its sensitive and precise opto-mechanics is in place, it is possible to directly generate super-resolution images. These do not necessarily have to be post-processed or reconstructed, as is the case with many other super-resolution methods. STED offers a wide range of biological applications [148,149,153–155]. Despite the high STED intensities required, it is possible to obtain life cell images and dynamic processes [156,157]. During observations of colloidal-crystal nanostructures, STED was able to achieve up to 200 frames per second (fps) [158]. Due to continuous development, the first two-color STED microscopes now exist [159,160].

In the zoo of super-resolution methods, STED belongs to the generic term RESOLFT (reversible saturable optical fluorescence transitions). RESOLFT describes all those methods that deterministically suppress the fluorescence process using light [161]. However, STED is by far the best known RESOLFED method. Among others, GSD (ground-state depletion, uses triplet states) and the use of fluorophores (often proteins) that can be deterministically turned on or off also belong to the RESOLFT methods [57,161].

2.2.2 Single molecule localization microscopy

SMLM (single molecule localization microscopy) is based on the stochastic blinking or switching of fluorophores [32]. This can be considered as additional information about the fluorescent response of the sample, which can ultimately be converted into additional sample information. The basic idea is that very few individual (separable) fluorophores are active at any given time, so the position of the fluorophore can be determined by fitting the point spread function (PSF) [32]. Usually, Gaussian fits are used to approximate the PSF [162,163]. The lateral xy position, height, and width of the PSF resulting from the fit provide information about the xy position, photon number, and defocus of the fluorophore. The error estimate of the fit results is related to the achievable resolution and depends on multiple parameters [164]. The localization accuracy σ_{loc} depends mainly on the number of photons N emitted and detected by the fluorophore [140]:

$$\sigma_{loc} \sim \frac{1}{\sqrt{N}} \tag{42}$$

Thomson et al. and Mortensen et al. demonstrated that localization accuracy is as follows [165,166]:

$$\sigma_{loc} = \sqrt{\frac{\sigma_{PSF}^2 + \frac{a^2}{12}}{N}\left(\frac{16}{9} + \frac{8\pi b\left(\sigma_{PSF}^2 + \frac{a^2}{12}\right)}{Na^2}\right)} \tag{43}$$

Using the Gaussian standard deviation of the PSF σ_{PSF}, the area of a camera pixel a^2 and the average background noise per pixel b. The higher σ_{loc}, the higher the labeling density must be, to ensure that areas without localization are not due to missing fluorophores but in fact correspond to the structure under investigation. In biological applications, tens of nanometers of resolution are achieved [32].

To obtain a super-resolution image, several thousand individual frames are usually acquired in which only a few fluorophores are active. This so-called blinking [41] ensures that there is sufficient distance between the fluorophores in each individual frame so that their PSFs do not overlap, i.e. they can be separated [167,168].

To achieve the blinking of fluorophores, there are different approaches. **dSTORM** (direct stochastic optical reconstruction microscopy) [45,46] uses special fluorophores [169], which after a certain average amount of emitted fluorescence photons are randomly switched to the triplet state T_1 by intersystem crossing and thus are not available for fluorescence for a longer time until the phosphorescence process is completed. **STORM** (stochastic optical reconstruction microscopy) [44] is based on a similar approach, but the fluorophores are not switched off randomly after a certain number of fluorescence processes but are switched off stochastically for a longer time by illumination with an additional (usually blue) laser. **PALM** (photo-activated localization microscopy) [43] also uses switchable fluorophores (mostly proteins) that are switched off by default [140]. By a pulse with an additional activation laser (often 405 nm) these fluorophores can be activated stochastically. The pulse duration can be used to adjust the number of activated fluorophores. After activated fluorophores have been excited by the excitation laser and have subsequently completed the fluorescence process, they are usually photo-destroyed and, in contrast to dSTORM and STORM, cannot be reactivated or excited. While dSTORM and STORM use mostly red lasers for excitation, PALM uses rather blue lasers for excitation. There are also methods that work with much higher blink rates. **SOFI** (super-resolution optical fluctuation microscopy), as an example, is based on the temporal correlation of the pixels and not on a localization approach [58,170,171].

Regardless of the specific method for blinking, all that is needed for SMLM is a standard wide-field fluorescence microscope equipped with the appropriate lasers and a good camera. Especially due to the development of the camera market in the last 10 years, SMLM can be implemented comparatively inexpensively. Thus, SMLM images could already be acquired with industry-grade and cell phone cameras [81,172].

Strictly speaking, the measurement result of an SMLM image is not a super-resolved image, but a list of localizations. From this list the super-resolved images can be rendered with various settings and filters [173]. The creation of the localization list is computationally and time consuming, while the rendering is comparatively fast. QuickPALM [174], RapidSTORM [175] and ThunderSTORM [176] are available as appropriate software, each with special features and drawbacks [177].

There are a variety of biological and medical applications for SMLM [178–182]. The comparatively long acquisition time and high laser intensities for one super-resolved image make the technique especially interesting for fixed samples. Nevertheless, there is some live cell compatibility conditionally at, for example, 60 nm resolution and 25 s per super-resolved frame [168,183]. There are also approaches to generate super-resolution SMLM images in real time [184]. By introducing asymmetries along the optical axis (z dimension) into the PSF, it is possible to obtain three-dimensional SMLM images [185,186]. Multi-color acquisitions are also feasible to a certain extent [187,188].

2.2.3 Structured illumination microscopy

The third basic super-resolution technique is Structured Illumination Microscopy (SIM). This is based on sample illumination with varying sinusoidal intensity patterns and can recover sample information above the cut-off frequency [28]. The (linear) SIM [189] presented here, developed by Heintzmann et al. [47] and Gustafsson et al. [33], permits doubling of lateral resolution down to about 100 nm and further enables axial resolution enhancement down to 300 nm [28]. SIM has established itself in the zoo of super-resolution techniques and continues to be developed today [28,65,190]. Since STED and SMLM require high excitation intensities, very long illumination times and/or special dyes (fluorophores), SIM could establish itself mainly as the super-resolution method for live cell experiments [28,65,86,87,190]. The excitation intensities required for SIM are comparable to those of a wide-field microscope. For the reconstruction of one super-resolved image, only 9 or 15 individual raw images with different phase shifts and orientations of the illumination pattern are required to unmix the frequency components introduced by the structured illumination [33,34,48].

Non-linear SIM, which requires fluorophores with a non-linear response of fluorescence to illumination intensity, typically achieved by employing switchable fluorophores and introducing an additional (also structured) switching wavelength, enables resolutions as

low as 50 nm [52,191]. The tradeoff is a limited selection of suitable fluorophores, a higher number of raw images needed, and more complex instrumentation.

SIM can also be combined with SMLM, resulting in a doubling of localization accuracy [49–51]. Here, all drawbacks of SMLM, mainly the very high count of raw images needed for a reconstruction, still apply.

The superposition of the structures of the sample with the illumination pattern results in so-called moiré effects, from which actually hidden information about the sample can be obtained [33]. Illustratively, by illuminating the sample with sinusoidal patterns, which have a spatial frequency close to the cut-off frequency, high-frequency sample information (above the cut-off frequency) is shifted to lower ones. This allows them to be collected by the optical system (microscope) and recovered using a reconstruction algorithm. In order to understand SIM, it is necessary to know the mathematical basis behind the process. The following explanations are based on the lecture of Dr. Marcel Müller, who is the leading developer of the SIM reconstruction software fairSIM [192,193].

General principle

From section 2.1.3 we know that the image formation in a microscope can be formulated via the convolution of the sample $\tilde{S}(\vec{k})$ with the illumination pattern $\tilde{I}(\vec{k})$ multiplied by the OTF [34,194,195]:

$$\widetilde{D}(\vec{k}) = \left[\tilde{S}(\vec{k}) * \tilde{I}(\vec{k})\right] \cdot OTF(\vec{k}) \tag{44}$$

In general, a sinusoidal illumination pattern $I_{q,n}(\vec{r})$ can be described as a sum of cosine terms:

$$I_{q,n}(\vec{r}) = I_0 \sum_{m=0}^{M} a_{q,m} \cdot \cos\left(2\pi m\left(\vec{r}\vec{p}_q + \phi_n\right)\right) \tag{45}$$

The following definitions are used:

- $\vec{p}_q$: Wave vector, spacing and orientation of the SIM pattern
  - q: Pattern orientation index
  - Q: Amount of orientations
- ϕ_n: Phase shift of the SIM pattern
  - n: Phase shift index
  - N: Amount of phases
- m: Harmonic index
  - M: Amount of harmonics
- $a_{q,m}$: Modulation strength of a certain harmonic

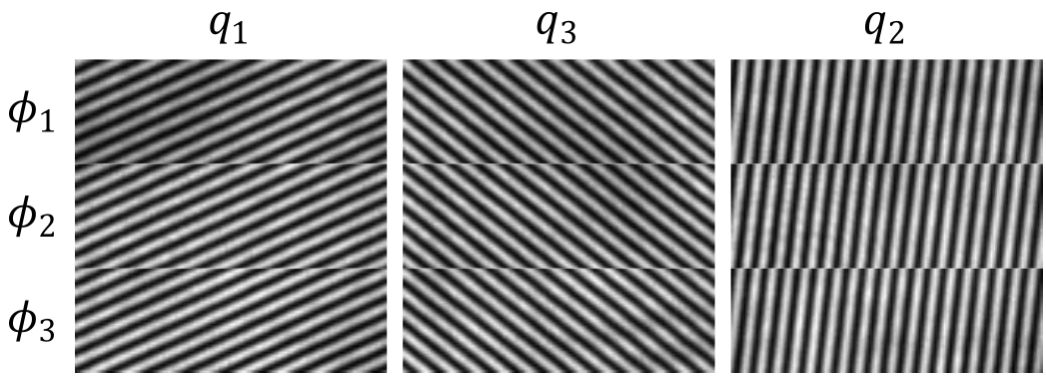

Figure 14: Example of SIM illumination patterns measured in the sample plane

SIM illumination patterns acquired via the detection camera of a two-beam SIM microscope with an excitation wavelength of 631 nm. To obtain good visibility of the pattern, a reflective metal surface was positioned in the sample plane. The phase shifts and orientations differ by 2/3 π and 60°, respectively. Although the frequency of the pattern here is close to the Abbe limit, the images are very high in contrast thanks to the coherent imaging process. In the case of incoherent imaging, e.g. with a fluorescent surface layer, the contrast would be much worse.

It is important that the sum starts at $m = 0$ and not at 1, yielding the addition of a constant off-set intensity $a_{q,0}$. Thus, by choosing $a_{q,0}$ appropriately, negative illumination intensities can be mathematically excluded, which are physically impossible. For the description of a simple sinusoidal pattern $M = 1$ is chosen (see Figure 14). For the following calculations, the representation of the illumination pattern in frequency domain via the Fourier transform is essential:

$$\tilde{I}_{q,n}(\vec{k}) = I_0 \sum_{m=0}^{M} a_{q,m} \cdot e^{\pm i m \phi_n} \cdot \delta(\vec{k} \mp m \cdot \vec{p}_q) \tag{46}$$

Here, the sum over cosine terms becomes a sum over the multiplication of an exponential function with two delta peaks. The exponential function reflects the phase shift ϕ_n, while the two delta peaks represent the frequency and the orientation of the pattern. In frequency domain, the image formation for a SIM microscope results in the following:

$$\widetilde{D}_{q,n}(\vec{k}) = \left[I_0 \sum_{m=0}^{M} a_{q,m} \cdot e^{\pm i m \phi_n} \cdot \delta(\vec{k} \mp m\vec{p}_q) * \tilde{S}(\vec{k}) \right] \cdot OTF(\vec{k}) \tag{47}$$

Using the convolution theorem for Dirac delta functions eq. (26), the convolution of the delta peaks $\delta(\vec{k} \mp m\vec{p}_q)$ with the sample $\tilde{S}(\vec{k})$ can be described as a shift of the sample information to the positions of the delta peaks:

$$\widetilde{D}_{q,n}(\vec{k}) = \left[I_0 \sum_{m=0}^{M} a_{q,m} \cdot e^{\pm im\phi_n} \cdot \tilde{S}(\vec{k} \mp m\vec{p}_q) \right] \cdot OTF(\vec{k}) \tag{48}$$

This transition of convolution into a shift of sample information is the central aspect that makes SIM microscopy possible. By shifting high frequency sample information to lower frequencies, this information is preserved when imaged by a band-limited optical system (microscope). However, to obtain a super-resolution image, it is necessary to make this high-frequency sample information visible. More precisely, the sample information shifted to lower frequencies must be separated (band separation) and shifted back to the high original frequencies. The band separation process is based on a linear system of equations which can be derived from eq. (48). For this purpose, it is useful to define the band vector $\widetilde{\boldsymbol{T}}'_{\boldsymbol{q}}(\vec{k})$ with $m = -M \dots -0, +0 \dots M$ entries (with double 0):

$$\widetilde{\boldsymbol{T}}'_{\boldsymbol{q}}(\vec{k}) \to \tilde{T}_{m,q}(\vec{k}) = \tilde{S}(\vec{k} - m\vec{p}_q) \cdot OTF(\vec{k}) \cdot I_0 \tag{49}$$

These measurements $\widetilde{D}_{q,n}(\vec{k})$ can be taken as the measurement vector $\widetilde{\boldsymbol{D}}'_{\boldsymbol{q}}(\vec{k})$:

$$\widetilde{\boldsymbol{D}}'_{\boldsymbol{q}}(\vec{k}) \to \widetilde{D}_{q,n}(\vec{k}) \tag{50}$$

Furthermore, we define a band separation matrix $\overline{\boldsymbol{E}}$:

$$\overline{\boldsymbol{E}} \to \overline{E}_{mn} = a_{q,m} \cdot e^{im\phi_n} \tag{51}$$

In a summation notation, eq. (48) for N measurements result in the following linear system of equations:

$$\sum_{n=1}^{N} \widetilde{D}_{q,n}(\vec{k}) = \sum_{n=1}^{N} \sum_{m=-M}^{M} \overline{E}_{mn} \cdot \tilde{T}_{m,q}(\vec{k}) \tag{52}$$

Equivalently, the linear system of equations can be formulated compactly:

$$\widetilde{\boldsymbol{D}}'_{\boldsymbol{q}}(\vec{k}) = \overline{\boldsymbol{E}}\, \widetilde{\boldsymbol{T}}'_{\boldsymbol{q}}(\vec{k}) \tag{53}$$

To obtain $\widetilde{\boldsymbol{T}}'_{\boldsymbol{q}}(\vec{k})$ this system of equations can be solved by inverting the band separation matrix $\overline{\boldsymbol{E}}$:

$$\overline{\boldsymbol{E}}^{-1}\, \widetilde{\boldsymbol{D}}'_{\boldsymbol{q}}(\vec{k}) = \widetilde{\boldsymbol{T}}'_{\boldsymbol{q}}(\vec{k}) \tag{54}$$

In order that $\overline{\boldsymbol{E}}$ is really invertible and thus the system of equations becomes uniquely solvable, $N = M + 1$ measurements $\widetilde{D}_{q,n}(\vec{k})$ with different phase shifts ϕ_n must be acquired [194]. For the matrix $\overline{\boldsymbol{E}}$ to be well conditioned, the phases ϕ_n should be equally spaced, so usually implementations aim to achieve $\phi_{shift} = n \cdot \frac{2\pi}{N} + \phi_{global}$. For the case $M = 1$ with $N = 3$ (e.g. for the three-phase two-beam SIM), eq. (54) looks as follows:

$$\begin{pmatrix} 2a_{q,0} & a_{q,1}e^{i\phi_1} & a_{q,2}e^{-i\phi_1} \\ 2a_{q,0} & a_{q,1}e^{i\phi_2} & a_{q,2}e^{i\phi_2} \\ 2a_{q,0} & a_{q,1}e^{i\phi_3} & a_{q,2}e^{i\phi_3} \end{pmatrix}^{-1} \begin{pmatrix} \widetilde{D}_{q,1}(\vec{k}) \\ \widetilde{D}_{q,2}(\vec{k}) \\ \widetilde{D}_{q,3}(\vec{k}) \end{pmatrix} = \begin{pmatrix} \tilde{S}(\vec{k}) \cdot OTF(\vec{k}) \cdot I_0 \\ \tilde{S}(\vec{k} - \vec{p}_1) \cdot OTF(\vec{k}) \cdot I_0 \\ \tilde{S}(\vec{k} + \vec{p}_2) \cdot OTF(\vec{k}) \cdot I_0 \end{pmatrix} \quad (55)$$

The parameters $a_{q,m}$ and ϕ_n can usually be calculated or estimated from the raw SIM images. Note that the separated bands $\tilde{T}_{m,q}(\vec{k})$ can be extracted from the raw data $\widetilde{\boldsymbol{D}}'_{\boldsymbol{q}}(\vec{k})$ without knowledge of the wave vector $\vec{p}_q$, so the band separation step can be carried out without knowledge of the precise pattern orientation and spacing.

In the right part of eq. (55) (the band vector $\widetilde{\boldsymbol{T}}'_{\boldsymbol{q}}(\vec{k})$) the first row corresponds to the wide-field spectrum. The second and third rows correspond to the frequency-shifted spectra containing sample information above the cut-off frequency. These can now be shifted back to the position in frequency space:

$$\tilde{T}_{m,q}(\vec{k}) = \tilde{S}(\vec{k} - m\vec{p}_q) \cdot OTF(\vec{k}) \cdot I_0 \quad \rightarrow \quad \tilde{T}_{m,q}(\vec{k} + m\vec{p}_q) = \tilde{S}(\vec{k}) \cdot OTF(\vec{k} + m\vec{p}_q) \cdot I_0 \quad (56)$$

The resulting frequency space thus becomes larger (Figure 15a,c,d), which results in a resolution increase along the orientation of the wave vector $\vec{p}_q$ in the spatial domain (Figure 15b,f,g). For an isotropic resolution increase it is therefore necessary to acquire the sample with different orientations q (mostly $Q = 3$) with $N = M + 1$ phase shifts ϕ_n of the illumination pattern each (Figure 15e,h) [195]. The number of required SIM raw images is therefore formed by the product of Q and N. For the two most frequent SIM realizations, the following requirement of SIM raw images results for the reconstruction of one super-resolved image:

- Two-beam SIM: $M = 1 \rightarrow N = 3$ with $Q = 3$ → 9 SIM raw images
    - Pure sine pattern, only the fundamental frequency without additional harmonics
- Three-beam SIM: $M = 2 \rightarrow N = 5$ with $Q = 3$ → 15 SIM raw images
    - Sinusoidal pattern, composed of the fundamental frequency and the first harmonic

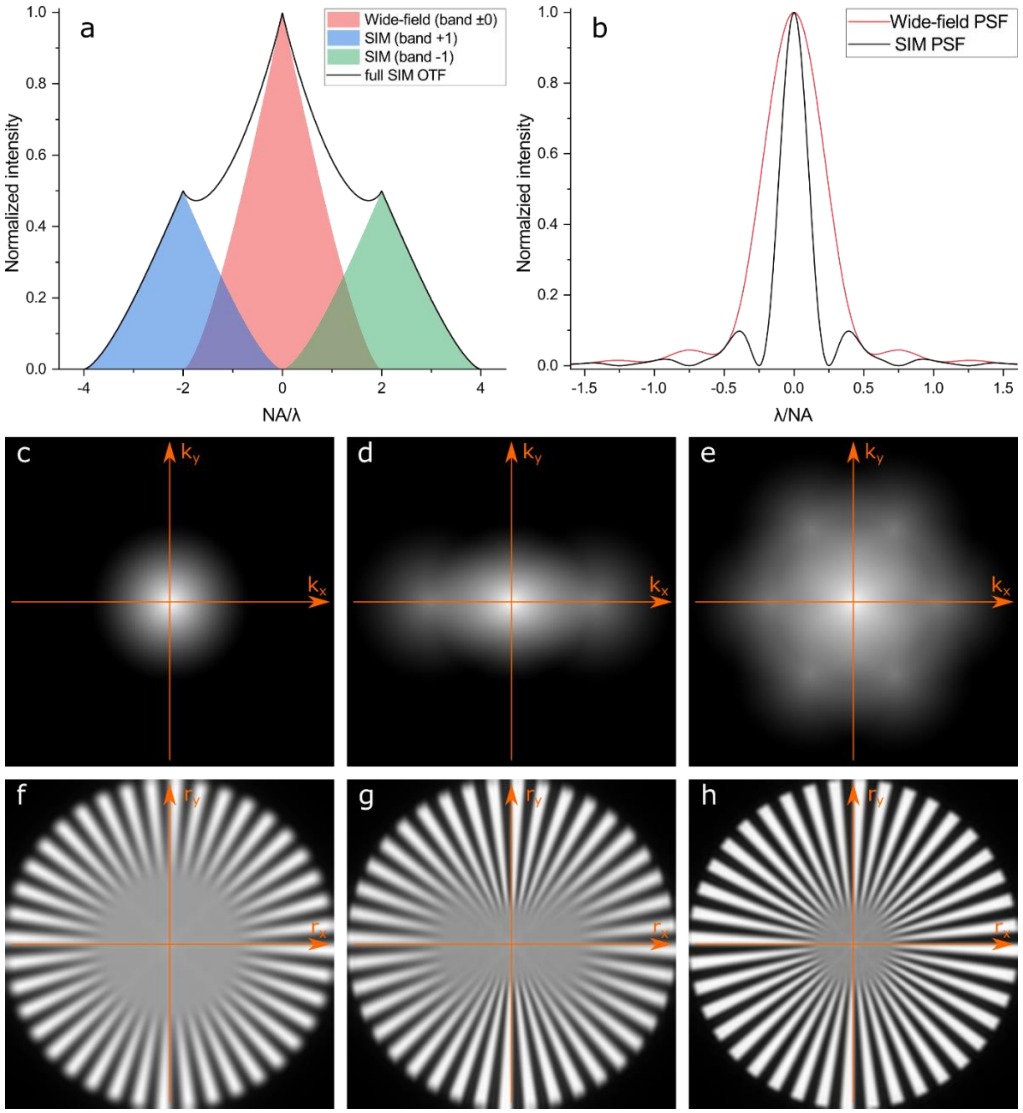

Figure 15: SIM-OTF, effective SIM-PSF and image formation

(a) Example OTF with ideal modulation contrast of a two-beam SIM microscope $M = 1$, with the two frequency-shifted SIM bands ($m = +1, -1$), the wide-field band ($m = +0, -0$) and the resulting entire SIM OTF. The whole SIM OTF is much wider than that of the wide-field, so higher-frequency information is preserved. (b) Wide-field and effective SIM PSF, the effective SIM PSF is obtained by the (inverse) Fourier transform of the total SIM OTF. The effective SIM-PSF is much narrower than that of the wide-field, resulting in higher lateral resolution. (c) Lateral wide-field OTF in frequency domain. (d) Lateral SIM OTF in frequency domain for $Q = 1$ angles. (e) Lateral SIM OTF in frequency domain for $Q = 3$ angles, each 60° apart, so that the OTF increases nearly isotropically with respect to the wide-field OTF. The SIM OTF fills the frequency space significantly more than the wide-field OTF, which provides in an increase in resolution by up to a factor of two. (f-h) Simulated image formation of a test object in wide-field (f), with SIM for $Q = 1$ angles (g) and with SIM for $Q = 3$ angles (h). The high frequencies (fine structures) in the center of the test object are attenuated much more in the wide-field and fall to zero sooner than is the case for SIM. This allows structures to be resolved that cannot be seen in the wide-field.

Both the relative phase shifts and the pattern orientations should be equidistant to each other to allow the best possible reconstruction. For a two-beam SIM microscope, for example, this means [34]:

$$\Delta\phi = \phi_2 - \phi_1 = \phi_3 - \phi_2 = \phi_1 - \phi_3 = \frac{2}{3}\pi \qquad \Delta q = q_2 - q_1 = q_3 - q_2 = q_1 - q_3 = 60°$$

Display and deconvolution of SIM images

A simple, yet at the same time naive, representation of a SIM reconstruction in frequency domain would be the sum over the back-shifted spectra $\tilde{T}_{m,q}(\vec{k} + m\vec{p}_q)$:

$$\tilde{S}^{SIM}_{naive}(\vec{k}) = \sum_{m=-M,q=1}^{M,Q} \tilde{T}_{m,q}(\vec{k} + m\vec{p}_q) = \sum_{m=-M,q=1}^{M,Q} \tilde{S}(\vec{k}) \cdot OTF(\vec{k} + m\vec{p}_q) \cdot I_0 \qquad (57)$$

Just as with wide-field images, the attenuation by the OTF in each band can be partially compensated for SIM images by means of deconvolution. A simple division of the bands by the OTF and the intensity I_0, however, would unintentionally strongly amplify the noise. To circumvent this problem, the Wiener filtering from eq. (39) can be used, which allows the SIM reconstruction to be represented as follows:

$$\tilde{S}^{SIM}_{Wiener}(\vec{k}) = \frac{\sum_{m=-M,q}^{M,Q} \tilde{T}_{m,q}(\vec{k} + m\vec{p}_q) \cdot OTF(\vec{k} + m\vec{p}_q)}{\omega^2 + \sum_{m=-M,q}^{M,Q} OTF^2(\vec{k} + m\vec{p}_q) \cdot I_0} \qquad (58)$$

Here ω is the Wiener parameter which describes the signal-to-noise ratio based on Gaussian noise and must be chosen accordingly. The Gaussian noise is a sufficient approximation for the dominating Poisson noise if the signal-to-noise ratio is sufficient. Often, $\tilde{S}^{SIM}_{Wiener}(\vec{k})$ is further multiplied by an apodization function $A(\vec{k})$, which serves to reduce the ringing artifacts of the first side maxima of the SIM PSF (Figure 15b) and make the filtered SIM reconstruction look like a wide-field image with more resolution [194]. One of several possibilities for $A(\vec{k})$ is:

$$A(\vec{k}) = 1 - \frac{|\vec{k}|}{k_{max} + M|\vec{p}|} \qquad (59)$$

In particular, this minimizes the noise in the reconstructed images. This ultimately leads to the super-resolved standard representation of SIM reconstructions [34,194]:

$$\tilde{S}^{SIM}_{std.}(\vec{k}) = \tilde{S}^{SIM}_{Wiener}(\vec{k}) \cdot A(\vec{k}) \qquad (60)$$

Filtering of SIM data is also possible with other filters (e.g. Richardson-Lucy deconvolution eq. (40)) and can be a better or nicer representation, depending on the case [196]. The representation and filtering of SIM reconstructions are constantly

developed further whereby today among other things special filters for SIM (e.g. Hessian filtering [197]), different reconstruction algorithms [198,199], and tools for the quality analysis of SIM reconstructions are available [200].

The reconstruction procedure presented above can be performed among others [201–203] with the software "fairSIM" [193]. In addition to the reconstruction algorithm, this software contains many other features, such as estimation of the parameters required for the reconstruction from the raw images [199,204].

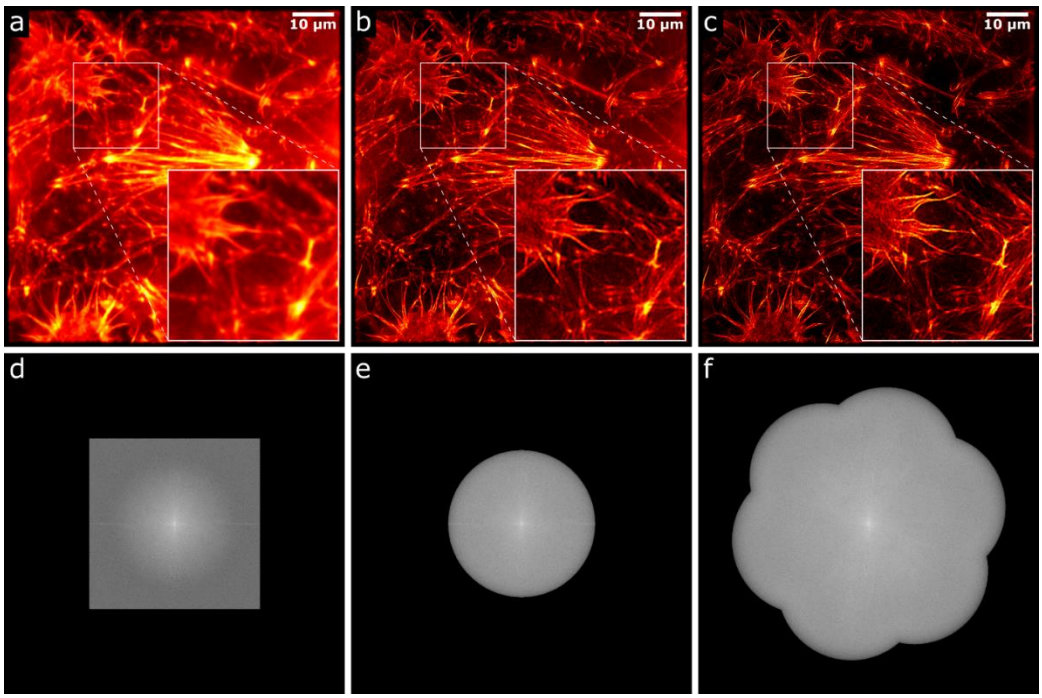

Figure 16: SIM compared to wide-field and Wiener-filtered wide-field

Actin cyto-skeleton of U2OS imaged at approximately 525nm fluorescence [93] using a (three-beam) DeltaVision OMX v4 SIM microscope reconstructed via fairSIM [193]: wide-field (a, d), Wiener-filtered wide-field (b, e), and SIM reconstruction (c, f) in the spatial domain (a-c) and frequency domain (d-f). In the spatial domain, it can be seen how the SIM reconstruction can resolve structures not seen in the wide-field, or Wiener-filtered wide-field. The frequency space of the wide-field initially appears to be larger than that of the Wiener-filtered wide-field, but these regions are above the cut-off frequency in the wide-field and therefore contain only noise and no sample information, which is why they were specifically filtered out in the Wiener-filtered wide-field. The frequency space of the SIM reconstruction is significantly larger than that of the wide-field or Wiener-filtered wide-field.

Besides the Gustafsson & Heintzmann approach of SIM microscopy presented here [33,47], deconvolution-based approaches also exist [205]. These often work with numerical, iterative solvers to obtain additional sample information, given a known structured illumination. Methods that work with unknown structured illuminations are

called blind SIM [206]. The use of neural networks in recent research has significantly improved the quality of SIM reconstructions (especially in terms of noise) [207].

Illumination and pattern generation

Usually, the illumination patterns required for SIM microscopy are generated by the interference of two (Figure 17b) or three (Figure 17c) mutually coherent laser beams within the sample [33,208]. This allows the generation of high contrast (modulation depths) sinusoidal illumination pattern, which are desirable for good reconstructions with few artifacts [48,199]. Usually, the illumination of the sample takes place through the objective through which the fluorescence is also collected. For this purpose, two or three coherent laser beams are focused into the back focal plane of the objective in such a way that they interfere with each other in the sample. For two-beam SIM, the spatial wavelength of the pattern produced in the sample is given by the wavelength and the angle to the optical axis θ at which the two outer beams interfere:

$$\Lambda_{spatial} = \frac{\lambda_{ex}}{2 \cdot \sin(\theta)} \geq \frac{\lambda_{ex}}{2 \cdot NA} \tag{61}$$

Similar to the Abbe limit for detection, the NA of the objective lens limits the spatial wavelength of the pattern generated in the sample. To generate the focused spots in the back focal plane, often optical gratings or spatial light modulators (SLM) are used, on which a grating is displayed, which are irradiated by a collimated laser (see Figure 17a). The resulting diffraction orders are coherent with each other and can be collected by a lens (L1) and focused as a Fourier plane. Filtering with a Fourier mask can be used to filter out all unwanted diffraction orders if required, for example when using binary SLMs that produce spurious interference orders. The filtered Fourier plane of the focused coherent beams is then projected through a telescope (L2, L3) into the back focal plane of the objective, producing the desired pattern in the sample by interference. The pattern generation in the sample can also be understood of as a Fourier-filtered mapping of the grating into the sample. To obtain a pattern with the highest possible modulation depths (contrast), the polarization of the individual beams must also be controlled so that the polarization of the beams in the sample is ideally parallel to each other [209,210]. The achievable resolution increase can be calculated from the wavelength of the pattern in the sample and the wavelength of the fluorescence:

$$r = 1 + \frac{\Lambda_{spatial}}{\lambda_{fl}} \tag{62}$$

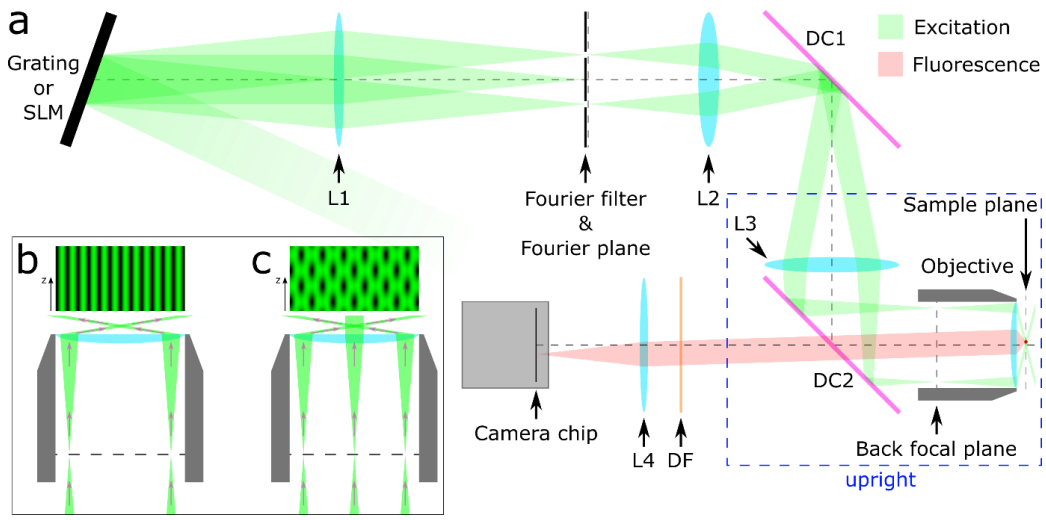

Figure 17: SIM-Microscope

(a) Schematic setup of a two-beam SIM microscope. The collimated coherent excitation laser is directed at a reflective grating or SLM at the smallest possible angle. The diffraction orders produced by the grating or SLM are focused into the Fourier plane by the lens L1. All diffraction orders except the -1st and +1st (and 0th for three-beam SIM) are blocked by the Fourier filter. Through the telescope of L2 and L3, and the two dichroic mirrors DC1 and DC2, the filtered Fourier plane is projected into the back focal plane of the objective lens. The objective lens collimates the two focused beams from the back focal plane so that they interfere with each other in the sample plane, producing a sinusoidal intensity distribution. The fluorescence is collected by the objective lens, separated from the excitation light using the dichroic mirror DC2, spectrally cleaned by the detection filter (DF), and focused onto the camera chip using the tube lens L4. For reasons of polarization conservation, a dichroic mirror DC1 (same batch as DC2, see section A.II) is used between L2 and L3 to deflect the excitation beams. (b) Exposure scheme for a two-beam SIM microscope. By focusing two coherent beams into the outer back focal plane of the objective, they interfere collimated in the sample plane. The result is a laterally pure sinus pattern (only the fundamental frequency) which has no modulation along the optical axis. (c) Exposure scheme for a three-beam SIM microscope. By focusing three beams (two outside, one centered) into the back focal plane of the objective, they interfere collimated in the sample plane. A sinusoidal pattern of two frequencies (fundamental & first harmonic) in a 1:2 ratio is created laterally. In addition, there is an axial modulation of the pattern along the optical axis.

Modern SIM microscopes use both gratings and SLMs for pattern generation. Mechanical gratings [33] (e.g. made of glass) are efficient in light yield for the desired diffraction orders, but unlike SLMs have a fixed grating constant, orientation, and phase. Therefore, the use of mechanical motion to adjust these quantities during operation is necessary. Spatial light modulators (SLMs) [195] can circumvent this problem. They have a pixel structure and can adjust the displayed gratings without mechanical motion. SLMs for pattern generation in SIM microscopy are further subdivided. Liquid crystal displays (LCDs) assign a freely selectable phase shift to each pixel. Binary LCDs such as Ferroelectric Liquid Cristal on Silicon (FLCoS) [87,88] can only assign two different states (phase shifts) to each pixel. This makes them less efficient in light output for the desired diffraction orders, but much faster than LCDs (<400µs switching cycle) [62,63,211].

FLCoS SLMs also do not allow continuous display of patterns, since each displayed pattern must be rebalanced by the negative of the pattern within a few milliseconds, which is an undesirable drawback. For Digital Micromirror Devices (DMDs) [212], the pixels correspond to small micromirrors that can flip between two orientations. The resulting jagged surface of DMDs leads to the so-called "blazed grating effect" and therefore makes them problematic, especially when using multiple excitation wavelengths. Nevertheless, DMDs are interesting, especially for high-speed SIM microscopes, due to their very high speed (<250µm switching cycle) and comparatively low cost.

Optical sectioning and 3D SIM microscopy

From section 2.1.3 we know that an ordinary incoherent wide-field OTF has a so-called missing cone for lateral frequencies close to zero (see Figure 18a,b). By illumination with SIM patterns, the wide-field OTF is copied laterally (along k_r) in the frequency domain and shifted to the positions of the SIM delta peaks, which increases the effectively usable frequency space and thus the achievable resolution. If the illumination pattern chosen for the two-beam SIM corresponds to the maximum resolution increase by a factor of two, missing cones appears for lateral frequencies near zero as well as near the wide-field cut-off frequency (see Figure 18c). If, on the other hand, the resolution increase is chosen to be slightly smaller than the maximum factor of two, the copies of the wide-field OTF caused by the SIM illumination are not shifted quite so far outward. As a result, the wide-field and SIM OTFs then overlap, avoiding the missing cones (see Figure 18d). During reconstruction, the algorithm can be adjusted accordingly with a so-called OTF attenuation or notch filtering (see Figure 19 & Figure 20), so that frequencies lying in the missing cone of the wide-field are not filled with information from the wide-field OTF, but with information from the SIM OTF. This allows better axial resolution along the optical axis (optical sectioning). For three-beam SIM, there is an additional harmonic ($M = 2$). In addition to the laterally shifted copies of the wide-field OTF, the three-beam SIM OTF also has axially shifted copies (see Figure 18e) [34]. Thus, the missing cones from (c) are filled and disappear. Thus, with the three-beam SIM, even with full lateral resolution increase by a factor of two, a higher axial resolution (optical sectioning) can be achieved than is possible in wide-field or with two-beam SIM.

Three-beam SIM is generally more suitable when axial resolution is important. However, this usually involves more complicated opto-mechanics and is slower due to the 15 raw images required per z slice, instead of 9 for two-beam SIM. Also, entire z-stacks of the sample must be acquired with 15 images per slice, respectively, which also takes time and exposes the sample to more excitation light in terms of photo-toxicity. Therefore, two-beam SIM microscopes are particularly useful for observing fast dynamic processes in living cells.

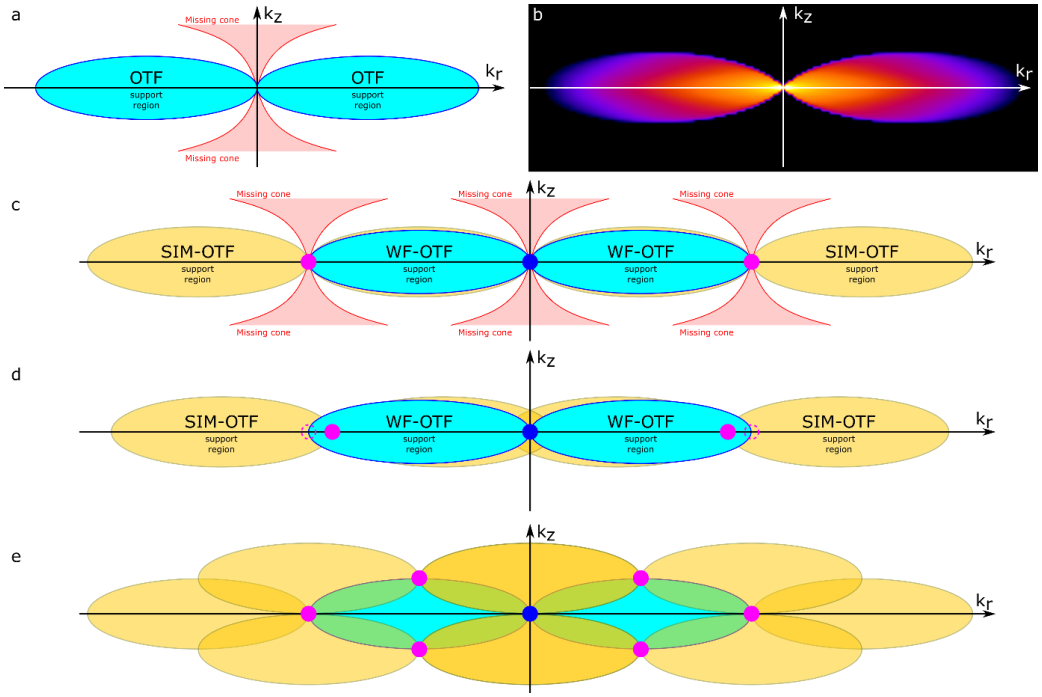

Figure 18: Three-dimensional SIM-OTF

(a) Schematic representation of the scope of a three-dimensional OTF (blue) and the missing cone (red). (b) Exemplary representation of a real OTF [100]. (c) Schematic representation of the scope of a two-beam SIM-OTF with the maximum increase in resolution by a factor of two. The wide-field OTF (blue) is copied by the SIM illumination to the SIM delta peaks (magenta dots) resulting in the SIM OTF (beige). A missing cone is produced not only for lateral frequencies near zero, but also for lateral frequencies near the wide-field cut-off frequency. (d) Schematic representation of the scope of a two-beam SIM-OTF with a resolution increase slightly below the maximum factor of two. Because the wide-field and SIM OTFs now overlap, the missing cones disappear. The magenta dashed circles indicate the position of the delta peaks (magenta dots) from (c). (e) Schematic representation of the scope of a three-beam SIM-OTF with the maximum resolution increase of two. The wide-field OTF is copied not only laterally but also axially to the magenta points. This results in no missing cones, which is why the sectioning, i.e. the axial resolution, is generally better with the three-beam SIM than with the two-beam SIM.

In addition to the previously mentioned possibilities, it is also possible to combine TIRF (section 2.1.4) and two-beam SIM to form TIRF-SIM [213,214], in which the two SIM beams for pattern generation both totally reflect at the interface between cover glass and sample. This limits the penetration depth of the illumination pattern to about 100 nm within the sample, thus defining the axial resolution. A combination of light sheet microscopy with SIM has also already been demonstrated to improve optical sectioning [215]. SIM, with an appropriately designed microscope, even allows the detection of multiple z-sections in parallel, making the acquisition of z-stacks much faster [216,217].

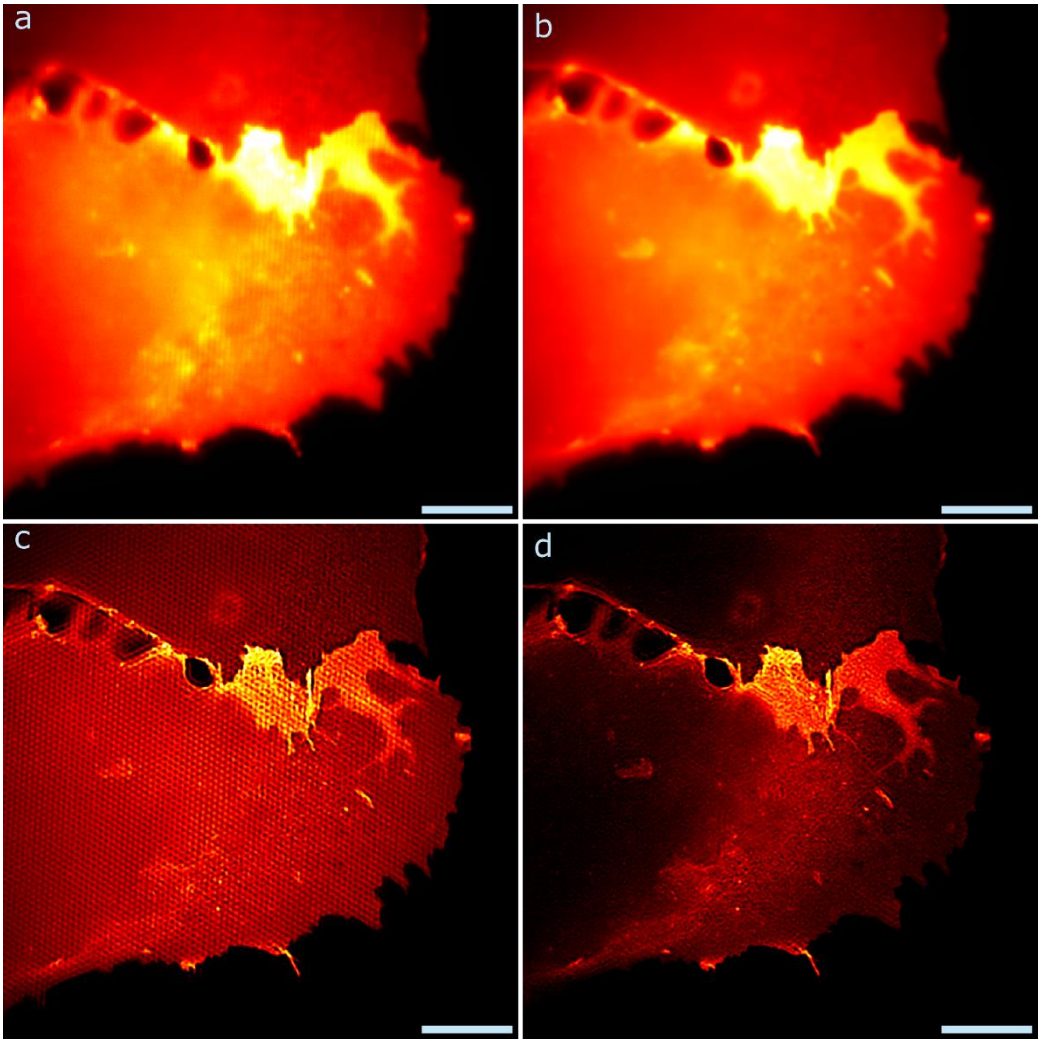

Figure 19: Optical sectioning in SIM images, with a standard SIM pattern

U2OS cells stained with Vybrant DiD (cell membrane), excited at 631 nm. Raw images (a) show a fine SIM pattern, with a pattern spacing of 305nm (Abbe limit approx. 265nm for 700nm emission), the widefield image (b) hints at significant out-of-focus background. A SIM reconstruction without OTF attenuation (c) shows severe out-of-focus artifacts, but also a reconstruction using OTF attenuation (d) still shows patterning artifacts that are likely due to out-of-focus background not being sufficiently suppressed, as the overlap between SIM bands needed for this to work is too low (see Figure 20 for increased overlap by using a coarser SIM pattern). Scale bar 10 µm. Figure taken from our publication [8].

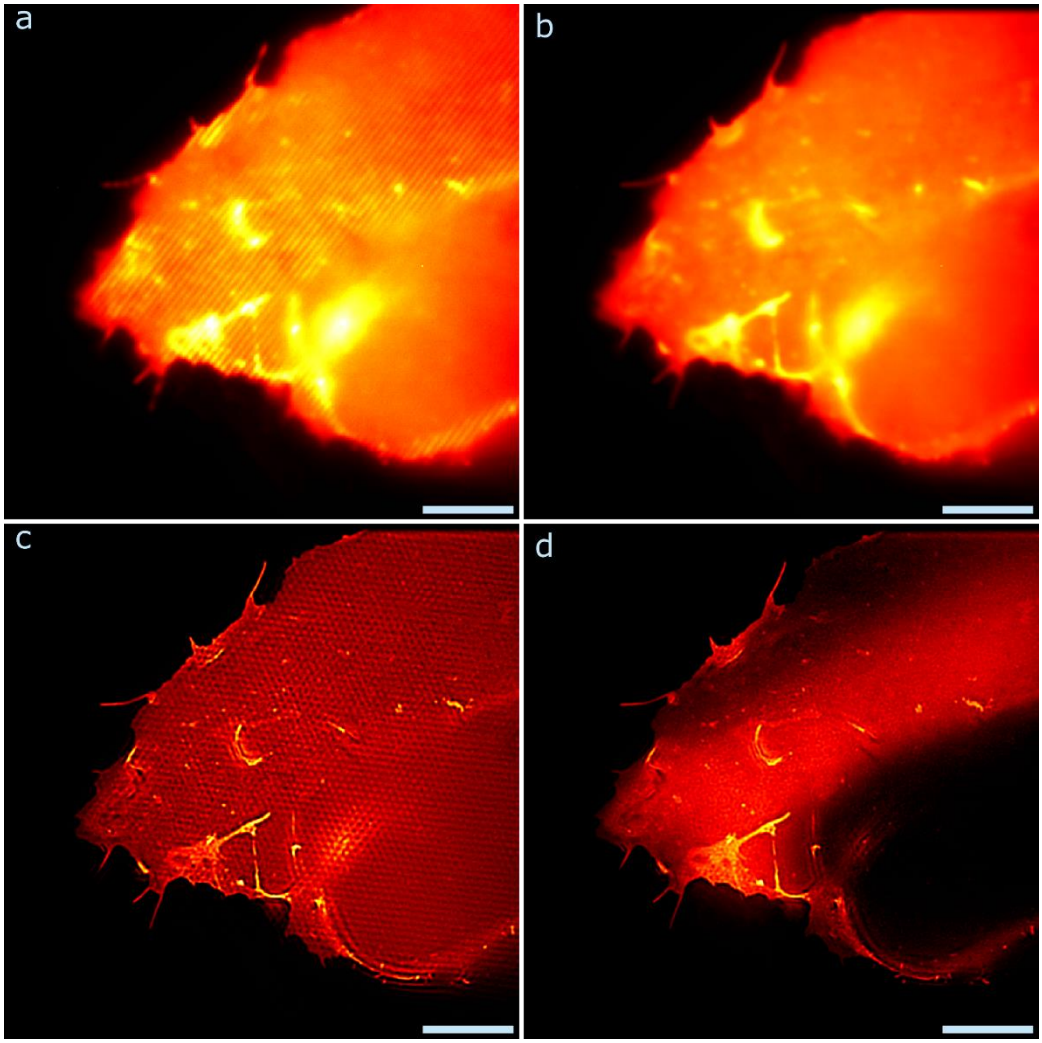

Figure 20: Optical sectioning in SIM images, with an optimized, coarse SIM pattern

U2OS cells stained with Vybrant DiD (cell membrane), excited at 631 nm. Raw images (a) show a coarser SIM pattern, with a pattern spacing of 360nm (Abbe limit approx. 265nm for 700nm emission), the widefield image (b) hints at significant out-of-focus background. A SIM reconstruction without OTF attenuation (c) shows noticeable out-of-focus artifacts (but less severe than in Figure 19, hinting at more OTF overlap between the SIM bands) and a reconstruction using OTF attenuation (d) quite successfully suppresses artifacts that usually arise from out-of-focus light. When directly comparing the raw data (a) and the reconstruction with optical sectioning (d), it also becomes very apparent that background is removed in regions where the raw data shows less or (to the eyes) no SIM pattern modulation. This is expected, as regions with out-of-focus background still receive SIM modulated excitation light (using coherent excitation, the pattern is stable over a wide axial range), but out-of-focus detection does not have enough resolution to still show this pattern. Using the OTF attenuation, this allows to remove such background contributions, and lead to the darkened areas observed in (d). Scale bar 10 µm. Figure taken from our publication [8].

2.3 Mesoscopic imaging with optical projection tomography

After the previous introduction to super-resolution microscopy, it might almost seem that it is always about obtaining even higher resolution images of biological samples. However, better resolution usually comes with a smaller Field of View. In optical microscopy and nanoscopy, the sample size is usually between 100 µm and 1 mm with resolutions from 5 µm down to a few nanometers [218]. Especially when imaging comparatively large biological samples (e.g. whole rodent organs), super-resolution and classical microscopy methods thus reach their limits.

The counterpart to microscopy for small samples are the macroscopic three-dimensional imaging techniques, such as X-ray computed tomography (CT) [66,67], positron emission tomography (PET) [219] and magnetic resonance imaging (MRI) [68], among others. Usually, these methods are used for diagnosis in medicine and can image the whole human body. Depending on the respective method, different levels of specificity and resolutions between 0.2 mm and 8 mm can be achieved [220].

The range of three-dimensional imaging techniques between microscopic and macroscopic techniques is called mesoscopy [221]. The two best known techniques are micro-CT [222] and micro-MRI [223] with resolutions down to about 50 µm [220]. Due to the different contrast mechanisms, the techniques have different specificities in imaging. Both techniques have applications in in vivo veterinary medicine, including small animal cancer research [224]. Other representatives of mesocopy include functional ultrasound imaging [225], optoacoustic tomography [226,227], and bioluminescence imaging [228].

Light-sheet microscopy [229] or Ultramicroscopy [230] is the most widely used technique of mesoscopic fluorescent imaging. Here, a thin light sheet is used for fluorescence excitation in (usually) optically transparent samples, whereas the fluorescent light is collected perpendicular to the light sheet. While the field of light-sheet microscopy is more concerned with increasing resolution towards super-resolution [215], the efforts of Ultramicroscopy are to develop imaging capabilities for small animals [231–238]. In some cases, cellular resolutions can be achieved [239].

Optical projection tomography (OPT) is a solid alternative to Ultramicroscopy and is based on the same principle as computed tomography (CT) [76]. The main difference lies in the wavelength of the electromagnetic radiation used. CT uses X-rays (10 pm to 10 nm), whereas OPT uses visible light (400 nm to 700 nm). The technique was developed in 2002 for 3D imaging of mesoscopic samples (5 mm - 20mm) by James Sharpe [240]. The achievable isotropic resolution of centimeter-sized samples is down to 6.8 µm [77]. Fluorescent dyes can be used for specific contrasting [240]. OPT has been successfully applied to observe the zebrafish vasculature in vivo [241]. Furthermore,

mouse pancreas, mouse brain neuroanatomy and mouse embryos could be examined [76,242–245].

To obtain an OPT image it is necessary to take projections of the transparent sample from all directions with respect to one axis of rotation. In medical CT, the detector is rotated around the patient for this purpose. In OPT, on the other hand, the transparent sample is usually rotated with the help of a motorized stage [246,247]. In practice, 400 [240] to 1200 [245] individual projections are acquired for this purpose, representing the raw data. Final OPT images are usually computed using filtered back-projection (FBP) of the raw data [248]. However, there are also more advanced approaches to reconstruct the raw data [249,250]. Since biological tissue is generally not transparent (10-20 µm penetration depth for light [221]), samples are often cleared using organic solvents to minimize the scattering and absorption of light [78,251].

2.3.1 Transmission vs. emission OPT

Basically, there are two different physical mechanisms how the contrast of the projections (raw data) can be generated. In transmission OPT (tOPT), the sample is homogeneously irradiated with light. The shadows cast by the absorbing tissue generate the contrast, similar to X-ray or CT acquisitions. The tissue of the sample absorbs the radiation from the light source. Lambert-Beer's law describes the absorption A of radiation (e.g. X-ray or light) when passing through a medium with the material and wavelength dependent absorption coefficient µ with the thickness l [252]:

$$A = \log_{10}\left(\frac{I_0}{I}\right) = \mu l \tag{63}$$

Here with the radiation intensity I_0 in front of and I behind the medium. In emission OPT (eOPT), the sample is illuminated homogeneously with fluorescence-exciting light, but here the contrast is created specifically via fluorescent dyes or autofluorescence, comparable to emission computed tomography.

2.3.2 Tomographic reconstruction from projections

This section (2.3.2 Tomographic reconstruction from projections) is largely based on the lecture "Reconstruction from parallel projections and the Radon transform" by Richard J. Radke, Professor in the ECSE (Electrical, Computer, and Systems Engineering) department at Rensselaer Polytechnic Institute (RPI) in Troy, NY, USA [253].

In order to understand how an image of a 2D object $f(x, y)$ can be reconstructed by taking multiple (400 - 1200) 1D projections of the object, it is first important to describe the projection itself mathematically (see Figure 21). Usually, straight line equations in a two-dimensional coordinate system are described as follows:

$$y = ax + b \tag{64}$$

However, if you want to describe a line using polar coordinates, i.e. the arbitrary projection angle θ and the distance of the line to the origin t, the following equivalent form can be used:

$$x\cos(\theta) + y\sin(\theta) = t \tag{65}$$

Radon transform

Each value of a projection $P_\theta(t)$ can be described as a line integral of the object $f(x, y)$ along a straight line (eq. (65)) using the Dirac delta function δ and is called Radon transform:

$$P_\theta(t) = \iint_{-\infty}^{\infty} f(x, y) \cdot \delta(x\cos(\theta) + y\sin(\theta) - t)\, dx\, dy \tag{66}$$

This was introduced in 1917 by Johann Radon [254], who also provided a formula for the inverse transformation.

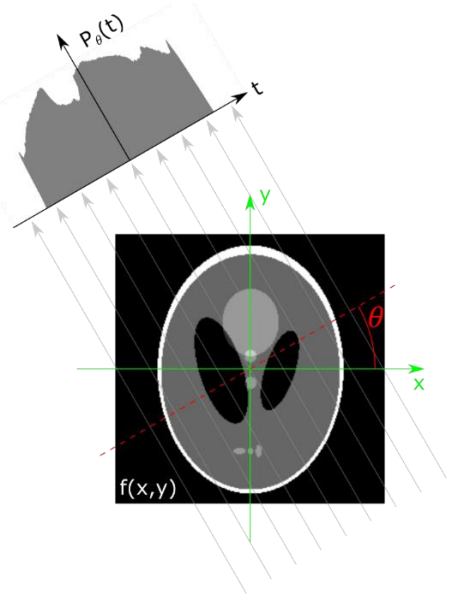

Figure 21: Projection as Radon transform

Schematic representation of the projection at angle θ of a 2D section of an object $f(x, y)$ (Shepp–Logan phantom) by line integrals. Figure created using the Radon Transform Fiji plugin [255].

A simple but at the same time naive method for the inversion the projection or Radon transform is the direct inverse Radon transform. This simply copies the values of the projection $P_\theta(t)$ (Figure 22a) to all locations of the corresponding straight lines (Figure 22b):

$$f_{bp_\theta}(x,y) = P_\theta(x\cos(\theta) + y\sin(\theta)) \tag{67}$$

Since all depth information along the projection lines (eq. (65)) is lost when taking the 1D projection of a 2D object, it can only be recovered by back-projecting many projections from different angles. This is the reason why so many images (400 - 1200) are needed to produce a satisfactory back-projection. The projections P_θ and $P_{\theta+\pi}$ taken at 180° to each other logically contain the same information:

$$P_{\theta+\pi}(t) = P_\theta(-t) \tag{68}$$

Therefore, it is sufficient to sum up or integrate the back-projections over a half circle, which leads to the direct inversion of the Radon transform:

$$f_{bp}(x,y) = \int_0^\pi P_\theta(x\cos(\theta) + y\sin(\theta))\, d\theta \tag{69}$$

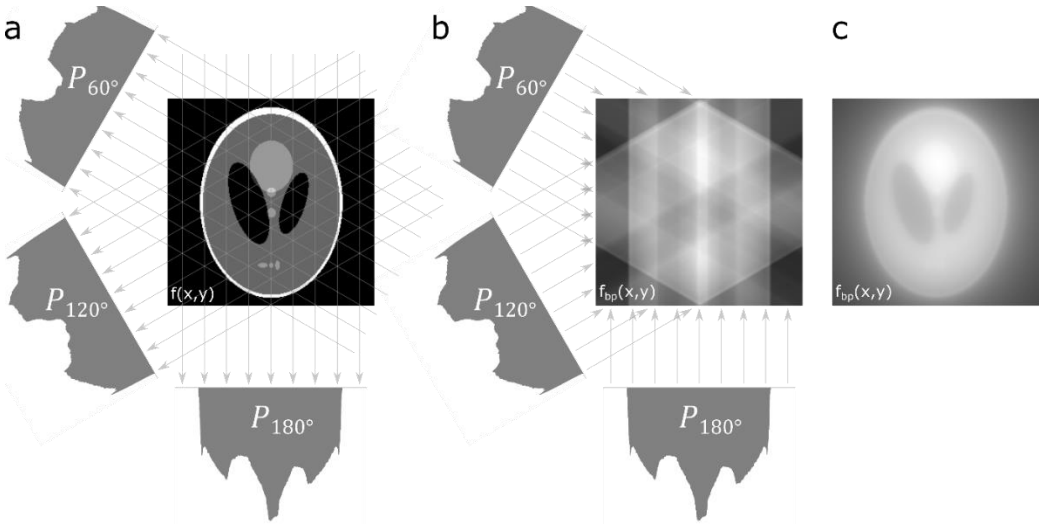

Figure 22: Direct inverse radon transform – unfiltered back-projection

Three acquired projections (a) for $\theta = \{60°, 120°, 180°\}$ generate via the direct inversion of the Radon transform, the unfiltered back-projection (b). Each projection is copied along the direction of its acquisition throughout the entire depth of the reconstruction space. The unfiltered back-projection (c), obtained from 180 raw projections with 1° step size, produces a blurred image of the object. Figure created using the Radon Transform Fiji plugin [255].

As can be seen in Figure 22c, an image of the object can be reconstructed via the (unfiltered) back-projection. However, this image is very blurred, which leads to a kind of halo around the object and prevents fine structures (high spatial frequencies) from being visible. To reduce these unwanted effects, the filtered back-projection, which includes an additional filter step, is a good method. The central slice theorem is essential for this.

Central slice theorem

As shown below, the central section theorem (also called Fourier-slice theorem or projection-slice theorem) states that the 1D Fourier transform of a 1D projection corresponds to a 1D central section through the 2D Fourier image of the 2D object [256]. The 1D Fourier transform of a 1D projection $P_\theta(t)$ is:

$$\tilde{P}_\theta(k) = \int_{-\infty}^{\infty} \left[\iint_{-\infty}^{\infty} f(x,y) \cdot \delta(x\cos(\theta) + y\sin(\theta) - t)\, dx\, dy \right] e^{-2\pi i k t} dt \tag{70}$$

$$= \iint_{-\infty}^{\infty} f(x,y) \left[\int_{-\infty}^{\infty} \delta(x\cos(\theta) + y\sin(\theta) - t) e^{-2\pi i k t} dt \right] dx\, dy \tag{71}$$

$$= \iint_{-\infty}^{\infty} f(x,y) \cdot e^{-2\pi i k (x\cos(\theta) + y\sin(\theta))}\, dx\, dy \tag{72}$$

By a change to the following polar coordinates in Fourier space,

$$k_x = k\cos(\theta) \quad \text{and} \quad k_y = k\sin(\theta)$$
$$\text{with} \quad k = \sqrt{k_x^2 + k_y^2} \quad \text{and} \quad \theta = \arctan\left(\frac{k_x}{k_y}\right) \tag{73}$$

it becomes clear that the Fourier transform of a projection (Radon transform) corresponds to a central section with angle θ in the Fourier space of the object (see Figure 23a,b):

$$\tilde{P}_\theta(k) = \iint_{-\infty}^{\infty} f(x,y) \cdot e^{-2\pi i (k_x x + k_y y)}\, dx\, dy$$
$$= \tilde{f}_\theta(k_x, k_y) = \tilde{f}_\theta(k\cos(\theta), k\sin(\theta)) \tag{74}$$

If many projections of the object are taken at different angles θ, this results in just as many central slices of the Fourier space belonging to the object, which all intersect at the origin. The information density is thus very large for low frequencies near $k = 0$, while it decreases outward for high frequencies (see Figure 23c). For this reason, the unfiltered back-projection appears blurred (see Figure 22c), which can be avoided or reduced by an appropriate filtering.

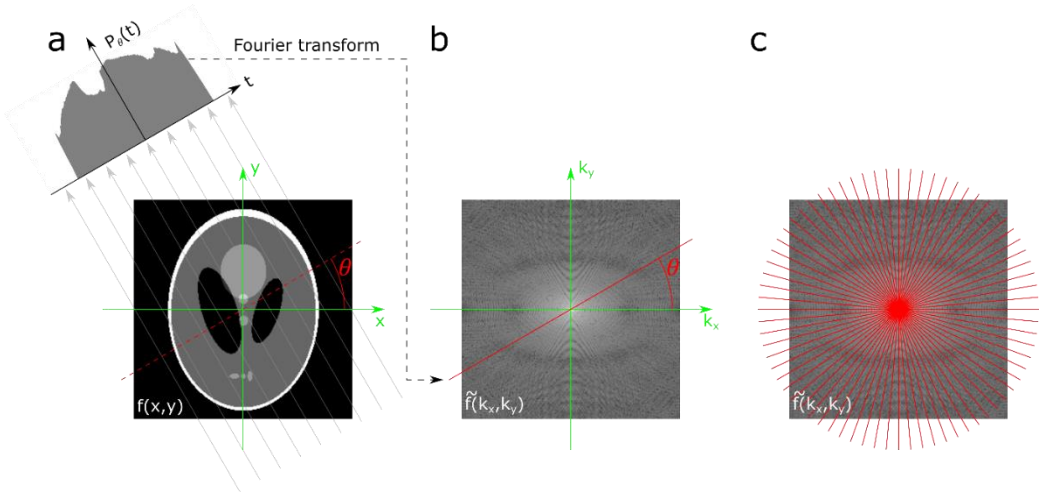

Figure 23: Central slice theorem

(a) One projection at angle θ as Radon transform $P_\theta(t)$ of the Shepp-Logan phantom. The Fourier transform of $P_\theta(t)$ corresponds in Fourier space (b) to the central slice with angle θ. By taking many projections (Radon transforms) at different angles θ, the Fourier space (c) can be filled up with central slices. Here it is noticeable that the data density in the center is much higher than at the outer region.

Filtered back-projection

Via the inverse Fourier transform, the object can be reconstructed from the Fourier image $\tilde{f}(k_x, k_y)$:

$$f(x,y) = \iint_{-\infty}^{\infty} \tilde{f}_\theta(k_x, k_Y) \cdot e^{2\pi i(k_x x + k_y y)}\, dk_x\, dk_y \tag{75}$$

Due to the polar coordinates in Fourier space (eq. (73)) applies:

$$dk_x\, dk_y = k\, dk\, d\theta \tag{76}$$

This transfers eq. (75) to:

$$f(x,y) = \int_0^{2\pi} \int_{-\infty}^{\infty} \tilde{f}_\theta(k\cos(\theta), k\sin(\theta)) \cdot e^{2\pi i k(x\cos(\theta) + y\sin(\theta))} k\, dk\, d\theta \tag{77}$$

Using the Fourier-slice theorem (eq. (74)), this leads to:

$$f(x,y) = \int_0^{2\pi} \int_{-\infty}^{\infty} \tilde{P}_\theta(k) \cdot e^{2\pi i k(x\cos(\theta) + y\sin(\theta))} k\, dk\, d\theta \tag{78}$$

Equivalent to eq. (68) is also valid in Fourier space:

$$\tilde{P}_{\theta+\pi}(k) = \tilde{P}_{\theta}(-k) \tag{79}$$

Therefore, eq. (75) can also be written as follows:

$$f(x,y) = \int_0^{\pi} \int_{-\infty}^{\infty} |k| \tilde{P}_{\theta}(k) \cdot e^{2\pi i k(x\cos(\theta)+y\sin(\theta))} dk\, d\theta \tag{80}$$

With the equation of straight lines (65) this results in the filtered back-projection:

$$f_{fbp}(x,y) = \int_0^{\pi} \int_{-\infty}^{\infty} |k| \tilde{P}_{\theta}(k) \cdot e^{2\pi i k t} dk\, d\theta \tag{81}$$

The integral over k is here just the inverted Fourier transform of $\tilde{P}_{\theta}(k)$ multiplied by the filter function $|k|$ (called Ram-Lak filter). Since in practice not infinitely many projections P_{θ} are available for a reconstruction with the filtered back-projection, gaps in the Fourier space still occur for high frequencies (see Figure 23c). These cause reconstruction artifacts which can be reduced by attenuating high frequencies of the filter function $|k| \rightarrow |k|h(k)$:

$$f_{fbp}(x,y) = \int_0^{\pi} \int_{-\infty}^{\infty} |k| h(k) \cdot \tilde{P}_{\theta}(k) \cdot e^{2\pi i k t} dk\, d\theta \tag{82}$$

The Shepp-Logan filter with $h(k) = sinc(\pi k)$ is often used to attenuate higher frequencies (see Figure 24).

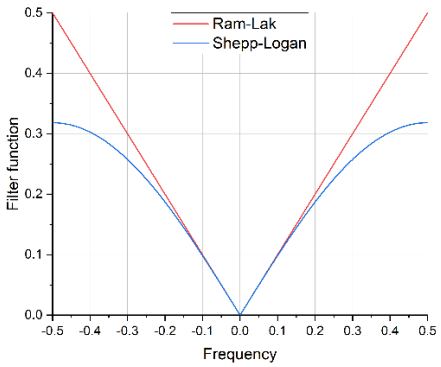

Figure 24: Ram-Lak vs. Shepp-Logan

When comparing the two filter functions, it is noticeable that the Shepp-Logan filter attenuates the high frequencies compared to the Ram-Lak filter. This reduces possible high frequency reconstruction artifacts that can occur with the filtered back-projection.

Practical implementation

Based on eq. (82), the following algorithm can be formulated for the mathematically correct reconstruction of an object via its projections:

1. Calculation of the 1D Fourier transform $\tilde{P}_\theta(k)$ of each projection $P_\theta(t)$
2. Multiplication with the filter function $|k|h(k)$
3. Calculation of the inverse 1D Fourier transform
4. Integrate (summing up) over all angles to get the object $f(x,y)$

So-called sinogams have established themselves as a representation of all 1D projections of a 2D object. They have the respective projection angle θ on the x-axis and the projection coordinate t on the y-axis. Figure 25a shows a 2D object whose 1D projections can be seen as a not yet filtered sinogram (Figure 25b) and filtered sinogram (Figure 25c). The back-projection of the filtered projections (Figure 25d) results in a sharp and non-blurred image of the object (Figure 25a) compared to Figure 22c.

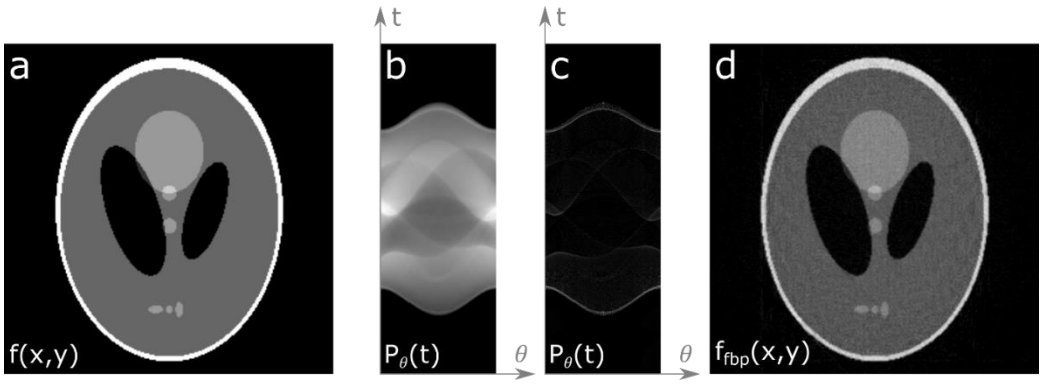

Figure 25: Main reconstruction steps of the filtered back-projection algorithm

The 2D plane of the object (a) is acquired via projections (Radon transforms) from all angles θ. Each of these 1D projections is then mapped into a matrix called a sinogram (b). This sinogram is then filtered (c) column by column with a filter (in this case a Ram-Lak filter) in the Fourier domain. The back-projection of the filtered sinogram yields the filtered back-projection (d), which corresponds to a comparatively sharp representation of the object. Figure created using the Radon Transform Fiji plugin by [255]

Since $|k| = 0$ is valid for $k = 0$, the DC value of the filtered back-projection is lost. This means that the brightness scaling of each filtered back-projection must be chosen freely. This becomes problematic if reconstructions are to be compared with each other, as is the case, for example, with the reconstruction of 3D objects.

Projections of 3D objects are two-dimensional and can be considered as a string of 1D projections of cross-sections along the rotation axis. For example, the rotation axis of a 3D object could be along the y-axis in space. For captured 2D projections (Figure 26a), each row of pixels (in the t direction) then corresponds to the 1D projection of a 2D xz

cross-section of the object at location y. Thus, for each pixel row y, a sinogram (Figure 26c) and reconstruction (Figure 26c) of an xz cross-section of the 3D object can be created independently of the other pixel rows. Stacking the xz cross-sections in an image stack then results in the reconstruction of the entire 3D object (Figure 26d). In order to be able to compare e.g. two neighboring xz cross-sections it is necessary to match the brightnesses of the reconstructions (e.g. by histogram matching algorithms, see section 4.2).

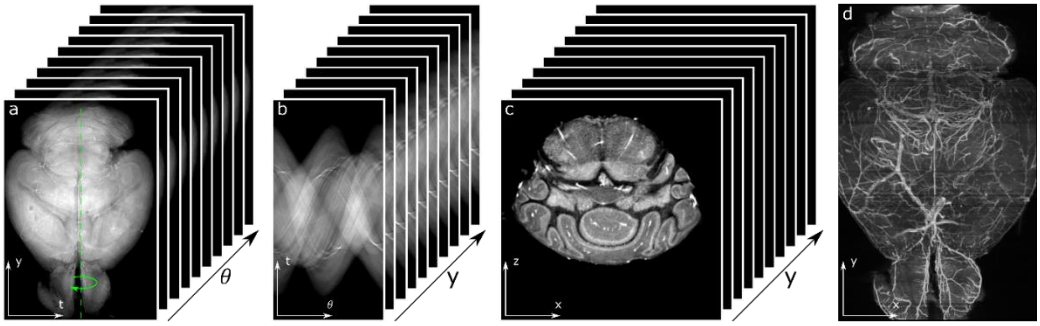

Figure 26: Reconstruction of three-dimensional samples via filtered back-projection

The projections taken from the sample at different angles θ result in a stack of projections (a). This is transformed into a stack of sinograms (b). Each sinogram belongs to a pixel line (y) of the projection stack. From this, a virtual cross-section through the sample can be calculated using filtered back-projection. The result is a stack of cross sections. This can be used to create three-dimensional models and visualizations. Like for example in this case a maximum intensity projection (d).

The filtered back-projection presented here is based on projections with parallel beams. However, modern CT systems do not use parallel beams but so-called fan beams, for which the filtered back-projection must be adapted accordingly [257].

2.3.3 Depth of focus and resolution

OPT systems are basically wide-field microscopes (see section 2.1) with a comparatively small numerical aperture (NA). This is necessary because the point spread function (PSF, see section 2.1.2) must be extended along the optical axis so that it roughly corresponds to the sample thickness. This is essential because otherwise the conditions for tomographic reconstruction (see section 2.3.2) are not given. The extended PSF can be considered as the line integral of the Radon transform (eq. (66)) through the sample, which is ultimately detected by a camera pixel. The extent of the PSF along the optical axis is called depth of focus (DOF) and can be defined as follows [258]:

$$DOF = n_{bath}\left(\frac{\lambda}{NA^2} + \frac{e}{M \cdot NA}\right) \tag{83}$$

Here with the refractive index n_{bath} of the surrounding sample medium, the (emission) wavelength λ, the pixel size e of the detector and the magnification of the optical imaging system M. For projected pixel sizes (sampling rates) below the Nyquist-Shannon sampling theorem (eq. (31)), the DOF can be approximated as follows [259]:

$$DOF \approx n_{bath} \cdot \frac{5}{4} \frac{\lambda}{NA^2} \tag{84}$$

The thicker the sample to be examined, the larger the NA must be selected. This is at the expense of the achievable resolution (see section 2.1.2) [259]. However, the DOF can also be set to about half the sample thickness. The focal plane of the objective lens must then be placed in the center of the front half (1/4) of the sample. However, projections must then also be taken along a full 360° rotation, instead of the 180° required according to eq. (82) [260]. This allows the NA to be chosen larger, increasing the achievable resolution. In practice, the NA can be set by the radius r of an aperture in the back focal plane of the objective lens with focal length f. It is important to note that the smaller the aperture is chosen, the more light is blocked, resulting in less light reaching the detector (camera chip), which results in a poorer signal-to-noise ratio. In paraxial approximation, the NA can be determined as follows:

$$NA \approx \frac{r}{f} \tag{85}$$

For the DOF and the achievable resolution d the following expressions result:

$$DOF \approx n_{bath} \cdot \frac{5}{4} \frac{\lambda f^2}{r^2} \quad \text{and} \quad d \approx \frac{\lambda f}{2r} \tag{86}$$

Over the range of the DOF along the optical axis, it is imperative that the magnification remains constant, otherwise the acquired projections will not satisfy the Radon transform. This property of an imaging system is called telecentric. This can be ensured by positioning the aperture diaphragm in the back focal plane (Fourier plane).

2.3.4 Image artefacts

The filtered back-projections of OPT images can be afflicted with various artifacts that degrade the quality. For example, it is important that each projection is taken under the same lighting conditions. Otherwise, unequal weighting of the projections will occur, resulting in shadowing of the reconstructed images [261]. However, by using LEDs [262] with high quality power sources, fluctuations of the light source can be avoided [263].

In fluorescence (emission) OPT, photobleaching of the fluorophores additionally occurs, which also results in shadow-like artifacts in the filtered back-projections [261]. This can

be avoided in the post-process before reconstruction by exponential brightness correction. However, an increase of the noise level must be accepted.

Non-uniformities in the photon response of the camera pixels lead to concentric ring artifacts in the reconstructions [261]. These can be circumvented mainly by choosing a high-quality camera (e.g. sCMOS, see section 2.1.4). Possible hot or cold pixels should be filtered out in the acquired projections during post-processing. Median filters or binning can be used to reduce pixel variations, but with regard to the Nyquist-Shannon sampling theorem (eq. (31)) a loss of resolution may occur. The edges of the camera chip (or the selected region of interest) also produce concentric ring artifacts on the outside, but these can be eliminated by subtracting a reconstruction without a sample [261].

The positioning of the center of rotation for the filtered back-projection is of major importance. If this is not precisely matched, shadow-like smearing artifacts will occur [261]. To avoid this, reconstruction with different centers of rotation with the goal of minimal variance in the reconstructed image is a good option. Furthermore, there are correlation-based approaches that can determine the center of rotation from the acquired projections.

3 DMD based coherent SIM microscopy

This section (3 DMD based coherent SIM microscopy) and its subsections are based in major parts on the following publications:

Markwirth, A., Lachetta, M., Mönkemöller, V., Heintzmann, R., Hübner, W., Huser, T., & Müller, M. (2019). Video-rate multi-color structured illumination microscopy with simultaneous real-time reconstruction. Nature communications, 10(1), 1-11.

Lachetta, M., Sandmeyer, H., Sandmeyer, A., Schulte am Esch, J., Huser, T., & Müller, M. (2021). Simulating digital micromirror devices for patterning coherent excitation light in structured illumination microscopy. Philosophical Transactions of the Royal Society A, 379(2199), 20200147.

Sandmeyer, A., Lachetta, M.*, Sandmeyer, H., Hübner, W., Huser, T., & Müller, M. (2021). Cost-Effective Live Cell Structured Illumination Microscopy with Video-Rate Imaging. ACS Photonics 8(6), 1639–1648. (*equal contribution)*

Lachetta, M., Wiebusch, G., Hübner, W., Schulte am Esch, J., Huser, T. & Müller, M. Dual color DMD-SIM by temperature-controlled laser wavelength matching. Optics Express, accepted, submitted September 2021.

SIM is based on the spatial modulation of fluorescence excitation light, which is achieved by the targeted interference of coherent laser beams in the sample plane [195]. For this purpose, spatial light modulators (SLMs) are often used as robust and fast electronically controllable gratings [85]. In particular, for high-speed SIM, the use of ferroelectric liquid crystal on silicon SLMs (FLCoS) is very popular [62,63,86–89]. However, their main drawback is, the necessary compensation of each pattern shown by the corresponding negative, which limits illumination and system timing. In addition, FLCoS SIM systems are often less cost-effective and only available in a limited number of models and from currently one manufacturer (Forth Dimension Displays).

Digital micromirror devices (DMDs) form a special subcategory of SLMs based on a pixel array of electro-mechanical micromirrors. These can tilt between two predefined states (e.g. ±12° tilt angle [264]), allowing them to steer and modulate light. Compared to other SLMs (such as FLCoS), DMDs are widely available in various versions, cost-effective, extremely fast (10 kHz switching time) and, depending on the coating,

insensitive to light polarization. Therefore, they are popular not only in consumer electronics such as video projectors, but also in scientific applications such as SIM microscopy [49,265–268]. Choosing a relatively small pixel size (<10 µm) from the wide range of DMD models enables compact designs of SIM systems that are less complex and significantly less expensive compared to similarly fast FLCoS systems.

When using coherent light sources (lasers), as is usually the case for SIM, DMDs have a disadvantage that cannot be neglected. Due to the tilted micromirrors, DMDs have a jagged surface, which introduces the so-called blazed grating effect (BGE) [90,91]. Unlike other SLMs, when designing a DMD-based SIM microscope, it is important to understand and consider the BGE. Otherwise, an asymmetric intensity distribution will occur in the Fourier plane, resulting in poor interference contrast for pattern generation in the sample plane.

Within the scope of this thesis, in order to understand the BGE, DMDs were mathematically modeled, and different approaches were developed to simulate the diffraction patterns (Fourier plane) generated by coherent light. The evaluation of the simulation results allowed to first design and optimize a fast, compact and cost-effective one-color DMD-SIM microscope. This setup also has the capability for instantaneous parallel GPU-based reconstruction of the raw images into super-resolution SIM images that can be displayed in real time, during acquisitions. To enable this, the operating software of a FLCoS SIM microscope was adapted and ported accordingly. Based on the simulations, it was subsequently possible to find setup configurations that enable multicolor SIM microscopes with a DMD as SLM. This could be demonstrated by extending the one-color DMD-SIM microscope to two colors.

3.1 Coherent illumination of DMDs and blazed grating effect

3.1.1 Description of the blazed grating effect

To obtain an ideal interference contrast (high modulation depths) in the sample plane of a two-beam SIM microscope, the two laser beams interfering in the sample should have the same intensity (and polarization). Otherwise, poor interference will occur, resulting in a superposition of the sinusoidal pattern with a constant offset. As a result, the signal to noise ratio (SNR) of the reconstructed signal drops, as it is directly linked to the modulation depth of the SIM pattern. This results in a poor reconstruction with undesirable artifacts [48,199].

When using incoherent light (e.g. an LED) with DMDs, the interference effects of the phase shift produced by the micromirrors can be neglected. Thus, the DMD can be considered as a reflective amplitude modulating SLM for the incoherent case [212].

When coherent light (laser) is used, the DMD can no longer be described as amplitude modulating, but must be considered as a phase modulating SLM. Unlike LCD-based SLMs, the phase shift of DMDs is not constant over a pixel, which is ultimately the cause of the BGE. A one-dimensional description of the BGE can be traced back to Harvey & Pfisterer [90]. However, due to the two-dimensional nature of DMDs, this model needs to be extended. Texas Instruments (a large manufacturer of DMDs) provides a white-paper that serves as an introduction to the BGE for the use of DMDs with lasers [269]. In parallel with this thesis, a (semi-)analytical framework for modeling DMDs was developed by Brown et al. [270]. This is based on the same physical model describing the interaction of electromagnetic waves with the DMD surface. The results shown in this thesis are consistent with those of Brown et al. [270].

Briefly and illustratively, the BGE arises from the fact that the entire diffraction pattern of the DMD results from the superposition of an envelope with the grating diffraction (see Figure 27), similarly as it is the case in the Young double-slit experiment. The envelope corresponds to the diffraction pattern of a single micromirror (see Figure 27b), whose intensity distribution in the far field can be described simplified by a sinc function [269]:

$$I(\theta) = sinc^2\left(\pi \frac{w}{\lambda}\sin(\theta)\right) = \left[\frac{\sin\left(\pi \frac{w}{\lambda}\sin(\theta)\right)}{\pi \frac{w}{\lambda}\sin(\theta)}\right]^2 \tag{87}$$

Here with θ as observation angle, w the slit width respectively the mirror edge length, and λ as wavelength of the coherent light. The grating diffraction splits again into the native diffraction orders and the diffraction produced by the displayed patterns. The native diffraction orders result from the native grating structure of the DMD with the pixel pitch as the grating constant (see Figure 27a), while the diffraction pattern of the pattern displayed on the DMD forms around the native diffraction orders (see Figure 27d) [271,272].

The positions of the envelope and the native diffraction orders both depend on the angle of incidence, but they do not move congruently to each other. The position (of the center) of the envelope results from the reflection at the surface of a micromirror and depends on the angle of incidence and the tilt angle of the micromirrors. Therefore, there is an envelope for both the ON and OFF states of the micromirrors. The positions of the native diffraction orders result from the interference of all micromirrors (independent of the ON-OFF state), which can be described as diffraction at a reflective grating and thus depends on the angle of incidence, the pixel pitch (grating constant) and the wavelength. This has the consequence that the center of the envelope in most cases does not coincide with the position of a diffraction order, which then in turn has

the consequence that the diffraction images of the patterns displayed on the DMD show asymmetric intensity distributions (see Figure 27d). When using a DMD as SLM in a SIM microscope, this effect is undesirable. Therefore, the blaze condition must be fulfilled when using DMDs in SIM microscopes. The blaze condition is fulfilled if the center of the envelope coincides with the position of a native diffraction order. Since the pixel pitch and tilt angle for a DMD are usually constant, the angle of incidence and wavelength of light remain as adjustable parameters to satisfy the blaze condition.

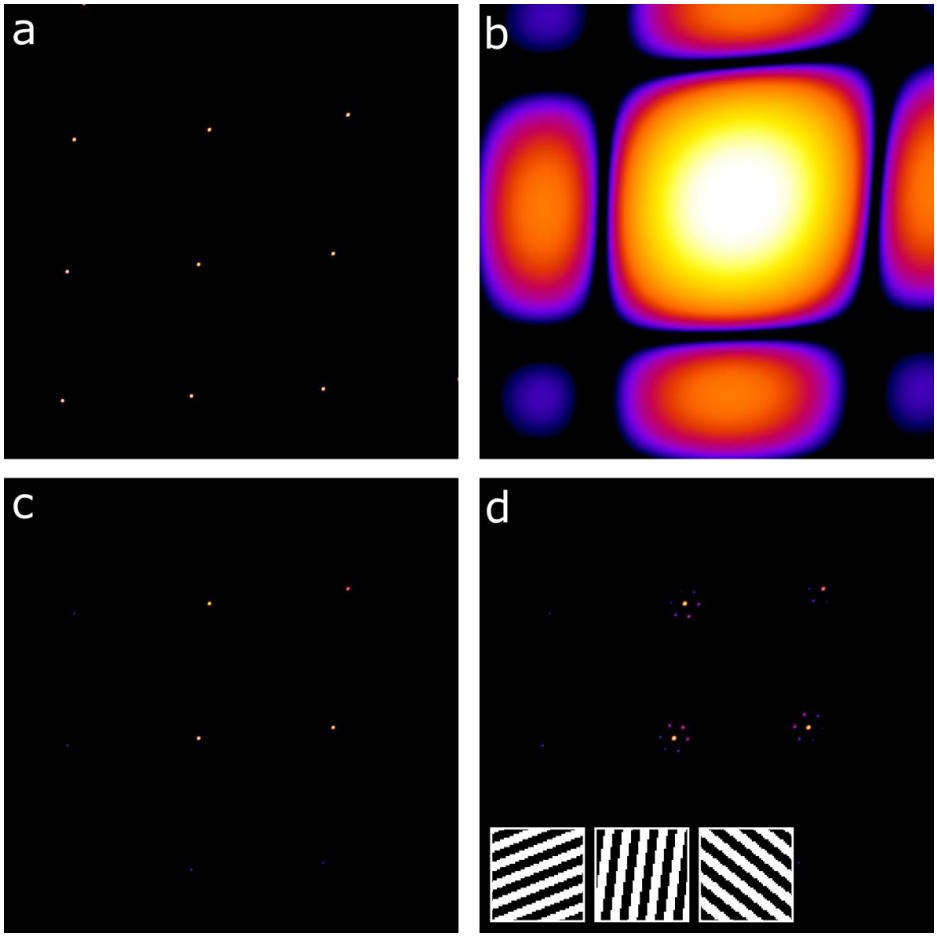

Figure 27: Simulated blazed grating effect of DMDs with coherent light

(a) Diffraction image of the native DMD grating without consideration of the envelope. (b) Diffraction image of a single micromirror (envelope) in the "on" position on the DMD. (c) Diffraction image of the native DMD grating resulting from multiplying (a) with (b). (d) Diffraction image of the DMD integrated over typical SIM patterns (inlays) for three SIM angles. All diffraction images shown are in logarithmic intensity representation and were simulated by using 50 x 50 micromirrors at 631 nm wavelength using parameters of the DLP® LightCrafter™ 6500 (Texas Instruments) [264]. The laser beam hits the DMD surface perpendicularly ($\varphi_a = \vartheta_a = 0°$). The diffraction images have a field of view of 17.5° x 17.5° ($7.5° \leq \varphi_b, \vartheta_b < 25°$). Images (a-c) were simulated using the grating approach, while image (d) was simulated using the analytic phase shifting approach. Figure taken from our corresponding publication [92].

3.1.2 The blazed grating effect in the laboratory

To approach the BGE from more than just the theoretical side, my colleague Dr. Alice Sandmeyer measured the native diffraction pattern of the DMD DLP® LightCrafter™ 6500 at various angles of incidence (Figure 28). Since the DLP® LightCrafter™ 6500, like many other DMDs, has the tilt axis of the micromirrors along the diagonal, the DMD was rotated 45° so that the incident and emergent angles are parallel to the optical table. The angle of emergence β of the brightest diffraction order (main order, mathematically 4th diffraction order along the 45° diagonal) of the DMD and the intensity of the four nearest diffraction orders (side orders, see Figure 28b) were measured. It was observed that the intensity of the side orders changes asymmetrically when the angle of incidence α is varied (see Figure 28c,d). For the OFF state at $\alpha = 24.5° \pm 1°$ a nearly symmetric intensity distribution of the secondary orders is obtained (blaze condition fulfilled). For the ON position, no clear incident angle α could be determined under which the side orders show a symmetric intensity distribution. The angle of emergence β of the main order changes almost linearly as a function of the angle of incidence α (see Figure 28e). From Figure 28c-e it can be seen that the ON and OFF states of the DMD do not behave identically, which is due to different tilt angles for ON and OFF. In the data sheet of the DLP® LightCrafter™ 6500, the tilt angle variance is given as ±1°. The asymmetric behavior of the side orders confirms the BGE described before. If the (invisible) envelope is centered in the main diffraction order (blaze angle: $\alpha \approx 24.5°$), the blaze condition is fulfilled and a symmetric intensity distribution of the side orders results.

Slightly elliptical polarization after the DMD

During the measurements, it was also noticed that the DMD slightly changes the polarization of incident laser light. Specifically, the S-polarized light in front of the DMD was slightly elliptically polarized behind the DMD. Presumably, this effect stems from the cover glass located immediately in front of the micromirror array. Since the polarization can have a significant effect on the modulation depths that can be achieved in the sample plane [209,210], it is recommended to restore the desired polarization (e.g. by using a linear polarization filter).

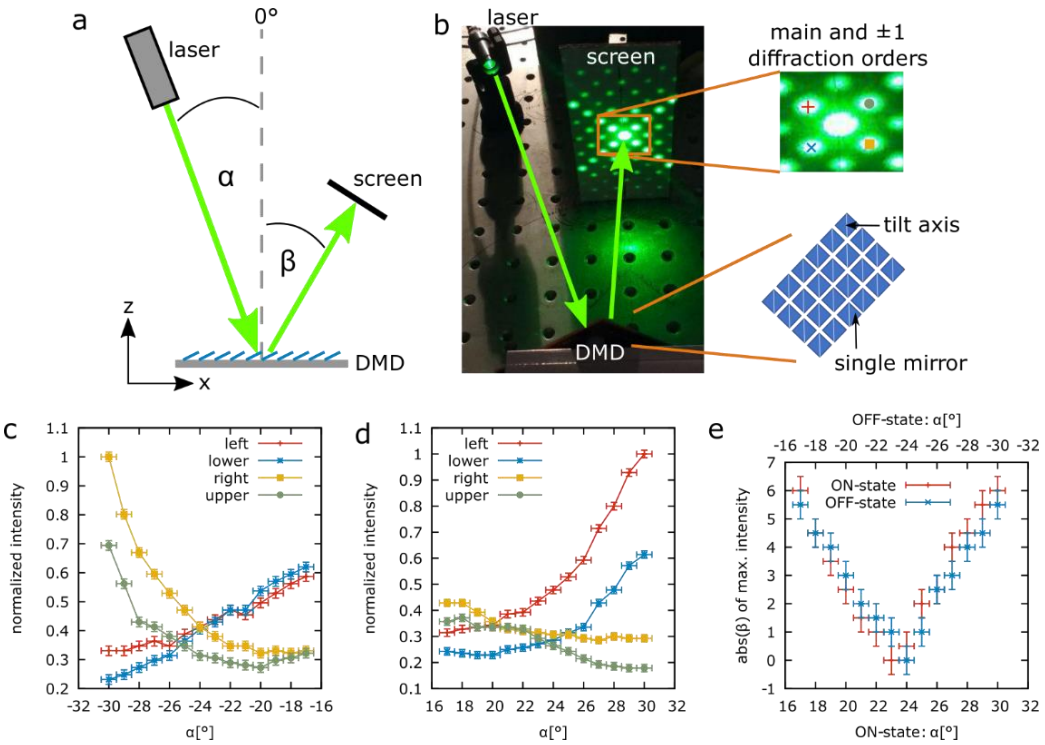

Figure 28: Investigation of the blazed grating effect of a coherently illuminated DMD

(a) Schematic drawing of the experiment. All mirrors of the DMD are tilted in one direction, where a tilt angle of +12° represents the ON state and a tilt angle of −12° represents the OFF state. α is the incident angle, whereas β is the diffraction angle of the main (4th) diffraction order. (b) Photograph of the experiment in the laboratory. Here, the entire DMD is rotated by 45°, so that the diffraction pattern is also rotated. The side diffraction orders of the underlying structure are labeled with symbols and colors which are also represented in (c) and (d). Normalized intensity measured at the side diffraction orders if all mirrors are switched to the OFF-state (c) or ON-state (d). (e) Absolute value of the diffraction angle β of the main diffraction order depending on the angle of incidence α. Figure taken from our corresponding publication [8].

3.2 Coherent DMD simulation software

For the use of DMDs in coherent SIM microscopes, it is necessary to understand the BGE in order to be able to consider it correctly in the design of a corresponding setup. Measurements in the laboratory (see Figure 28) are only suitable to a limited extent for this purpose, since the parameters (wavelength, angle of incidence, ...) can only be adjusted with great effort or comparatively low precision. For this purpose, a simulation framework was developed within the scope of this thesis, which is able to numerically simulate the interaction of coherent light with the DMD surface and the resulting far field (intensity distribution). The simulations are based on a physical model of propagating (coherent) electromagnetic fields interacting with the mathematically modeled DMD surface. From this, three simulation algorithms can be derived, each with different assumptions and thus constraints on the simulated system, but also different numerical complexity, i.e. simulation runtime. Along the 45° diagonal of DMDs, an analytical description of the BGE could also be found, which is particularly relevant for practical implementation in the laboratory. The simulation framework is motivated by DMD-based SIM microscopy but is generally applicable to other light pattern applications.

3.2.1 Mathematical and physical model of DMDs and coherent light

Choice of coordinates

First of all, it is important to find suitable coordinates to describe vectors (rays) and the resulting diffraction patterns. It has been found useful to place the DMD in the center of a Cartesian coordinate system (x, y, z) so that the DMD surface lies within the xy-plane (Figure 29a). When describing diffraction patterns in the far-field, a paraxial small-angle approximation is usually adopted, allowing for a Euclidean Cartesian coordinate system (x, y, z) of the diffraction space. This approximation is generally not satisfied for vectors pointing toward or away from the DMD. Angular coordinates (φ, ϑ) can be chosen that can be associated with the x and y axes of a Cartesian coordinate system (Figure 29b). The normalized vectors $\vec{a} = (a_x, a_y, a_z)$ and $\vec{b} = (b_x, b_y, b_z)$ with the angular coordinates (φ_a, ϑ_a) and (φ_b, ϑ_b) are used to describe the angles of incidence and emergence:

$$\begin{aligned} \vec{a}(\varphi_a, \vartheta_a) &= \begin{pmatrix} a_z \cdot \tan(\varphi_a) \\ a_z \cdot \tan(\vartheta_a) \\ a_z \end{pmatrix} \quad \text{with} \quad a_z = \sqrt{\frac{1}{\tan^2(\varphi_a)+\tan^2(\vartheta_a)+1}} \\ \vec{b}(\varphi_b, \vartheta_b) &= \begin{pmatrix} b_z \cdot \tan(\varphi_b) \\ b_z \cdot \tan(\vartheta_b) \\ b_z \end{pmatrix} \quad \text{with} \quad b_z = \sqrt{\frac{1}{\tan^2(\varphi_b)+\tan^2(\vartheta_b)+1}} \end{aligned} \tag{88}$$

To obtain a diffraction pattern for one angle of incidence $\vec{a}$ it is necessary to consider all angles of incidence $\vec{b}$ (e.g. 45° x 45°).

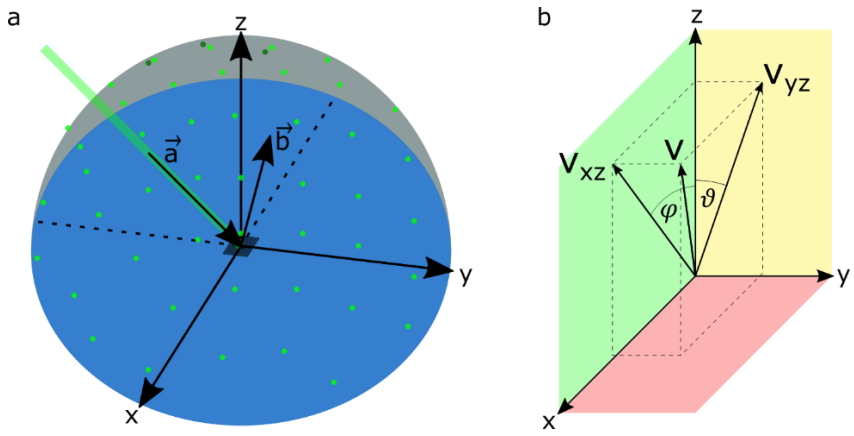

Figure 29: Visualization of angle parameterized vectors

(a) Visualization of light input and output vectors in the 3-dimensional space of the DMD. (b) Visualization of the tip/tilt angular coordinate system used to represent directionality of e.g. the directions $\vec{a}$ and $\vec{b}$. Figure taken from our corresponding publication [8].

DMD surface modeling

DMDs are essentially a two-dimensional array of small tilting micromirrors. The surface area of a quadratic micromirror $\vec{c}$ can be parameterized using its edge length w, and the parameters s and t (see Figure 30a):

$$\vec{c}(s,t) = (s,t,0) \quad \text{with} \quad 0 \leq s \leq w, 0 \leq t \leq w \tag{89}$$

The tilting of the micromirrors can be described as a rotation by the angle γ around the normalized diagonal axis $\vec{n} = (n_x, n_y, n_z) = \frac{1}{\sqrt{2}}(1,1,0)$ using the following rotation matrix:

$$R_n(\gamma) = \begin{pmatrix} n_x^2(1-\cos\gamma)+\cos\gamma & n_x n_y(1-\cos\gamma)-n_z\sin\gamma & n_x n_z(1-\cos\gamma)+n_y\sin\gamma \\ n_y n_x(1-\cos\gamma)+n_z\sin\gamma & n_y^2(1-\cos\gamma)+\cos\gamma & n_y n_z(1-\cos\gamma)-n_x\sin\gamma \\ n_z n_x(1-\cos\gamma)-n_y\sin\gamma & n_z n_y(1-\cos\gamma)+n_x\sin\gamma & n_z^2(1-\cos\gamma)+\cos\gamma \end{pmatrix} \tag{90}$$

To be able to move the individual micromirrors to their corresponding position on the DMD, the native grid of the DMD $\vec{m}(m_x, m_y) = m(m_x, m_y, 0)$ is used. The micromirror pitch $m = w + g$ is given by the edge length w and the gap g between the micromirrors. Thus, each micromirror on the DMD can be described by the following expression (see Figure 30):

$$\vec{d}_{m_x,m_y}\left(\gamma_{m_x,m_y}, s, t, m\right) = R\left(\gamma_{m_x,m_y}\right) \cdot \vec{c}(s,t) + m(m_x, m_y, 0) \tag{91}$$

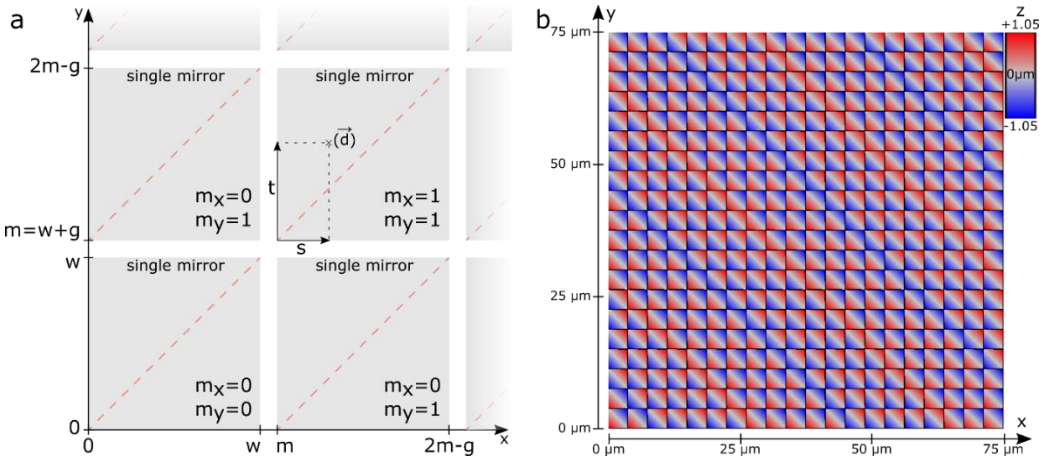

Figure 30: Surface modeling of DMDs

(a) Physical dimension and rotation axis of the micromirrors. (b) Resulting height profile of the DMD surface, which corresponds to phase delay. Figure taken from our corresponding publication [8].

Coherent light propagation

For modeling the diffraction behavior of monochromatic coherent light (laser) in the far field, the far field/Fraunhofer approximation is suitable. This allows the time-independent scalar description of the electric field, as planar wavefronts, which depends on the intensity distribution of the beam profile $I_0(\vec{a},\vec{d}) = \left|E_0(\vec{a},\vec{d})\right|^2$ projected onto the DMD:

$$E\left(E_0(\vec{a},\vec{d}),\Phi\right) = E_0(\vec{a},\vec{d}) \cdot e^{i\Phi} \quad \text{with} \quad \Phi = l \cdot \frac{2\pi}{\lambda} = \vec{d}\left(\vec{a}-\vec{b}\right)\frac{2\pi}{\lambda} \tag{92}$$

Here with E_0 as input amplitude and Φ as resulting phase, which depends on the path length $l_a + l_b = \vec{d}\vec{a} - \vec{d}\vec{b}$ and the wavelength λ (Figure 31).

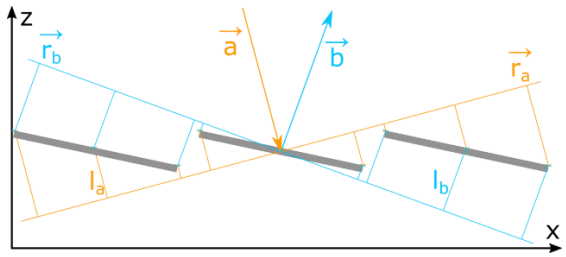

Figure 31: Phase shift of planar wavefronts to the DMD surface

(a) General determination of the phase shift for different points of a planar wave front, which is incident on the DMD in direction $\vec{a}$ and is diffracted in direction $\vec{b}$. This approach is correct in the far field/Fraunhofer approximation. Figure taken from our corresponding publication [92].

Consequently, for the electric field diffracted at any defined point on the DMD, the following is obtained:

$$E_{m_x,m_y}^{one\ point}\left(\vec{a},\vec{b},\gamma_{m_x,m_y},s,t,m,\lambda\right) = E_{m_x,m_y}^{0}\left(\vec{a},\gamma_{m_x,m_y},s,t\right) \cdot \exp\left(\frac{2\pi i}{\lambda}\vec{d}_{m_x,m_y}\left(\gamma_{m_x,m_y},s,t,m\right)\cdot\left(\vec{a}-\vec{b}\right)\right) \tag{93}$$

To obtain the resulting field distribution of the diffraction pattern it is necessary to integrate over each individual micromirror and then sum up the fields of all micromirrors (N_x x N_y):

$$E_{DMD}\left(\vec{a},\vec{b},\gamma_{m_x,m_y},w,m,N_x,N_y,\lambda\right) = \sum_{m_x=0,m_y=0}^{N_x-1,N_y-1}\iint_0^w E_{m_x,m_y}^{0}\left(\vec{a},\gamma_{m_x,m_y},s,t\right) \cdot \exp\left(\frac{2\pi i}{\lambda}\vec{d}_{m_x,m_y}\left(\gamma_{m_x,m_y},s,t,m\right)\cdot\left(\vec{a}-\vec{b}\right)\right) ds\ dt \tag{94}$$

This expression depends on many parameters and cannot be further analytically simplified without additional assumptions. In order to be able to calculate diffraction images of a DMD in adequate time, it is possible to make certain assumptions, which can simplify and accelerate the calculation. Depending on how these are chosen, different numerical simulation approaches (ray tracing, analytic phase shifting, grating) with different system constraints can be derived from eq. (94).

The diffraction patterns shown in the following sections were generally simulated with an array of only 50 x 50 micromirrors. Of course, the algorithms can also consider significantly more micromirrors. However, the diffraction orders then become smaller and smaller, whereby a clear visualization becomes noticeably worse (Fourier broadening). When choosing a comparatively small angular section of the diffraction space, with a correspondingly high angular resolution, more micromirrors can and should be taken into account.

3.2.2 Ray tracing approach

The first approach presented here is the ray tracing approach. Here, the sum and integral of eq. (94) is approximated by a Monte Carlo simulation with random rays. Further assumptions or restrictions are not necessary. Since each ray has to be calculated individually, the required computational effort is relatively large and thus the simulation is comparatively slow. To generate an incident collimated Gaussian laser beam, a Gaussian probability distribution is used to generate K random beams with the following equation of line:

$$\vec{f}_k = \vec{h}_k + u\vec{a} \quad \text{with} \quad k \in \mathrm{N}_0, \quad u \in \mathbb{R} \quad \text{and} \quad k < K \tag{95}$$

Here with $\vec{h}_k$ as support vector and $\vec{a}$ as normalized incidence direction vector with the parameter u. For simplicity, all $\vec{h}_k$ lie in a plane through the origin, which is why $\vec{h}_k$ and $\vec{a}$ are perpendicular to each other and $\vec{h}_k \cdot \vec{a} = 0$. The support vector $\vec{h}_k$ of each ray is randomly Gaussian distributed. The intersection points $\vec{p}_k = (m_x, m_y, s, t, u)$ of the rays $\vec{f}_k$ with the DMD surface $\vec{d}$ can be determined by solving the following linear system of equations:

$$\begin{pmatrix} m & 0 & \frac{1}{2}(1+\cos\gamma) & \frac{1}{2}(1-\cos\gamma) & -ax \\ 0 & m & \frac{1}{2}(1-\cos\gamma) & \frac{1}{2}(1+\cos\gamma) & -ay \\ 0 & 0 & -\frac{1}{\sqrt{2}}\sin\gamma & \frac{1}{\sqrt{2}}\sin\gamma & -az \end{pmatrix} \begin{pmatrix} m_x \\ m_y \\ s \\ t \\ u \end{pmatrix} = \begin{pmatrix} h_x \\ h_y \\ h_z \end{pmatrix} \tag{96}$$

This system of equations is underdetermined without restriction to one micromirror. Therefore, each micromirror (m_x, m_y) must be considered individually to solve it:

$$\begin{pmatrix} \frac{1}{2}(1+\cos\gamma) & \frac{1}{2}(1-\cos\gamma) & -ax \\ \frac{1}{2}(1-\cos\gamma) & \frac{1}{2}(1+\cos\gamma) & -ay \\ -\frac{1}{\sqrt{2}}\sin\gamma & \frac{1}{\sqrt{2}}\sin\gamma & -az \end{pmatrix} \begin{pmatrix} s \\ t \\ u \end{pmatrix} = \begin{pmatrix} h_x \\ h_y \\ h_z \end{pmatrix} - m \begin{pmatrix} m_x \\ m_y \\ 0 \end{pmatrix} \tag{97}$$

This system of equations can be solved analytically for each micromirror (see ray-dmd-intersection.nb [273]). The only valid solution can then be found by restricting s and t to the mirror edge length w. If there is still more than one solution left, the solution with the smallest u is the valid one, since the resulting intersection of the ray with the DMD is the first one in the ray direction.

Since the Gaussian beam profile is already considered by the Gaussian random distribution of the beams an intensity of $E^0_{m_x,m_y} = 1$ can be assumed for all beams, which eq. (93) simplifies as follows:

$$\begin{aligned} E^{one\ ray}_{m_x,m_y}(\vec{a}, \vec{b}, \vec{p}_k, \lambda) &= E_{in}(\vec{a}, \vec{p}_k, \lambda) \cdot E_{out}(\vec{b}, \vec{p}_k, \lambda) \\ &= \exp\left(\frac{2\pi i}{\lambda} \vec{d}(\vec{p}_k)\vec{a}\right) \cdot \exp\left(-\frac{2\pi i}{\lambda} \vec{d}(\vec{p}_k)\vec{b}\right) \end{aligned} \tag{98}$$

An illustration of the phase shift of individual rays is shown in Figure 32. Summing up the individual rays yields the final ray tracing equation with which the field distribution

of the resulting diffraction pattern can be calculated. Thus eq. (94) can be rewritten as follows:

$$E_{DMD}\left(\vec{a},\vec{b},\gamma_{m_x,m_y},w,m,N_x,N_y,\lambda\right)=\sum_{k=0}^{K-1}\exp\left(\frac{2\pi i}{\lambda}\vec{d}(\vec{p}_k)(\vec{a}-\vec{b})\right) \tag{99}$$

With respect to the beam profile and in particular the assumption of completely monochromatic (i.e. coherent) light, the ray tracing approach can be easily extended. The beam profile can be adjusted by changing the support vector distribution. By introducing a wavelength and phase distribution of the individual beams, the monochromatic coherent boundary condition could be softened (e.g. for LEDs as light source).

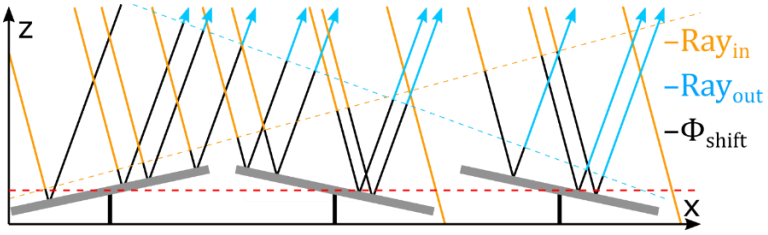

Figure 32: Schematic representation of the ray tracing approach

Modeling of rays and their phase shift, which are incident on the DMD in the direction $\vec{a}$ and diffracted in the direction $\vec{b}$. For the sake of clarity, only one angle of emergence is shown for one angle of incidence. To obtain a complete diffraction image for one angle of incidence, however, it is necessary to consider all angles of emergence. Figure taken from our corresponding publication [92].

3.2.3 Analytic phase shifting approach

For the analytic phase shifting approach, we assume that the field amplitude across a micromirror is constant $E^0_{m_x,m_y}\left(\vec{a},\gamma_{m_x,m_y},s,t\right)\rightarrow E^0_{m_x,m_y}\left(\vec{a},\gamma_{m_x,m_y}\right)$. Moreover, it is assumed that each micromirror is either in tilt state γ^- or γ^+, which is a reasonable assumption for the steady state of a micromirror of a DMD. The desired Gaussian beam profile can be approximated by adjusting $E^0_{m_x,m_y}$ over the different micromirrors. Since usually enough mirrors are illuminated, the approximation error is negligible. With these assumptions, the integral over a single micromirror from eq. (94) becomes solvable for γ^- and γ^+ and leads to the analytic determined field distribution (see dmd.nb [273]):

$$E^{single\ mirror}\left(\vec{a},\vec{b},\gamma^{\pm}_{m_x,m_y},w,\lambda\right)=\iint_0^w\exp\left(\frac{2\pi i}{\lambda}\left(R\left(\gamma^{\pm}_{m_x,m_y}\right)\cdot(s,t,0)\right)\cdot(\vec{a}-\vec{b})\right)ds\,dt \tag{100}$$

Instead of calculating the field distribution for each micromirror, it is possible to calculate the field distribution once for γ^- and γ^+ for a reference micromirror on the

DMD and then shift the phase with respect to the reference micromirror according to the grating position (m_x, m_y) (see Figure 33):

$$E^{shift}_{m_x,m_y}(\vec{a},\vec{b},m,\lambda) = \exp\left(\frac{2\pi i}{\lambda}\vec{m}(m_x,m_y)\cdot(\vec{a}-\vec{b})\right) \tag{101}$$

This simplifies eq. (94) to:

$$\begin{aligned} E_{DMD}\left(\vec{a},\vec{b},\gamma_{m_x,m_y},w,m,N_x,N_y,\lambda\right) = & \sum_{m_x=0,m_y=0}^{N_x-1,N_y-1} E^{0}_{m_x,m_y}\left(\vec{a},\gamma_{m_x,m_y}\right) \\ & \cdot E^{single\ mirror}\left(\vec{a},\vec{b},\gamma^{\pm}_{m_x,m_y},w,\lambda\right) \\ & \cdot E^{shift}_{m_x,m_y}(\vec{a},\vec{b},m,\lambda) \end{aligned} \tag{102}$$

This expression is significantly less computationally intensive compared to the ray tracing approach (eq. (99)), while only small negligible approximations were made. Chronologically, this was the first simulation approach implemented and was therefore used to design and optimize the one-color DMD-SIM microscope (section 3.4).

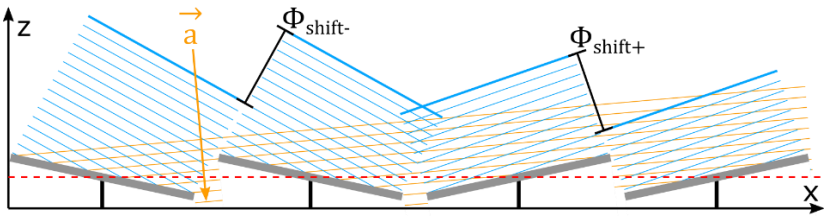

Figure 33: Schematic representation of the analytic phase shifting approach

Simplified modelling of diffraction images in the form of wave fronts reflected by micromirrors, where the diffraction image of a single mirror is analytically known. Figure taken from our corresponding publication [92].

Ray tracing vs. analytic phase shifting

Both the ray tracing approach and the analytic phase shifting approach can be used to simulate arbitrary patterns on the DMD. Figure 34 compares the simulation results of the ray tracing approach for different amounts of rays with those of the analytic phase shifting approach. The more rays are used for ray tracing, the more distinct the diffraction orders are compared to the background noise. From about 100000 rays on (with 50 x 50 micromirrors), there is hardly any qualitative difference between ray tracing and analytic phase shifting. Therefore, both approaches are well suited to perform simulations with patterns (e.g. for SIM). However, due to its noticeably shorter runtime, the analytic phase shifting approach is usually preferable. However, the ray tracing approach remains interesting for variations of the beam profile or the introduction of wavelength and phase shift distributions (incoherence).

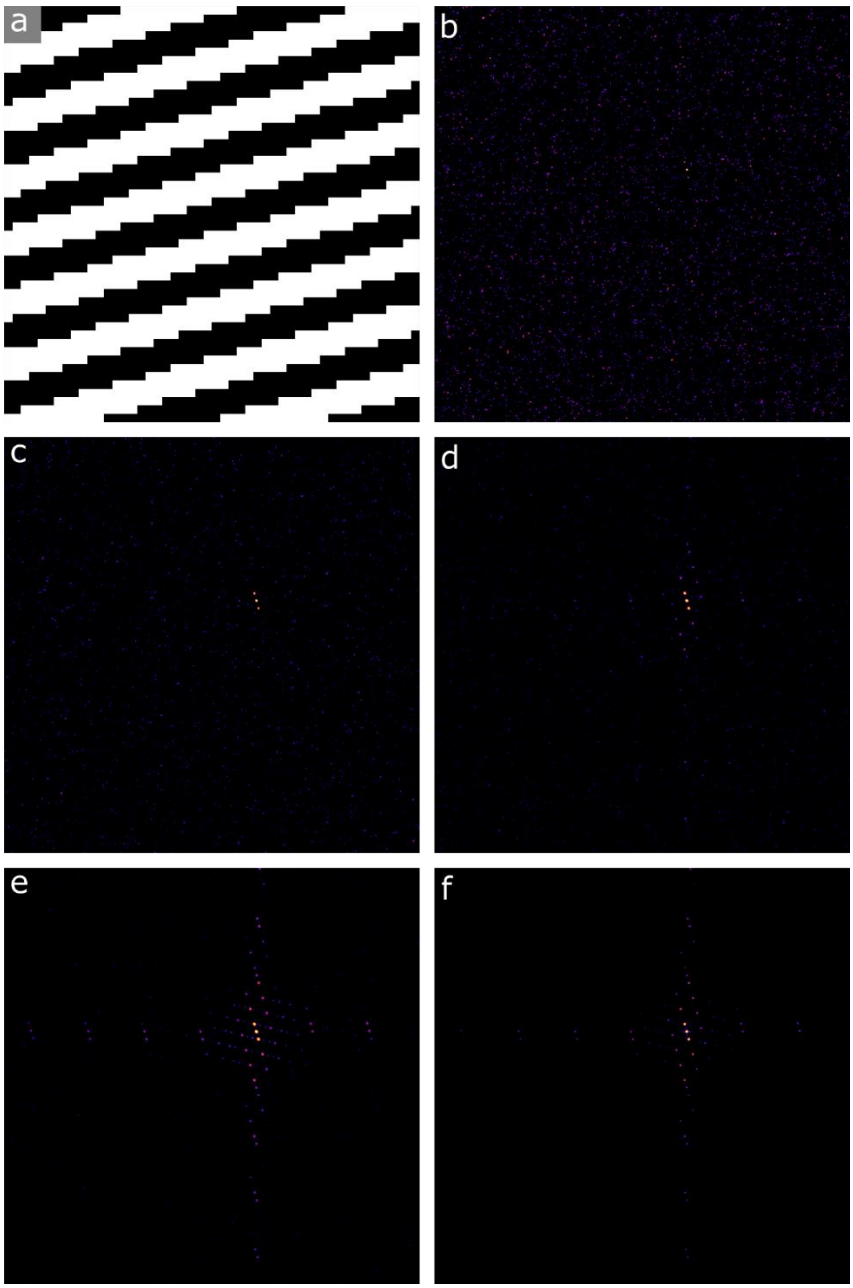

Figure 34: Comparison between ray tracing and analytic phase shifting approach

(a) shows a 50x50 pixel section of a typical SIM pattern, which is displayed on a SLM (DMD). (b-e) show diffraction images of (a) which have been simulated using the raytracing approach with 100, 1000, 10000 and 100000 rays. (f) shows the diffraction image of (a) which was simulated using the Analytic Phase Shifting Approach. All diffraction images shown are in logarithmic intensity representation and were simulated via an array of 50 x 50 micromirrors at $\lambda = 532\ nm$. Each micromirror has a size of 7.56 µm x 7.56 µm. $\varphi_a = -\vartheta_a = -21°$ (blaze condition) was chosen as angle of incidence. The diffraction images are shown for both angles φ_b and ϑ_b with an angle range of -15° to 15°. Figure taken from our corresponding publication [92].

For the sake of completeness, Figure 35 demonstrates that not only SIM patterns can be simulated with the analytic phase shifting approach, but also any other patterns on the DMD. Of course, the same is true for the ray tracing approach, but it requires significantly more computing time.

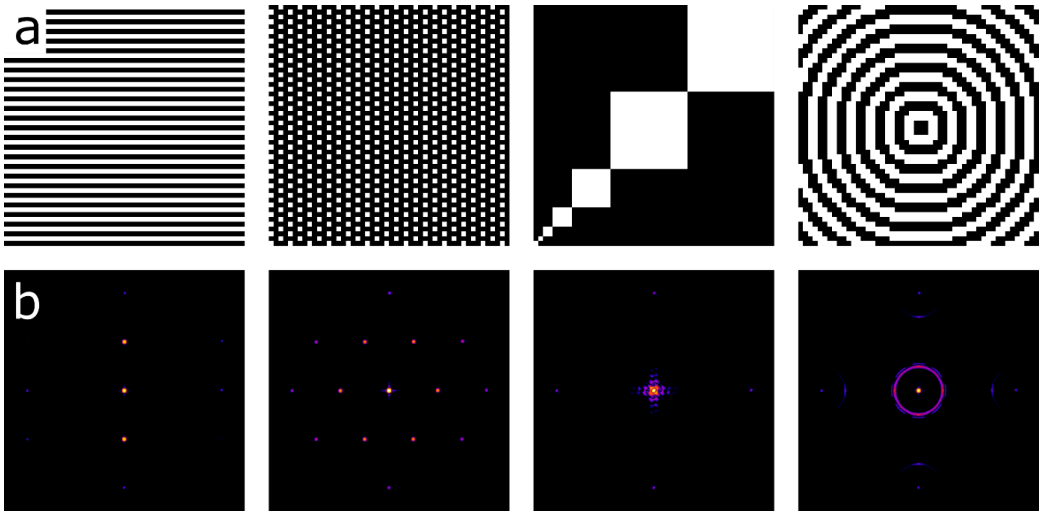

Figure 35: Comparison of diffraction patterns generated with a DMD

(a) Different DMD patterns. From left to right: Horizontal lines; MAP-SIM example; MAP-SIM calibration pattern [202,203,274]; concentric circles. (b) Diffraction images of the DMD patterns shown in (a), simulated with the analytic phase shift approach with 50 × 50 micromirrors at 532 nm wavelength. For the angles of incidence $\varphi_a = -\vartheta_a = -21°$ (blaze condition) was chosen. The diffraction images are shown for a range of −1.8° to 8.2° for φ_b (x-axis) and −8.2° to 1.8° for ϑ_b (y-axis). The intensity distribution corresponds to a logarithmic scale. Figure taken from our corresponding publication [92].

3.2.4 Grating approach

In addition to the assumptions of the analytic phase shifting approach, we assume in the following that the field amplitude of the incident wavefront is constant over the entire DMD ($E^0_{m_x,m_y}\left(\vec{a},\gamma_{m_x,m_y}\right) = 1$). Furthermore, we assume that all micromirrors are in either γ^- or γ^+ state. The field of a single micromirror $E^{single\ mirror}_{\gamma^\pm}\left(\vec{a},\vec{b},w,\lambda\right)$ from eq. (100) can now be viewed as an envelope over the field of the native DMD

lattice $E^{grating}\left(\vec{a},\vec{b},m,N_x,N_y,\lambda\right)$. The field of the native DMD lattice is given by the sum over the phase shifts from eq. (102), which can be written down as follows:

$$\begin{aligned} E^{grating}\left(\vec{a},\vec{b},m,N_x,N_y,\lambda\right) &= \sum_{m_x=0,m_y=0}^{N_x-1,N_y-1} E^{shift}_{m_x,m_y}\left(\vec{a},\vec{b},m,\lambda\right) \\ &= \sum_{m_x=0,m_y=0}^{N_x-1,N_y-1} \exp\left(\frac{2\pi mi}{\lambda}\left((a_x-b_x)m_x+(a_y-b_y)m_y\right)\right) \\ &= \frac{\left(-1+\exp\left(\frac{2\pi mi}{\lambda}(a_x-b_x)N_x\right)\right)\left(-1+\exp\left(\frac{2\pi mi}{\lambda}(a_y-b_y)N_y\right)\right)}{\left(-1+\exp\left(\frac{2\pi mi}{\lambda}(a_x-b_x)\right)\right)\left(-1+\exp\left(\frac{2\pi mi}{\lambda}(a_y-b_y)\right)\right)} \end{aligned} \quad (103)$$

Thus, eq. (94) can be written as follows:

$$E_{DMD}\left(\vec{a},\vec{b},\gamma^{\pm},w,m,N_x,N_y,\lambda\right) = E^{single\ mirror}\left(\vec{a},\vec{b},\gamma^{\pm},w,\lambda\right)\cdot E^{grating}\left(\vec{a},\vec{b},m,N_x,N_y,\lambda\right) \quad (104)$$

Similar to what is known from the Young double-slit experiment, the intensity distribution of the total diffraction pattern can be calculated as multiplication of the intensity distribution of the single slit diffraction (single micromirror diffraction) $I_{envelope}$ with the native grating diffraction $I_{grating}$ (see Figure 36):

$$I_{DMD} = |E_{DMD}|^2 = \left|E^{single\ mirror}\right|^2 \cdot \left|E^{grating}\right|^2 = I_{envelope}\cdot I_{grating} \quad (105)$$

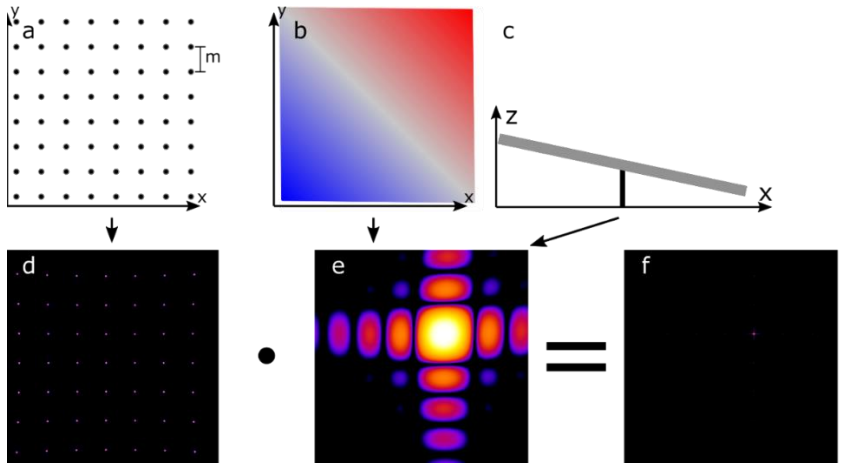

Figure 36: Schematic representation of the grating approach

In the upper row the native grating of the DMD array (a), and a single mirror (b, c) are shown schematically. In the lower row the corresponding diffraction images (d, e) and their product (f), which results in the diffraction image of the entire DMD, are shown. All diffraction images shown are in logarithmic intensity representation and were generated with an array of 50 x 50 micromirrors at 532 nm wavelength. Each micromirror has a size of 7.56 µm x 7.56 µm. $\varphi_a = -\vartheta_a = -21°$ (blaze condition) was chosen as angle of incidence. The diffraction images are shown for both angles φ_b and ϑ_b with an angle range of -15° to 15°. Figure taken from our corresponding publication [92].

Due to the restriction of all micromirrors to be in tilt state γ^- or γ^+ the grating approach is not able to simulate arbitrary patterns on the DMD in contrast to the ray tracing approach and the analytic phase shifting approach. On the other hand, the approach is very efficient in terms of computational effort and the associated computational time. It is particularly well suited for investigating the general diffraction properties of a DMD.

3.2.5 Blaze condition approach

Restricting the incidence angles to the 45° diagonal perpendicular to the tilting axis of the micromirrors $\vec{n}$ and that all micromirrors are either in γ^- or γ^+ state, the problem of BGE and finding the blaze angle to fulfill the blaze condition simplifies to a one-dimensional analytically solvable problem. As seen in Figure 37a, the DMD can be considered rotated by 45°, which satisfies the following for the incident and the emergent angles along the 45° diagonal:

$$\begin{aligned} \vec{a} &= (a_x, -a_x, a_z) \quad \text{and} \quad -\varphi_a = \vartheta_a \\ \vec{b} &= (b_x, -b_x, b_z) \quad \text{and} \quad -\varphi_b = \vartheta_b \end{aligned} \tag{106}$$

Due to the 45° rotation, the transition from the previously used angular coordinates (φ, ϑ) to the angles α and β (see Figure 37b) lends itself to the description of the incidence and emergence angles:

$$\alpha = \arctan\left(\sqrt{2} \cdot \tan\left(\varphi_a\right)\right) \quad ; \quad \beta = \arctan\left(\sqrt{2} \cdot \tan\left(\varphi_b\right)\right) \tag{107}$$

The axis $\vec{k} = (1, -1, 0)$ is defined in the direction of the 45° diagonals. Along this, a new effective lattice constant $m' = \frac{1}{\sqrt{2}} m$ is obtained. As illustrated in Figure 37b, this results in a path length for planar wavefronts (collimated coherent light) diffracted by the DMD of:

$$l = l_{in} - l_{out} = m'\left(\sin(\alpha) - \sin\left(-\beta_{grating}\right)\right) \tag{108}$$

As it is known for diffraction at gratings, this path length must be just the integer multiple of the wavelength λ to get perfect constructive interference:

$$n\lambda = m'\left(\sin(\alpha) + \sin\left(\beta_{grating}\right)\right) \tag{109}$$

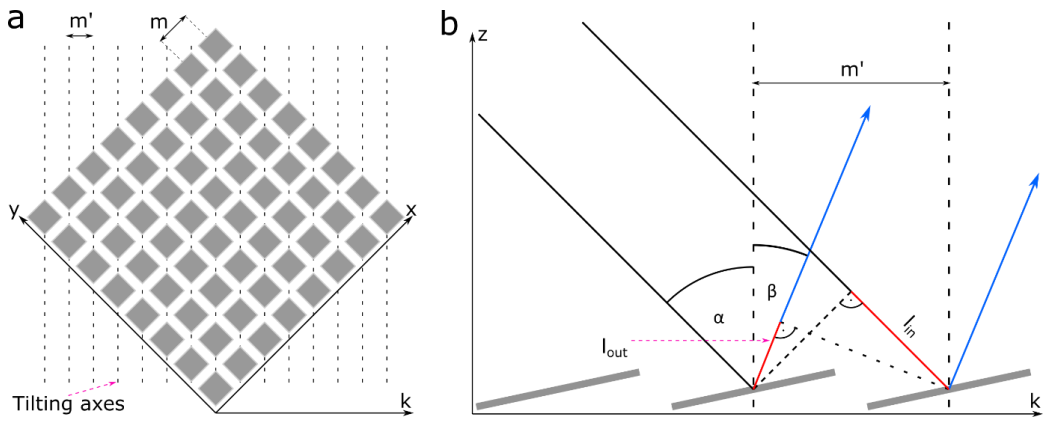

Figure 37: Blaze condition approach

(a) Schematic illustration of a DMD rotated by 45° around the z-axis. Furthermore, the tilt axes of the micromirrors, the grid constants m and m' and the coordinate axis k are shown. (b) Graphical representation of the calculation of the phase shift for light, which is incident along the kz-plane on a DMD. Figure taken from our corresponding publication [92].

The blaze condition is satisfied exactly when the emergence angle $\beta_{grating}$ for perfect constructive interference coincides with the emergence angle $\beta_{envelope}$ of the center of the envelope ($\beta_{grating} = \beta_{envelope}$). $\beta_{envelope}$ can be determined by the reflection of α at the micromirror surface:

$$\beta_{envelope} = -\alpha + 2\gamma \tag{110}$$

By substituting eq. (110) into eq. (109) the generally non-integer lattice diffraction order for the diffraction angle of the envelope $\beta_{envelope}$ can be determined:

$$n = \frac{m'}{\lambda}(\sin(\alpha) + \sin(-\alpha + 2\gamma)) \tag{111}$$

In case n is an integer, the nth diffraction order lies in the center of the envelope. The blaze condition is therefore fulfilled. To visualize the blaze condition, the quantity v is introduced with the help of the sine function:

$$v = |\sin(n\pi)| = \left|\sin\left(\frac{\pi m'}{\lambda}(\sin(\alpha) + \sin(-\alpha + 2\gamma))\right)\right| \tag{112}$$

A blaze condition is always satisfied when $v = 0$. The choice of $|\sin(n\pi)|$ lends itself to visualization, since both negative and positive deviations are considered equally nonlinear (small deviations around $v = 0$ contribute more strongly).

3.2.6 Discussion of the different simulation approaches

All the approaches presented are used depending on the problem and have certain advantages and disadvantages. Figure 38 shows that the ray tracing approach, the analytic phase shifting approach, and the grating approach deliver qualitatively the same results. The positions of the individual diffraction orders are identical in all three approaches.

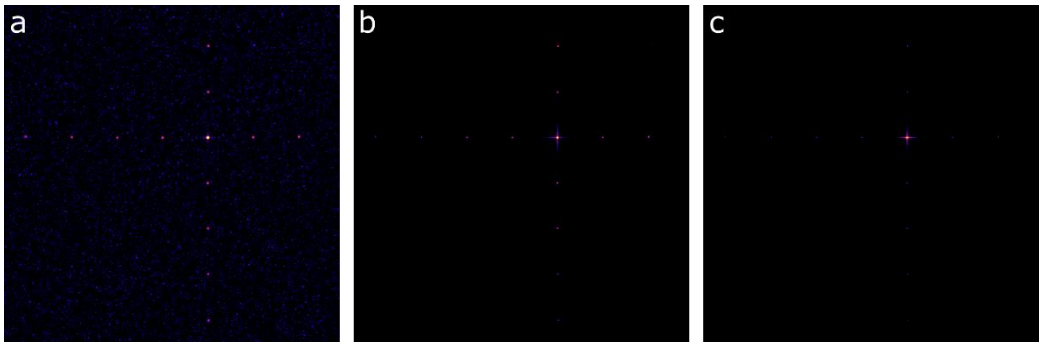

Figure 38: Simulation approaches in comparison

Comparison of the diffraction images (from left to right): Ray tracing approach (a), analytic phase shifting approach (b), grating approach (c). Simulated at 532 nm, with $\varphi_a = -\vartheta_a = -21°$ (blaze condition), for a micromirror pitch of 7.56 µm and a micromirror tilt angle of $\gamma^{\pm} = \pm 12°$ with 50 x 50 micromirrors, corresponding to the dimensions of the DLP® LightCrafter™ 6500 (Texas Instruments) [264]. The diffraction images are shown for both angles φ_b and ϑ_b with an angle range of -15° to 15°. Figure taken from our corresponding publication [92].

The ray tracing approach is the most flexible with the fewest assumptions or constraints, but it is also the slowest. Therefore, it is particularly suitable for further development for the investigation of partially incoherent light, as is the case for LEDs. As of now, the introduction of wavelength and phase distributions for modeling the incoherent case has not yet been implemented but would be comparatively easy to implement. In addition, with a corresponding extension, it would be possible to use this approach to investigate the influence of deformations of the DMD surface (i.e. non-flat surface structure) and the influence of arbitrary incident (collimated, convergent or divergent) beam profiles.

Both the ray tracing approach and the analytic phase shifting approach are able to consider arbitrary patterns on the DMD. However, since the latter is much more efficient and faster, it is preferable in the general coherent case (section 3.3). The extensions proposed for the ray tracing approach could also be implemented for the analytic phase shifting approach under restrictions, but the required computational effort would become immense, so that there would be no more advantages compared to an extended ray tracing approach.

Compared to the first two approaches, the grating approach seems unimportant at first due to its lack of ability to consider patterns on the DMD. However, it is much faster compared to the previous two. Therefore, it is particularly suitable for the general investigation of the diffraction properties of a DMD. It allows the search for blaze angles satisfying the blaze condition for arbitrary entrance and emergence angles in an efficient way and provides valuable insights for the design and optimization of DMD based SIM microscopes (section 3.5).

Due to the reduction to one dimension along the 45° diagonal $\vec{k}$, the blaze condition approach is suitable for visualizing the blaze condition for different wavelengths λ against different angles of incidence α. The practical implementation of DMD-based SIM systems often takes place along the 45° diagonal $\vec{k}$ as well, as this simplifies the opto-mechanical construction of the setups. Thus, this approach provides important insights, especially for multicolor DMD-based SIM microscopy, despite its seemingly far-reaching limitations (see section 3.5). Since it is a purely analytical approach, it requires negligible computational power, making the results instantaneously computable.

All four approaches presented were implemented in the Java programming language as well as partially graphics card accelerated via CUDA and are provided as a Fiji plugin [273]. Table 1 compares the four approaches and summarizes their strengths and weaknesses.

	Ray tracing	Analytic phase shifting	Grating	Blaze condition
Capable of patterns	+ Yes	+ Yes	- No	- No
Speed (Time CPU/GPU)	-- Very slow (84 min/------)	- Slow (7.5 min/3 sec)	+ Fast (3.2 sec/1.2 sec)	++ Instant
Use case	Incoherent light	Specific DMD-patterns	Native pattern under different conditions	Analysis of the diagonal

Table 1: Comparison of the four discussed approaches.

This table gives a compact summary of the discussed approaches. The runtimes for the approaches were measured with 50 × 50 mirrors at a resolution of 1500 × 1500 pixels in diffraction space on an Intel Core i5 4690 4×3.50 GHz with a NVIDIA GeForce GTX1060 6GB. The ray tracing approach was measured with 100 000 rays. The runtimes can vary significantly depending on the approach, the number of mirrors, the resolution and the computer used. Table taken from our corresponding publication [92].

All four approaches have contributed to the understanding and handling of the BGE in relation to DMD based SIM microscopy. The simulation results shown in section 3.3 have led to the design and optimization of a one-color DMD SIM microscope (section 3.4). With further simulation results shown in section 3.5 it was subsequently possible to extend the one-color DMD-SIM microscope to two colors (section 3.6). A subsequent extension to three colors is also being planned based on the simulation results.

3.2.7 Software architecture and Fiji-Plugin

The four simulation approaches presented in the previous sections were implemented using the Java and CUDA programming languages. A Fiji plugin is available under open-source license for easy access without required programming skills [273]. The results of the algorithms invoked via the Fiji plugin are stored on disk as TIFF files and can be opened and further processed via Fiji. The underlying software architecture is presented in the following Figure 39.

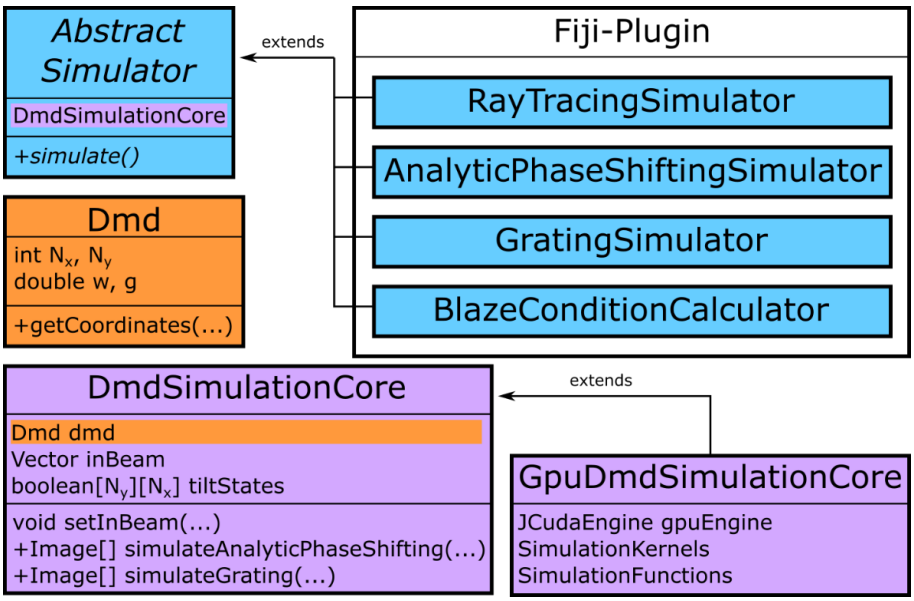

Figure 39: Schematic overview of the coherent DMD simulation framework

The four simulation approaches presented above were each implemented within a separate Java class and embedded in a Fiji plugin (see Figure 40). In addition to being called via Fiji, the simulations can also be started via the command line or a development environment. GPU support is currently implemented only for the analytic phase shifting approach and the grating approach via call from command line or development environment. The classes of the simulation approaches are derived from an abstract superclass, the AbstractSimulator. This includes a method to start a simulation and the class DmdSimulationCore, which contains the surface model of the DMD and provides the basic mathematical algorithms for the simulations. In addition to the CPU-based DmdSimulationCore, there is also a GPU-based variant, the GpuDmdSimulationCore. The simulation algorithms for the GPU were implemented as CUDA kernels, which can be called via the interface to CUDA, the JCudaEngine [275].

A quick guide to the installation of the Fiji plugin can be found in the supplemental material of the corresponding publication [92]. After successful installation, all four simulation algorithms are available via the plugins menu of Fiji (see Figure 40a). Due to the required computing capacity, the ray tracing approach and the analytic phase shifting approach simulate only a single diffraction image (see e.g. Figure 34).

The grating approach, on the other hand, is designed to compute many diffraction images and examine them at runtime with respect to the BGE and the possible fulfillment of the blaze condition. For this purpose, the position of the brightest diffraction order and the distance to the center of the envelope are stored (see Figure 52b). The stored data can then be further processed via the "Diffraction Space Analysis" to images like Figure 53, so that statements can be made about the diffraction angles in the diffraction space at which the blaze condition can be fulfilled.

The blaze condition approach is primarily used to investigate the blaze condition along the 45° diagonal for different wavelengths and angles of incidence and emergence. As a result, images similar to Figure 54b are obtained. After selecting a simulation approach, an input mask appears in which the system constraints can be defined (Figure 40b) before the simulation is started.

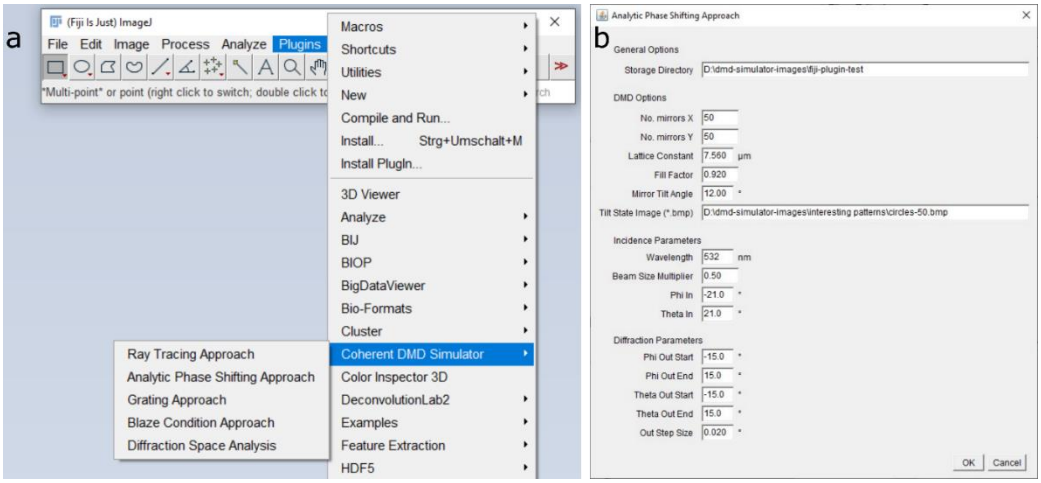

Figure 40: Plugins menu of Fiji and input mask to start a simulation

(a) After opening the plugins menu of Fiji, the four presented simulation approaches can be started via the tab "Coherent DMD Simulator" with a few mouse clicks. The results are saved on the hard disk as TIFF files. The "Diffraction Space Analysis" is used for further analysis of the results of the grating approach. (b) Input mask before starting a simulation, exemplified by the analytic phase shifting approach.

3.3 One-color simulation results

The simulation results shown in this section are all based on the analytic phase shifting approach, because this was the first one developed and implemented. The simulations were all performed with a wavelength of 532 nm for the DMD *DLP® LightCrafter™ 6500* (Texas Instruments) [264] to advance the development of the one-color dmd-sim microscope (see section 3.4).

By calculating the diffraction pattern of a single micromirror (Figure 41a, for OFF- and ON-state γ^- and γ^+), the envelope could be visualized for the first time using the simulations. As expected, the envelope has the intensity distribution of a sheared two-dimensional sinc function (eq. (87)).

By simulating 100 x 100 micromirrors, all in the OFF-state, it was possible for the first time to display the native diffraction pattern (superimposed with the OFF-envelope) (see Figure 41b). Apart from the fact that the brightest diffraction order has the shape of a cross due to the logarithmic intensity representation, the simulated native diffraction pattern qualitatively corresponds to what can be observed in the laboratory (see section 3.1.2). Through various comparisons between the simulation results and the experience with DMDs in the laboratory, it can be assumed that the simulations produce valid results.

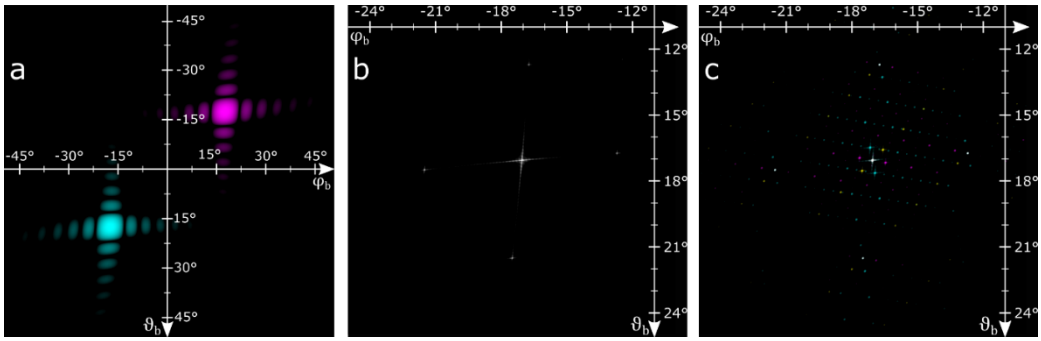

Figure 41: Wave propagation and interference pattern simulation of a DMD surface

A fully coherent light source is simulated illuminating the DMD head-on (angle of incidence 0°) and with a Gaussian intensity profile (b and c). The diagrams show the reflected intensity plotted against the output angle (Figure 29), on a logarithmic scale. (a) Diffraction pattern of a (hypothetical) single mirror, in its two possible tilt states ("teal" is OFF and "magenta" is ON). (b) Diffraction pattern of the DMD surface (100 x 100 micromirrors) when all micromirrors are oriented into the same OFF position (native diffraction orders). (c) DMD displaying a typical SIM pattern, while illuminated with coherent light. The full diffraction pattern arises from the inert diffraction properties of the DMD (mechanical mirror size and tilt) with the pixelated and binary SIM pattern superimposed. The three colors indicate a different SIM pattern for each typical angle used for SIM. Figure taken from our corresponding publication [8].

Regarding the use of a DMD as SLM in a SIM microscope, the next logical step was to simulate typical SIM patterns (three angles, each rotated by 60°) on the DMD (see Figure 41c). As expected, the diffraction orders of the native diffraction pattern are modulated by the structure displayed on the DMD.

For the simulations of Figure 41, no further thought was initially given to the angle of incidence and the BGE. Looking at Figure 41c, it seems at first glance that the BGE is negligible, since the diffraction orders appear equally bright. However, this is a fallacy, since for the simulated wavelength of 532 nm the angle of incidence of $\varphi_a = \vartheta_a = 0°$ fortuitously lies near a blaze condition ($\alpha_{blaze} = 5°$, see Figure 42d,e). With an appropriately chosen intensity plot, it would be noticeable that the $\pm 1^{st}$ diffraction orders of the SIM patterns have an asymmetric intensity distribution, which would result in poor modulation depths in the sample plane.

The effect of the BGE on the intensity of the $\pm 1^{st}$ diffraction orders of the SIM patterns is again clearly illustrated in Figure 42a-c using simulation results. The closer the center of the envelope is to a native diffraction order, the more symmetrical the intensity distribution of the $\pm 1^{st}$ diffractions order relevant for SIM becomes. The distance between the center of the envelope and the brightest native diffraction order can be considered as a metric for satisfying the blaze condition. If a native diffraction order and the center of the envelope are exactly on top of each other, the blaze condition is fulfilled.

Diffraction images without patterns on the DMD (all micromirrors in OFF-state) were simulated as a function of the angle of incidence with -40° to +40° for φ_a and ϑ_a respectively. The distance between the brightest native diffraction order and the envelope was determined for each diffraction image and plotted as a heat map (Figure 42d). The dark ring-shaped structures in Figure 42d mark angles of incidence where the blaze condition is fulfilled. The 45° diagonal ($\varphi_a = -\vartheta_a$) is of particular importance here, because the tilt angles are then perpendicular to the plane of incidence (and thus also the plane of emergence), which makes practical implementation in the laboratory much easier. From Figure 42e it can be seen that the blaze condition along the 45° diagonal is fulfilled for $\alpha \approx \{-30°, 5°, 34°, 56°\}$, which according to eq. (110) for $\gamma^- = -12°$ results in the emergence angles $\beta \approx \{6°, -19°, -58°, -80°\}$. The smaller the emergence angle, the smaller the shear of the SIM pattern and thus the ellipticity of the Fourier plane. The smallest possible emergence angle ($\beta \approx 6°$ with $\alpha \approx -30°$), for which the blaze condition is fulfilled, is the ideal basis for the setup shown in section 3.4 Here, the slight shear could even be neglected due to the small angle of emergence.

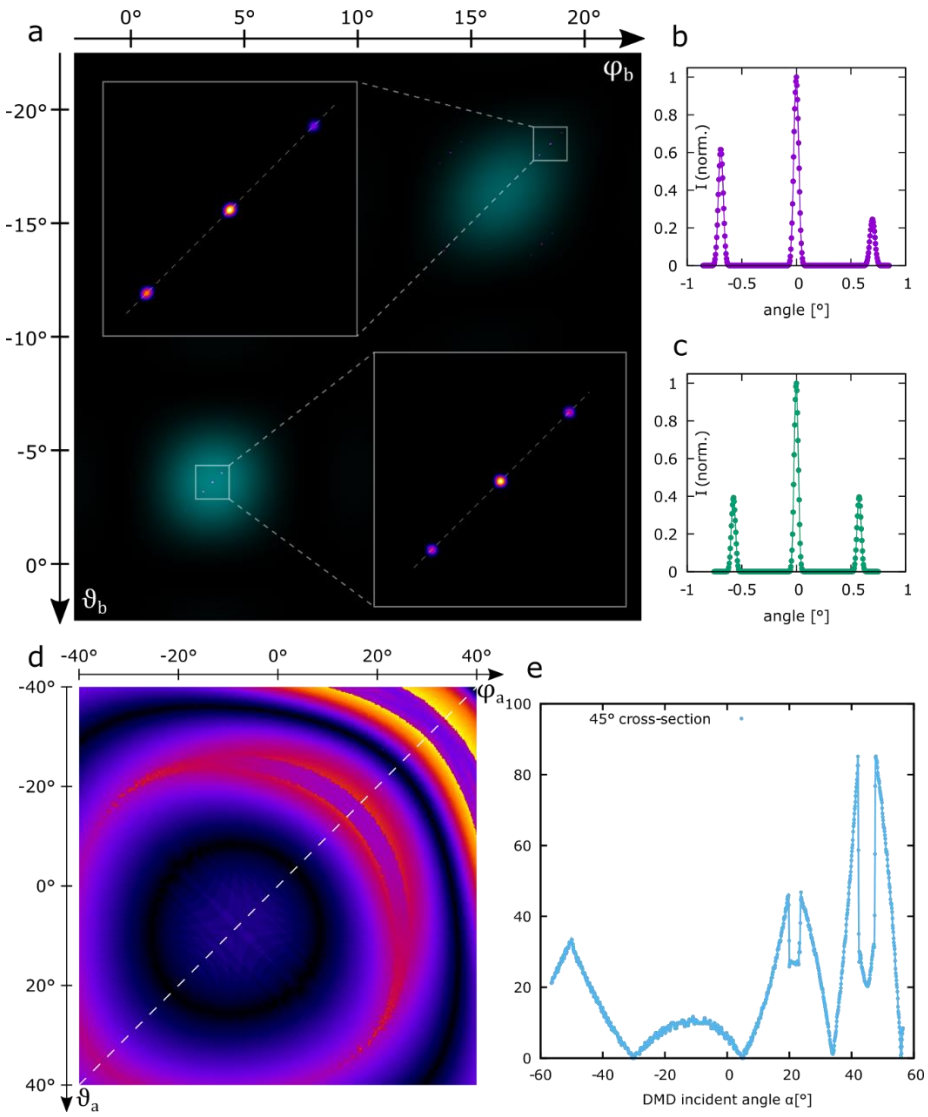

Figure 42: Simulations of DMD wave propagation for optimized use with SIM

For all panels, the envelope of the OFF state is the relevant one. (a) Visualization of the diffraction orders generated by a SIM pattern (magenta/blue/white) and the envelope (cyan). The top row shows the undesired case for SIM: The 0th diffraction order of the SIM pattern (native diffraction order of the DMD) and the center of the envelope do not coincide. The $\pm 1^{st}$ diffraction orders of the SIM pattern show an asymmetric intensity distribution. The lower row shows the ideal case, the blaze condition: The 0^{th} diffraction order of the SIM pattern (native diffraction order of the DMD) and the center of the envelope coincide. The $\pm 1^{st}$ diffraction orders of the SIM pattern show a symmetric intensity distribution. In (b, c), cross-section plots through the SIM diffraction orders are plotted for the undesired (blaze condition not satisfied) and desired (blaze condition satisfied) case. (d) Misalignment between the brightest native diffraction order and center of the envelop, depending on the input angles and along the 45° diagonal cross-section (dotted line in (d), plot in (e)). Alignments close to -30° and 5° on the 45° diagonal yield equal intensities in the SIM side orders. The 45° line was chosen as it allows for an easy alignment of all angles in one plane (DMD mounted to a table). Figure taken from our corresponding publication [8].

3.4 One-color DMD-SIM microscope

In parallel to the development of the simulations and the gradually emerging knowledge (see section 3.3), my colleague Dr. Alice Sandmeyer and the author of this thesis started to develop the (two-beam) one-color dmd-sim microscope. While Dr. Sandmeyer's focus was mainly on the optical setup and measurements, the athor was primarily responsible for the simulations, the (electronic) control and the operating software. The theoretical ideal incidence angle of $\alpha \approx -30°$ found in section 3.3 provided a solid basis for the first iteration of the later final setup (see Figure 43a). The one-color dmd-sim microscope features inexpensive green 532 nm excitation laser (which is actually used in light shows), the DMD *DLP® LightCrafter™ 6500* (Texas Instruments) [264] as SLM, and an industry-grade CMOS camera (detailed component list: Table 4 in section A.I). This makes it a low-cost compact (40 cm x 90 cm) high-speed SIM microscope that sets new standards in terms of speed (60 super-resolved fps). The industry-grade CMOS camera is an appropriate choice because it has been used successfully in super-resolution microscopy before [81,276]. With a total cost of about 20 k€, the setup is far below the cost of typical custom-made FLCoS-based SIM microscopes (60 k€ - 100 k€) and commercial SIM solutions (multiple 100 k€).

The microscope is operated with the open-source software fairSIM-VIGOR [63]. This runs on a computer, which is responsible for control, acquiring and live reconstruction (see Figure 43b). A microcontroller (Arduino Uno) forms the core for the precise timing of DMD, laser and camera. A detailed description of the operating software and the timings using the microcontroller can be found in section 3.7.

In addition to the DMD, the industry-grade global shutter CMOS camera used plays a significant role in the high achievable speed of the one-color DMD-SIM microscope. As a rule, sCMOS cameras with a rolling shutter are used for scientific microscopes. This significantly reduces the global exposure time of the camera chip due to the rolling readout and reset process. For example, FLCoS-based SIM microscopes with rolling shutter cameras achieve a duty cycle of only 28% at 63 super-resolution fps, because the camera chip is only completely sensitive to light for 0.5 ms, while 1.78 ms is actually available for each raw image. Our setup achieves exposure times of 1.75 ms, while 1.84 ms are available per raw image. This corresponds to a duty cycle of 95%. This means that our system is not only similarly fast, but also has a much higher light yield per raw image. This allows our system to acquire images about three times faster than usual with the same photon dose. The global shutter camera is the main reason for the high duty cycle. With FLCoS-based SIM microscopes, duty cycles of up to 85% at 47 fps with 2 ms exposure at 2.35 ms per raw image could be realized, depending on system conditions (QXGA implementation). The comparatively high switching speeds of DMDs

(11.547 kHz) of course also increase the duty cycle, but the influence is noticeably less than that of the global shutter camera.

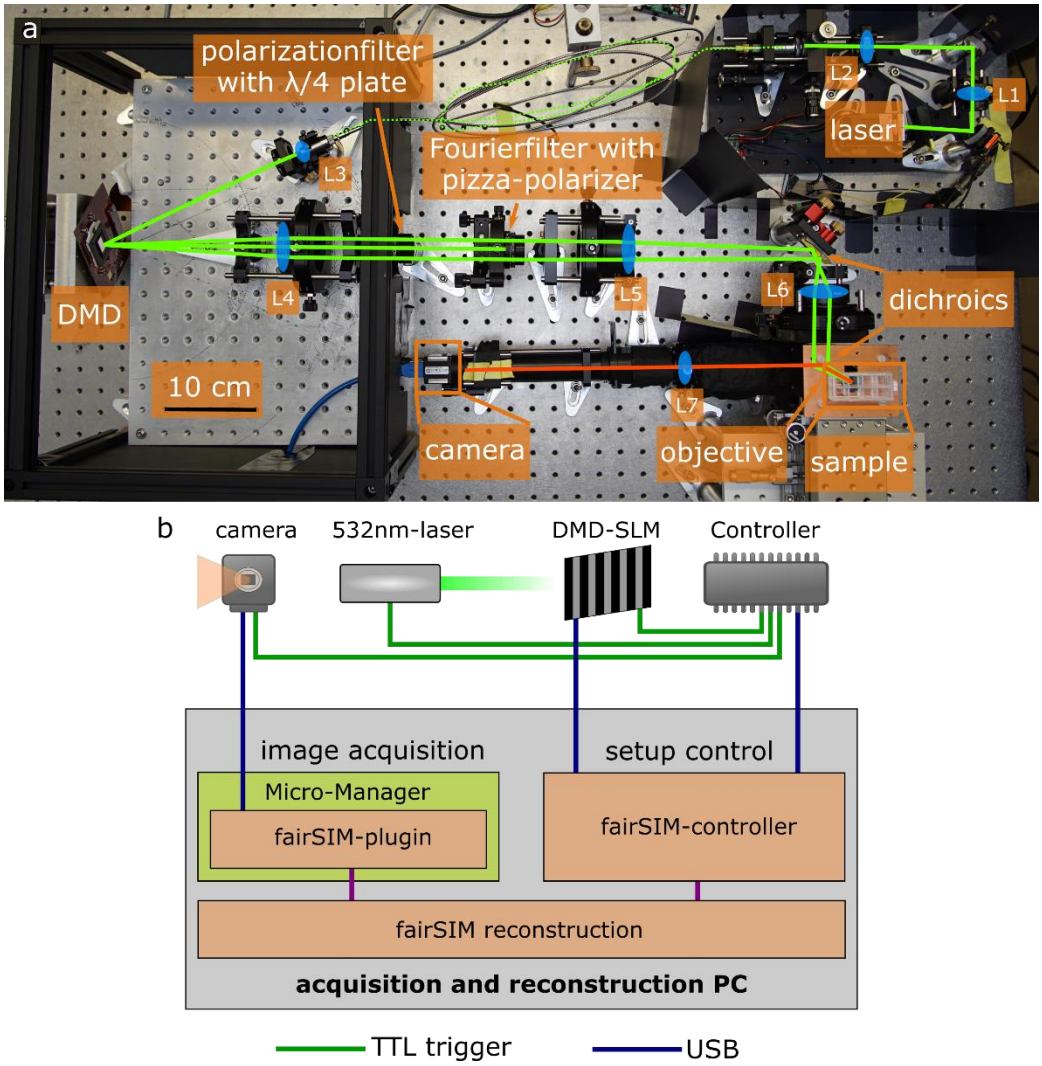

Figure 43: Phot of the one-color DMD-SIM microscope and schematic data stream

(a) A 532 nm laser beam (green) is coupled into a fiber before illuminating the DMD at the blaze angle. Polarization optics are required to achieve the same linear polarization in the corresponding SIM angles. Two dichroic mirrors from the same batch are used to maintain the polarization state and to separate the excitation light from the fluorescence (red) signal. The same objective lens is used to excite the sample and to collect the fluorescence signal, which is detected with an industry-grade CMOS camera. (b) Timing control and image data flow. Binary SIM pattern are stored on-board the DMD and selected in sequence by sending TTL trigger pulses to the DMD control board. The DMD, camera, and laser light source are synchronized using a microcontroller. The raw image data is fed into a GPU-based, real-time data processing system [63]. Figure taken from our corresponding publication [8].

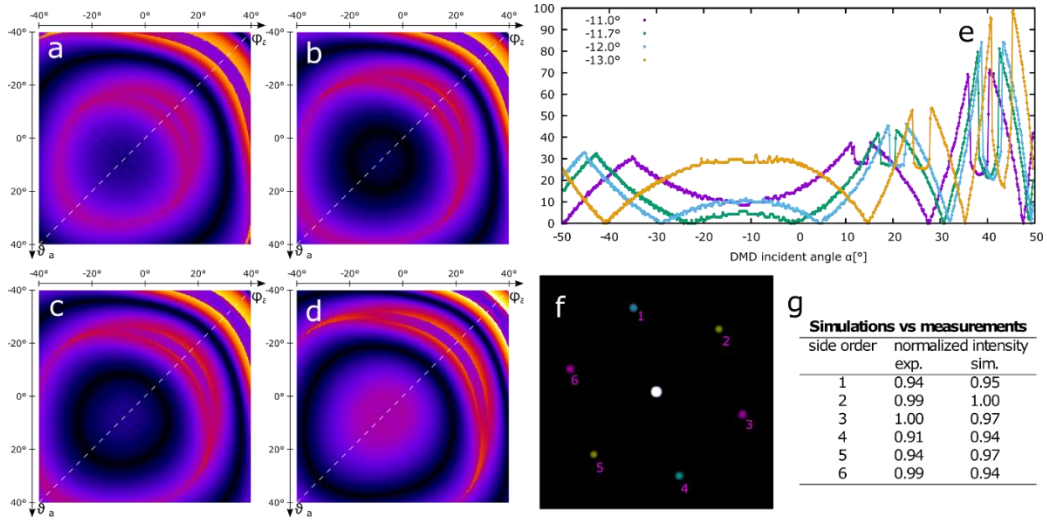

g

Simulations vs measurements

side order	normalized intensity	
	exp.	sim.
1	0.94	0.95
2	0.99	1.00
3	1.00	0.97
4	0.91	0.94
5	0.94	0.97
6	0.99	0.94

Figure 44: Dependence of the blaze angle on the tilt angle of the micromirrors

Misalignment between main SIM diffraction order and maximum of envelope depending on γ (a: −11°, b: −11.7°, c: −12°, d: −13°). In each simulated panel the incident angle has been changed in order to find the blaze angle. Again, cross-sections at the 45° diagonal were chosen to compare the simulation results (e) to the experimental data. The blaze condition at $\gamma = 0$, where the plotlines come down to the x-axis, shifts clearly due to small changes of γ. For a direct comparison to the experimental results ($\alpha = -23.9°, \gamma = -11.7°$), the same case is simulated (f). Again, a log scale was set for a better visualization. Same colors of the first orders belong to the same SIM angle. The mean of the side orders in the displayed ROI is listed and directly compared to the experimental data of Figure 45c (g). Figure taken from our corresponding publication [8].

The final realization of the setup (Figure 43a) shows an angle of incidence of $\alpha \approx 24°$ to fulfill the blaze condition. Using eq. (111), it is easy to understand that this is probably due to a deviation of the tilt angles to $\gamma^{\pm} = \pm 11.75°$, instead of $\pm 12°$ of the micromirrors. According to the *DLP® LightCrafter™ 6500* (Texas Instruments) datasheet [264], the tolerance of the tilt angles is $\pm 1°$. Which further emphasizes the assumption of deviations in the tilt angle. Since even small deviations within the manufacturer's tolerance result in significant effects in the setup alignment, it is worth analyzing these more closely with the help of simulations. Figure 44a-e, using evaluated simulations similar to Figure 42d,e, shows how small deviations from $\gamma^{\pm}$ affect the blaze angle. Since at the time of completion of the one-color DMD-SIM microscope eq. (111) of the blaze condition approach was not yet available, we used the simulation results of the analytic phase shifting approach as a guide.

Since a symmetrical intensity distribution in the Fourier plane of a SIM microscope is essential for high modulation depths, we measured this experimentally for the blaze angel for both the OFF and ON states (see Figure 45). The deviations for the OFF-state are much smaller than for the ON-state. Therefore, this was used for the final implementation of the one-color DMD-SIM microscope. A comparison between the

simulated Fourier plane (Figure 44f) and the measured OFF Fourier plane is shown in Figure 44g. It is noticeable that, as would be expected for the blaze angle, only negligible deviations of at most 6% occur in the intensities of the diffraction orders in both the simulated and the measured Fourier planes. Thus, the Fourier plane generated is ideally suited for SIM.

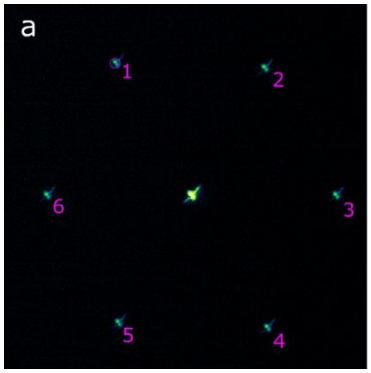

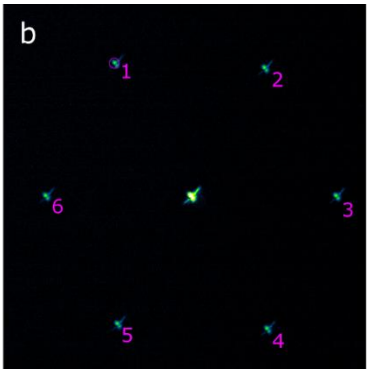

c

Measured intensities		
side order	normalized intensity on	of
1	0.88	0.94
2	0.87	0.99
3	0.93	1.00
4	0.92	0.91
5	0.98	0.94
6	1.00	0.99

Figure 45: Fourier plane with fulfilled blaze condition

Measured diffraction intensity pattern in the Fourier plane with the SIM pattern displayed on the DMD. With a lens the intensity pattern is focused on a camera chip (IDS uEye UI-3060CP-M-GL Rev.2). In both cases ((a) ON and (b) OFF, exposure time 5 ms, DMD display time 105 µs) the measured blaze angle is chosen as the incident angle, which is +25.3° for ON and −23.9° for OFF. The difference compared to the simulated data is due to a different tilt angle. For a better visualization a log scale was set. The mean value of the circled area in (a and b) was analyzed to evaluate the quality of the found blaze angle (c). Figure taken from our corresponding publication [8].

During the development of the one-color DMD-SIM microscope, we found that both DMDs and FLCoS-based two-beam SIM microscopes do not require light source modulation. Until recently, it has been assumed that during pattern restructuring on a phase modulating SLM, the light source should remain off to ensure that the sample is not illuminated with incorrect or unmodulated light. However, using modulation depths determined via fairSIM [93], we were able to demonstrate that this is unnecessary for both DMD and FLCoS SLMs (see supporting information of our related publication [8]). In our opinion, the reason for this is the filter mask of the Fourier plane, which, as soon as the pattern on the SLM changes, blocks all diffraction orders that do not contribute to the desired pattern. This is amplified in the case of a DMD by the fact that by tilting the micromirrors, the envelope is tilted out of the optical path, and thus hardly any excitation light ends up in the optical path. This is generally not true for three-beam SIM, since the central diffraction order is not blocked by the Fourier mask, and this cannot be specifically switched on or off by the SLM. Due to the high switching speed of 11.547 kHz and the possibility to switch all micromirrors in such a way that the envelope disappears from the excitation beam path of the microscope, it might be possible with DMDs to do without light source modulation also for three-beam SIM.

One-color DMD-SIM microscope measurements of synthetic samples

To demonstrate the quality and function of the setup, my colleague Dr. Alice Sandmeyer, in close collaboration with the author of this thesis, performed and evaluated various measurements with the one-color DMD-SIM microscope. Dried monolayer fluorescent beads (200 nm & 100 nm, see Figure 46) are ideal samples to investigate the pattern quality in the sample of a two-beam SIM microscope [277]. Using Fourier Ring Correlation [278] for resolution estimation, we were able to achieve a resolution increase by a factor of 1.62 using the 100 nm beads, which fits well with the expected factor of 1.75 that results from the spatial frequency of the patterns displayed on the DMD.

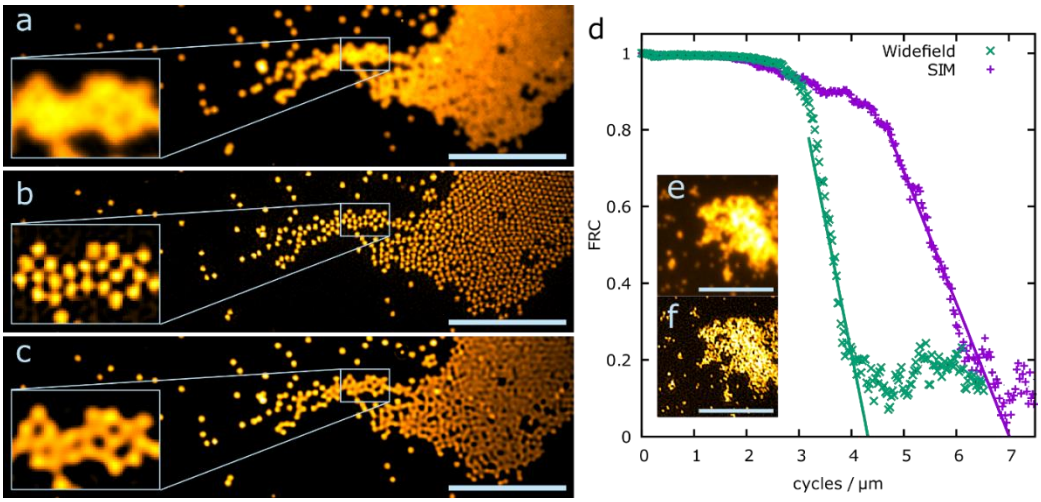

Figure 46: 200 nm fluorescent beads and FRC statistics on 100 nm fluorescent Beads

Fluorescence images of 200nm TetraSpeck (TS) beads (a-c) and FRC statistics (d). (a) Summed up wide-field image of the acquired nine SIM frames and filtered wide-field image (c) determined by Wiener filtering. (b) Reconstructed SIM image of the 200nm TS beads by fairSIM [193]. The inset clearly shows that single beads can be distinguished through SIM (scale bar 5 µm, inset 2.1 µm x 1.4 µm, exposure time per raw frame 20 ms). Quantification of the resolution enhancement via FRC analysis on 100nm beads (see inset (e) WF, (f) SIM), which are approximate point sources better than 200nm beads (scale bar 5 µm, exposure time per raw frame 50 ms). Two successive SIM images were acquired, reconstructed and analyzed via frc analysis [62,88]. The resulting graph (d) for both wide-field and SIM can be interpreted as the available signal (y-axis) at any given structure-size (x-axis). By fitting both WF and SIM, a shift of 1.62× is found, which corresponds well with the expected resolution enhancement of 1.75×. Figure taken from our corresponding publication [8].

The next step was to demonstrate not only the function and quality of the system, but also the very high acquisition speed of up to 540 raw images per second (60 super-resolved fps, at 3 angles with 3 phases). With a region of interest of 256 x 256 pixels (18 x 18 µm) at 1.75 ms exposure time, 200 nm fluorescent beads could be observed in Brownian motion in a mixture of glycerol and water (see Figure 47). Two adjacent beads

moving together through the sample cannot be distinguished from each other in the wide-field but can be distinguished in the (live) SIM reconstruction. By using interleaved reconstructions [214], the effective super-resolved fps could even be increased by a factor of 3 or 9 to 180 fps or 540 fps. However, this is purely a post-processing step, the applicability of which is still under discussion. Thus, our presented system achieves the same speed as the current generation of SIM microscopes trimmed for speed [62,63] and is well above fast commercial systems that achieve about 15 fps at 1 ms exposure time.

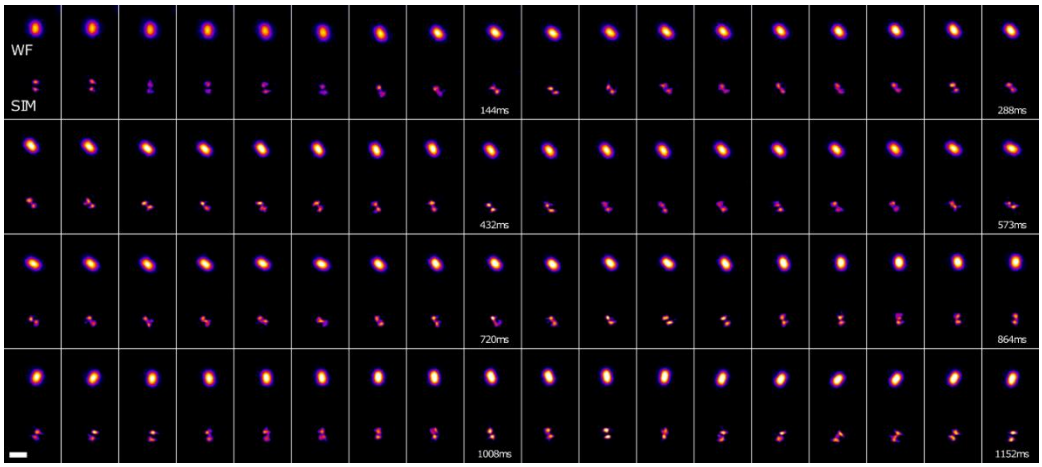

Figure 47: High speed (60 super resolved fps) diffusing 200 nm beads

High speed SIM at 16 ms (60fps) per reconstructed frame, with 1.84 ms (540 fps) raw data rate, and 1.75 ms illumination per frame (95% duty cycle). Diffusing 200 nm fluorescent beads, full field of view 20 µm square, here zoomed in to two beads (for full data, see Supporting Information, video 1 of our corresponding publication [8]). Each frame contains the widefield view (top) and SIM reconstruction (bottom) of the two beads that apparently move and turn as a cluster. While the shape visible in the widefield hints at more than one bead, only the SIM reconstruction makes both of them clearly visible. The high duty cycle achieved through the combination of a fast-switching DMD and a global shutter camera made these measurements possible at modest laser powers and without an active light source power modulation. Scale bar 1 µm. Figure taken from our corresponding publication [8].

One-color DMD-SIM microscope measurements of fixed cells

To demonstrate that the one-color DMD-SIM microscope is compatible with biological samples, we first imaged the actin cytoskeleton of fixed U2OS cells stained with phalloidin Atto532 and reconstructed it with fairSIM [93] (Figure 49). We did the same with the actin skeleton (Figure 48a,b) and the outer membrane of lysosomes (Figure 48c-g) of fixed HEK293T cells using the red fluorescent protein mScarlet by gene transfection. The increase in resolution enabled by SIM can be seen directly in the images and is also further emphasized by the cross-section plots in Figure 48f,g.

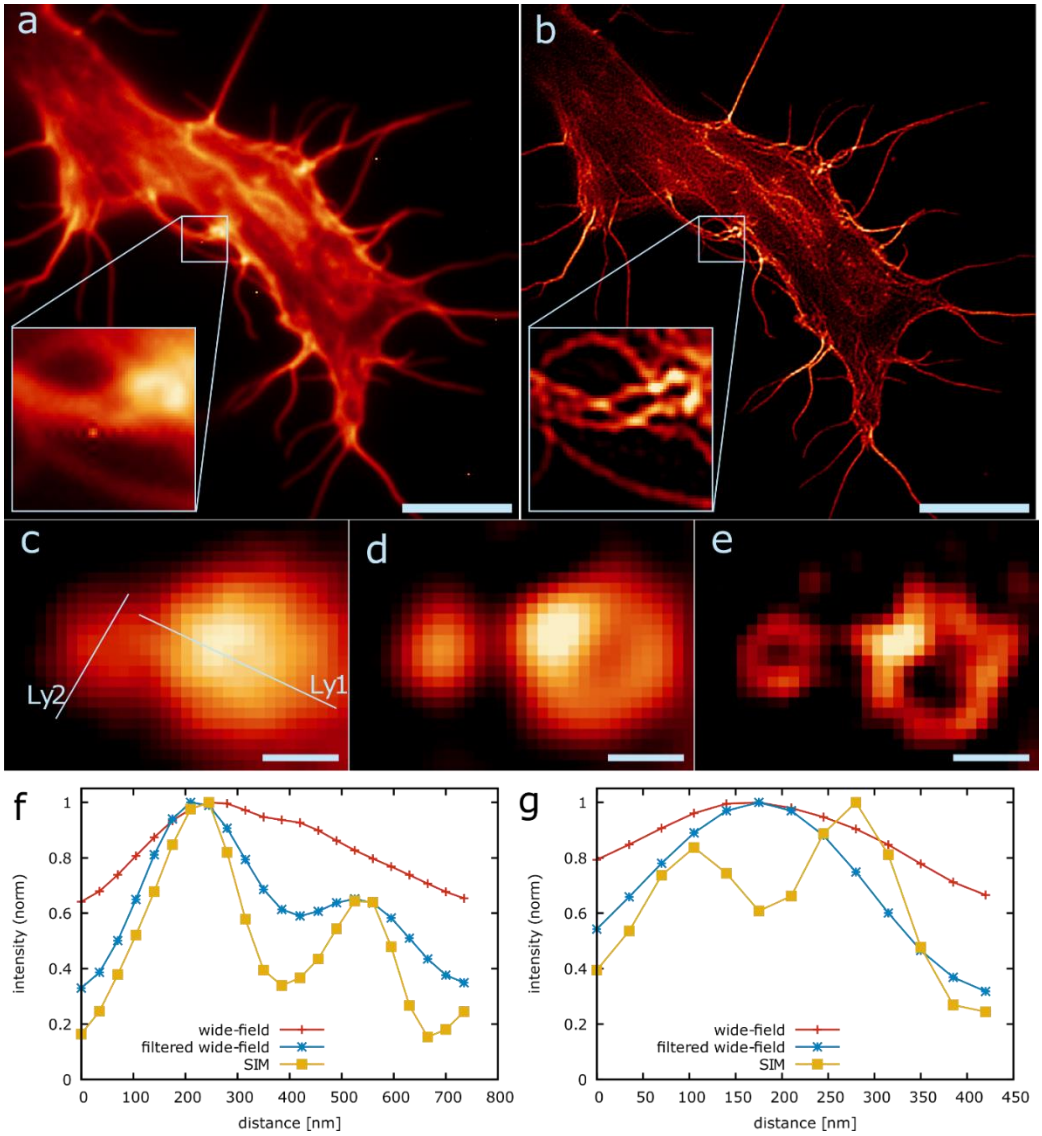

Figure 48: Actin and lysosomes of fixed HEK293T cells

Fixed HEK293T cells transfected with the fluorescent protein mScarlet, to either label actin (a, b) or lysosomes (c–e). Actin filaments that are very close to each other cannot be distinguished in the WF image (a), but the SIM image reveals that more than one filament is present (b; scale bar 5 µm, inset 2.1 µm × 2.1 µm, exposure time per raw frame 50 ms). Lysosomes have different diameters, and with the used plasmid, the outer membrane was stained. The membrane structure of bigger lysosomes (cross-section Ly1, plot f) can be revealed with conventional WF imaging (c) and additional filtering (d), but for smaller lysosomes (cross-section Ly2, plot g), SIM imaging (e) is required (scale bar 250 nm, exposure time per raw frame 50 ms). Figure taken from our corresponding publication [8].

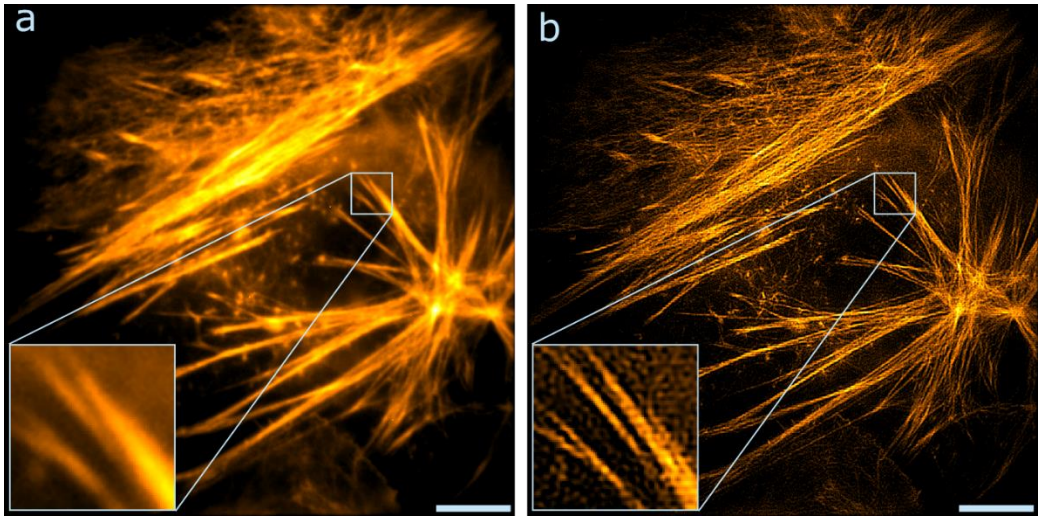

Figure 49: Actin filaments of fixed U2OS cell

Fixed U2OS cell labeled with Phalloidin Atto532, WF (a) and SIM (b) image (exposure time per raw frame 20 ms). The size of the images is 36 µm x 36 µm which is also the possible field of view with the microscope. The actin filaments are now distinguishable in the SIM image (scale bar 5 µm, inset 2.8 µm x 2.8 µm). Figure taken from our corresponding publication [8].

However, not only synthetic and fixed biological samples can be imaged in super-resolution with the one-color DMD-SIM microscope, but also living cells. Using MitoTrackerRed stained mitochondria in U2OS cells, with Richardson-Lucy as filter [196] and Hessian denoising in post-process [197], we were able to resolve the folded membrane (so-called cristae, see Figure 50). In the wide-field, the cristae cannot be resolved. A video belonging to the measurement and further details can be found in our related publication and the supporting information [8].

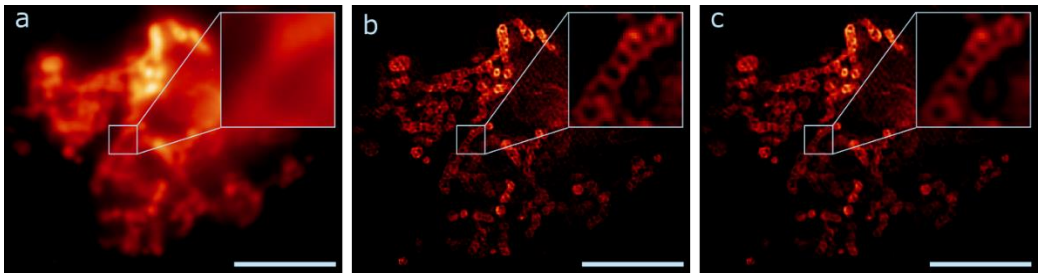

Figure 50: Live cell images of mitochondrial motility in U2OS cells

The organelle was stained with MitoTrackerRed and the data were acquired at room temperature. The insets show clearly that their inner structure cannot be resolved with WF imaging (a). For the SIM reconstruction, background signal from the raw data was subtracted and Richardson-Lucy deconvolution (10 iterations) was applied to the input and output images (b). Hessian denoising [197] leads to further improvement of the image quality (c; scale bar 5 µm, inset 1.4 µm × 1.4 µm, exposure time per raw frame 100 ms). Figure taken from our corresponding publication [8].

In addition, we were able to demonstrate live cell compatibility by acquiring movements of the endoplasmic reticulum of U2OS cells stained with ER-TrackerRed (see Figure 51). Thanks to the deliberately low acquisition rate of 4 fps (36 raw fps), we were able to acquire a live cell video of 2 min length, which can also be found in the supporting information of our related publication [8].

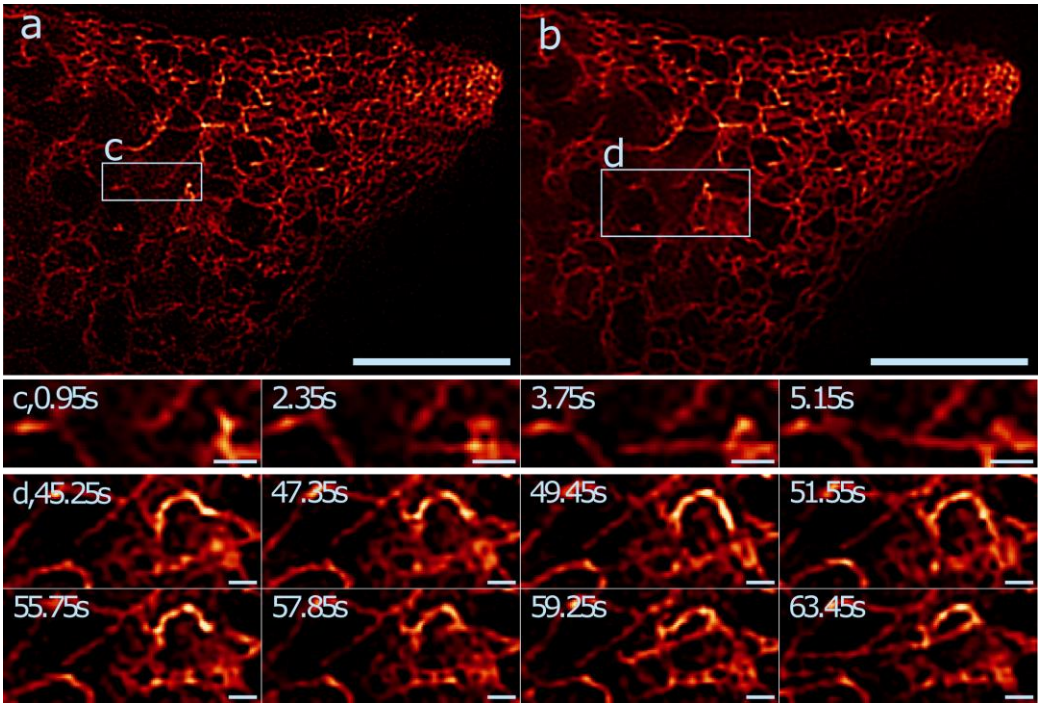

Figure 51: Endoplasmic reticulum (ER) network in a living U2OS cell

The organelle was stained with ER-TrackerRed and the data was acquired with a delay of 250 ms between each SIM sequence at room temperature. (a) SIM image at time point 0 s reveals many filaments. (b) Hessian denoising of the SIM frame reduces the background signal and smoothes the filaments (scale bar 5 µm, exposure time per raw frame 50 ms). The time sequence (c) is at inset 1 and shows the elongation of a fiber (scale bar 500 nm). In addition, a detachment can be observed with a subsequent attachment to another point and a further elongation (d, inset 2, scale bar 500 nm). Both insets display the Hessian denoised data. Figure taken from our corresponding publication [8].

3.5 Multi-color simulation results

After the successful implementation of a DMD (*DLP® LightCrafter™ 6500 (Texas Instruments)* [264]) in a one-color SIM microscope, the next step was to approach the multi-color problem from the theoretical side using simulations. In contrast to the position (center) of the envelope, the positions of the (native) diffraction orders depend on the excitation wavelength. This means that the blaze angles of one excitation wavelength do not generally coincide with those of other wavelengths. Figure 52a illustrates with the help of simulations via grating approach that the native diffraction orders at the same angle of incidence are at different positions relative to the envelope depending on the wavelength, so that the blaze condition is fulfilled only for one wavelength (532 nm in this case). In Figure 52b (similar to Figure 42d), the black circular structures for the wavelengths 488 nm, 532 nm and 561 nm show the angles of incidence (φ_a, ϑ_a) for which the blaze condition is fulfilled. Since these circular structures generally do not overlap, a multi-color DMD-SIM microscope is not readily implementable. The same becomes clear when looking at the diffraction space (angle of emergence, φ_b, ϑ_b) in Figure 52c. Similar to the case for the angles of incidence (Figure 52b), circular structures of the angles of emergence, for which the blaze condition is fulfilled, are also formed in the diffraction space depending on the wavelength.

Each of the circular structures corresponds to the blaze condition of a diffraction order of the native DMD grating. For multi-color SIM it is mandatory that the central (native) diffraction order of the SIM pattern of all used wavelengths is superimposed. This means that the circular structures from Figure 52c would have to overlap or intersect. In general, however, they do not (see Figure 53a). It is possible to find intersections of the circular structures by using the OFF and ON states (γ^- and γ^+) for one wavelength each (see Figure 52a), but these lie outside the 45° diagonal and are therefore very difficult to realize in the laboratory. If the wavelengths are cleverly chosen, the blaze conditions of the -4th and -3th diffraction order (circular structures) of two wavelengths can be superimposed for the same (OFF) state (see Figure 52b). With a clever choice of a third wavelength for the (ON) state, it is even possible to find configurations for a DMD-based SIM microscope which simultaneously fulfills the blaze condition for three excitation wavelengths along the 45° diagonal.

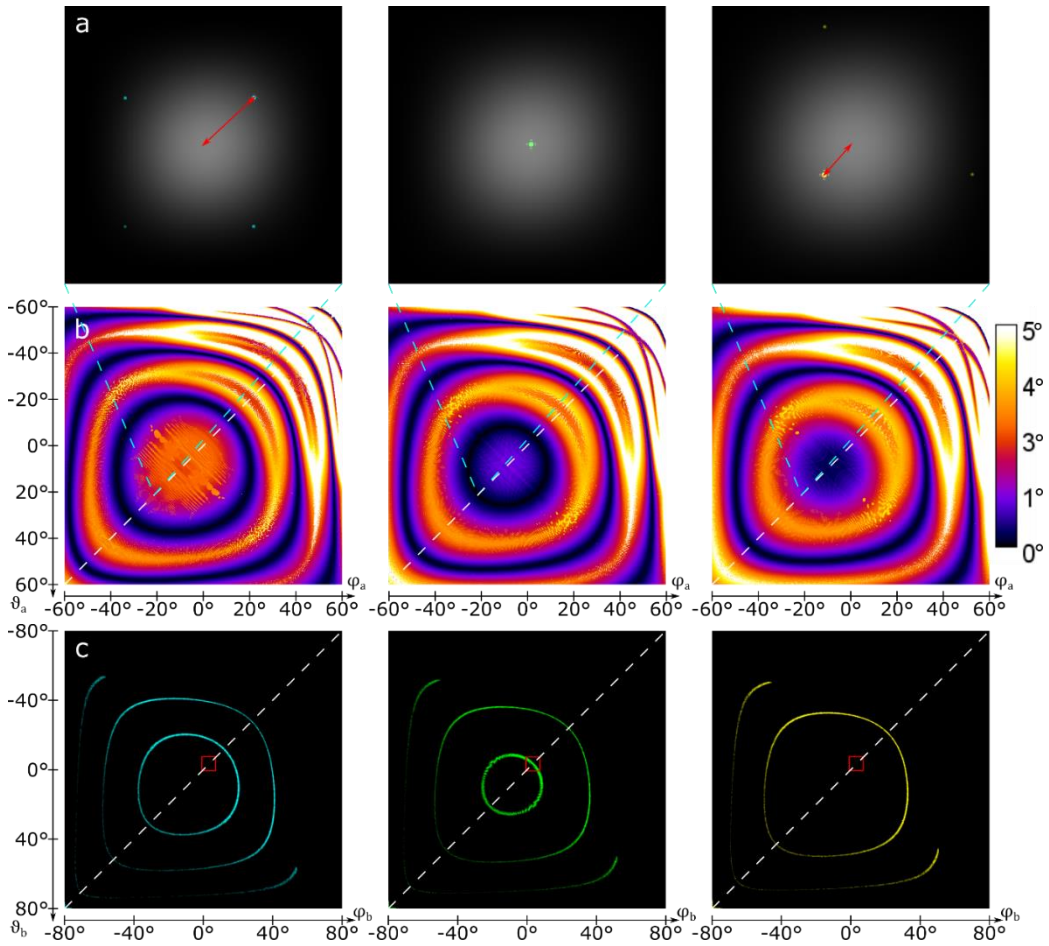

Figure 52: Displacement between the envelope and the brightest diffraction order

The columns from left to right correspond to the wavelengths 488 nm, 532 nm and 561 nm. Row (a) illustrates the displacement between the center of the envelope (grey, linear intensity representation) and the brightest diffraction order of the native DMD grating (cyan, green, yellow, logarithmic intensity representation) using red arrows. The field of view ranges from −1° to 7° for φ_b and −7° bis 1° for ϑ_b with a sampling rate of 0.1° at an angle of incidence of $\varphi_a = -\vartheta_a = -21°$. Row (b) visualizes the displacement which can be determined from (a) for the angles of incidence φ_a and ϑ_a ranging from −60° to 60° with a sampling rate of 0.2°. The dark areas with a displacement close to 0° indicate angles which fulfil a blaze condition and are well suited for SIM illumination with coherent light. The cyan dotted lines between (a) and (b) indicate an angle of incidence of $\varphi_a = -\vartheta_a = -21°$ for the diffraction images seen in (a). Row (c) shows the areas in the diffraction space of φ_b and ϑ_b from −80° to 80°, each, in which the displacement between the centre of the envelope and the brightest diffraction order of the DMD is not more than 0.1°. Therefore, angles of incidence in a range of −60° to 60° used in (b) were used for φ_a and ϑ_a. The red boxes mark the diffraction space shown in (a). The white dotted lines in (b) and (c) correspond to the 45° diagonal angles of incidence that are considered in the blaze condition approach. Figure taken from our corresponding publication [92].

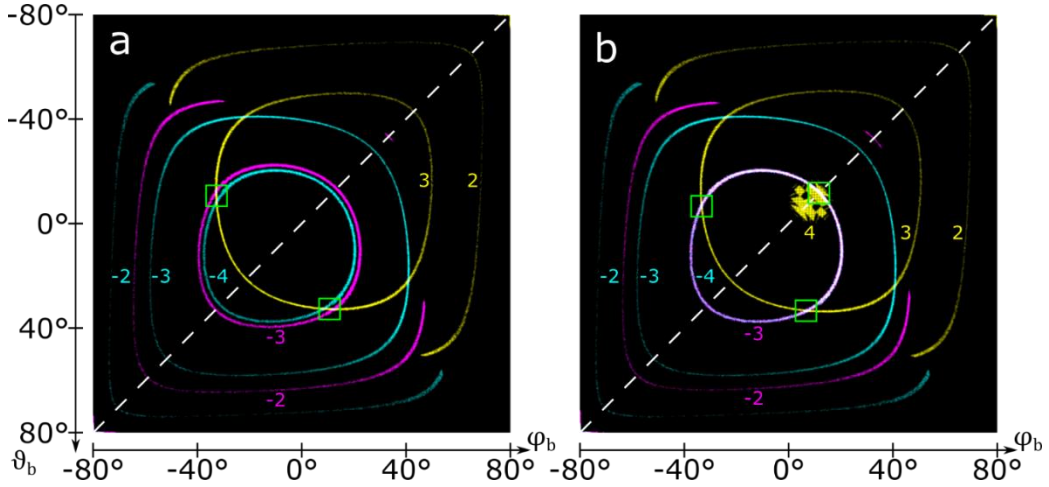

Figure 53: Multicolor diffraction angles with blaze condition

Areas in the diffraction space for φ_b and ϑ_b of −80° to 80°, each, in which the displacement between the center of the envelope and the brightest diffraction order of the DMD is not more than 0.1°. Therefore, angles of incidence in a range of −60° to 60° were used for φ_a and ϑ_a. The white dotted lines correspond to the 45° diagonal angles of incidence that are considered in the blaze condition approach. The colored numbers near the ring structures represent the corresponding diffraction orders. (a) Typical wavelengths 488 nm (displayed in cyan) & 638 nm (displayed in magenta) with $\gamma^- = -12°$ and 561 nm (displayed in yellow) with $\gamma^+ = 12°$ are not well suited for multicolour applications. The green boxes mark possible configurations for two colour configurations of 488 nm & 561 nm or 638 nm & 561 nm. (b) Optimized multicolor wavelengths 488 nm (cyan) and 651 nm (magenta) with $\gamma^- = -12°$ and 554 nm (yellow) with $\gamma^+ = 12°$. The green boxes mark possible configurations for three color configurations. Figure taken from our corresponding publication [92].

In order to understand how to select the wavelengths, it is useful to take a closer look at the blaze condition along the 45° diagonal. For this purpose, both the grating approach (Figure 54a) and the blaze condition approach (Figure 54b) are suitable to analyze the blaze condition depending on the excitation wavelength λ, the angle of incidence α and thus also the angle of emergence β. As can be seen in Figure 54, both approaches deliver qualitatively the same results along the 45° diagonal. However, since the blaze condition approach is analytically accessible, it is preferable for the further multi-color analysis along the 45° diagonal.

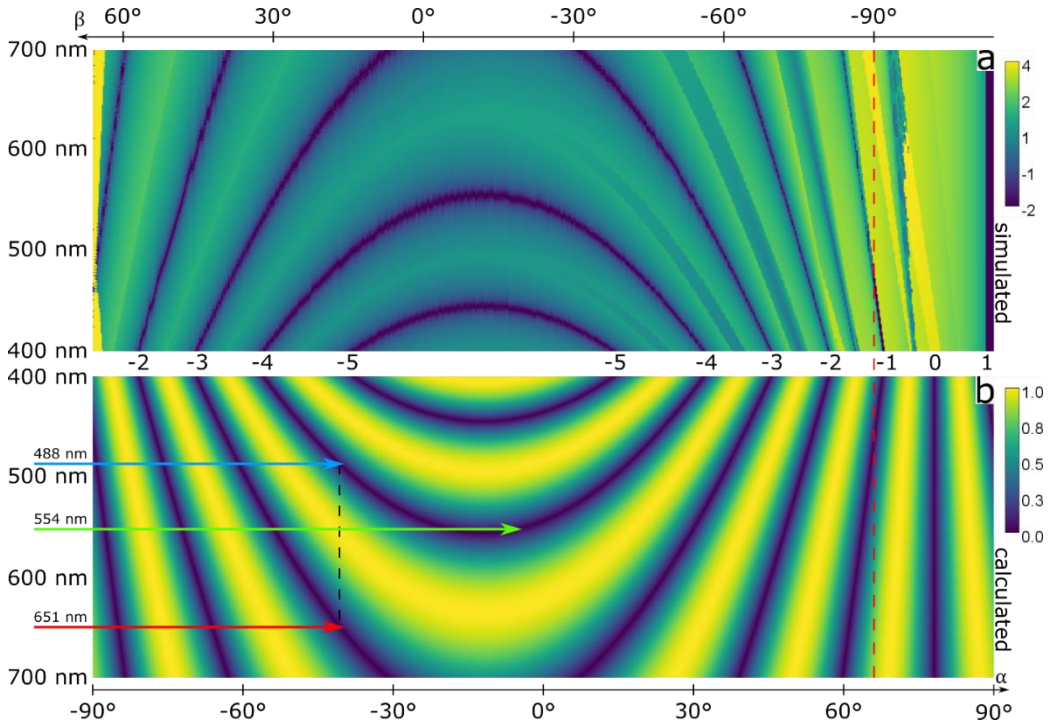

Figure 54: Blaze condition along the 45° diagonal

Visualization of the blaze condition along the diagonals shown in Figure 52b for the visible spectrum. In the dark areas the blaze condition can be considered fulfilled. For orientation, the wavelength range is shown on the left-hand side. The angles of incidence and diffraction are shown at the bottom and the top of the graph. The vertical red dashed line marks the diffraction angle of 90°. Angles above 90° are irrelevant for practical applications. (a) The blaze condition is measured by the distance between the center of the envelope and the brightest diffraction order of the DMD, which was simulated by the grating approach. The measured distances in degrees are shown as logarithmic intensity distribution. (b) Visualization $v = |sin(n\pi)|$ *of the blaze condition using the blazed grating approach. The integer diffraction orders belonging to the blaze conditions are shown in the middle between (a) and (b). The blue, red and green arrows point to an exemplary three-color combination for a DMD-SIM microscope with 488 nm, 651 nm and 554 nm. The black vertical dotted line is intended to illustrate that 488 nm and 651 nm fall on the DMD at the same angle of incidence. See also [267] for a visualization in similar style, obtained by Li et al. with their DMD modelling approach. Figure taken from our corresponding publication [92].*

It is possible to use two different wavelengths λ_1 and λ_2 with the same angle of incidence $\alpha_{1,2}$ and angle of emergence β with the same tilting state γ^-. From eq. (109) the following relation can be derived for this purpose:

$$n_1\lambda_1 = n_2\lambda_2 \tag{113}$$

Formulated this means nothing else than that the two wavelengths must be in the integer ratio which corresponds to the ratio of the diffraction orders used. As can be seen in Figure 54, only the following combinations are suitable in the visible electromagnetic spectrum: (-3, -2); (-4, -3); (-5, -4). Of these, (-4, -3) is particularly interesting, since it allows typical wavelengths from the blue and red spectra to be combined. For a DMD with a tilt angle of $\gamma^- = -12°$, with $n_1 = -4$ and $n_2 = -3$, choosing $\lambda_1 = 488\,nm$ gives the following as an example:

$$\lambda_2 = \frac{n_1}{n_2} \cdot \lambda_1 = 650.67\,nm \quad \text{with} \quad \alpha_{1,2} = -40.6° \quad \text{and} \quad \beta = 16.6° \tag{114}$$

To obtain the possible third wavelength using the other tilt state $\gamma^+ = 12°$, we must first determine the incident angle $\alpha_3 = -\beta + 2\gamma^+ = 7.4°$ resulting from the emergent angle β. To obtain a wavelength from the green spectrum, $n_3 = 4$ should be chosen. The third wavelength is then obtained from eq. (87):

$$\lambda_3 = \frac{m'}{n_3}(\sin(\alpha_3) + \sin(\beta)) = 553.93\,nm \tag{115}$$

The combination of these three wavelengths (-40.6°, 488 nm), (-40.6°, 651 nm) and (7.4°, 554 nm) is indicated in Figure 54b by corresponding arrows for three-color DMD-SIM. Other possible three-color combinations that are close to typical excitation wavelengths are 473 nm, 631 nm and 551 nm or 491 nm, 655 nm and 555 nm. At this point it is important to mention that the third wavelength λ_3 is strongly dependent on the actual tilt angle of the particular DMD used. As already shown in section 3.4 the tilt angle can vary by a few tenths of a degree, therefore corresponding deviations should be measured and considered accordingly in the design of a three-color DMD-SIM microscope. For the first two wavelengths, the tilt angle is of secondary importance, since it only changes the angle of incidence and angle of emergence, while the blaze condition is maintained for both wavelengths.

3.6 Dual-color DMD-SIM microscope

As previously shown and suggested in section 3.5 there is the possibility for DMD-based SIM microscopes to use two (or even three) excitation wavelengths despite the blazed grating effect (BGE). For this, the excitation wavelengths λ_1 and λ_2 have to be matched into a certain integer ratio. The DMD we used, the *DLP® LightCrafter™ 6500* (Texas

Instruments) [264], has a micromirror tilt angle of 12° and a 7.56 µm pixel pitch. For the reasons stated in section 3.5, the following matching condition is the most promising for the design of a dual-color DMD-SIM microscope:

$$\frac{\lambda_1}{\lambda_2} = \frac{n_2}{n_1} = \frac{3}{4} \tag{116}$$

If this matching condition is fulfilled, the 4th and 3rd diffraction order of λ_1 and λ_2 lie exactly on each other along the 45° diagonal. If now by appropriate choice of the angle of incidence α the envelope is placed congruent to it, the blaze condition is automatically fulfilled for both wavelengths. Based on eq. (116), the choice of a combination of a blue and a red laser is reasonable, since otherwise the visible range of the electromagnetic spectrum, which is of interest for biological applications, would be left. Table 2 (left-hand column) lists typical potential laser wavelengths that are commercially available.

Blue wavelength	Red wavelength
425 nm	594 nm
445 nm	633 nm
450 nm	637 nm
457 nm	638 nm
458 nm	639,7 nm
460 nm	640 nm
473 nm	642 nm
488 nm	647 nm
491 nm	660 nm
505 nm	

Chosen blue wavelength	Chosen red wavelength	$\frac{\lambda_1}{\lambda_2}$
445 nm	594 nm	0.749
473 nm	633 nm	0.747
488 nm	647 nm	0.754
491 nm	660 nm	0.744

Table 2: Available and chosen laser wavelength combinations

Left: Selection of laser wavelengths available from different manufacturers (Toptica, Oxxius, Coherent, Qioptiq, HÜBNER Photonics). With regard to wavelength matching, the blue and red wavelength range was defined as 425 nm to 505 nm and 594 nm to 660 nm. Right: Laser wavelength combinations and their ratios that fulfill the matching condition most closely. Table taken from our corresponding publication [64].

When considering all possible combinations of blue and red wavelengths (see Figure 55a), it is noticeable that four combinations lie very close to the matching condition (Table 2, right-hand column). However, the matching condition is not exactly fulfilled, as is mandatory for a SIM microscope, because the 4th and 3rd diffraction orders of blue and red are not exactly superimposed. By shifting the wavelength of a laser by a few nanometers, however, it would be possible to fulfill the matching condition exactly. The red laser wavelengths are suitable for this purpose, since they are often available as diode lasers whose wavelength can be shifted by a few nanometers via temperature. Other important requirements for such a diode laser are a single transverse spatial mode (TEM-00 mode), i.e. a Gaussian beam profile, with at least 50 mW output power.

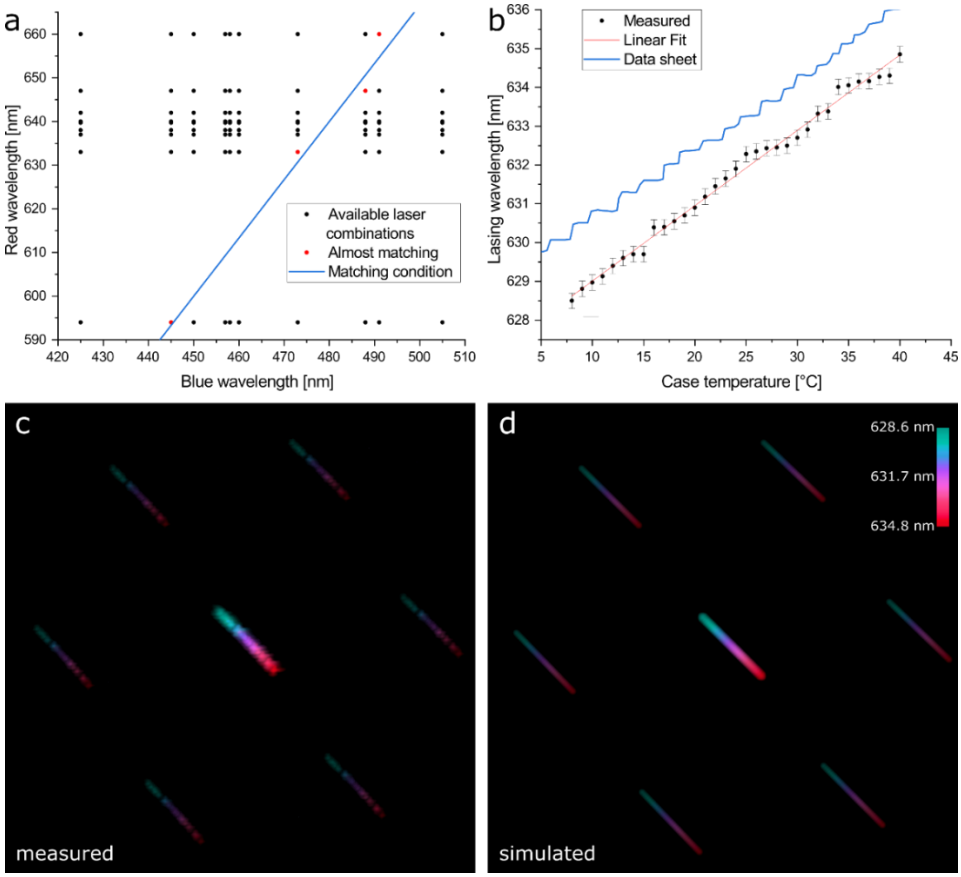

Figure 55: Matching wavelength and shifting diffraction orders

(a) Graphical representation of all possible combinations of commercially available blue and red laser wavelengths (black dots). The blue line shows the required matching condition, where the blue wavelength is 3/4 of the red wavelength. The lasers represented by red dots almost fulfill the matching condition. (b) Lasing wavelength of the laser diode (HL63163DG) from data sheet (blue) and measured (black) with RGB-Photonics Qwave Compact Spectrometer as a function of the case temperature measured by the control unit. During the measurement, the laboratory temperature was 20°C and the diode current was kept at a constant 170 mA. The red line corresponds to the linear fit through all measured data points. The deviation between the measured data points and the data sheet can be explained by the usual manufacturing tolerance of 633 nm ± 3 nm for the lasing wavelength of the laser diode. Both the measured data and the data from the data sheet show mode jumps, as is usual for a laser diode (details in section A.II). (c) Color-coded measured diffraction images (1.3° × 1.3° / 4.5 mm x 4.5 mm) of the DMD as a function of the lasing wavelength (628.6 nm to 634.8 nm) of the laser diode in logarithmic intensity representation. Measured with an IDS uEye UI-3060CP-M-GL Rev.2 CMOS camera in the Fourier plane of the setup (Figure 56 & Figure 57). The small irregularities are caused by mode hops in the laser diode. (d) Color-coded simulated diffraction images (1.3° × 1.3°) of the DMD as a function of the lasing wavelength (628.6 nm to 634.8 nm) of the laser diode in logarithmic intensity representation. The simulation was conducted with 350×350 individual mirrors, with a grating constant of m=7.56 µm, a tilt angle of $\gamma = 12°$ and an incidence angle of $\alpha = 43.7°$ ($\varphi_a = -\vartheta_a = 34.05°$). The SIM patterns used are those of the 631 nm channel. All diffraction images shown are integrated over the three SIM angles. Figure taken from our corresponding publication [64].

The most promising candidate for our project turned out to be the laser diode HL63163DG 633nm/100mW. This can be tuned from 629 nm to 636 nm via the case temperature (see Figure 55b, details in section A.II) [279]. Setting the red diode laser to 630.67 nm, this should perfectly match a 473 nm DPSS (diode pumped solid state) laser to satisfy the blaze condition (eq. (116)). To verify whether temperature tuning can be used to shift the Fourier plane of typical SIM patterns as expected, we performed and compared corresponding measurements (Figure 55c) and simulations (Figure 55d). The measurements matched the simulations with impressive accuracy.

The blue laser used is the Spectra Physics Excelsior 473, 473nm/50mW, with a measured wavelength of $\lambda_1 = 473.1\ nm$. At a case temperature of 19°C, the red diode laser has a wavelength of $\lambda_2 = 630.8\ nm$. Thus, the matching condition from eq. (116) is exactly fulfilled, making the two lasers ideal for the setup of a dual-color DMD-SIM microscope:

$$\frac{\lambda_1}{\lambda_2} = \frac{473.1\ nm}{630.8\ nm} = \frac{3}{4} = 0.75 \tag{117}$$

With the previously selected lasers we were able to extend our two-beam DMD-SIM microscope with originally one excitation wavelength (532 nm, see section 3.4) to two excitation wavelengths (473.1 nm and 630.8 nm) (see Figure 56 & Figure 57, detailed component list Table 5 in section A.I). Just like its one-color predecessor, the DMD is rotated by 45° so that the tilt axis of the micromirrors is perpendicular to the plane of the excitation lasers (45° diagonal). The operating software for control and live reconstruction is also fairSIM-VIGOR [63] (see section 3.7). As this is a typical two-beam SIM microscope, nine raw images (3 angles with 3 phases each) are required per channel, per super-resolution image. Since due to the use of a DMD the fast modeling of the lasers between the raw images is not necessary (see section 3.4), the high precision timing control of the microcontroller (Arduino Uno) is limited to the DMD and the camera. To ensure that there is no crosstalk between the channels during an acquisition despite the Fourier filter mask, the laser that is not needed is shuttered.

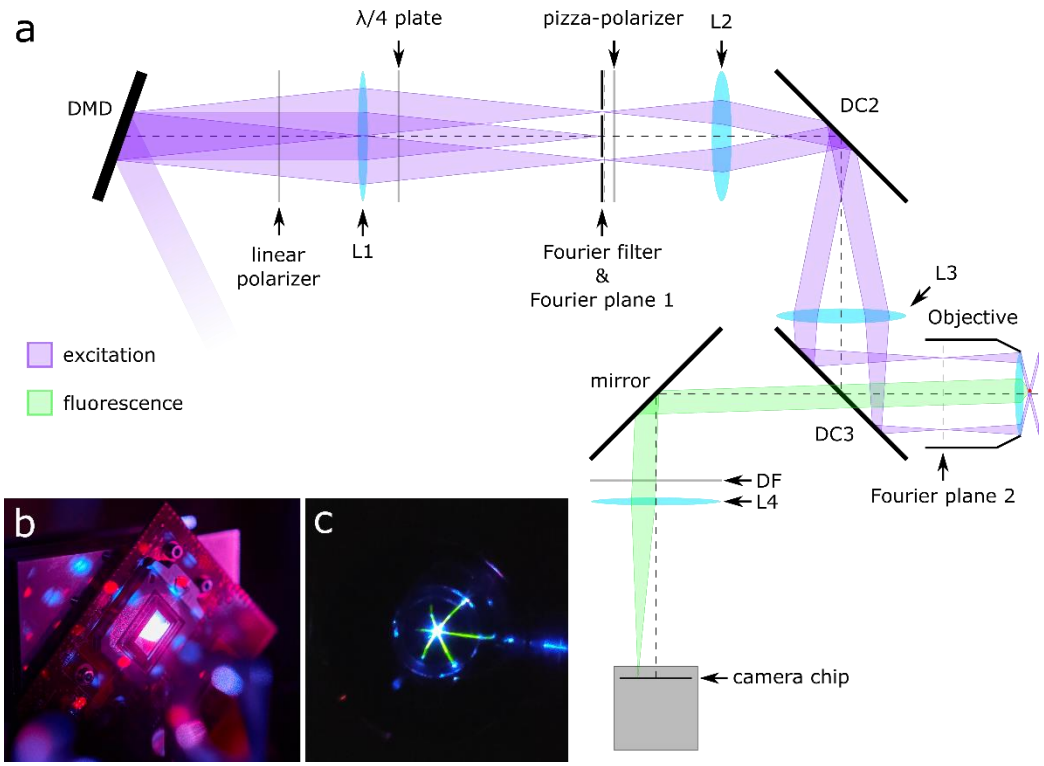

Figure 56: The dual-color DMD SIM Microscope

(a) Schematic representation of the setup (photo of the setup, see Figure 57). For excitation, 473 nm (blue) and 631 nm (red) laser beams are coupled into two separate single mode fibers. Behind the fibers, the two s-polarized and collimated beams with diameters of 18.5 mm FWHM are superimposed (purple) by means of dichroic mirror DC1 before they hit the DMD at an angle of approx. $\alpha = 43.7°$. The laser beams reflected/diffracted by the DMD at an angle of approx. $\beta = -19.7°$ create the Fourier plane at the position of the Fourier filter by passing through lens L1. The linear polarizer, the λ/4 plate and the pizza-polarizer ensure the correct linear alignment of the polarization of the individual SIM angles [210]. Lenses L2 and L3 act as a telescope, focusing the laser beams filtered by the Fourier mask into the back focal plane of the objective. The objective collimates the focused laser beams and causes them to propagate through each other in the sample plane, resulting in the desired sinusoidal SIM pattern in the sample due to interference. Two dichroic mirrors DC2 and DC3 are used to compensate the different phase delay off s- and p-polarized light and thus maintain the linear polarization of the excitation light (details in the appendix section A.II). The fluorescence emitted by the sample is collected by the objective. The dichroic mirror DC3 separates the fluorescence light (green) from the excitation light. The detection filter DF additionally blocks excitation light before the fluorescence light is focused on the camera by means of the tube lens L4. (b) Photo of the DMD in operation, while various diffraction orders are generated natively by the DMD itself and by the patterns displayed on it. (c) Photo taken from above the objective lens with 473 nm excitation while two beams for each of the three SIM angles propagate through each other in the sample (in this case water on a cover glass). Figure taken and modified from our corresponding publication [64].

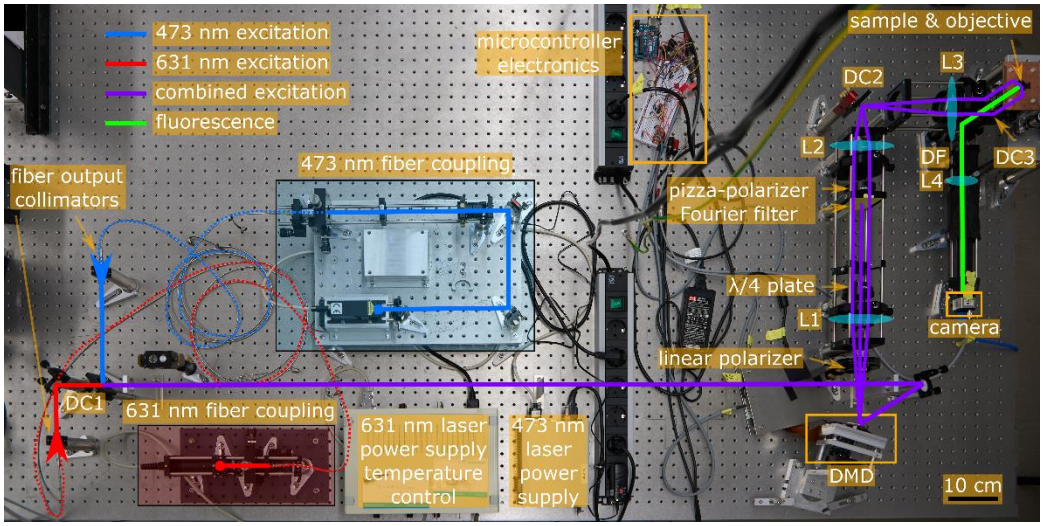

Figure 57: Photo of the custom-built dual-color DMD-SIM microscope

The designations and description are equivalent to Figure 56a. Figure taken and modified from our corresponding publication [64].

The dual-color DMD-SIM microscope is essentially an extension of its one-color predecessor (see section 3.4). Thus, many features that characterize the one-color DMD-SIM microscope have been retained. Up to 540 raw images per second can still be captured. This corresponds to 60 super-resolution SIM reconstructions per second in one channel or 30 in both channels. This continues to outperform current commercial systems and is on par with FLCoS-based SIM microscopes optimized for high-speed [62,63]. The high duty-cycle of the previous system is also maintained, thanks to the global-shutter camera and DMD. By using a faster camera or two cameras (one for each channel), the speed of the system could be further increased. From the technical side, the setup would then be essentially limited by the switching speed of the DMD (105 µs) [264]. However, the biological samples or the fluorescent dyes for staining then limit the acquisition speed, as these only allow a certain level of brightness and photostability.

Based on eq. (111) of the blaze condition approach, for 473 nm and 631 nm for the 4th and 3rd diffraction orders, the incident angle is $\alpha \approx 43.7°$ and the emergence angle is $\beta \approx -19.7°$ to fulfill the blaze condition. These are consistent with the final design of the dual-color DMD-SIM microscope in terms of measurement accuracy. For the one-color version (see section 3.4), which had an emergence angle close to zero, the shear of the patterns shown on the DMD due to an emergence angle could be neglected. However, for the dual-color version with $\beta \approx -19.7°$, this shear must be taken into account, otherwise there would be an elliptical distribution of the $\pm 1^{st}$ SIM diffraction orders in the Fourier plane, resulting in an unequal (anisotropic) increase in resolution

for the different SIM angles. For this purpose, the Fiji plugin "fastSIM-GratingSearch", which allows the calculation of multi-color SIM patterns on SLMs, was extended accordingly (details can be found in the corresponding GitHub repository: [280]).

To ensure that the Fourier plane of the dual-color DMD-SIM microscope meets the requirements of a SIM microscope, it was measured for both channels with one camera (see Figure 58). The desired diffraction orders of both channels are superimposed. The $\pm 1^{st}$ diffraction orders of the three SIM angles are equidistantly arranged around the central 0^{th} diffraction order. With a deviation of the average intensities of less than 9% (15% brightest pixel deviation) between the $\pm 1^{st}$ diffraction orders (see Table 3) the generated Fourier plane meets the requirements of a SIM microscope.

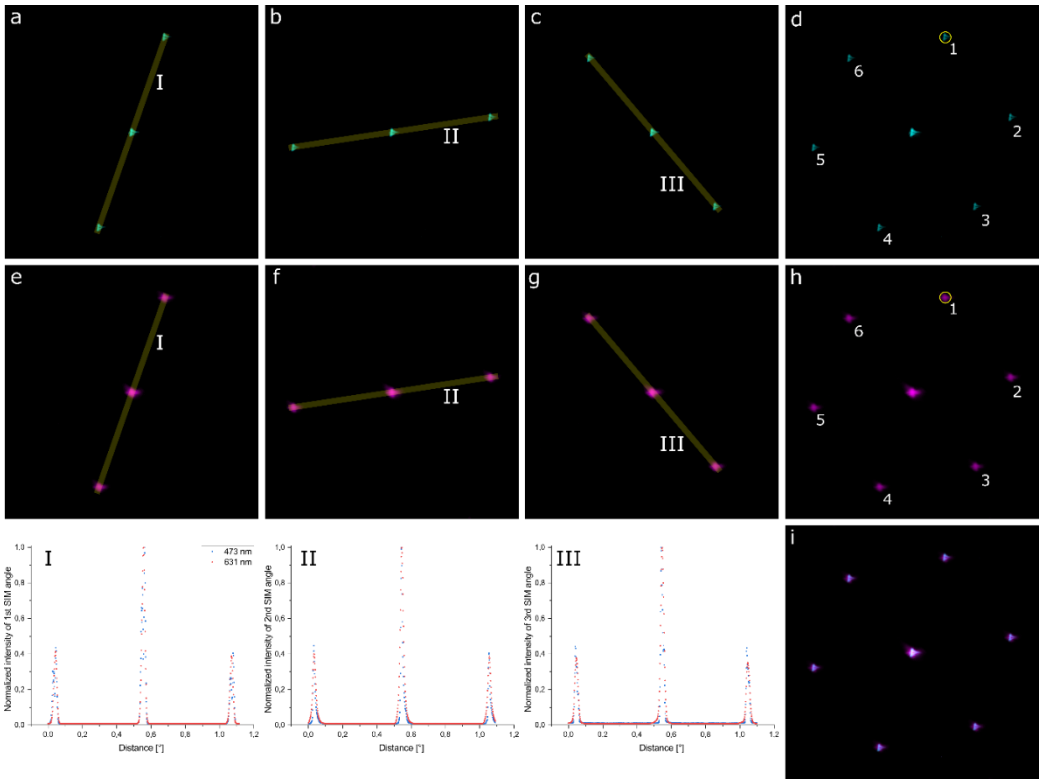

Figure 58: Fourier plane and diffraction order analysis

Diffraction image (1.3° × 1.3° / 4.5 mm x 4.5 mm) in the Fourier plane of the setup of the individual three SIM angles at 473 nm (a-c) and 631 nm (e-g) in logarithmic intensity representation. All images were acquired with an industrial grade CMOS camera (IDS uEye UI-3060CP-M-GL Rev.2) held in the Fourier plane of the setup. (I-III) Cross-section plots (10 pixels / 0.017° wide) through the diffraction maxima in the Fourier plane at 473 nm (blue) and 631 nm (red). (d, h, i) Summed diffraction images at 473 nm (d), 631 nm (h) and superimposed (i) in logarithmic intensity representation. The small yellow circle in (d, h) indicates the area for the measured spot intensities in Table 3. Figure taken from our corresponding publication [64].

Side order	Normalized mean	Normalized max
1	0.95	0.93
2	0.92	0.88
3	0.93	0.99
4	1.00	1.00
5	0.96	0.93
6	0.91	0.85
1	0.95	0.89
2	0.99	0.95
3	0.97	0.87
4	0.99	0.95
5	1.00	1.00
6	0.99	0.93

Table 3: Diffraction order intensities in the Fourier plane

Average and maximum normalized diffraction order intensities in the Fourier plane at 473 nm (upper half) and 631 nm (lower half) measured in a circle with 30 pixels / 0.05° diameter around the diffraction maxima. The symmetrical intensity distribution of the diffraction order in both channels with deviations of less than 9% in the average and 15% in the maximum can be a good quality feature for the correct angle of incidence (blaze angle) of 43.7° on the DMD. Table taken from our corresponding publication [64].

As an additional cross-check for quality assurance of the Fourier plane, we compared the measured and simulated Fourier planes of 473.1 nm and 630.8 nm (see Figure 59). The Fourier planes of both wavelengths were created using the SIM pattern set of the red channel so that the $\pm 1^{st}$ diffraction orders of both channels land at different positions to distinguish them. The measured and simulated Fourier planes agree well except for the third SIM angle. The small deviation is presumably due to non-linearities in the diffraction space of the simulations, especially along the 45° diagonal (see Figure 78 in section A.II).

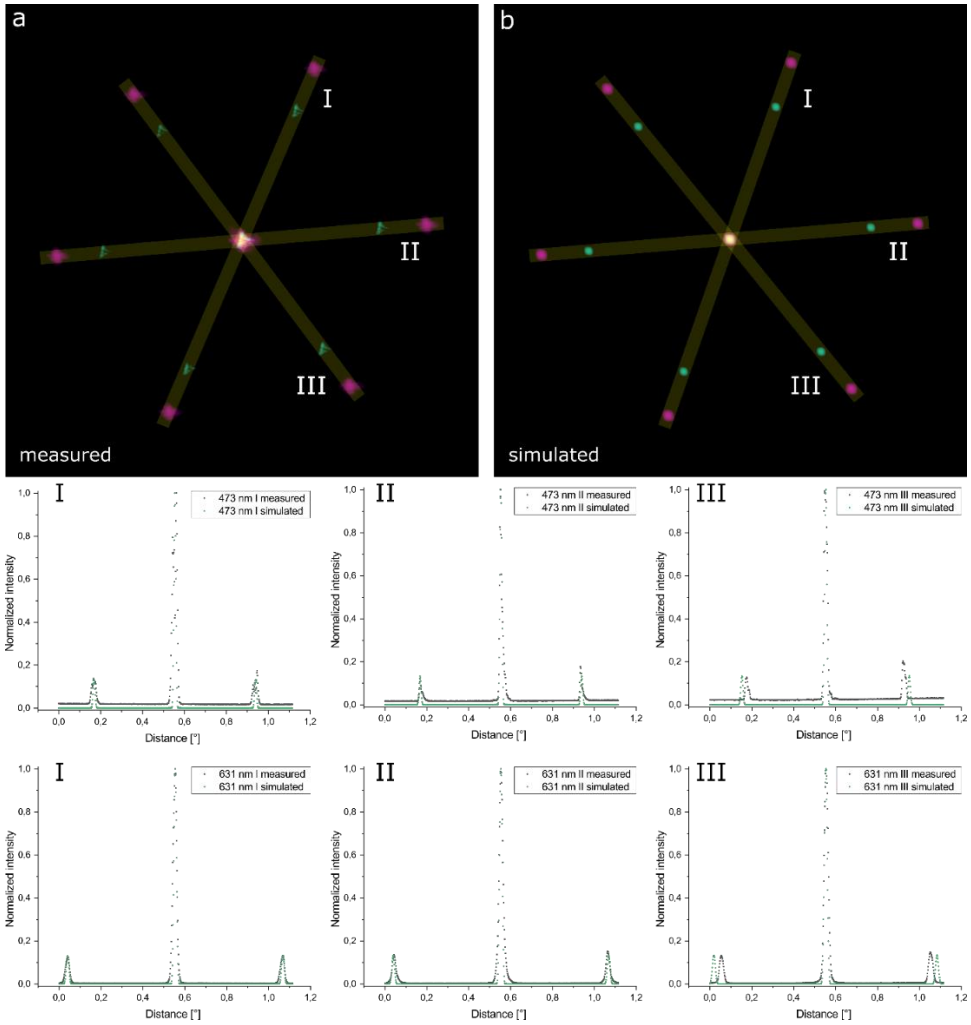

Figure 59: Comparison of the measured and simulated diffraction orders

(a) Measured diffraction image of the DMD with 473.1 nm (cyan) and 630.8 nm (magenta) in logarithmic intensity representation. Measured with an IDS uEye UI-3060CP-M-GL Rev.2 in the Fourier plane of the setup. (b) Simulated diffraction image of the DMD with 473.1 nm (cyan) and 630.8 nm (magenta) in logarithmic intensity representation. Simulated with 350×350 individual mirrors, with a grating constant of $m = 7.56\ \mu m$*, a tilt angle of* $\gamma = 12°$ *and an incidence angle of* $\alpha = 43.7°$ *(*$\varphi_a = -\vartheta_a = 34.05°$*). The measured and simulated diffraction images are integrated over the three SIM angles and were formed using the SIM patterns intended for the 631 nm channel. For this reason, the intensity of the central diffraction order is higher by a factor of three than it would be for a single SIM angle. The position of the first side orders do not overlap because the pattern of the 631 nm channel was used for both channels. As a result, the first side orders of the 473 nm channel are closer to the central diffraction order. (I-III) Cross-section plots (10 pixels / 0.017° wide) through the measured (black) and simulated (green) diffraction maxima in the Fourier plane. For SIM angles I and II, the measurements and simulations agree very well. SIM angle III deviates slightly from the simulations in the measurement. We see non-linearities in the diffraction/angle space of the simulations as the reason for this. These increase along the diagonals as soon as the small angle approximation is no longer fulfilled (*$\beta = -19.7°$*). SIM angle III is oriented almost identically to the diagonal. Figure taken from our corresponding publication [64].*

The SIM patterns and the Fourier mask for the dual-color DMD-SIM microscope are selected in such a way that they increase the resolution by a factor of 1.65 relative to the excitation wavelengths. This corresponds to a pattern spacing in the sample plane of 274 nm (for 473 nm excitation) and 365 nm (for 631 nm excitation), respectively. Due to the Stokes shift of the fluorescence to longer wavelengths, the cut-off frequency (Abbe limit) of the detection is reduced, so that an effective lateral resolution increase by a factor of 1.70 can be expected. Even though lateral resolution increases up to a factor of 2 (even more with TIRF-SIM) are possible with SIM, this has to be weighed against the possible optical sectioning (axial resolution) with two beam SIM (see section 2.2.3, OTF attenuation / notch filtering) [281,282]. Figure 19 & Figure 20 from section 2.2.3 were acquired with the dual-color DMD-SIM microscope to demonstrate the improvement of optical sectioning. However, with SLM-based SIM microscopes (such as the one presented here), the trade-off between lateral and axial resolution enhancement can be varied comparatively easily by adjusting the SIM patterns and Fourier mask accordingly [283].

To demonstrate the functionality and quality of the dual-color DMD-SIM microscope, images of 200 nm fluorescent beads were acquired first (see Figure 60a-c). When comparing the wide-field (Figure 60a) or Wiener-filtered data (Figure 60b) with the SIM reconstructions (Figure 60c), it is obvious that the resolution of the SIM reconstructions is higher, as expected. Acquisitions of 100 nm fluorescent beads (Figure 60e,f) analyzed using Fourier Ring Correlation (FRC, Figure 60d) make the actual gain in resolution of the setup quantifiable for both channels [277,278]. In the wide-field, the Abbe limit of the two channels is 197.4 nm (for 525 nm fluorescence in the 473 nm channel) and 263.6 nm (for 700 nm fluorescence in the 631 nm channel). The resolutions for the wide-field determined via FRC analysis are 203.5 nm $\pm$ 8.2 nm (473 nm channel) and 274.7 nm $\pm$ 13.9 nm (631 nm channel), which agrees very well with the expected Abbe limit. The resolutions achieved in the SIM reconstructions are 121.3 nm $\pm$ 3.4 nm (473 nm channel) and 171.7 nm $\pm$ 4.7 nm (631 nm channel). Thus, this corresponds to a resolution gain by a factor of 1.68 $\pm$ 0.08 (473 nm channel) and 1.6 $\pm$ 0.09 (631 nm channel), which is in good agreement with the expected factor of 1.7.

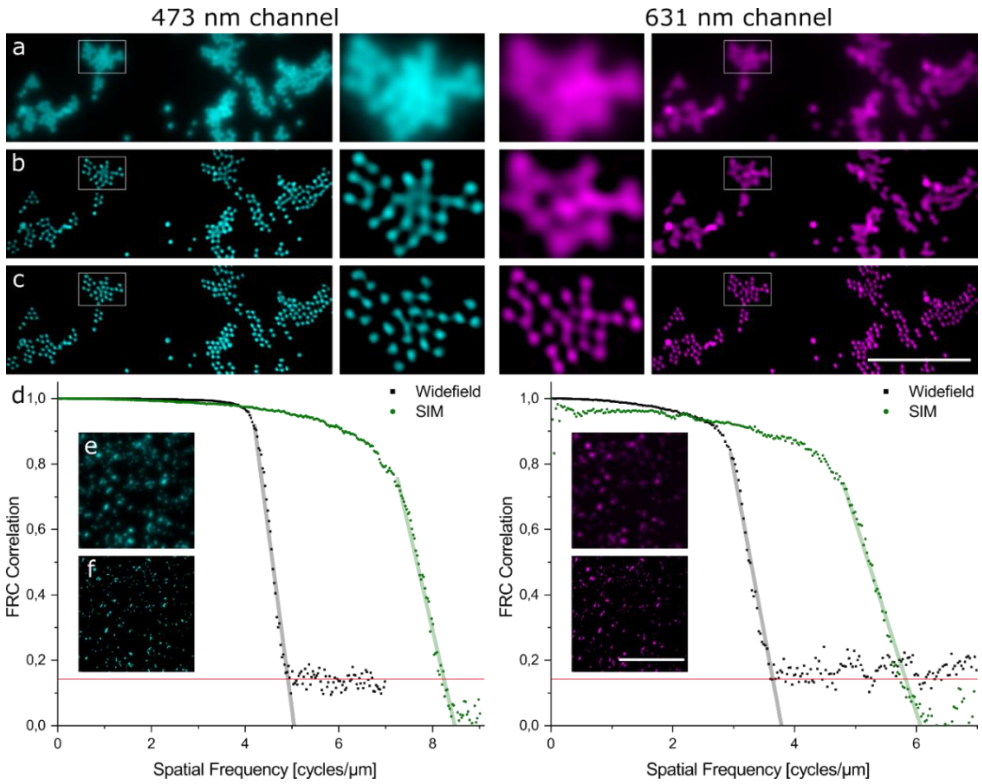

Figure 60: 200 nm fluorescent beads and 100 nm fluorescent beads FRC statistics

The left and right columns correspond to measurements in the 473 nm and 631 nm color channels. (a-b) show images of 200 nm fluorescent beads (scalebar 5 µm, 200 ms / 50 ms exposure time per raw image for the 473 nm / 631 nm channel). (line a) Summed wide-field image of the nine raw SIM images, (line b) Wiener-filtered wide-field image, (line c) SIM reconstruction with fairSIM [193]. In the 2.1 µm x 1.6 µm magnifications, individual beads are distinguishable in the SIM reconstruction, which are not distinguishable in the wide-field or filtered image. (d) FRC analysis [277,278] on 100 nm fluorescent beads from (e) widefield and (f) SIM reconstructions (scalebar 5 µm, 200 ms exposure time per raw image for both channels). The spatial frequency at which the linear fit of the FRC data points falls below a correlation of 1/7 was used to determine the resolution. This results in 203.5 nm ± 8.2 nm (wide-field) and 121.3 nm ± 3.4 nm (SIM) for the 473 nm channel and 274.7 nm ± 13.9 nm (wide-field) and 171.7 nm ± 4.7 nm (SIM) for the 631 nm channel. This corresponds to a resolution increase of 1.68±0.08 (473 nm channel) and 1.6±0.09 (631 nm channel). The determined and expected resolution increases match. Figure taken from our corresponding publication [64].

In addition to the FRC analysis, the cross-section plots from images of 100 nm fluorescent beads are used to estimate the resolution gain (see Figure 61). By fitting the intensity distribution of a single bead with a Gaussian bell curve (Figure 61 II,IV) and the resulting FWHM, resolution increases by a factor of 1.61 (473 nm channel) and 1.75 (631 nm channel) could be determined. These values are also in good agreement with the expected factor of 1.7. In addition, the cross-section plots (Figure 61 I,III) support the distinguishability of two individual beads in the SIM reconstructions (Figure 61c), which is not possible in the wide-field (Figure 61a) or Wiener-filtered wide-field (Figure 61b).

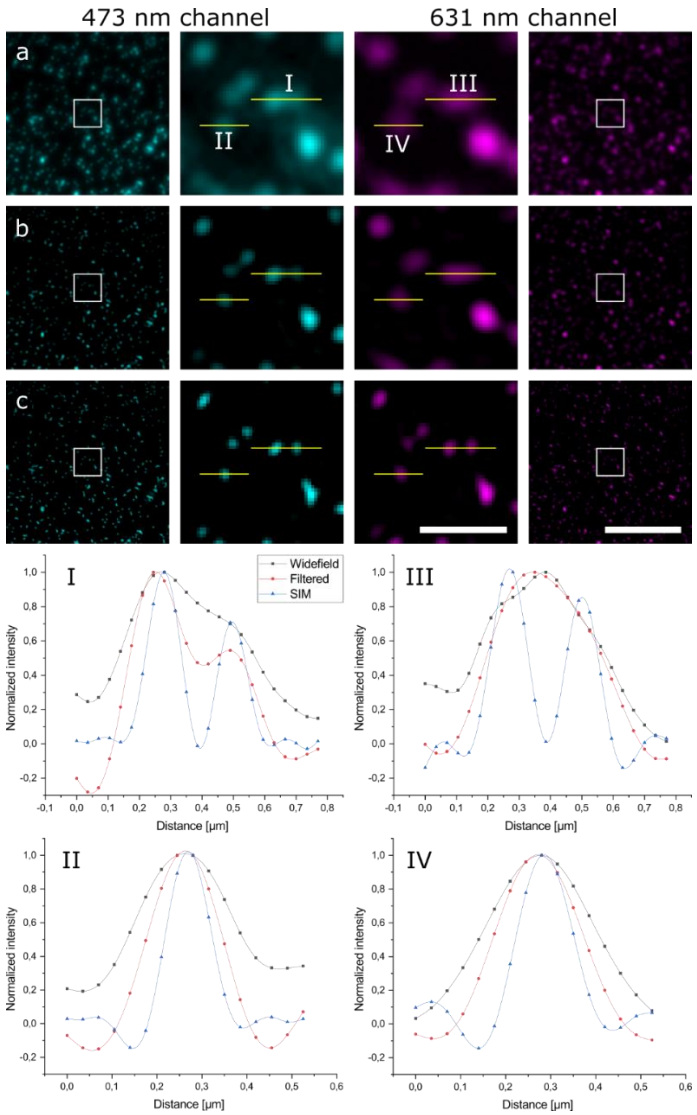

Figure 61: 100 nm TS beads with cross-section plots

Images of 100 nm TS beads in the 473 nm (left column) and 631 nm channel (right column), scalebars 5 µm and 1 µm in the magnification, 200 ms exposure time per raw image. (line a) Summed wide-field image of the nine SIM images, (line b) wiener filtered wide-field image, (line c) SIM reconstruction with fairSIM [193]. In the SIM reconstruction individual beads are distinguishable, which are not distinguishable in the wide-field or filtered image. This is further supported by the cross-section plots (I, III). While in the wide-field and filtered image no or hardly any dip is recognizable, in the SIM reconstruction the intensity between the beads clearly goes down. (II, IV) is a cross-section plot over a single bead. Due to its size of 100 nm, which is below the Abbe limit [10], this can be regarded as a point light source. From the fit with a Gaussian bell curve, the FWHM are 192.8 nm (WF), 150.9 nm (fitered) and 94.0 nm (SIM) for the 631 nm channel and 252.2 nm (WF), 204.9 nm (fitered) and 117.3 nm (SIM) for the 631 nm channel. If we consider the FWHM as a measure of the achieved resolution and compares the filtered image with the SIM reconstructed image, the result is an increase in resolution of 1.61 (473 nm channel) and 1.75 (631 nm channel). Figure taken from our corresponding publication [64].

To prove the compatibility with biological samples, the actin skeleton (473 nm channel in cyan) and the membrane (631 nm channel in magenta) of fixed U2OS cells were acquired (see Figure 62 & Figure 63). In the SIM reconstructions, thanks to the increased resolution, details can be seen that are not visible in the (filtered) wide-field. This is supported by the cross-section plots of closely spaced actin strands (Figure 62 I) and unstained regions of the membrane (Figure 62 II). It is unclear why some parts of the membrane were not stained. We suspect that either disruptions during the fixation process or washing away of an initial staining is the cause.

Figure 63 illustrates that the use of Richardson-Lucy as the deconvolution filter instead of the usual Wiener filtering may be useful during SIM reconstruction [196]. The contrast of some structures is noticeably higher in the RL-SIM reconstruction than in the Wiener-SIM reconstruction.

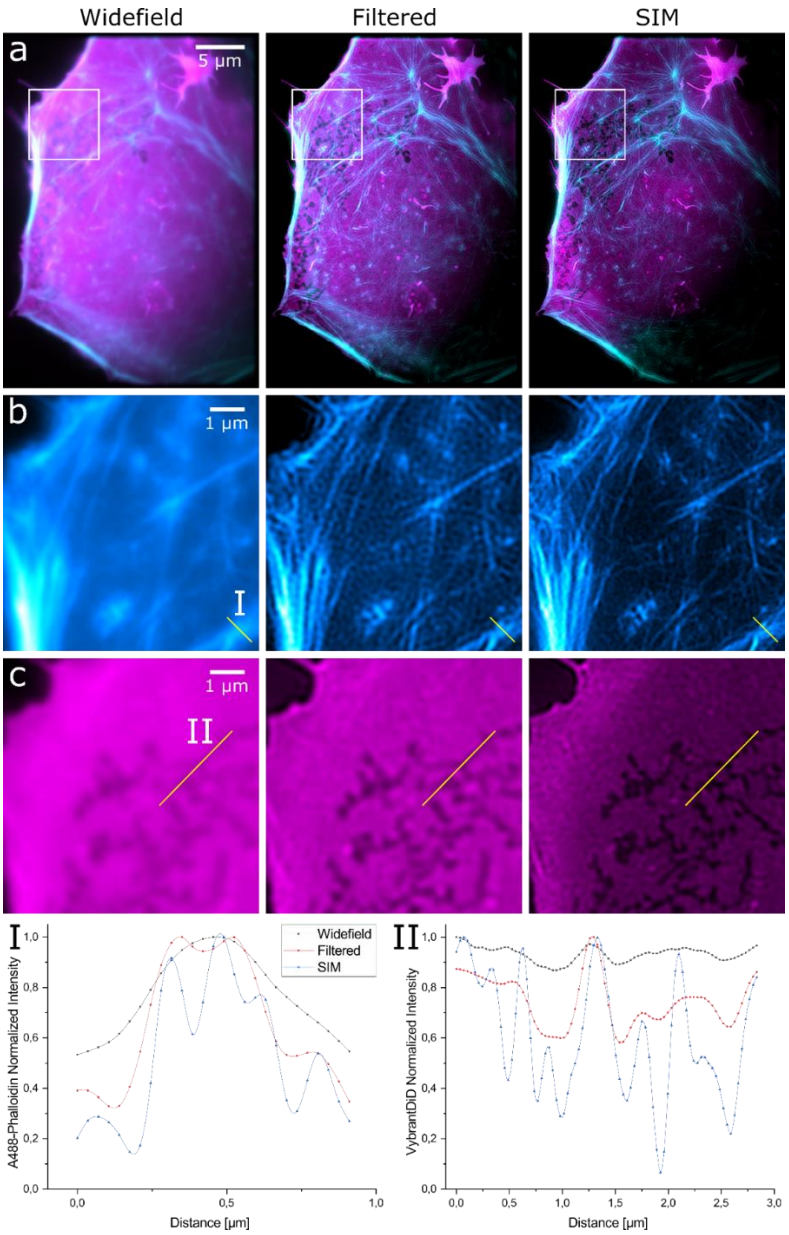

Figure 62: Dual-color fluorescent micrographs of a fixed U2OS cell

Fluorescent micrographs of a fixed U2OS cell (200 ms exposure time) shown as an overlay (row a) of actin (Alexa 488 phalloidin) in the 473 nm channel (row b) and the membrane (Vybrant DiD) in the 631 nm channel (row c). In the fairSIM [193] reconstruction (3rd column), structures are resolved in both channels which are not detectable in the wide-field (1st column) and Wiener filtered image (2nd column). The cross-section plot (I) illustrates that in the SIM reconstruction closely spaced actin filaments can be distinguished from each other, which cannot be separated in the wide-field and Wiener-filtered image. The same can be observed in cross-section plot (II) based on the unstained areas of the plasma membrane. In the SIM reconstruction, many unstained areas in the membrane are visible, which blur into each other in the wide-field and Wiener-filtered image. Figure taken from our corresponding publication [64].

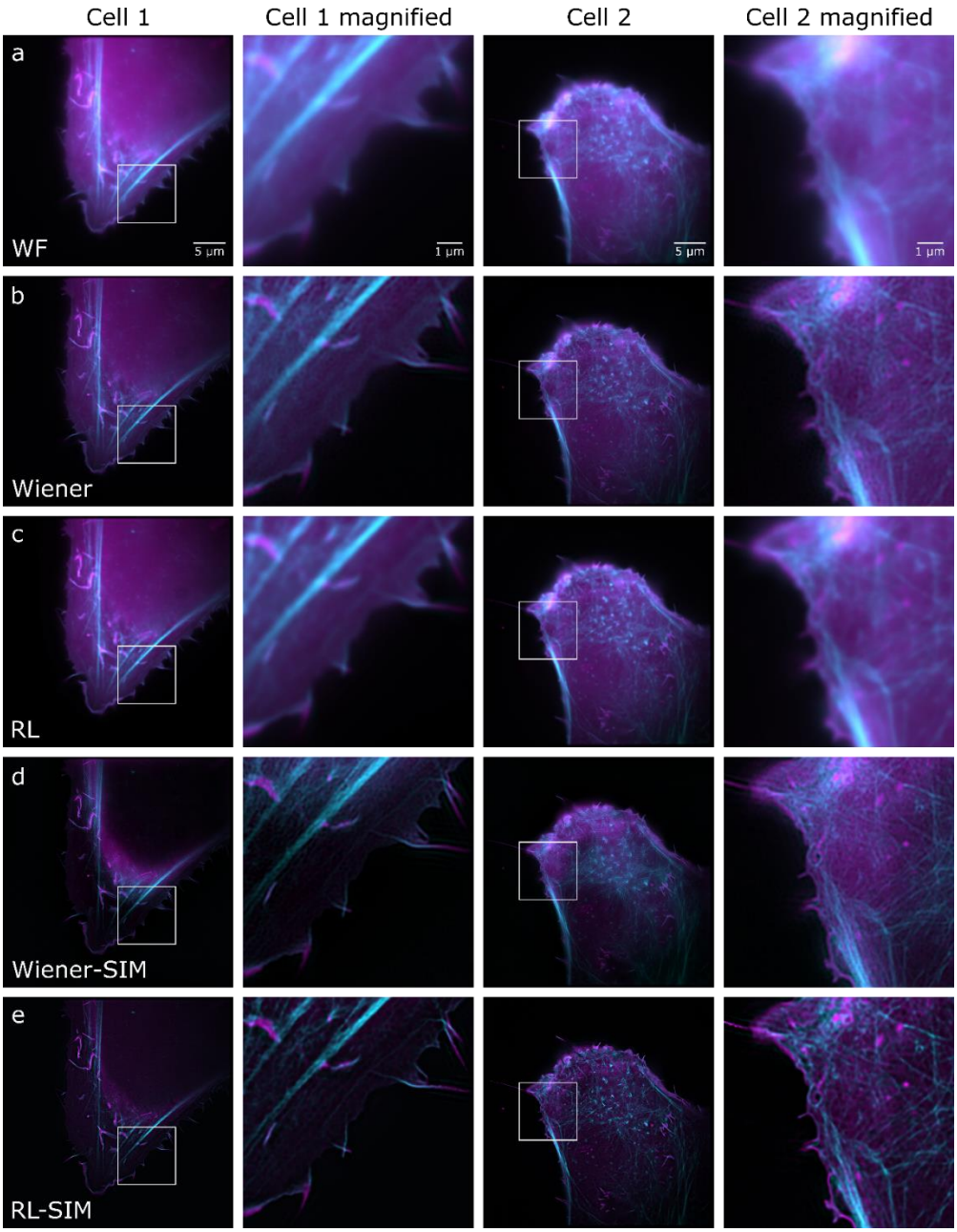

Figure 63: Dual-color fixed U2OS cells

Images of fixed U2OS cells as an overlay of actin (Alexa 488 phalloidin, 200 ms exposure time) in the 473 nm channel and the membrane (Vybrant DiD, 100 ms (cell 1) / 200 ms (cell 2) exposure time) in the 631 nm channel. From left to right: cell 1, magnification of cell 1, cell 2 and magnification of cell 2. Shown as wide-field (line a), wiener filtered wide-field (line b), Richardson-Lucy filtered wide-field (line c), SIM reconstruction with fairSIM [193] using wiener filter (line d) and SIM reconstruction with fairSIM using Richardson-Lucy filter (line e). In the SIM reconstructions, structures and details are recognizable which cannot be resolved in the unfiltered or filtered wide-field. Figure taken from our corresponding publication [64].

3.7 fairSIM-VIGOR: operating software for SIM microscopes

The operating software used for the one- and dual-color DMD-SIM microscope, among others, is called fairSIM-VIGOR [63], which can essentially be divided into two main parts. The first part is the GPU- and network-based real-time reconstruction of the raw SIM data to super-resolved SIM reconstructions. The second part is the network-based control of the entire SIM microscope with a microcontroller as the central timing unit for the SLM, the cameras and the light sources.

3.7.1 Real-time reconstruction

The real-time reconstruction was developed and implemented by Dr. Marcel Müller. The following information about the real-time reconstruction is part of this thesis for the sake of completeness but is not an own contribution of the author of this thesis.

FairSIM (free analysis and interactive reconstruction for structured illumination microscopy) was originally developed as a Fiji plug-in for reconstructing raw SIM data [193]. Java was chosen as the programming language because, on the one hand, the software should function independently of the system and, on the other hand, compatibility with the Fiji program written in Java can be ensured in this way.

In order to be able to perform the SIM reconstructions in real time, fairSIM was extended by the VIGOR engine (video-rate GPU-accelerated open-source reconstruction). This engine makes it possible to perform the entire image processing on an Nvidia graphics card (GPU). The algorithms on the GPU were implemented using CUDA. The interface between the fairSIM Java code and the GPU CUDA code is the Java Native Interface (JNI). The JNI provides the possibility to call functions or methods of compiled libraries (C, C++, CUDA) from Java. To perform a SIM reconstruction, the captured raw data is copied from the CPU to the GPU, which is followed by the execution of the reconstruction algorithm. Finally, the reconstructed image is copied from the GPU to the CPU. If multiple reconstructions are queued up, e.g. when acquiring a time lapse SIM measurement, data transfers and GPU-based reconstructions are also automatically run in parallel, as long as hardware resources suffice. If no CUDA-capable Nvidia GPU is available or the compiled CUDA library is not available, the reconstruction takes place on the CPU. However, real-time reconstruction with reasonable speed is only possible with GPU support.

In addition to the VIGOR engine, fairSIM has been extended by a network communication package, which enables the sending and receiving of images. The objects sent over the network are so called ImageWrappers, which contain the raw image of a camera with additional meta data like timestamp, image number, etc. For sending and receiving the classes ImageSender and ImageReceiver were implemented.

Furthermore, a package for live operation on a SIM microscope was added, which contains, among others, the classes SimSequenceExtractor and ReconstructionRunner, which are responsible for extracting the SIM sequences from the raw data and for real-time reconstruction. A schematic representation of the underlying software architecture and data flow can be seen in Figure 64.

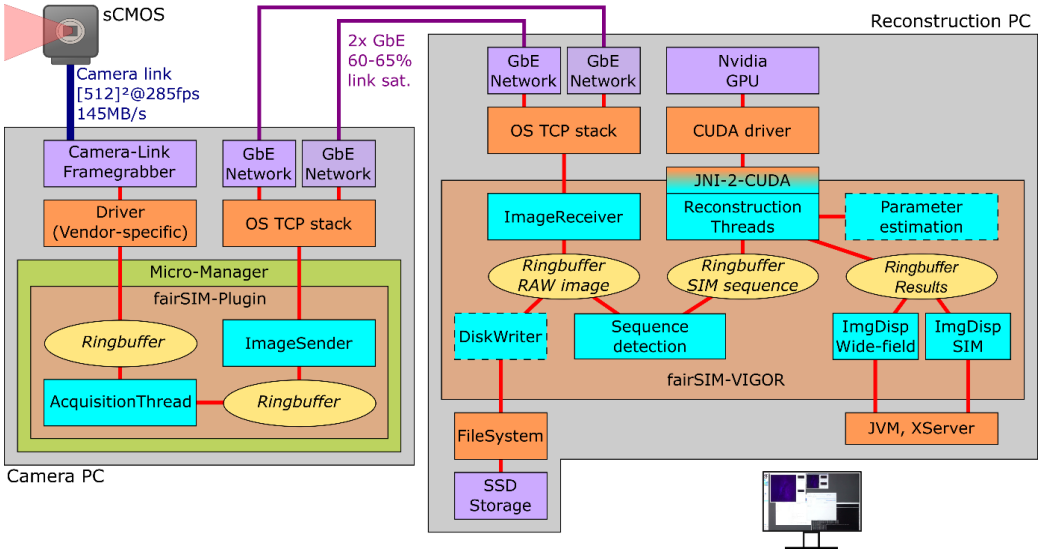

Figure 64: Structure of the real-time reconstruction software fairSIM-VIGOR

These schematics show the data flow of the raw images from the cameras to the high-resolution reconstructed image. The raw images are acquired by a sCMOS camera and are forwarded via Camera Link to a frame grabber card belonging to the camera. Via the corresponding driver and device adapter, the raw images are placed in a first ring buffer of the fairSIM-Plugin running in Micro-Manager. The AcquisitionThread of the fairSIM-Plugin takes the raw images from this first buffer, adds additional meta information (channel number, sequence number & timestamp) and places them in a second ring buffer. The second ring buffer is being cleared by the ImageSender, which sends the images to the reconstruction computer via one (or more) Gigabit Ethernet TCP connections. If there is sufficient computer power, the cameras could also be connected directly to the reconstruction computer by establishing an internal network connection ("localhost"). The image receiver of the fairSIM-VIGOR running on the reconstruction computer receives the images from the camera computer and places them in the raw image ring buffer. The Sequence detection forms complete SIM sequences from the raw data and places them in the corresponding ring buffer. Optionally, the data in the raw image ring buffer can simultaneously be written to the SSD Storage using DiskWriter, thus allowing to actually save the full raw data stream for later, offline analysis. The SIM sequence ring buffer is being cleared by the reconstruction threads. Via the JNI (Java Native Interface), the SIM sequences are transferred to an Nvidia graphics card on which the reconstruction algorithm is then executed. If necessary, it is possible to estimate and apply new reconstruction parameters during runtime. The high-resolution reconstructed images are placed in the results ring buffer together with the wide-field image generated from the raw images, in which they are waiting to be displayed on the screen. Figure taken from our corresponding publication [63].

3.7.2 Control software for SIM microscopes

The control software for SIM microscopes presented below originate from the master thesis of the author of this thesis and are part of this thesis for the sake of completeness.

The control of the individual components of a SIM microscope was integrated into fairSIM-VIGOR in a separate controller package. The TCP connections required for network communication between the computers involved are established using abstract server and client classes, whose communication is based on strings. The server-client communication is structured in such a way that the client sends a command to the server and the server sends back a corresponding response after executing the command. The response is used by the client to detect the success or failure of the command to be executed or to exchange information between the server and the client.

The SLM and the microcontroller are usually connected to the same computer. Therefore, it makes sense to implement the control of both devices over the same network connection. The TCP connection is established by a concrete controller implementation of the server and client classes.

The API provided by the manufacturer of the SLM is included in the SlmController class. The SlmController serves the ControllerServer as a communication interface with the SLM. Its methods execute the desired command and depending on the reaction of the SLM, return a corresponding string for the response to the ControllerClient.

Communication with the microcontroller is realized via its serial interface. The hard-coded running orders of the microcontroller are represented in its C++ programming by running order objects. These objects include the name of the running order, the delays needed for SIM sequence bundling, the exposure time relevant to the cameras, a method containing the code to execute the running order on the microcontroller, and a toString() method for transmitting the running orders to the reconstruction computer. The fixed programming of the timings of each running order can and should be optimized using an oscilloscope to obtain the highest possible duty-cycle. Each running order can be started in either movie or photo mode. Movie mode is used to acquire many reconstructed SIM images in succession and can be executed with delays between the individual SIM sequences if required. Photo mode is used to capture a single SIM sequence.

When the microcontroller is started, an array of all executable running orders is created. This array can be queried via the serial interface. In this way, it is possible to dynamically transfer all running orders available on the microcontroller to the reconstruction

computer via the controller server. The computer-side connection to the microcontroller is implemented using the ArduinoController class. This enables the sending and receiving of strings via the serial interface and serves the ControllerServer as an interface to the microcontroller. The methods of the ArduinoController forward the desired command to the microcontroller equivalent to the SlmController and return, depending on the reaction of the microcontroller, a corresponding string for the response to the client. The schematic structure of the control software is illustrated in Figure 65.

The µManager plugin (fairSIM Camera Controller) is used to control the cameras via fairSIM-VIGOR. The plugin was developed as part of fairSIM-VIGOR in a standalone package. For the required TCP connection, the controller package was extended by the CameraClient class, among others. The CameraServer is located in the package for the µManager plugin. Similar to the SLM and the microcontroller, the CameraController class serves as an interface between the CameraServer and the camera. Here, the CameraController uses the methods available from µManager to control the camera. The commands coming from the CameraClient reach the CameraController via the CameraServer. Depending on the reaction of the camera or µManager, a corresponding response is sent back to the CameraClient. The data transfer of the raw images (as ImageWrappers) to fairSIM-VIGOR via further independent TCP connections has also been integrated into the µManager plugin. The status for the transfer of the ImageWrappers is regularly transmitted to the reconstruction computer together with the camera FPS. µManager (Micro-Manager) is a free available open-source software for control and automation of microscope hardware [284,285].

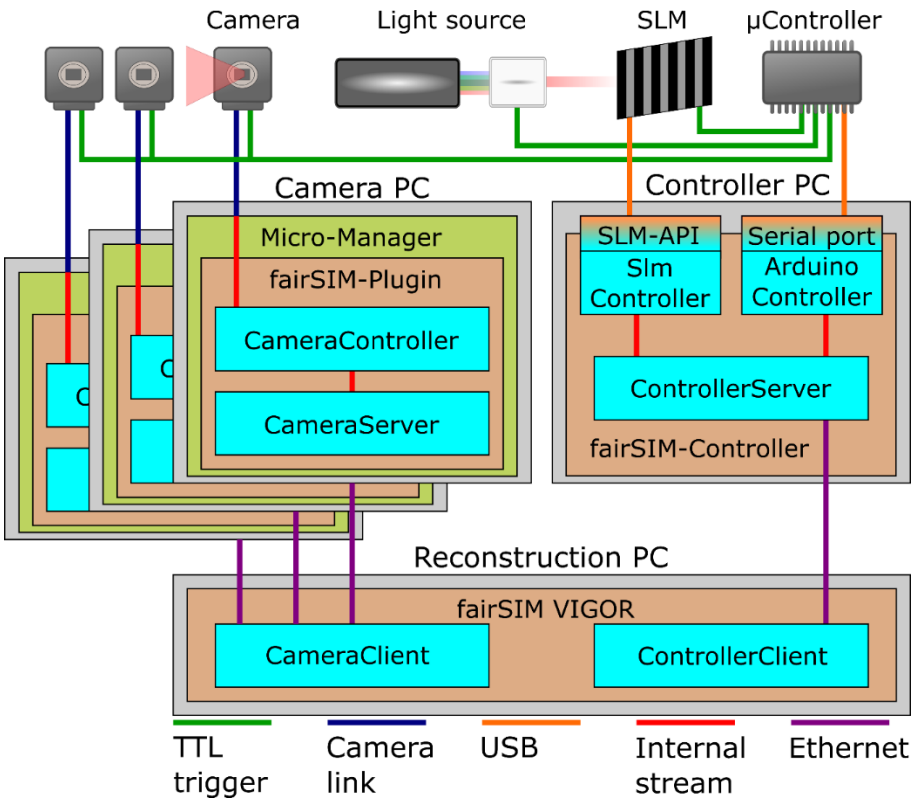

Figure 65: Structure of the instrument control portion of fairSIM-VIGOR

The entire setup is managed and run from the reconstruction computer, which in turn controls the camera computers, the SLM and the microcontroller via TCP/IP network links. The network connections required for this are implemented using abstract client and server Java classes. Network communication is based on strings and the question-and-answer principle, so that each command sent from the client to the server is answered, indicating the success or failure of the command to be executed. It is not necessary that the client and server are on different computers. This means that with sufficient computer performance, the entire setup can also be controlled from a single computer. Each camera is connected to its camera computer, on which Micro-Manager runs with the fairSIM camera plugin. The camera plugin includes the Java classes CameraServer and CameraController. The commands sent by the CameraClient are transmitted from the CameraServer to the CameraController, which ultimately controls the camera using the interface provided by µManager. The SLM (FLCoS or DMD) and the Arduino are connected via USB to the controller computer on which the fairSIM controller software runs. The fairSIM controller software includes the Java classes ControllerServer, SlmController and ArduinoController. The SlmController implements the specific API for the SLM. The ArduinoController uses the serial port as communication interface to the Arduino. The communication between the ArduinoController and the Arduino is also based on strings and the question-and-answer principle. The commands sent by the ControllerClient are forwarded from the ControllerServer to the SlmController or ArduinoController, which ultimately control the SLM or the Arduino via the SLM-API or the serial port. A microcontroller (Arduino Uno) controls the precise timing of the setup. It triggers the cameras, the light sources and the SLM via digital I/O pins, so that each individual device performs the action previously determined via fairSIM at the right time. Figure taken and modified from our corresponding publication [63].

The graphical user interface (GUI) shown in Figure 66 can be used by the user to control the SLM, the microcontroller and the cameras. It is integrated into the GUI of fairSIM-VIGOR as an advanced control panel. It also allows the adjustment of synchronization settings for SIM sequence bundling and the use of the bUnwarpJ-based real-time image registration of the channels against each other [286].

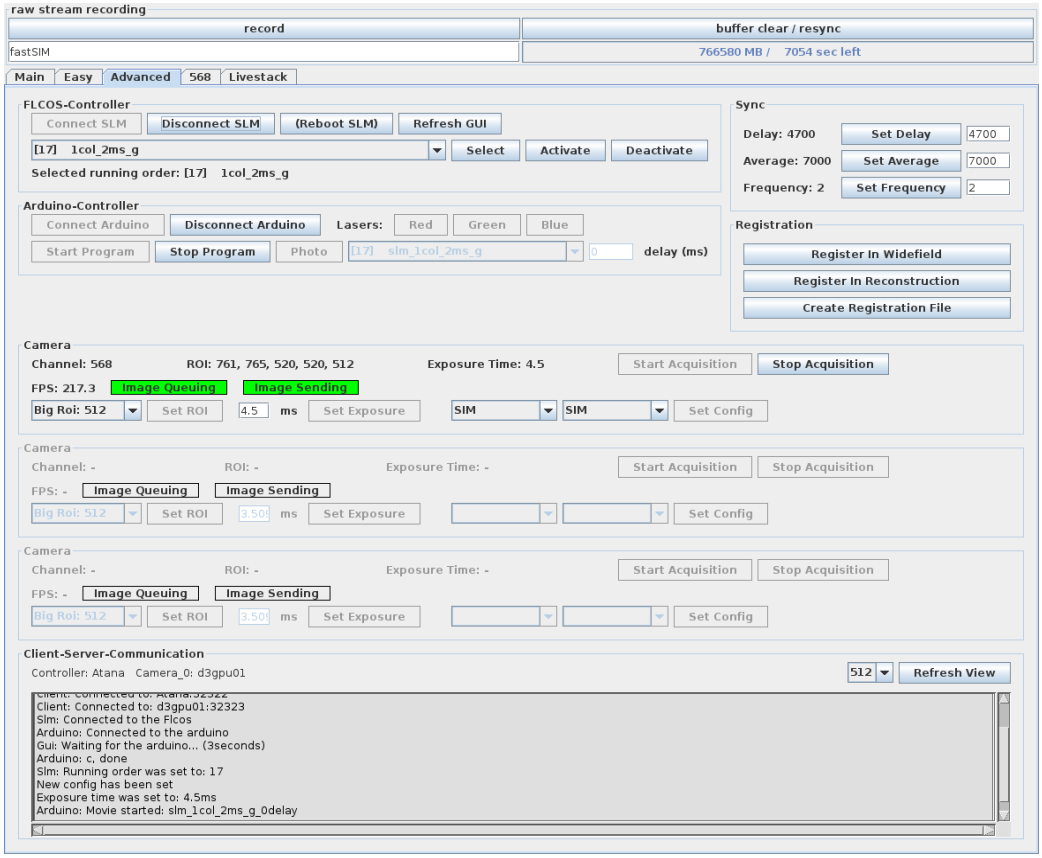

Figure 66: fairSIM-VIGOR Advanced-GUI

The Advanced-GUI serves as the user interface for the software described in Figure 65 to control the individual components of the setup. Via the SLM and Arduino controller panels, the existing running orders and timing programs can be selected, started, and stopped. With the help of the three camera panels, individual settings can be made for each camera. Besides the possibility to start and stop acquisitions it is possible to choose between a ROI of 512×512 and 256×256 pixels. Furthermore, the exposure time and presets can be set. The Client-Server-Communication panel provides the user with information about the network connections and the result of the desired actions. The "Refresh View" button reloads the display windows for the reconstructed and wide-field image to adjust it for the display of a 512×521 or 256×256 region of interest. The Registration panel can be used to register the different channels against each other. Both the reconstructed and the wide-field images can be registered. To do this, a registration file must first be created, which can then be applied. The creation of the registration file uses the API of the image registration software bUnwarpJ [286]. Figure taken from our corresponding publication [63].

The acquisition of one or more SIM sequences requires various coordinated settings in the Advanced GUI (Figure 66). For practical use, it is necessary to have further simplified this process. The Easy GUI shown in Figure 67 serves this purpose. If an action is performed via the Easy GUI, the Advanced GUI is operated in the background to set all the required settings. To use the SIM microscope via the Easy GUI, the user only has to select the excitation lasers used and the exposure time to be able to start a measurement. Optionally, there is also the possibility to (de)activate the real-time image registration, to insert delays between the SIM sequences and to re-estimate the parameters for the reconstruction of all used channels. The buttons "Run" or "Take a photo" can be used to start and stop measurements in movie or photo mode. For the dynamic assignment to work for the Easy GUI, it is necessary that the names of the running orders on the microcontroller and the SLM are matched.

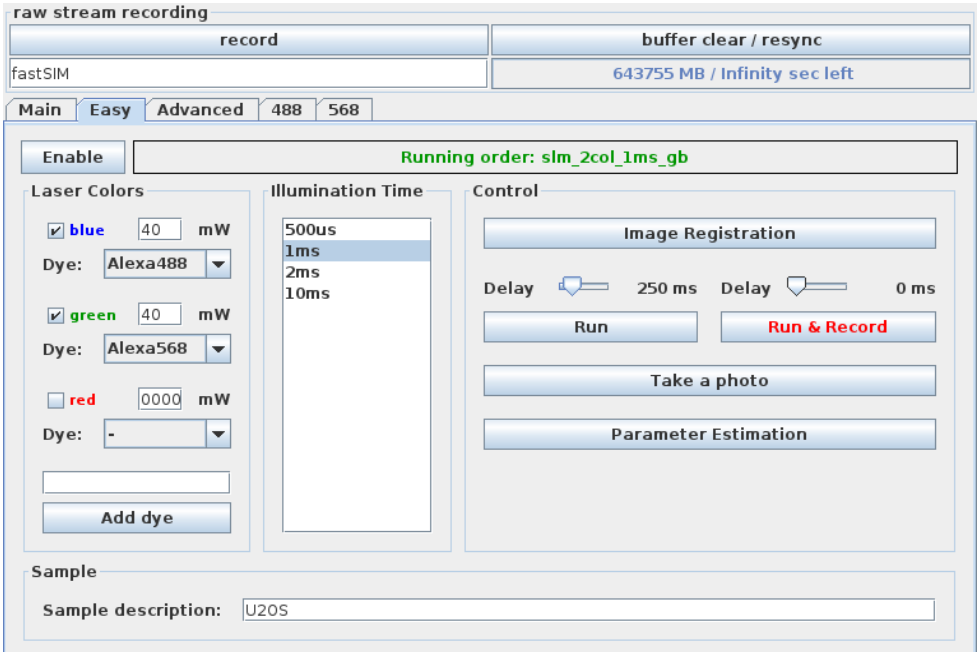

Figure 67: fairSIM-VIGOR Easy-GUI

The Easy-GUI serves the user as a simple and intuitive interface for controlling the entire setup. It is closely linked in the background with the Advanced-GUI (Figure 66). It provides automatization of all day-to-day tasks needed to operate the microscope. I.e., it configures all components (cameras, SLM, microcontroller) for the desired imaging mode, starts and stops them, and allows the user to store the image stream for later, offline analysis. The Enable button establishes all necessary connections (SLM, Arduino and cameras). After selecting a combination of laser wavelengths, the desired exposure time can be selected. Acquisitions can then be made and optionally stored. Using the Run (or Run & Record) button, acquisitions can be started and stopped with an adjustable delay (≥ 50 ms) between the individual SIM sequences. The "Take a photo"-button is used to acquire exactly one SIM sequence. If desired, image registration and parameter estimation can be carried out using the corresponding buttons. Entered or selected metadata (laser power, dye and sample description) are written to the image file when saving data on the storage and are available for later use along with other metadata. Figure taken from our corresponding publication [63].

3.7.3 Integration of the DMD into fairSIM-VIGOR

The original version of the fairSIM-VIGOR control software was developed for the FLCoS-SLM (ForthDD, SXGA-3DM). To ensure compatibility for the DMD (Texas Instruments, DLP® LightCrafter™ 6500) used for the one- and dual-color DMD-SIM microscope, it was necessary to extend the programming accordingly as part of this thesis. In order to run both SLMs with the same software, the original SlmController class with the concrete implementation of the SXGA-3DM API was replaced by a generalized interface, which was then implemented in the form of the classes FlcosControllers and DmdController. The FlcosController takes over one-to-one the function of the original SlmController for the SXGA-3DM, while the DmdController is the equivalent for the DLP® LightCrafter™ 6500. Since no directly usable Java API is available from the manufacturer for the DLP® LightCrafter™ 6500, this was implemented using the Java Native Interface (JNI) as an interface between the provided C++ API and Java.

The concept of running orders, which are an integral part of the SXGA-3DM, has been retained for the DLP® LightCrafter™ 6500 for simplicity and compatibility. Similar to the SXGA-3DM, the running orders consist of a sequence of SIM patterns that are displayed on the DMD for a well-defined time. In the case of the one- and dual-color DMD-SIM microscope, this sequence is started by a trigger pulse from the microcontroller to ensure high-precision timing with the cameras and, if required, with the light sources. The running orders on the DMD can be built and tested using the software provided by the manufacturer (Texas Instruments) via the so-called "Pattern On-The-Fly Mode". For the actual operation of the DMD-SIM microscope, however, the so-called "Pre-Stored Pattern Mode" is used. For this, it is necessary that the required SIM patterns are located in the flash memory of the DLP® LightCrafter™ 6500. Batch files consisting of a set of batch command sequences are used to load the respective running order. Details can be found in the corresponding Users- and Programmers-Guide provided by the manufacturer [287,288].

3.7.4 Metadata storage with LiveStack

When storing and processing raw SIM data, the metadata associated with the acquisition is very important. For this purpose, the LiveStack concept was developed in the scope of this thesis. It is used to store raw SIM images including all important metadata on a (fast SSD) hard disk at high speed immediately after or during the acquisition.

A LiveStack consists of two main components, the header, and the raw images. The header consists of the metadata that is valid for the entire acquired raw image stack:

- Name of the SIM microscope
- Start time of the measurement
- Sample identification
- Identification of the objective
- Width and height of the raw images in pixels
- Number of z-sections
- Number of SIM angles and phases
- Number of SIM bands
- Exposure time per raw image
- Delay between individual SIM sequences
- Synchronization times for SIM sequence bundling
- Projected pixel size (in nm for x,y,z)
- Channel metadata
    - Detector (camera)
    - Fluorescence dye
    - Excitation wavelength and intensity
    - Real-time reconstruction parameters

The raw images correspond to the ImageWrappers introduced in 3.7.1, which, in addition to the raw image data as a 16-bit short array, contain, among other things, a uniquely assignable channel and sequence number and a timestamp.

A LiveStack can exist in four different, but informationally equivalent forms:

- As LiveStack file on the hard disk.
- As LiveStack object in a Java program (e.g. fairSIM-VIGOR)
- As LiveStack TIFF file on the hard disk
- As ImagePlus object, i.e. opened image in Fiji

The order of the previous list corresponds to the path that the raw data of our SIM recordings usually take. At the beginning of the measurement, the header and then all captured raw images (ImageWrapper) are streamed in real time to the (fast SSD) hard disk into a LiveStack file. Using the GUI shown in Figure 68, the LiveStack files can be converted to LiveStack TIFF files. Both the raw data (livestack.tif) and the real-time SIM reconstructions made during the measurement (livestack.recon.tif) can be saved. Furthermore, a text file with all metadata can be created if required. The latter helped us several times during commissioning and troubleshooting of our SIM microscopes.

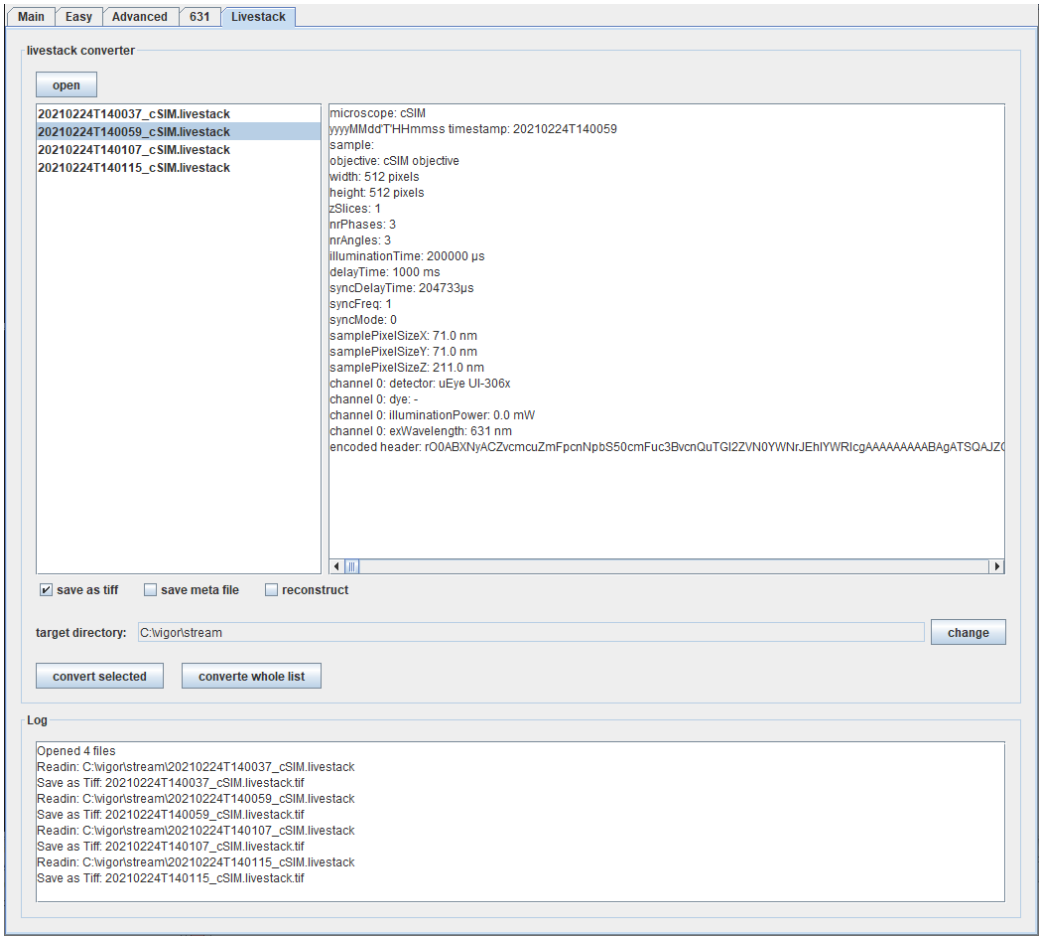

Figure 68: fairSIM-VIGOR LiveStack converter GUI

The graphical interface allows to load and process LiveStack or LiveStack-TIFF files from the hard disk. The left column shows the loaded LiveStacks, while the right column shows the metadata of the selected LiveStack. Below that, corresponding checkboxes can be used to select the LiveStack conversion to be performed. In addition, the storage location of the converted files can be defined. By clicking the corresponding button, either all loaded LiveStacks or only the selected one will be converted. The log in the lower part gives additional information about the conversion process.

Once the data is available as a TIFF file, it can be further processed with any TIFF-compatible program. All metadata are still available and can be accessed, for example, in Fiji via the information window (Image -> Show Info...). The code implementation of the LiveStack concept can be seen in the corresponding LiveStack class in the fairSIM-VIGOR GitHub repository [289].

3.8 Summary and outlook

The knowledge gained within the scope of this thesis on DMD-based SIM microscopy makes a significant contribution to the establishment of DMDs in SLM-based SIM microscopes. DMDs are cost effective, readily available and very fast. Compared with FLCoS SLMs, they are therefore particularly suitable for the development of fast, compact and cost-effective SIM systems. However, the major disadvantage of DMDs, the so-called blazed grating effect (BGE), is a major hurdle. The BGE becomes particularly problematic when multiple excitation wavelengths are used. To overcome the BGE, a practical solution, wavelength matching, has been developed.

The basis for this was created with the help of a specially developed simulation framework. The framework essentially consists of four different simulation approaches that mathematically and physically model the interaction of (coherent) light with the DMD surface. The resulting diffraction images and their analysis enabled the design and construction of a one-color DMD-SIM microscope. Thanks to new findings from the simulations, this could be further developed into a dual-color DMD-SIM microscope.

Both the one- and dual-color setups are just as fast as FLCoS-based systems, but much more cost-efficient. A comparatively simple timing scheme and a higher duty cycle are further arguments in favor of DMDs instead of FLCoS in SIM microscopes. The quality and the achieved resolution increase of the presented DMD-SIM microscopes could be proven by synthetic reference samples. Furthermore, the DMD-SIM microscopes are fully capable of imaging fixed and live cells. Chemical dyes as well as fluorescent proteins were used for staining. An extension from dual- to three-color is possible based on the simulation results. However, an experimental proof is still pending on our part.

In parallel with the progress of this work, another approach to multi-color DMD-SIM microscopy has been developed independently by Brown et al. [270]. This approach uses a 473 nm and 635 nm laser that nearly satisfies the necessary matching condition. Instead of achieving matching by shifting an excitation wavelength as we did, a moving voice-coil mirror is used to adjust the angle of incidence during microscope operation when switching from one channel to the other. Brown et al. were also even able to successfully incorporate a third excitation wavelength (532 nm) via the other tilt state

of the micromirrors. This makes us optimistic that we can similarly advance the dual- to three-color DMD-SIM microscope.

The control and real-time reconstruction software for SIM microscopes fairSIM-VIGOR has been further developed, among other things, for the use of the DMD (DLP® LightCrafter™ 6500, Texas Instruments). Moreover, thanks to the new LiveStack concept, a convenient option for storing the important metadata is now available.

This work supports the *democratization* of super-resolution microscopy and follows the spirit of open science, especially by providing detailed plans and open-source code particularly related to DMD-based SIM microscopy.

4 Mesoscopic fluorescence OPT

The subsection “4.3.3 Mesoscopic imaging of human liver biopsies” of this section is based in major parts on the following publication, where the instrument introduced in the following was used for image acquisition:

Kong, C., Bobe, S., Pilger, C., Lachetta, M., Øie, C. I., Kirschnick, N., Mönkemöller, V., Hübner, W., Förster C., Schüttpelz, M., Kiefer, F., Huser, T., & Schulte am Esch, J. (2021). Multiscale and Multimodal Optical Imaging of the Ultrastructure of Human Liver Biopsies. Frontiers in Physiology, 12, 149.

Having now dealt extensively with the development and application of a super-resolution SIM microscope, a swing in the opposite direction is now made to mesoscopy. From very high resolutions and very small samples, the focus now shifts to much larger (centimeter-sized) samples with moderate resolutions. Unlike mesoscopic light sheet microscopes, optical projection tomography (OPT) systems are not commercially available. Therefor custom-built OPT systems are very popular in mesocopic research [77,290]. They can be customized for the investigation of specific biomedical issues. Thus, in addition to the numerical aperture (NA), optics, filters, camera, etc. can be customized as needed. Custom-build OPT systems have been used to study neuroanatomical phenotyping of the mouse brain [245] and in Alzheimer's disease research [75], among others. In this thesis, an optical projection tomography system was built and put into operation. In addition to the optical setup, the required operating software to control the individual components was implemented. Furthermore, it required the investigation and selection of a reconstruction software to convert the acquired projections into filtered back-projections. In addition, a histogram matching algorithm was developed to match the brightness of different filtered back-projection cross sections to make them comparable with each other.

4.1 The epifluorescence OPT setup

The optical setup of our custom-made epifluorescence OPT setup (see Figure 69) is based on the OPT instrument developed by David Nguyen [74]. It differs mainly in the choice of a cost-effective high-resolution CMOS camera (Tucsen FL-20BW, instead of Hamamatsu ORCA-Flash 4.0 V2) with 20 megapixels at 2.4 µm pixel edge length. Four different LEDs with 405 nm, 470 nm, 565 nm and 625 nm as nominal wavelength are available for fluorescence excitation. The filter sets (dichroic mirror, excitation and detection filters) belonging to the LEDs or the corresponding fluorophores are installed in magnetically locked filter cubes, which can be exchanged within a few seconds. The

LEDs are also magnetically locked and can be changed similarly quickly and easily. Thus, up to four different channels can be acquired consecutively from the same sample, which can be combined into multicolor images in post-processing. The power supply to the LEDs is electronically coupled to the flash output (signaling an ongoing exposure) of the camera, so that the LED only lights up when the camera is sensitive to light. This keeps phototoxicity and photobleaching of the sample to a minimum.

Due to the internal dimensions of the sample cuvette and the size of the camera chip, the maximum sample diameter is approx. 17.5 mm. Usually, the (clarified) transparent samples are placed in an agarose cylinder, which is glued to a stamp and is magnetically held on the motorized sample rotation stage. This in turn is connected to a motorized xyz stage, which allows precise positioning along the optical axis and on the camera chip. A tip-tilt device is also built into the stage to adjust the rotation axis of the sample relative to the focal plane. A detailed component list of the setup can be found in section A.I (Table 6).

The continuously adjustable aperture diaphragm in the back focal plane (Fourier plane) allows the numerical aperture (NA) to be set and thus the depth of focus (DOF, see section 2.3.3) suitable for the size of the sample to be selected. In addition, the required telecentricity of the optical imaging system is ensured by positioning the aperture diaphragm in the back focal plane. The maximum achievable resolution without aperture diaphragm is limited to about twice the projected pixel size, i.e. a resolution of about 10 µm, due to the Nyquist-Shannon sampling theorem (eq. (31)). In practice, however, the NA must be set between 0.01 to 0.02 using the aperture stop for the appropriate DOF. This corresponds to DOF of about 10 mm down to 2.5 mm and resolutions of about 35 µm down to 12 µm. For a satisfactory signal-to-noise ratio, the captured projections are usually processed with a 2x2, 3x3 or 4x4 binning for noise reduction before processing the filtered back-projection. Due to the Nyquist-Shannon sampling theorem, the effective resolution is thus limited to about 20 µm, 30 µm or 40µm, respectively.

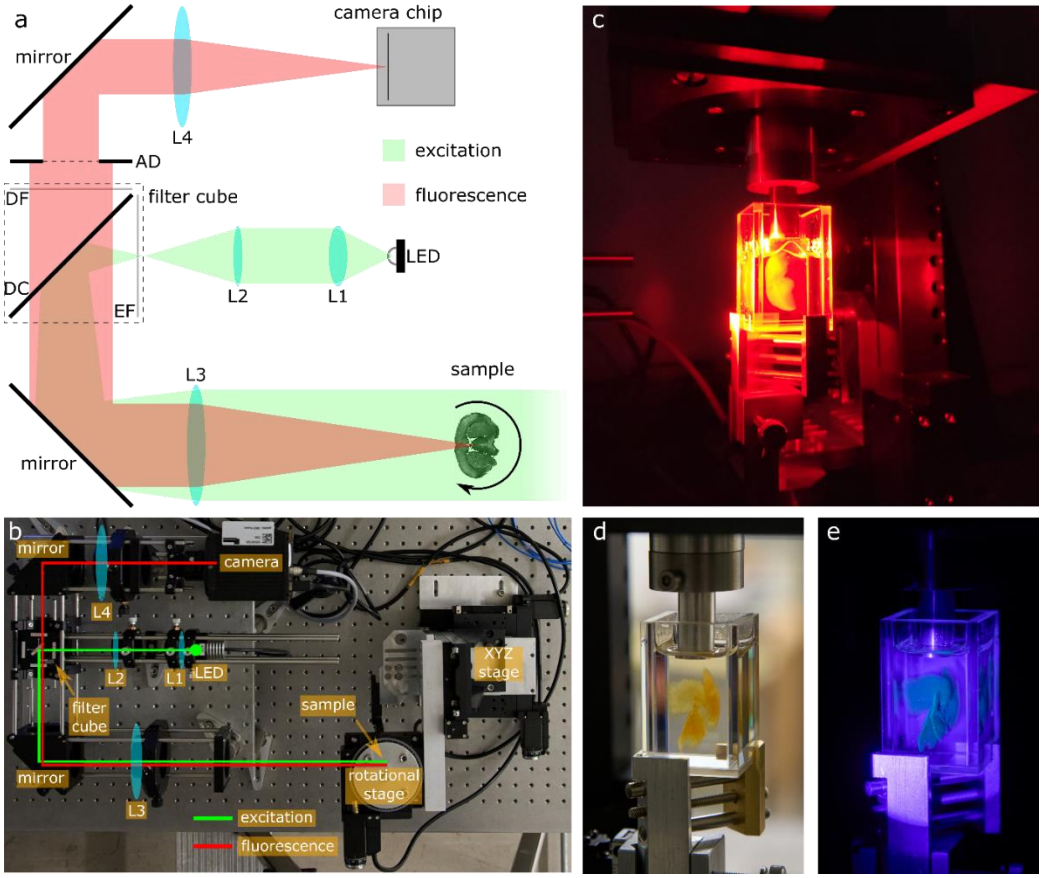

Figure 69: The fluorescence OPT setup

(a) Schematic representation of the custom-build epifluorescence OPT setup. The excitation light generated by an LED is collimated using the aspheric lens L1 and homogenized with a diffuser if required. The achromatic lens L2 and achromatic objective lens L3 expand the collimated excitation light so that the sample is illuminated as homogeneously as possible. The excitation filter (EF) and dichroic mirror (DC, reflective for excitation) located in the filter cube spectrally purify the light from the LED for ideal excitation of fluorescence. The fluorescence emitted from the sample is collected by the objective lens L3 and separated from the excitation light by the dichroic mirror (DC, transmitting for fluorescence) and spectrally purified by the detection filter (DF), both located in the filter cube. The variable aperture diaphragm in the back focal plane allows the NA to be adjusted to match the DOF to the sample size. The achromatic tube lens L4 forms a 4f configuration with the objective lens L3 and focuses the fluorescence onto the camera chip. The sample, embedded in an agarose cylinder and BABB-cleared (BABB protocol, see section A.III), is adhered to a stamp that is magnetically held to the rotation stage. The surrounding liquid is BABB which is in a glass cuvette. A detailed component list can be found in section A.I (Table 6). (b) Photo of the custom-built OPT setup. Sample (mouse liver embedded in an agarose cylinder) in the glass cuvette filled with BABB illuminated with 625 nm excitation light (c), room light (d) and 405 nm excitation light (e).

Sample alignment

Before a measurement, it must be ensured that the sample is positioned as ideally as possible. The following points should therefore be ensured before a start-up:

- Using the tip-tilt stage, the rotation axis should be oriented parallel to the pixel columns of the camera chip. If necessary, this can also be corrected in post-processing, but this leads to interpolation artifacts that reduce the quality of the projections and thus also of the filtered back-projections.
- Using the tip-tilt stage, the rotation axis should be placed parallel to the image plane. This step should be done very carefully, as it cannot be corrected in post-processing (at least with currently available reconstruction algorithms).
- Using the xyz stage, the sample should be positioned in the center of the camera chip. The smaller the sample, the more leeway is available in this step.

After each sample change, the following points should be ensured before a measurement.

- The agarose cylinder with the sample, which is glued to the stamp that is magnetically attached to the rotation stage, should be positioned manually so that the axis of rotation passes centrally through the sample or the agarose cylinder. For this purpose, the iterative comparison of acquired test projections P_0 with P_π and $P_{\pi/2}$ with $P_{3\pi/2}$ is useful.
- Using the xyz stage, the sample should be positioned so that the focal plane of the objective lens is in the center of the front half (1/4) of the sample. For this purpose, it is usually advisable to open the aperture diaphragm to the maximum, in order to obtain a focal plane that is as sharply defined as possible with a low DOF. This step should also be performed when changing the color channel, since the exact position of the focal plane can be wavelength-dependent despite achromatic optics.
- The aperture diaphragm should be adjusted before taking the projections so that the DOF (eq. (84)) is equal to half the sample diameter. Since the DOF is wavelength dependent, this step should also be performed when changing the color channel.

4.2 Software

The software needed for the fluorescence OPT setup splits into three independent parts. The first one is responsible for the acquisition of the projections. The second one is needed for the reconstruction of the acquired projections into cross sections using the filtered back-projection (see section 2.3.2). The third part is a histogram matching algorithm, which is needed to compensate the brightness fluctuations in the reconstructed cross sections.

Acquisition

Since the LED is electronically coupled to the camera, it is sufficient to integrate the camera and the rotation stage into the acquisition software. For both, corresponding adapters for µManager [284,285] are available, so it is possible to implement the acquisition process in µManager. For this purpose, a Beanshell script was developed in µManger, which alternately captures an image (projection) and rotates the rotation stage by a predefined angle. The acquired images are stored on the hard disk in parallel to the acquisition. The predefined rotation angle results from the freely selectable number of projections to be acquired. With 600 projections, for example, the rotation stage is rotated by $360°/60 = 0.6°$ between two acquisitions.

Reconstruction

Before reconstruction, it is important that the rotation axis is centered in the projections. Since corresponding existing algorithms could not be applied successfully, the rotation axis is positioned centrally by hand using Fiji. For estimating the rotation axis, the minimum and maximum intensity projections have proven to be very helpful.

To create sinograms and ultimately a filtered back-projection, the OpenCL-accelerated open-source Fiji plugin called OptiJ [291,292] has prevailed. Unfortunately, other corresponding software could not be applied by us with comparable success. OptiJ is essentially an easy-to-use implementation of the reconstruction procedure presented in Section 2.3.2 using filtered back-projection. This is presented in detail in the related publication and supplementary information [293].

Histogram matching

As already explained in section 2.3.2, the filtered back-projection often leads to massive brightness differences in the reconstructed cross sections of a stack (see Figure 70c). To overcome these, a corresponding algorithm was developed. This algorithm uses the cross-section histograms as a basis for matching the brightness. Specifically, the algorithm assumes that each cross-section histogram has a background peak (see Figure 70a) that can be separated from the signal by comparatively low gray values. It is

additionally assumed that the background of each cross-section is statistically similarly distributed. This means that the position and width of the background peak of each cross-section histogram should be approximately the same. Using a Gaussian fit, these two values can be estimated for each cross section. By shifting and stretching or compressing all cross-section histograms accordingly, the background peaks can be superimposed (see Figure 70b), whereby the differences in brightness disappear or are significantly reduced (see Figure 70d). The Java code for the developed histogram matching algorithm is open-source and freely available on GitHub [294].

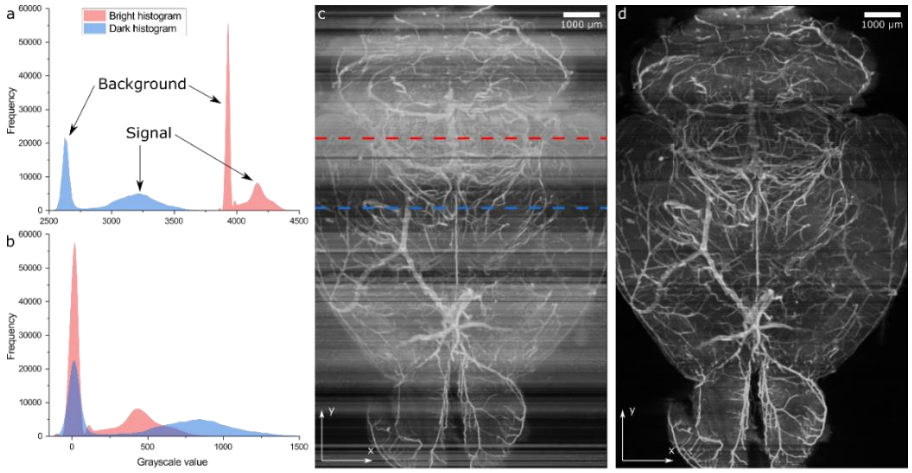

Figure 70: Histogram matching algorithm

(a) Histogram of a bright (red) and dark (blue) cross section selected from a stack reconstructed via OptiJ (c, maximum intensity projection) as an example. In general, all cross-section histograms have a background peak with significantly lower gray values than the actual signal. With the help of a Gaussian fit, the background peaks of all cross-section histograms of a stack can be aligned (b). This makes it possible to overcome the differences in brightness that occur in the cross sections of a reconstructed stack (d, maximum intensity projection). The data shown correspond to those of the mouse brain of Figure 73.

4.3 Measurements

To prove the operability of the fluorescence OPT setup, the point spread function (PSF) of the setup was first measured and compared to the calculated DOF. In a next step, artificial reference samples were measured, using TetraSpeck beads and round cells in agarose cylinders, and successfully reconstructed via filtered back-projection. The first biological measurements and reconstructions were obtained using fixed mouse organs. Finally, the first OPT images of human liver tissue were obtained and compared with light sheet images. For the acquisition of projections with the fluorescence OPT setup, exposure times of one to ten seconds have proven to be recommended, depending on the sample and the aperture opening. All filtered back-projections shown in this section were created using 600 acquired projections.

4.3.1 Reference samples

For the fluorescence OPT setup to operate as desired, it is important that the PSF in the region of the calculated depth-of-field (DOF) approximates a straight line parallel to the optical axis (z-axis). Otherwise, the acquired projections would not satisfy the Radon transform, which is a basic requirement for the reconstruction algorithm, the filtered back projection. To ensure this, the PSF with and without aperture was measured and compared with the DOF calculated accordingly (see Figure 71). The measured PSFs correspond exactly to the desired and expected behavior, so the setup can be considered ready for projection acquisition.

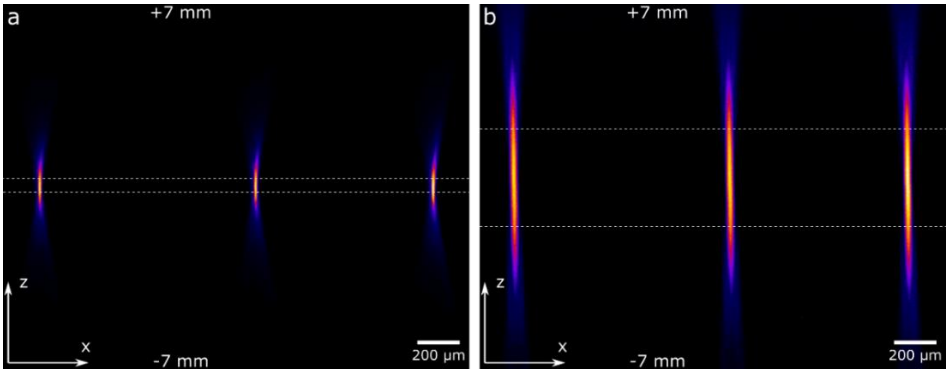

Figure 71: Point spread function for projections

PSF (maximum intensity projection) of the epi-fluorescence OPT setup of 4 µm TetraSpeck beads (1:1000 dilution dried on a coverslip) at 625 nm excitation. (a) PSF without aperture diaphragm, corresponding to an aperture diameter of about 25 mm, i.e. a NA of 0.042 and a DOF of 0.5 mm. (b) PSF with aperture diaphragm with a diameter of 9 mm, i.e. a NA of 0.015, corresponding to a DOF of 3.8 mm. The white dashed lines mark the range of the DOF in which the PSF can be approximated as a line, as required for acquiring projections. By inserting/closing the aperture, the PSF can be stretched as expected and thus the DOF can be adjusted to the sample size. The underlying measurements were performed by Jasmin Schürstedt with a step size of 40 µm along the optical axis [295].

Before measuring biological samples, it was necessary to gain experience with reference samples. These can be prepared easily, quickly and as often as required without the need for a sample donor animal. First, 4 µm TetraSpeck beads were dissolved in agarose cylinders and cleared according to the BABB protocol (section A.III) and stored in BABB (benzyl alcohol and benzyl benzoate in a 1:2 ratio). It was noticed here that BABB bleached or destroyed the TetraSpeck beads. Dehydration with methanol alone resulted in the agarose cylinder no longer adhering to the stamp. Thus, we ultimately stored the beads in the agarose cylinder in water and neither dehydrated nor clarified them. However, since acquisitions of biological samples usually take place in BABB as the surrounding medium and the beads are to serve as a reference sample, they were measured in BABB (Figure 72a). Due to the optical interface effects that occur as a result

of the refractive index differences between the agarose and the BABB, the beads, which are actually point-shaped, appear arrowhead-shaped with increasing distance from the center of rotation. For this reason, TetraSpeck beads are not really suitable for making reference samples for optical projection tomography.

Small (10 µm - 15 µm) trypsonized (rounded) U2OS cells have emerged as a promising alternative to TetraSpeck beads. These can be stained with appropriate fluorophores and dissolved in an agarose cylinder. The agarose cylinder containing the cells can then be dehydrated and clarified using the BABB protocol. As can be seen in Figure 72b, the undesirable effects that occur with unclarified samples do not occur here. Reference samples prepared in this manner have proven to be a much better tool for verifying the operation of the fluorescence OPT setup. The prerequisites for high quality images of biological samples can now be considered to be given.

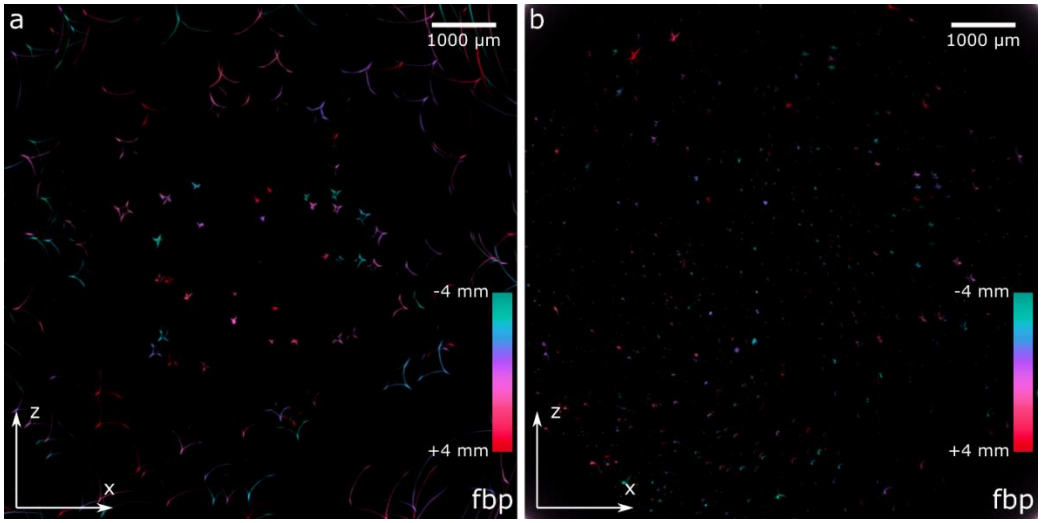

Figure 72: Filtered back-projection of synthetic reference samples

Depth-color-coded filtered back-projection of approximate point-shaped (below resolution limit of approx. 20 µm) fluorescence emitters, excited at 625 nm, randomly distributed in an agarose cylinder and serving as a reference sample for OPT imaging in BABB. Color coding indicates the y position of the emitters according to the color scale. (a) 4 µm TetraSpeck beads dissolved in an agarose cylinder previously stored in water. The arrowhead-shaped appearance of the actually point-shaped beads, which becomes more and more obvious towards the outside, is due to the refractive index difference at the interface between the agarose cylinder and BABB. (b) Fixed, trypsinized (rounded) and Syto 16 stained U2OS cells (10 µm - 15 µm) dissolved in an agarose cylinder, cleared according to the BABB protocol (section A.III). The arrowhead-shaped artifacts do not appear here because the refractive index of the sample was adjusted to that of the surrounding medium (BABB) by clearing. During clarification, the TetraSpeck beads bleach out or are destroyed. Therefore, trypsonized (rounded) cells are much better suited as reference samples for acquisitions in BABB. The acquisition of the underlying projections was performed by Jasmin Schürstedt [295].

4.3.2 Mouse organs

After the successful measurement and reconstruction of reference samples, the next step was to do the same with biological samples. In this specific case, fixed mouse organs cleared according to the BABB protocol (section A.III) were provided by Stefanie Bobe from the Max Planck Institute for Molecular Biomedicine in Münster. The MPI in Münster has great expertise in sample preparation, especially in clarifying tissues [296]. Specific staining of the samples was omitted, as the priority was to ensure the compatibility of the fluorescence OPT setup with biological samples. Thus, it could be excluded that any problems that might occur were related to staining. Figure 73 shows the results of the measurements as projections and cross-sections (reconstructions) of the mouse organs (brain, heart, kidney, and liver). The resolutions achieved are between 45 µm and 68 µm with acceptable to very good signal-to-noise ratios. Based on the successful measurement and reconstruction of the mouse organs, we were able to demonstrate compatibility with biological samples of appropriate quality.

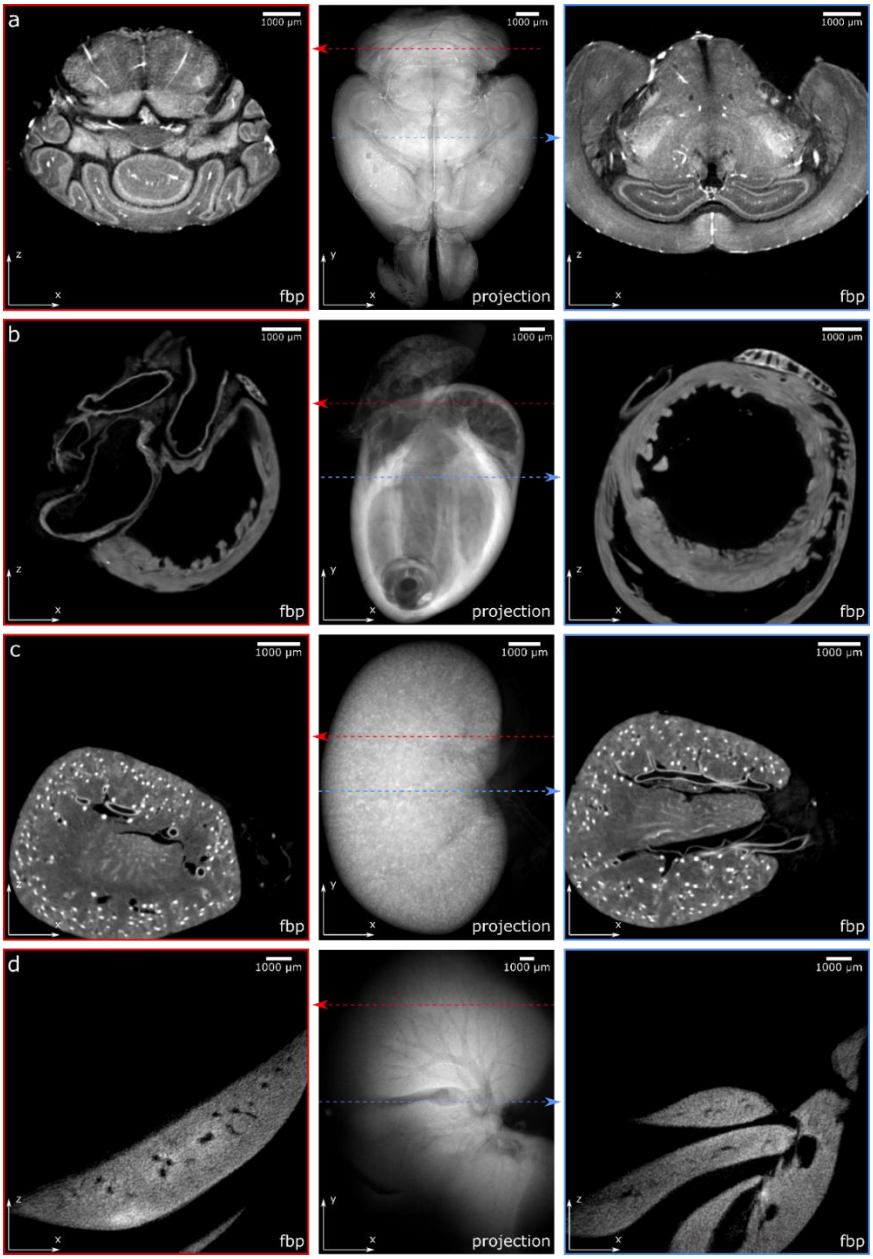

Figure 73: OPT measurements of autofluorescent mouse organs

In each row, one of the 600 recorded projections is shown in the center and two reconstructed cross-sections using filtered back-projection (fbp) are shown on the left and right of: Clarified (a) brain, (b) heart, (c) kidney, and (d) liver. Due to the lack of autofluorescence within the blood vessels, they can be well detected in the fbp. In some cases (especially in the liver), they can also be seen in the projections. Sample diameters are approximately 9 mm (a), 7.5 mm (b-c), and 17 mm (d). Accordingly, images were acquired with apertures of 8 mm (a), 9 mm (b-c) and 6 mm (d) diameter, corresponding to resolutions of 50 µm, 45 µm and 68 µm, respectively. For this reason, 4x4 binning could be applied without loss of resolution. The signal-to-noise ratio of (a-c) is very good, while it is noticeably weaker for (d) due to the smaller aperture opening.

4.3.3 Mesoscopic imaging of human liver biopsies

The liver is one of the largest organs in the human body and consists of complex macroscopic and microscopic structures. Structural sizes range from a few centimeters (liver lobes) down to the nanometer scale (fenestrations of sinusoidal endothelial cells, LSECs). Imaging these requires a whole zoo of optical imaging techniques (light sheet, OPT, confocal, SRS, CARS, SHG, SIM). Optical projection tomography (OPT) and light sheet microscopy are particularly useful for revealing mesoscopic structures in the millimeter range. Due to the strong absorption and scattering of visible light, the optical penetration depth is only about 0.5 mm, which is why clarification of the tissue is mandatory for mesoscopic images. In this context, the fluorescence OPT setup was successfully applied for the first time in scientific biomedical applications. Moreover, a direct comparison with light sheet images from the same sample was possible.

Two PFA-fixed tissue samples from a liver biopsy of an elderly patient of the Protestant Hospital of Bethel Foundation serve as samples. These were prepared by Stefanie Bobe of the Max Planck Institute for Molecular Biomedicine in Münster for light sheet and OPT imaging. For this purpose, whole-mount staining was performed. Here, smooth muscle actin (pericytes surrounding blood vessels) was stained with anti-αSMA-Cy3 and cytokeratin 19 (bile ducts) was stained using an anti-cytokeratin-19 primary antibody in combination with an Alexa647-coupled secondary antibody. Subsequently, both samples were each enclosed in a cylinder of 1% low melting agarose and dehydrated and cleared using the BABB protocol (section A.III).

Due to the sample size of approx. 3x3x5 mm^3, an aperture diameter of 12 mm was selected for the OPT images, which corresponds to a depth-of-focus (DOF) of approx. 2 mm. The Cy3 (walls of blood vessels, 565 nm excitation) and Alexa647 (bile ducts, 625 nm excitation) channels were imaged sequentially, each with 600 projections each in 0.6° rotation steps. The results are shown in Figure 74. In addition to autofluorescence, the background in the Cy3 channel, which cannot be overlooked, is due to the fact that the liver, and thus the entire sample, is permeated by blood vessels. Nevertheless, the path of the blood vessels and bile ducts can be traced well. For this purpose, we recommend a look at the videos deposited in our associated publication [9].

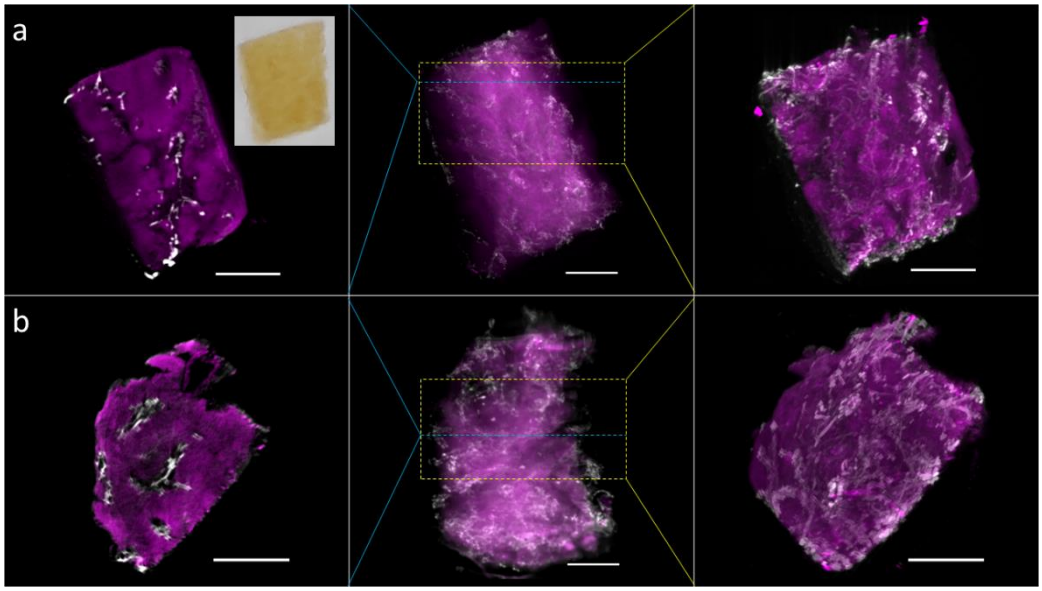

Figure 74: Fluorescence OPT measurements of the human liver biopsies

(a) and (b) are two different liver biopsies obtained from the same patient, each covering a volume of approximately 3 mm × 3 mm × 5 mm. The images in the center column panels are projections of the fluorescence from the entire sample. The images in the left panels show single cross sections that were reconstructed via filtered back-projection at the regions indicated by the blue dashed lines in each row. The images in the right panels are projections of a stack of cross sections, the extent of which is indicated by the yellow dashed box. The samples were stained with antibodies against a smooth muscle actin identifying smooth muscle cells (magenta) and cytokeratin 19 identifying bile ducts (white) and subsequently cleared following the BABB protocol (section A.III). The inset in the upper left panel shows a photograph of the optically cleared liver sample in BABB. Scale bars are 1 mm. Figure taken from our corresponding publication [9].

Before the OPT images were taken, the samples had already been measured by Stefanie Bobe on the commercial UltraMicroscope II (LaVision BioTec). For this purpose, magnifications of 1.6 to 5 times and a step size of 2 µm were used. Figure 75 compares a reconstructed OPT cross-section with the same acquired cross-section from the light sheet microscope. It is noticeable that the quality and resolution of the light sheet images are appreciable better than those from the OPT. On the one hand, this is since the OPT setup is basically intended for measuring larger samples, because it can only demonstrate its potential with samples that are too large for light sheet images (larger than the working distance of the objective). On the other hand, it must be noted that due to the comparatively small sample, it was not possible to position the focal plane precisely in the center of the front half of the sample, which leads to a comprehensible decrease in the quality and resolution of the acquired and reconstructed images. Unfortunately, since the glue used to adhere the agarose cylinder gradually damaged the sample, the number of possible corrections to the focal plane was severely limited.

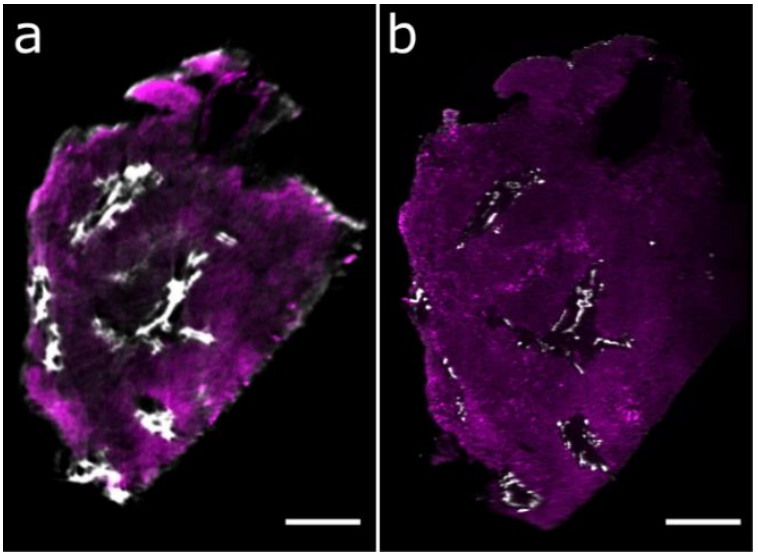

Figure 75: Optical projection tomography vs light sheet microscopy

Comparison of liver volumes imaged by optical projection tomography (a) and light sheet microscopy (b). Optical sections of the same wholemount immunostained liver biopsy (for antibodies and colors also see Figure 74) were acquired with both optical projection tomography (a) and light sheet microscopy (b). Image stacks were visualized using the volume rendering software package Voreen. Subsequently, rendered volumes were digitally oriented such that the sectional planes were approximately matching and virtually isolated, thin optical section corresponding to 9.6 µm (a) and 5 µm (a) are shown for direct comparison. Scale bars represent 500 µm. Figure taken from our corresponding publication [9].

Whether mesoscopic volumetric imaging is performed with optical projection tomography or light sheet microscopy, it has a major advantage over section-based approaches. When imaging a three-dimensional volume, the amount of tissue examined is significantly greater than with two-dimensional sections. Rare events or anomalies that occur in a sample are thus much more likely to be detected. In addition, it is possible to digitally reorient the acquired or reconstructed 3D datasets as desired, providing the ability to analyze structures and anatomy of the whole sample in arbitrary directions and virtual sections, which is not possible with section-based approaches.

4.3.4 Summary and outlook

Optical projection tomography (OPT) represents an important method in the zoo of visible light mesoscopic imaging techniques for the examination of samples approximately one centimeter in size. While light sheet microscopy is usually limited in sample size by the working distance of the imaging objective, OPT can play to its strengths here. As part of this thesis, a custom-made fluorescence OPT setup was successfully built and put into operation. The optical setup is based on that of David Nguyen [74]. As operating software for recording the raw data (projections) µManager with a custom developed Beanshell script is used. The open-source Fiji plugin OptiJ is used to reconstruct sample cross sections using filtered back-projection [293]. The reconstructed cross-section stacks exhibit disturbing brightness variations, which are compensated using a histogram matching algorithm developed for this purpose.

To ensure the proper function and quality of the fluorescence OPT setups, images of artificial reference samples and consecutively fixed mouse organs (brain, heart, kidney, liver) were successfully obtained. Subsequently, in the context of our publication [9], images of human liver tissue of approx. 45 mm^3 in size were taken in which the structure and anatomy of the blood vessels and bile ducts could be traced. These could also be compared with light sheet images of the same sample. The strength of volumetric images from mesocopic techniques such as OPT and light sheet microscopy over section-based approaches came into its own here, particularly for tracing three-dimensional anatomical structures.

Within the scope of Jasmin Schürstedt's master thesis [295] and beyond, projects around the fluorescence OPT setup are being continued. Some successes have already been achieved. For example, the setup was extended by a mesoscopic light sheet illumination (Figure 76a,b), which allows both OPT and light sheet images to be taken from the same sample. Although the light sheet images have lower z resolution along the optical axis than the OPT images, they have better lateral xy resolution and do not require reconstruction. In addition, human nasal mucosa and nasal polyps are examined (Figure 76c). The focus here is primarily on optimizing sample preparation (staining and clearing), which should ultimately provide new insights into the anatomy of the tissue. Similar projects are also being carried out in connection with mouse organs and mouse embryos (Figure 76d). In addition, the detection optics of the setup is being further developed with the aim of being able to variably adapt the magnification to the sample size. This will allow a consistent quality of the images independent of the sample size (approx. 3 mm - 18 mm), so that the problems encountered in section 4.3.3 due to the small samples can be avoided.

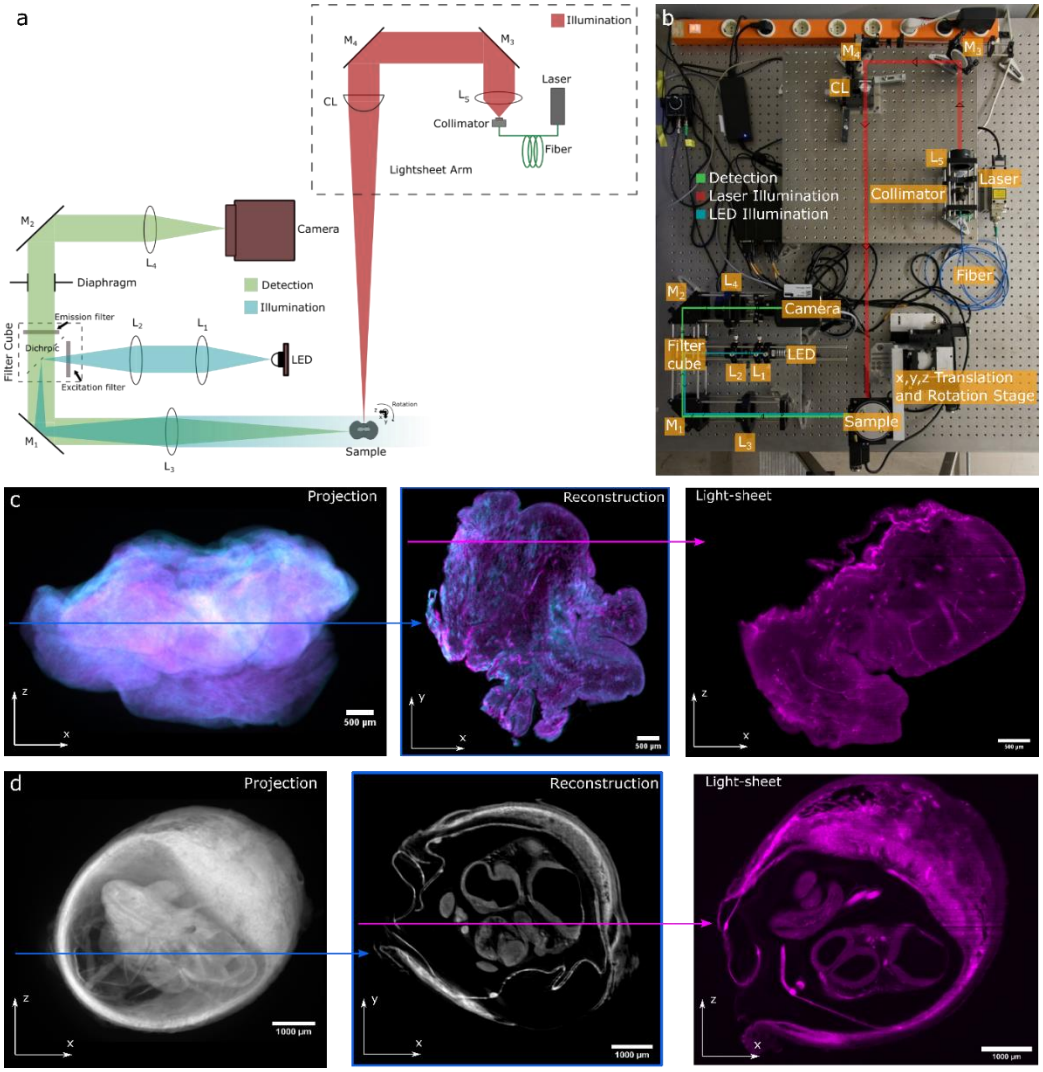

Figure 76: Summary illustration of the OPT projects beyond this thesis

Schematic drawing (a) and photo (b) of the setup from Figure 69 extended by mesoscopic light sheet illumination. (c) OPT and light sheet acquisitions of a nasal polyp, the endothelium (Alexa647 antibody staining) in magenta and the cell nuclei (Cyto 16 staining) in cyan. (d) OPT and light sheet acquisitions of a mouse embryo without staining, i.e. autofluorescence, at 565 nm excitation in gray (OPT) and 643 nm excitation in magenta (light sheet). Figure data courtesy of Jasmin Schürstedt [295].

Building on this thesis and the work of Jasmin Schürstedt, there are some algorithmic and software enhancements that could be made to the fluorescence OPT setup. Currently, the rotation axis in the recorded projection stack is still determined manually using maximum and minimum intensity projections in Fiji. This could and should be done by an algorithm in the future. For this purpose, iterative approaches in which the variance in the filtered back-projection is minimized or correlation-based approaches

are possible. During the recording process, it occasionally happens that the sample moves, e.g. because the glue becomes slightly loose. In this case, it would be advantageous to be able to correct or calculate out this movement using an appropriate algorithm. The reconstruction software, the Fiji plugin OptiJ [293], only supports projections with a certain maximum width with OpenCL acceleration, otherwise it crashes. It would be desirable to fix this bug. Another interesting future project could be the development of an algorithm that uses both projections and light sheet images as raw data to reconstruct higher quality cross sections.

This work supports the *democratizing* of optical projection tomography and follows the spirit of open science, especially by providing detailed blueprints and open-source code.

5 Conclusion and outlook

In this thesis, a super-resolution and a mesoscopic imaging technique of fluorescence microscopy have been experimentally realized and successfully applied to biomedical applications, such as imaging transport processes in individual osteosarcoma cells and revealing the ultrastructure of the human liver [8,9]. Among others, these techniques aim to provide a basis for the discovery of new biological insights and mechanisms. In the future, further biological and biomedical research will be enabled by these systems.

The first main topic of this thesis is super-resolution structured illumination microscopy (SIM), based on a digital micromirror device (DMD). The goal was to overcome the problematic blazed grating effect (BGE) in order to build a fast yet cost-efficient two-beam SIM microscope. To investigate and understand the BGE, a mathematical model of coherent light (laser) propagation, interacting with the DMD surface was developed. From this model, four different computational approaches can be derived, each with different system conditions and computational complexity. These were transferred to (partially GPU-accelerated) computer simulations. This in-depth modelling of the DMD enabled the design and construction of a fast (60 super-resolved fps) one-color DMD-SIM microscope (532 nm excitation). By evaluating further simulation results, solutions to the multi-color problem with DMDs were found. These allowed to extent the one-color DMD SIM system to a dual-color DMD-SIM microscope (473 nm & 631 nm excitation), and its successful application confirmed the solutions found in the simulations. Both, the one-color and the dual-color system were successfully tested and applied to several measurements of artificial reference samples and biological samples. For the latter, the actin skeleton, lysosomes, mitochondria, endoplasmic reticulum, and membranes of (living) U2OS, and HEK293T cells, were imaged with super-resolution. The system is operated with the fairSIM-VIGOR software [63], which has been extended for compatibility with DMD-based SIM systems. More precisely, interfaces were developed and implemented to integrate the DMD into the architecture of the control software. Likewise, microsecond-accurate timing sequences were developed on a microcontroller to control the individual components. In addition, a concept and file format for storing and processing the important metadata of SIM raw data was developed and implemented.

The DMD-based SIM microscope is currently in an experimental state and will be developed from a prototype to a more stable system on the level of opto-mechanics, usable for day-to-day biomedical applications, in the foreseeable future. Ideas and suggestions for this are already available from other custom-made SIM microscopes [283]. An extension of the system to three colors is also being considered, based on the simulation results. Its experimental implementation has already been demonstrated by

Brown et al. [270]. Due to their (nearly) polarization preserving properties, DMDs are also particularly interesting for the realization of (three-dimensional) three-beam SIM. With the help of a Pockels cell, the polarization in front of the DMD could be aligned accordingly, so that subsequent polarization optics (e.g. pizza-polarizer) could be dispensed with. The main advantage here would be that the polarization of the central beam would have the desired polarization, while the use of a Pockels cell provides high speed and low cost, unlike other active polarization controlling methods. For acquiring super-resolution three-dimensional image stacks, the integration of an electronically controllable xyz stage would be obligatory of course. Beyond the technical improvements mentioned above, the DMD-SIM microscope is to be used increasingly on ongoing research projects in the future, for example the investigation of intracellular molecular dynamics.

The second main topic of this thesis is mesoscopic imaging by optical projection tomography (OPT), which is considered to be the optical counterpart of X-ray computed tomography. Based on a system developed by David Nguyen [74], a fluorescence OPT setup for centimeter-sized, optically cleared samples was successfully built and applied. The main difference is the use of a cost-effective high-resolution CMOS camera (Tucsen FL-20BW), instead of a much more expensive sCMOS camera (Hamamatsu ORCA-Flash 4.0 V2). Quality and functionality were demonstrated by measurements on artificial reference samples and mouse organs (brain, heart, kidney, and liver). Imaging of the anatomical structure of human liver tissue was the first biomedical application of the fluorescence OPT setup. Beyond the scope of this thesis, the system was successfully further developed and applied to the study of nasal polyps and mouse embryos [295].

The fluorescence OPT setup is in constant development and application. It has already been successfully extended beyond the scope of this thesis to include light sheet illumination [295]. Likewise, the conversion of the detection optics with variable magnification is in progress. Furthermore, biomedical applications with human nasal polyps, mouse embryos and mouse organs (brain and spleen) are in progress and planned. Here, the focus is on three-dimensional volumetric imaging of anatomical structures as well as optimization of sample preparation (staining and clearing). The development of new algorithms among others for reconstruction is also pending. This should have fewer requirements for the acquisition of the raw images so that on the one hand the sensitive positioning of the rotation axis allows more tolerance and on the other hand the boundary condition of the projection over line integrals (Radon transform), is softened. This would lead to the advantage that the depth of focus (DOF) would no longer have to be extended over the sample radius, whereby a higher numerical aperture (NA) could be selected which ultimately results in a higher resolution. Such a reconstruction algorithm could use projections (OPT raw images) and/or light sheet images as raw data.

Both microscopy systems developed in the course of this thesis, the DMD-based SIM and the OPT, have been thoroughly documented. Besides their accompanying scientific publications [8,9,63,64,92], system blueprints and open-source software for both systems are freely available. This follows the spirit of open science and the ongoing efforts to *democratize* fluorescence microscopy. The presented results leave the scientific community with a cost-effective yet high performance basis for biomedical research applied in future. Both, on the sub-wavelength length scales of super-resolution SIM microscopy and on the mesoscopic level of optical projection tomography.

Bibliography

1. P. P. M. A. Antony, C. Trefois, A. Stojanovic, A. S. Baumuratov, and K. Kozak, "Light microscopy applications in systems biology: opportunities and challenges," Cell Communication and Signaling **11**(1), 24 (2013).
2. "Fundamentals of Light Microscopy," in *Fundamentals of Light Microscopy and Electronic Imaging* (John Wiley & Sons, Ltd, 2012), pp. 1–19.
3. A. V. Helden, S. Dupré, and R. van Gent, *The Origins of the Telescope* (Amsterdam University Press, 2010).
4. *Reading the Book of Nature in the Dutch Golden Age, 1575-1715* (BRILL, 2010).
5. *Lesen Sie Men of Physics: Galileo Galilei, His Life and His Works von Raymond J. Seeger | Bücher* (n.d.).
6. R. Hooke, *Micrographia* (BoD – Books on Demand, 2020).
7. K. Thorn, "A quick guide to light microscopy in cell biology," MBoC **27**(2), 219–222 (2016).
8. A. Sandmeyer, M. Lachetta, H. Sandmeyer, W. Hübner, T. Huser, and M. Müller, "Cost-Effective Live Cell Structured Illumination Microscopy with Video-Rate Imaging," ACS Photonics **8**(6), 1639–1648 (2021).
9. C. Kong, S. Bobe, C. Pilger, M. Lachetta, C. I. Øie, N. Kirschnick, V. Mönkemöller, W. Hübner, C. Förster, M. Schüttpelz, F. Kiefer, T. Huser, and J. Schulte am Esch, "Multiscale and Multimodal Optical Imaging of the Ultrastructure of Human Liver Biopsies," Frontiers in Physiology **12**, 149 (2021).
10. E. Abbe, "Beiträge zur Theorie des Mikroskops und der mikroskopischen Wahrnehmung," Archiv f. mikrosk. Anatomie **9**(1), 413–468 (1873).
11. O. Schulz, C. Pieper, M. Clever, J. Pfaff, A. Ruhlandt, R. H. Kehlenbach, F. S. Wouters, J. Großhans, G. Bunt, and J. Enderlein, "Resolution doubling in fluorescence microscopy with confocal spinning-disk image scanning microscopy," PNAS **110**(52), 21000–21005 (2013).
12. S. Gajghate, "Introduction to Microscopy," (November 8, 2017).
13. "The Nobel Prize in Chemistry 2008," https://www.nobelprize.org/prizes/chemistry/2008/summary/.
14. W. Rettig, B. Strehmel, S. Schrader, and H. Seifert, *Applied Fluorescence in Chemistry, Biology and Medicine* (Springer Science & Business Media, 2012).
15. I. Pavlova, M. Williams, A. El-Naggar, R. Richards-Kortum, and A. Gillenwater, "Understanding the Biological Basis of Autofluorescence Imaging for Oral Cancer Detection: High-Resolution Fluorescence Microscopy in Viable Tissue," Clin Cancer Res **14**(8), 2396–2404 (2008).
16. D. J. Stephens and V. J. Allan, "Light Microscopy Techniques for Live Cell Imaging," Science **300**(5616), 82–86 (2003).
17. C. F. Pereira, J. Rossy, D. M. Owen, J. Mak, and K. Gaus, "HIV taken by STORM: Super-resolution fluorescence microscopy of a viral infection," Virology Journal **9**(1), 84 (2012).

18. W. J. Godinez, M. Lampe, S. Wörz, B. Müller, R. Eils, and K. Rohr, "Deterministic and probabilistic approaches for tracking virus particles in time-lapse fluorescence microscopy image sequences," Medical Image Analysis **13**(2), 325–342 (2009).
19. J. Pawley, ed., *Handbook of Biological Confocal Microscopy*, 3rd ed. (Springer US, 2006).
20. J. Melngailis, "Focused ion beam technology and applications," Journal of Vacuum Science & Technology B: Microelectronics Processing and Phenomena **5**(2), 469–495 (1987).
21. D. G. Robinson, U. Ehlers, R. Herken, B. Herrmann, F. Mayer, and F.-W. Schürmann, "An Introduction to Electron Microscopy (EM)," in *Methods of Preparation for Electron Microscopy: An Introduction for the Biomedical Sciences*, D. G. Robinson, U. Ehlers, R. Herken, B. Herrmann, F. Mayer, and F.-W. Schürmann, eds. (Springer, 1987), pp. 1–21.
22. F. J. Giessibl, "Advances in atomic force microscopy," Rev. Mod. Phys. **75**(3), 949–983 (2003).
23. S. Jadavi, P. Bianchini, O. Cavalleri, S. Dante, C. Canale, and A. Diaspro, "Correlative nanoscopy: A multimodal approach to molecular resolution," Microscopy Research and Technique **84**(10), 2472–2482 (2021).
24. C. Loussert Fonta and B. M. Humbel, "Correlative microscopy," Archives of Biochemistry and Biophysics **581**, 98–110 (2015).
25. K. Narayan, C. M. Danielson, K. Lagarec, B. C. Lowekamp, P. Coffman, A. Laquerre, M. W. Phaneuf, T. J. Hope, and S. Subramaniam, "Multi-resolution correlative focused ion beam scanning electron microscopy: Applications to cell biology," Journal of Structural Biology **185**(3), 278–284 (2014).
26. S. Modrow, D. Falke, U. Truyen, and H. Schätzl, *Molekulare Virologie*, 3rd ed. (Springer Spektrum, 2010).
27. B. Alberts, A. D. Johnson, J. Lewis, D. Morgan, M. Raff, K. Roberts, and P. Walter, *Molekularbiologie der Zelle* (John Wiley & Sons, 2017).
28. L. Schermelleh, A. Ferrand, T. Huser, C. Eggeling, M. Sauer, O. Biehlmaier, and G. P. C. Drummen, "Super-resolution microscopy demystified," Nat Cell Biol **21**(1), 72–84 (2019).
29. "The Nobel Prize in Chemistry 2014 summary," https://www.nobelprize.org/prizes/chemistry/2014/summary/.
30. S. W. Hell and J. Wichmann, "Breaking the diffraction resolution limit by stimulated emission: stimulated-emission-depletion fluorescence microscopy," Opt. Lett., OL **19**(11), 780–782 (1994).
31. M. Sauer and M. Heilemann, "Single-Molecule Localization Microscopy in Eukaryotes," Chem. Rev. **117**(11), 7478–7509 (2017).
32. H. Deschout, F. C. Zanacchi, M. Mlodzianoski, A. Diaspro, J. Bewersdorf, S. T. Hess, and K. Braeckmans, "Precisely and accurately localizing single emitters in fluorescence microscopy," Nat Methods **11**(3), 253–266 (2014).

33. M. G. L. Gustafsson, "Surpassing the lateral resolution limit by a factor of two using structured illumination microscopy.," Journal of Microscopy **198**(2), 82–87 (2000).
34. M. G. L. Gustafsson, L. Shao, P. M. Carlton, C. J. R. Wang, I. N. Golubovskaya, W. Z. Cande, D. A. Agard, and J. W. Sedat, "Three-Dimensional Resolution Doubling in Wide-Field Fluorescence Microscopy by Structured Illumination," Biophysical Journal **94**(12), 4957–4970 (2008).
35. S. W. Hell, S. J. Sahl, M. Bates, X. Zhuang, R. Heintzmann, M. J. Booth, J. Bewersdorf, G. Shtengel, H. Hess, P. Tinnefeld, A. Honigmann, S. Jakobs, I. Testa, L. Cognet, B. Lounis, H. Ewers, S. J. Davis, C. Eggeling, D. Klenerman, K. I. Willig, G. Vicidomini, M. Castello, A. Diaspro, and T. Cordes, "The 2015 super-resolution microscopy roadmap," J. Phys. D: Appl. Phys. **48**(44), 443001 (2015).
36. C. G. Galbraith and J. A. Galbraith, "Super-resolution microscopy at a glance," Journal of Cell Science **124**(10), 1607–1611 (2011).
37. Y. M. Sigal, R. Zhou, and X. Zhuang, "Visualizing and discovering cellular structures with super-resolution microscopy," Science **361**(6405), 880–887 (2018).
38. S. Hell, K. Willig, M. Dyba, S. Jakobs, L. Kastrup, and V. Westphal, "Nanoscale resolution with focused light: STED and other RESOLFT microscopy concepts," Handbook of biological confocal microscopy, 571-579 (2006) (2006).
39. H. Singh, R. Lu, P. F. G. Rodríguez, Y. Wu, J. C. Bopassa, E. Stefani, and L. Toro, "Visualization and quantification of cardiac mitochondrial protein clusters with STED microscopy," Mitochondrion **12**(2), 230–236 (2012).
40. C. A. Wurm, D. Neumann, R. Schmidt, A. Egner, and S. Jakobs, "Sample Preparation for STED Microscopy," in *Live Cell Imaging: Methods and Protocols*, D. B. Papkovsky, ed., Methods in Molecular Biology (Humana Press, 2010), pp. 185–199.
41. R. M. Dickson, A. B. Cubitt, R. Y. Tsien, and W. E. Moerner, "On/off blinking and switching behaviour of single molecules of green fluorescent protein," Nature **388**(6640), 355–358 (1997).
42. I. M. Khater, I. R. Nabi, and G. Hamarneh, "A Review of Super-Resolution Single-Molecule Localization Microscopy Cluster Analysis and Quantification Methods," Patterns **1**(3), 100038 (2020).
43. S. T. Hess, T. P. K. Girirajan, and M. D. Mason, "Ultra-High Resolution Imaging by Fluorescence Photoactivation Localization Microscopy," Biophysical Journal **91**(11), 4258–4272 (2006).
44. M. J. Rust, M. Bates, and X. Zhuang, "Sub-diffraction-limit imaging by stochastic optical reconstruction microscopy (STORM)," Nat Methods **3**(10), 793–796 (2006).
45. M. Heilemann, S. van de Linde, M. Schüttpelz, R. Kasper, B. Seefeldt, A. Mukherjee, P. Tinnefeld, and M. Sauer, "Subdiffraction-Resolution Fluorescence Imaging with Conventional Fluorescent Probes," Angewandte Chemie International Edition **47**(33), 6172–6176 (2008).

46. S. van de Linde, A. Löschberger, T. Klein, M. Heidbreder, S. Wolter, M. Heilemann, and M. Sauer, "Direct stochastic optical reconstruction microscopy with standard fluorescent probes," Nat Protoc **6**(7), 991–1009 (2011).
47. R. Heintzmann and C. G. Cremer, "Laterally modulated excitation microscopy: improvement of resolution by using a diffraction grating," in I. J. Bigio, H. Schneckenburger, J. Slavik, K. Svanberg, and P. M. Viallet, eds. (Proc. SPIE, 1999), **3568**, pp. 185–196.
48. J. Demmerle, C. Innocent, A. J. North, G. Ball, M. Müller, E. Miron, A. Matsuda, I. M. Dobbie, Y. Markaki, and L. Schermelleh, "Strategic and practical guidelines for successful structured illumination microscopy," Nat Protoc **12**(5), 988–1010 (2017).
49. L. Reymond, L. Reymond, J. Ziegler, C. Knapp, F.-C. Wang, T. Huser, V. Ruprecht, V. Ruprecht, and S. Wieser, "SIMPLE: Structured illumination based point localization estimator with enhanced precision," Opt. Express, OE **27**(17), 24578–24590 (2019).
50. J. Cnossen, T. Hinsdale, R. Ø. Thorsen, M. Siemons, F. Schueder, R. Jungmann, C. S. Smith, B. Rieger, and S. Stallinga, "Localization microscopy at doubled precision with patterned illumination," Nat Methods **17**(1), 59–63 (2020).
51. L. Gu, Y. Li, S. Zhang, Y. Xue, W. Li, D. Li, T. Xu, and W. Ji, "Molecular resolution imaging by repetitive optical selective exposure," Nat Methods **16**(11), 1114–1118 (2019).
52. E. H. Rego, L. Shao, J. J. Macklin, L. Winoto, G. A. Johansson, N. Kamps-Hughes, M. W. Davidson, and M. G. L. Gustafsson, "Nonlinear structured-illumination microscopy with a photoswitchable protein reveals cellular structures at 50-nm resolution," PNAS **109**(3), E135–E143 (2012).
53. K. C. Gwosch, J. K. Pape, F. Balzarotti, P. Hoess, J. Ellenberg, J. Ries, and S. W. Hell, "MINFLUX nanoscopy delivers 3D multicolor nanometer resolution in cells," Nat Methods **17**(2), 217–224 (2020).
54. C. Eggeling, C. Ringemann, R. Medda, G. Schwarzmann, K. Sandhoff, S. Polyakova, V. N. Belov, B. Hein, C. von Middendorff, A. Schönle, and S. W. Hell, "Direct observation of the nanoscale dynamics of membrane lipids in a living cell," Nature **457**(7233), 1159–1162 (2009).
55. S. J. Sahl, M. Leutenegger, M. Hilbert, S. W. Hell, and C. Eggeling, "Fast molecular tracking maps nanoscale dynamics of plasma membrane lipids," PNAS **107**(15), 6829–6834 (2010).
56. J. Tønnesen, G. Katona, B. Rózsa, and U. V. Nägerl, "Spine neck plasticity regulates compartmentalization of synapses," Nat Neurosci **17**(5), 678–685 (2014).
57. S. W. Hell and M. Kroug, "Ground-state-depletion fluorscence microscopy: A concept for breaking the diffraction resolution limit," Appl. Phys. B **60**(5), 495–497 (1995).

58. T. Dertinger, R. Colyer, G. Iyer, S. Weiss, and J. Enderlein, "Fast, background-free, 3D super-resolution optical fluctuation imaging (SOFI)," PNAS **106**(52), 22287–22292 (2009).
59. M. G. L. Gustafsson, "Nonlinear structured-illumination microscopy: Wide-field fluorescence imaging with theoretically unlimited resolution," PNAS **102**(37), 13081–13086 (2005).
60. L. Schermelleh, R. Heintzmann, and H. Leonhardt, "A guide to super-resolution fluorescence microscopy," Journal of Cell Biology **190**(2), 165–175 (2010).
61. N. Kilian, A. Goryaynov, M. D. Lessard, G. Hooker, D. Toomre, J. E. Rothman, and J. Bewersdorf, "Assessing photodamage in live-cell STED microscopy," Nat Methods **15**(10), 755–756 (2018).
62. H.-W. Lu-Walther, M. Kielhorn, R. Förster, A. Jost, K. Wicker, and R. Heintzmann, "fastSIM: a practical implementation of fast structured illumination microscopy," Methods and Applications in Fluorescence **3**(1), 014001 (2015).
63. A. Markwirth, M. Lachetta, V. Mönkemöller, R. Heintzmann, W. Hübner, T. Huser, and M. Müller, "Video-rate multi-color structured illumination microscopy with simultaneous real-time reconstruction," Nature Communications **10**(1), 4315 (2019).
64. M. Lachetta, G. Wiebusch, W. Hübner, J. Schulte am Esch, T. Huser, and M. Müller, "Dual color DMD-SIM by temperature-controlled laser wavelength matching," Optics Express 14 (2021).
65. Y. Wu and H. Shroff, "Faster, sharper, and deeper: structured illumination microscopy for biological imaging," Nat Methods **15**(12), 1011–1019 (2018).
66. A. M. Cormack, "Representation of a Function by Its Line Integrals, with Some Radiological Applications," Journal of Applied Physics **34**(9), 2722–2727 (1963).
67. G. N. Hounsfield, "Computerized transverse axial scanning (tomography). 1. Description of system," Br J Radiol **46**(552), 1016–1022 (1973).
68. P. C. Lauterbur, "Image formation by induced local interactions. Examples employing nuclear magnetic resonance. 1973," Clin Orthop Relat Res (244), 3–6 (1989).
69. M. Rudin, N. Beckmann, and M. Rausch, "Magnetic Resonance Imaging in Biomedical Research: Imaging of Drugs and Drug Effects," in *Methods in Enzymology*, Imaging in Biological Research, Part A (Academic Press, 2004), **385**, pp. 240–256.
70. N. Tomiyama, O. Honda, M. Tsubamoto, A. Inoue, H. Sumikawa, K. Kuriyama, M. Kusumoto, T. Johkoh, and H. Nakamura, "Anterior mediastinal tumors: Diagnostic accuracy of CT and MRI," European Journal of Radiology **69**(2), 280–288 (2009).
71. O. Lubovsky, M. Liebergall, Y. Mattan, Y. Weil, and R. Mosheiff, "Early diagnosis of occult hip fractures: MRI versus CT scan," Injury **36**(6), 788–792 (2005).
72. J. Kalita and U. K. Misra, "Comparison of CT scan and MRI findings in the diagnosis of Japanese encephalitis," Journal of the Neurological Sciences **174**(1), 3–8 (2000).

73. M. Oldham, H. Sakhalkar, Y. M. Wang, P. Guo, T. F. Oliver, R. Bentley, Z. V. M.d, and M. W. D. D.v.m, "Three-dimensional imaging of whole rodent organs using optical computed and emission tomography," JBO **12**(1), 014009 (2007).
74. D. Nguyen, P. J. Marchand, A. L. Planchette, J. Nilsson, M. Sison, J. Extermann, A. Lopez, M. Sylwestrzak, J. Sordet-Dessimoz, A. Schmidt-Christensen, D. Holmberg, D. V. D. Ville, and T. Lasser, "Optical projection tomography for rapid whole mouse brain imaging," Biomed. Opt. Express, BOE **8**(12), 5637–5650 (2017).
75. D. Nguyen, V. Uhlmann, A. L. Planchette, P. J. Marchand, D. V. D. Ville, T. Lasser, and A. Radenovic, "Supervised learning to quantify amyloidosis in whole brains of an Alzheimer’s disease mouse model acquired with optical projection tomography," Biomed. Opt. Express, BOE **10**(6), 3041–3060 (2019).
76. J. Sharpe, "Optical projection tomography as a new tool for studying embryo anatomy," Journal of Anatomy **202**(2), 175–181 (2003).
77. M. D. Wong, J. Dazai, J. R. Walls, N. W. Gale, and R. M. Henkelman, "Design and Implementation of a Custom Built Optical Projection Tomography System," PLOS ONE **8**(9), e73491 (2013).
78. L. Silvestri, I. Costantini, L. Sacconi, and F. S. Pavone, "Clearing of fixed tissue: a review from a microscopist's perspective," JBO **21**(8), 081205 (2016).
79. P. G. Pitrone, J. Schindelin, L. Stuyvenberg, S. Preibisch, M. Weber, K. W. Eliceiri, J. Huisken, and P. Tomancak, "OpenSPIM: an open-access light-sheet microscopy platform," Nat Methods **10**(7), 598–599 (2013).
80. T. Holm, T. Klein, A. Löschberger, T. Klamp, G. Wiebusch, S. van de Linde, and M. Sauer, "A Blueprint for Cost-Efficient Localization Microscopy," ChemPhysChem **15**(4), 651–654 (2014).
81. R. Diekmann, K. Till, M. Müller, M. Simonis, M. Schüttpelz, and T. Huser, "Characterization of an industry-grade CMOS camera well suited for single molecule localization microscopy – high performance super-resolution at low cost," Sci Rep **7**(1), 14425 (2017).
82. Y. S. Zhang, J. Ribas, A. Nadhman, J. Aleman, Š. Selimović, S. C. Lesher-Perez, T. Wang, V. Manoharan, S.-R. Shin, A. Damilano, N. Annabi, M. R. Dokmeci, S. Takayama, and A. Khademhosseini, "A cost-effective fluorescence mini-microscope for biomedical applications," Lab Chip **15**(18), 3661–3669 (2015).
83. K. Yamagata, D. Iwamoto, Y. Terashita, C. Li, S. Wakayama, Y. Hayashi-Takanaka, H. Kimura, K. Saeki, and T. Wakayama, "Fluorescence cell imaging and manipulation using conventional halogen lamp microscopy," PLoS One **7**(2), e31638 (2012).
84. R. M. Power and J. Huisken, "Putting advanced microscopy in the hands of biologists," Nat Methods **16**(11), 1069–1073 (2019).
85. C. Maurer, A. Jesacher, S. Bernet, and M. Ritsch-Marte, "What spatial light modulators can do for optical microscopy," Laser & Photonics Reviews **5**(1), 81–101 (2011).

86. P. Kner, B. B. Chhun, E. R. Griffis, L. Winoto, and M. G. L. Gustafsson, "Super-resolution video microscopy of live cells by structured illumination," Nature Methods **6**(5), 339–342 (2009).
87. R. Fiolka, L. Shao, E. H. Rego, M. W. Davidson, and M. G. L. Gustafsson, "Time-lapse two-color 3D imaging of live cells with doubled resolution using structured illumination," PNAS **109**(14), 5311–5315 (2012).
88. R. Förster, H.-W. Lu-Walther, A. Jost, M. Kielhorn, K. Wicker, and R. Heintzmann, "Simple structured illumination microscope setup with high acquisition speed by using a spatial light modulator," Optics Express **22**(17), 20663 (2014).
89. L. Shao, P. Kner, E. H. Rego, and M. G. L. Gustafsson, "Super-resolution 3D microscopy of live whole cells using structured illumination," Nature Methods **8**(12), 1044–1046 (2011).
90. J. E. Harvey and R. N. Pfisterer, "Understanding diffraction grating behavior: including conical diffraction and Rayleigh anomalies from transmission gratings," OE **58**(8), 087105 (2019).
91. X. Chen, B. Yan, F. Song, Y. Wang, F. Xiao, and K. Alameh, "Diffraction of digital micromirror device gratings and its effect on properties of tunable fiber lasers," Appl. Opt., AO **51**(30), 7214–7220 (2012).
92. M. Lachetta, H. Sandmeyer, A. Sandmeyer, J. S. am Esch, T. Huser, and M. Müller, "Simulating digital micromirror devices for patterning coherent excitation light in structured illumination microscopy," Philosophical Transactions of the Royal Society A: Mathematical, Physical and Engineering Sciences **379**(2199), 20200147 (2021).
93. M. Müller, "The fairSIM project," https://www.fairsim.org/.
94. H. Kirshner, F. Aguet, D. Sage, and M. Unser, "3-D PSF fitting for fluorescence microscopy: implementation and localization application," Journal of Microscopy **249**(1), 13–25 (2013).
95. E. Abbe Hon., "VII.—On the Estimation of Aperture in the Microscope.," Journal of the Royal Microscopical Society **1**(3), 388–423 (1881).
96. J. W. Goodman, *Introduction to Fourier Optics* (Roberts and Company Publishers, 2005).
97. C. M. Sparrow, "On Spectroscopic Resolving Power," The Astrophysical Journal **44**, 76 (1916).
98. L. R. F.R.S, "XXXI. Investigations in optics, with special reference to the spectroscope," The London, Edinburgh, and Dublin Philosophical Magazine and Journal of Science **8**(49), 261–274 (1879).
99. R. T. Borlinghaus, *Konfokale Mikroskopie in Weiß: Optische Schnitte in allen Farben* (Springer Spektrum, 2016).
100. M. Müller, *FairSIM/Test-Datasets*, GitHub Repository (fairSIM, 2021).
101. J. R. Lakowicz, *Principles of Fluorescence Spectroscopy*, 3rd ed. (Springer US, 2006).
102. G. G. Stokes, "XXX. On the change of refrangibility of light," Philosophical Transactions of the Royal Society of London **142**, 463–562 (1852).

103. U. Kubitscheck, *Fluorescence Microscopy: From Principles to Biological Applications* (John Wiley & Sons, 2017).
104. B. H. Bransden and C. J. Joachain, *Physics of Atoms and Molecules* (Pearson Education, 2003).
105. Y. Li, M. Gecevicius, and J. Qiu, "Long persistent phosphors - From fundamentals to applications," Chemical Society reviews **45**, (2016).
106. J. Popp, V. V. Tuchin, A. Chiou, and S. H. Heinemann, *Handbook of Biophotonics* (Wiley, 2011).
107. M. Kasha, "Characterization of electronic transitions in complex molecules," Discuss. Faraday Soc. **9**(0), 14–19 (1950).
108. P. P. Mondal and A. Diaspro, *Fundamentals of Fluorescence Microscopy: Exploring Life with Light* (Springer Netherlands, 2014).
109. C. Greb, "Fluorescent Dyes," (2012).
110. P. J. Cranfill, B. R. Sell, M. A. Baird, J. R. Allen, Z. Lavagnino, H. M. de Gruiter, G.-J. Kremers, M. W. Davidson, A. Ustione, and D. W. Piston, "Quantitative assessment of fluorescent proteins," Nat Methods **13**(7), 557–562 (2016).
111. S. Uno, M. Kamiya, T. Yoshihara, K. Sugawara, K. Okabe, M. C. Tarhan, H. Fujita, T. Funatsu, Y. Okada, S. Tobita, and Y. Urano, "A spontaneously blinking fluorophore based on intramolecular spirocyclization for live-cell super-resolution imaging," Nature Chem **6**(8), 681–689 (2014).
112. M. E. Widdop, "Review of Work on Dichroic Mirrors and Their Light-Dividing Characteristics," Journal of the Society of Motion Picture and Television Engineers **60**(4), 357–366 (1953).
113. D. Axelrod, "Chapter 7: Total internal reflection fluorescence microscopy," Methods Cell Biol **89**, 169–221 (2008).
114. J. Vangindertael, R. Camacho, W. Sempels, H. Mizuno, P. Dedecker, and K. P. F. Janssen, "An introduction to optical super-resolution microscopy for the adventurous biologist," Methods Appl. Fluoresc. **6**(2), 022003 (2018).
115. M. Tokunaga, N. Imamoto, and K. Sakata-Sogawa, "Highly inclined thin illumination enables clear single-molecule imaging in cells," Nat Methods **5**(2), 159–161 (2008).
116. J. Huisken, J. Swoger, F. Del Bene, J. Wittbrodt, and E. H. K. Stelzer, "Optical Sectioning Deep Inside Live Embryos by Selective Plane Illumination Microscopy," Science **305**(5686), 1007–1009 (2004).
117. K. Greger, J. Swoger, and E. H. K. Stelzer, "Basic building units and properties of a fluorescence single plane illumination microscope," Review of Scientific Instruments **78**(2), 023705 (2007).
118. T. Jüstel and S. Schwung, *Leuchtstoffe, Lichtquellen, Laser, Lumineszenz* (Springer Spektrum, 2016).
119. D. R. Lide, *CRC Handbook of Chemistry and Physics, 84th Edition* (CRC Press, 2003).
120. "The Nobel Prize in Physics 2014," https://www.nobelprize.org/prizes/physics/2014/summary/.

121. M. Rudan, *Physics of Semiconductor Devices* (Springer-Verlag, 2015).
122. R. Diekmann, "Extending the application range of optical nanoscopy," (2017).
123. W. S. Boyle and G. E. Smith, "Charge coupled semiconductor devices," The Bell System Technical Journal **49**(4), 587–593 (1970).
124. J. Jung, S. Weisenburger, S. Albert, D. F. Gilbert, O. Friedrich, V. Eulenburg, J. Kornhuber, and T. W. Groemer, "Performance of scientific cameras with different sensor types in measuring dynamic processes in fluorescence microscopy," Microscopy Research and Technique **76**(8), 835–843 (2013).
125. M. S. Robbins, "Electron-Multiplying Charge Coupled Devices – EMCCDs," in *Single-Photon Imaging*, P. Seitz and A. J. Theuwissen, eds., Springer Series in Optical Sciences (Springer, 2011), pp. 103–121.
126. W. G. (Jay) Jerome, "Practical Guide to Choosing a Microscope Camera," Microscopy Today **25**(5), 24–29 (2017).
127. H. Nyquist, "Certain Topics in Telegraph Transmission Theory," Transactions of the American Institute of Electrical Engineers **47**(2), 617–644 (1928).
128. C. E. Shannon, "Communication in the Presence of Noise," Proceedings of the IRE **37**(1), 10–21 (1949).
129. M. Marvin, "Microscopy apparatus," United States patent US3013467A (December 19, 1961).
130. G. Cox and C. J. R. Sheppard, "Practical limits of resolution in confocal and non-linear microscopy," Microscopy Research and Technique **63**(1), 18–22 (2004).
131. W. Wallace, L. H. Schaefer, and J. R. Swedlow, "A Workingperson's Guide to Deconvolution in Light Microscopy," BioTechniques **31**(5), 1076–1097 (2001).
132. D. Sage, L. Donati, F. Soulez, D. Fortun, G. Schmit, A. Seitz, R. Guiet, C. Vonesch, and M. Unser, "DeconvolutionLab2: An open-source software for deconvolution microscopy," Methods **115**, 28–41 (2017).
133. M. Born and E. Wolf, *Principles of Optics: Electromagnetic Theory of Propagation, Interference and Diffraction of Light* (Elsevier, 2013).
134. N. Wiener, *Extrapolation, Interpolation, and Smoothing of Stationary Time Series, with Engineering Applications* (Martino Fine Books, 2013).
135. L. A. Shepp and Y. Vardi, "Maximum Likelihood Reconstruction for Emission Tomography," IEEE Transactions on Medical Imaging **1**(2), 113–122 (1982).
136. W. H. Richardson, "Bayesian-Based Iterative Method of Image Restoration*," J. Opt. Soc. Am., JOSA **62**(1), 55–59 (1972).
137. L. B. Lucy, "An iterative technique for the rectification of observed distributions," The Astronomical Journal **79**, 745 (1974).
138. M. Orrit, "Celebrating optical nanoscopy," Nature Photon **8**(12), 887–888 (2014).
139. "The Nobel Prize in Chemistry 2014 Betzig," https://www.nobelprize.org/prizes/chemistry/2014/betzig/lecture/.
140. E. Betzig, G. H. Patterson, R. Sougrat, O. W. Lindwasser, S. Olenych, J. S. Bonifacino, M. W. Davidson, J. Lippincott-Schwartz, and H. F. Hess, "Imaging Intracellular Fluorescent Proteins at Nanometer Resolution," Science **313**(5793), 1642–1645 (2006).

141. "The Nobel Prize in Chemistry 2014 Hell," https://www.nobelprize.org/prizes/chemistry/2014/hell/lecture/.
142. "The Nobel Prize in Chemistry 2014 Moerner," https://www.nobelprize.org/prizes/chemistry/2014/moerner/lecture/.
143. W. E. Moerner and L. Kador, "Optical detection and spectroscopy of single molecules in a solid," Phys. Rev. Lett. **62**(21), 2535–2538 (1989).
144. S. J. Sahl, S. W. Hell, and S. Jakobs, "Fluorescence nanoscopy in cell biology," Nat Rev Mol Cell Biol **18**(11), 685–701 (2017).
145. T. A. Klar and S. W. Hell, "Subdiffraction resolution in far-field fluorescence microscopy," Opt. Lett., OL **24**(14), 954–956 (1999).
146. M. Dyba and S. W. Hell, "Photostability of a fluorescent marker under pulsed excited-state depletion through stimulated emission," Appl. Opt., AO **42**(25), 5123–5129 (2003).
147. T. Müller, C. Schumann, and A. Kraegeloh, "STED Microscopy and its Applications: New Insights into Cellular Processes on the Nanoscale," ChemPhysChem **13**(8), 1986–2000 (2012).
148. T. A. Klar, S. Jakobs, M. Dyba, A. Egner, and S. W. Hell, "Fluorescence microscopy with diffraction resolution barrier broken by stimulated emission," PNAS **97**(15), 8206–8210 (2000).
149. K. I. Willig, S. O. Rizzoli, V. Westphal, R. Jahn, and S. W. Hell, "STED microscopy reveals that synaptotagmin remains clustered after synaptic vesicle exocytosis," Nature **440**(7086), 935–939 (2006).
150. S. W. Hell, "Far-Field Optical Nanoscopy," Science **316**(5828), 1153–1158 (2007).
151. G. Leménager, E. D. Luca, Y.-P. Sun, and P. P. Pompa, "Super-resolution fluorescence imaging of biocompatible carbon dots," Nanoscale **6**(15), 8617–8623 (2014).
152. D. Wildanger, B. R. Patton, H. Schill, L. Marseglia, J. P. Hadden, S. Knauer, A. Schönle, J. G. Rarity, J. L. O'Brien, S. W. Hell, and J. M. Smith, "Solid Immersion Facilitates Fluorescence Microscopy with Nanometer Resolution and Sub-Ångström Emitter Localization," Advanced Materials **24**(44), OP309–OP313 (2012).
153. P. Ilgen, S. Stoldt, L.-C. Conradi, C. A. Wurm, J. Rüschoff, B. M. Ghadimi, T. Liersch, and S. Jakobs, "STED Super-Resolution Microscopy of Clinical Paraffin-Embedded Human Rectal Cancer Tissue," PLOS ONE **9**(7), e101563 (2014).
154. E. D'Este, D. Kamin, F. Göttfert, A. El-Hady, and S. W. Hell, "STED Nanoscopy Reveals the Ubiquity of Subcortical Cytoskeleton Periodicity in Living Neurons," Cell Reports **10**(8), 1246–1251 (2015).
155. E. D'Este, D. Kamin, F. Balzarotti, and S. W. Hell, "Ultrastructural anatomy of nodes of Ranvier in the peripheral nervous system as revealed by STED microscopy," PNAS **114**(2), E191–E199 (2017).
156. V. Westphal, S. O. Rizzoli, M. A. Lauterbach, D. Kamin, R. Jahn, and S. W. Hell, "Video-Rate Far-Field Optical Nanoscopy Dissects Synaptic Vesicle Movement," Science **320**(5873), 246–249 (2008).

157. V. Westphal, M. A. Lauterbach, A. D. Nicola, and S. W. Hell, "Dynamic far-field fluorescence nanoscopy," New J. Phys. **9**(12), 435–435 (2007).
158. M. A. Lauterbach, C. K. Ullal, V. Westphal, and S. W. Hell, "Dynamic Imaging of Colloidal-Crystal Nanostructures at 200 Frames per Second," Langmuir **26**(18), 14400–14404 (2010).
159. H. Nishimune, Y. Badawi, S. Mori, and K. Shigemoto, "Dual-color STED microscopy reveals a sandwich structure of Bassoon and Piccolo in active zones of adult and aged mice," Sci Rep **6**(1), 27935 (2016).
160. G. Donnert, J. Keller, C. A. Wurm, S. O. Rizzoli, V. Westphal, A. Schönle, R. Jahn, S. Jakobs, C. Eggeling, and S. W. Hell, "Two-Color Far-Field Fluorescence Nanoscopy," Biophysical Journal **92**(8), L67–L69 (2007).
161. M. Hofmann, C. Eggeling, S. Jakobs, and S. W. Hell, "Breaking the diffraction barrier in fluorescence microscopy at low light intensities by using reversibly photoswitchable proteins," PNAS **102**(49), 17565–17569 (2005).
162. R. J. Ober, S. Ram, and E. S. Ward, "Localization Accuracy in Single-Molecule Microscopy," Biophysical Journal **86**(2), 1185–1200 (2004).
163. B. Zhang, J. Zerubia, and J.-C. Olivo-Marin, "Gaussian approximations of fluorescence microscope point-spread function models," Appl. Opt., AO **46**(10), 1819–1829 (2007).
164. U. Endesfelder, S. Malkusch, F. Fricke, and M. Heilemann, "A simple method to estimate the average localization precision of a single-molecule localization microscopy experiment," Histochem Cell Biol **141**(6), 629–638 (2014).
165. R. E. Thompson, D. R. Larson, and W. W. Webb, "Precise Nanometer Localization Analysis for Individual Fluorescent Probes," Biophysical Journal **82**(5), 2775–2783 (2002).
166. K. I. Mortensen, L. S. Churchman, J. A. Spudich, and H. Flyvbjerg, "Optimized localization analysis for single-molecule tracking and super-resolution microscopy," Nat Methods **7**(5), 377–381 (2010).
167. W. R. Legant, L. Shao, J. B. Grimm, T. A. Brown, D. E. Milkie, B. B. Avants, L. D. Lavis, and E. Betzig, "High-density three-dimensional localization microscopy across large volumes," Nat Methods **13**(4), 359–365 (2016).
168. H. Shroff, C. G. Galbraith, J. A. Galbraith, and E. Betzig, "Live-cell photoactivated localization microscopy of nanoscale adhesion dynamics," Nat Methods **5**(5), 417–423 (2008).
169. G. T. Dempsey, J. C. Vaughan, K. H. Chen, M. Bates, and X. Zhuang, "Evaluation of fluorophores for optimal performance in localization-based super-resolution imaging," Nat Methods **8**(12), 1027–1036 (2011).
170. T. Dertinger, M. Heilemann, R. Vogel, M. Sauer, and S. Weiss, "Superresolution Optical Fluctuation Imaging with Organic Dyes," Angewandte Chemie International Edition **49**(49), 9441–9443 (2010).
171. T. Dertinger, R. Colyer, R. Vogel, J. Enderlein, and S. Weiss, "Achieving increased resolution and more pixels with Superresolution Optical Fluctuation Imaging (SOFI)," Opt. Express, OE **18**(18), 18875–18885 (2010).

172. B. Diederich, P. Then, A. Jügler, R. Förster, and R. Heintzmann, "cellSTORM—Cost-effective super-resolution on a cellphone using dSTORM," PLOS ONE **14**(1), e0209827 (2019).
173. A. Cambi and D. S. Lidke, *Cell Membrane Nanodomains: From Biochemistry to Nanoscopy* (CRC Press, 2014).
174. R. Henriques, M. Lelek, E. F. Fornasiero, F. Valtorta, C. Zimmer, and M. M. Mhlanga, "QuickPALM: 3D real-time photoactivation nanoscopy image processing in ImageJ," Nat Methods **7**(5), 339–340 (2010).
175. S. Wolter, A. Löschberger, T. Holm, S. Aufmkolk, M.-C. Dabauvalle, S. van de Linde, and M. Sauer, "rapi d STORM: accurate, fast open-source software for localization microscopy," Nat Methods **9**(11), 1040–1041 (2012).
176. M. Ovesný, P. Křížek, J. Borkovec, Z. Švindrych, and G. M. Hagen, "ThunderSTORM: a comprehensive ImageJ plug-in for PALM and STORM data analysis and super-resolution imaging," Bioinformatics **30**(16), 2389–2390 (2014).
177. D. Sage, T.-A. Pham, H. Babcock, T. Lukes, T. Pengo, J. Chao, R. Velmurugan, A. Herbert, A. Agrawal, S. Colabrese, A. Wheeler, A. Archetti, B. Rieger, R. Ober, G. M. Hagen, J.-B. Sibarita, J. Ries, R. Henriques, M. Unser, and S. Holden, "Super-resolution fight club: assessment of 2D and 3D single-molecule localization microscopy software," Nat Methods **16**(5), 387–395 (2019).
178. A. Löschberger, S. van de Linde, M.-C. Dabauvalle, B. Rieger, M. Heilemann, G. Krohne, and M. Sauer, "Super-resolution imaging visualizes the eightfold symmetry of gp210 proteins around the nuclear pore complex and resolves the central channel with nanometer resolution," Journal of Cell Science **125**(3), 570–575 (2012).
179. A. Szymborska, A. de Marco, N. Daigle, V. C. Cordes, J. A. G. Briggs, and J. Ellenberg, "Nuclear Pore Scaffold Structure Analyzed by Super-Resolution Microscopy and Particle Averaging," Science **341**(6146), 655–658 (2013).
180. K. Xu, G. Zhong, and X. Zhuang, "Actin, Spectrin, and Associated Proteins Form a Periodic Cytoskeletal Structure in Axons," Science **339**(6118), 452–456 (2013).
181. A. Dani, B. Huang, J. Bergan, C. Dulac, and X. Zhuang, "Superresolution Imaging of Chemical Synapses in the Brain," Neuron **68**(5), 843–856 (2010).
182. R. Salvador-Gallego, M. Mund, K. Cosentino, J. Schneider, J. Unsay, U. Schraermeyer, J. Engelhardt, J. Ries, and A. J. García-Sáez, "Bax assembly into rings and arcs in apoptotic mitochondria is linked to membrane pores," The EMBO Journal **35**(4), 389–401 (2016).
183. H. Takakura, Y. Zhang, R. S. Erdmann, A. D. Thompson, Y. Lin, B. McNellis, F. Rivera-Molina, S. Uno, M. Kamiya, Y. Urano, J. E. Rothman, J. Bewersdorf, A. Schepartz, and D. Toomre, "Long time-lapse nanoscopy with spontaneously blinking membrane probes," Nat Biotechnol **35**(8), 773–780 (2017).
184. S. Wolter, M. Schüttpelz, M. Tscherepanow, S. V. D. Linde, M. Heilemann, and M. Sauer, "Real-time computation of subdiffraction-resolution fluorescence images," Journal of Microscopy **237**(1), 12–22 (2010).

185. B. Huang, W. Wang, M. Bates, and X. Zhuang, "Three-Dimensional Super-Resolution Imaging by Stochastic Optical Reconstruction Microscopy," Science **319**(5864), 810–813 (2008).
186. S. Quirin, S. R. P. Pavani, and R. Piestun, "Optimal 3D single-molecule localization for superresolution microscopy with aberrations and engineered point spread functions," PNAS **109**(3), 675–679 (2012).
187. A. Lampe, V. Haucke, S. J. Sigrist, M. Heilemann, and J. Schmoranzer, "Multi-colour direct STORM with red emitting carbocyanines," Biology of the Cell **104**(4), 229–237 (2012).
188. H. Shroff, C. G. Galbraith, J. A. Galbraith, H. White, J. Gillette, S. Olenych, M. W. Davidson, and E. Betzig, "Dual-color superresolution imaging of genetically expressed probes within individual adhesion complexes," PNAS **104**(51), 20308–20313 (2007).
189. J. T. Frohn, "Super-resolution fluorescence microscopy by structured ligth illumination," Doctoral Thesis, ETH Zurich (2000).
190. R. Heintzmann and T. Huser, "Super-Resolution Structured Illumination Microscopy," Chem. Rev. **117**(23), 13890–13908 (2017).
191. R. Heintzmann, T. M. Jovin, and C. Cremer, "Saturated patterned excitation microscopy—a concept for optical resolution improvement," J. Opt. Soc. Am. A, JOSAA **19**(8), 1599–1609 (2002).
192. M. Müller, "Nanoscopy lecture 2020," http://uni-bielefeld.cloud.panopto.eu/Panopto/Pages/Sessions/List.aspx.
193. M. Müller, V. Mönkemöller, S. Hennig, W. Hübner, and T. Huser, "Open-source image reconstruction of super-resolution structured illumination microscopy data in ImageJ," Nature Communications **7**(1), 10980 (2016).
194. K. Wicker, O. Mandula, G. Best, R. Fiolka, and R. Heintzmann, "Phase optimisation for structured illumination microscopy," Opt. Express, OE **21**(2), 2032–2049 (2013).
195. B.-J. Chang, L.-J. Chou, Y.-C. Chang, and S.-Y. Chiang, "Isotropic image in structured illumination microscopy patterned with a spatial light modulator," Opt. Express, OE **17**(17), 14710–14721 (2009).
196. V. Perez, B.-J. Chang, and E. H. K. Stelzer, "Optimal 2D-SIM reconstruction by two filtering steps with Richardson-Lucy deconvolution," Sci Rep **6**(1), 37149 (2016).
197. X. Huang, J. Fan, L. Li, H. Liu, R. Wu, Y. Wu, L. Wei, H. Mao, A. Lal, P. Xi, L. Tang, Y. Zhang, Y. Liu, S. Tan, and L. Chen, "Fast, long-term, super-resolution imaging with Hessian structured illumination microscopy," Nat Biotechnol **36**(5), 451–459 (2018).
198. Q. Yang, L. Cao, H. Zhang, H. Zhang, and G. Jin, "Method of lateral image reconstruction in structured illumination microscopy with super resolution," J. Innov. Opt. Health Sci. **09**(03), 1630002 (2016).
199. C. Karras, M. Smedh, R. Förster, H. Deschout, J. Fernandez-Rodriguez, and R. Heintzmann, "Successful optimization of reconstruction parameters in

structured illumination microscopy – A practical guide," Optics Communications **436**, 69–75 (2019).
200. G. Ball, J. Demmerle, R. Kaufmann, I. Davis, I. M. Dobbie, and L. Schermelleh, "SIMcheck: a Toolbox for Successful Super-resolution Structured Illumination Microscopy," Sci Rep **5**(1), 15915 (2015).
201. A. Lal, C. Shan, and P. Xi, "Structured Illumination Microscopy Image Reconstruction Algorithm," IEEE Journal of Selected Topics in Quantum Electronics **22**(4), 50–63 (2016).
202. P. Křížek, T. Lukeš, M. Ovesný, K. Fliegel, and G. M. Hagen, "SIMToolbox: a MATLAB toolbox for structured illumination fluorescence microscopy," Bioinformatics **32**(2), 318–320 (2016).
203. T. Lukeš, P. Křížek, Z. Švindrych, J. Benda, M. Ovesný, K. Fliegel, M. Klíma, and G. M. Hagen, "Three-dimensional super-resolution structured illumination microscopy with maximum a posteriori probability image estimation," Opt. Express **22**(24), 29805 (2014).
204. K. Wicker, "Non-iterative determination of pattern phase in structured illumination microscopy using auto-correlations in Fourier space," Opt. Express, OE **21**(21), 24692–24701 (2013).
205. Y. Zhang, S. Lang, H. Wang, J. Liao, and Y. Gong, "Super-resolution algorithm based on Richardson–Lucy deconvolution for three-dimensional structured illumination microscopy," J. Opt. Soc. Am. A, JOSAA **36**(2), 173–178 (2019).
206. E. Mudry, K. Belkebir, J. Girard, J. Savatier, E. Le Moal, C. Nicoletti, M. Allain, and A. Sentenac, "Structured illumination microscopy using unknown speckle patterns," Nature Photon **6**(5), 312–315 (2012).
207. Z. H. Shah, M. Müller, T.-C. Wang, P. M. Scheidig, A. Schneider, M. Schüttpelz, T. Huser, T. Huser, W. Schenck, and W. Schenck, "Deep-learning based denoising and reconstruction of super-resolution structured illumination microscopy images," Photon. Res., PRJ **9**(5), B168–B181 (2021).
208. E. H. Rego and L. Shao, "Practical Structured Illumination Microscopy," in *Advanced Fluorescence Microscopy: Methods and Protocols*, P. J. Verveer, ed., Methods in Molecular Biology (Springer, 2015), pp. 175–192.
209. M. Brunstein, K. Wicker, K. Hérault, R. Heintzmann, and M. Oheim, "Full-field dual-color 100-nm super-resolution imaging reveals organization and dynamics of mitochondrial and ER networks," Opt. Express, OE **21**(22), 26162–26173 (2013).
210. K. O'Holleran and M. Shaw, "Polarization effects on contrast in structured illumination microscopy," Optics Letters **37**(22), 4603 (2012).
211. L. Song, H.-W. Lu-Walther, R. Förster, A. Jost, M. Kielhorn, J. Zhou, and R. Heintzmann, "Fast structured illumination microscopy using rolling shutter cameras," Measurement Science and Technology **27**(5), 055401 (2016).
212. D. Dan, M. Lei, B. Yao, W. Wang, M. Winterhalder, A. Zumbusch, Y. Qi, L. Xia, S. Yan, Y. Yang, P. Gao, T. Ye, and W. Zhao, "DMD-based LED-illumination Super-resolution and optical sectioning microscopy," Scientific Reports **3**(1), (2013).

213. L. J. Young, F. Ströhl, and C. F. Kaminski, "A Guide to Structured Illumination TIRF Microscopy at High Speed with Multiple Colors," Journal of Visualized Experiments (111), (2016).
214. Y. Guo, D. Li, S. Zhang, Y. Yang, J.-J. Liu, X. Wang, C. Liu, D. E. Milkie, R. P. Moore, U. S. Tulu, D. P. Kiehart, J. Hu, J. Lippincott-Schwartz, E. Betzig, and D. Li, "Visualizing Intracellular Organelle and Cytoskeletal Interactions at Nanoscale Resolution on Millisecond Timescales," Cell **175**(5), 1430-1442.e17 (2018).
215. B.-C. Chen, W. R. Legant, K. Wang, L. Shao, D. E. Milkie, M. W. Davidson, C. Janetopoulos, X. S. Wu, J. A. Hammer, Z. Liu, B. P. English, Y. Mimori-Kiyosue, D. P. Romero, A. T. Ritter, J. Lippincott-Schwartz, L. Fritz-Laylin, R. D. Mullins, D. M. Mitchell, J. N. Bembenek, A.-C. Reymann, R. Böhme, S. W. Grill, J. T. Wang, G. Seydoux, U. S. Tulu, D. P. Kiehart, and E. Betzig, "Lattice light-sheet microscopy: Imaging molecules to embryos at high spatiotemporal resolution," Science **346**(6208), (2014).
216. S. Abrahamsson, H. Blom, A. Agostinho, D. C. Jans, A. Jost, M. Müller, L. Nilsson, K. Bernhem, T. J. Lambert, R. Heintzmann, and H. Brismar, "Multifocus structured illumination microscopy for fast volumetric super-resolution imaging," Biomed. Opt. Express, BOE **8**(9), 4135–4140 (2017).
217. A. Descloux, M. Müller, V. Navikas, A. Markwirth, R. van den Eynde, T. Lukes, W. Hübner, T. Lasser, A. Radenovic, P. Dedecker, and T. Huser, "High-speed multiplane structured illumination microscopy of living cells using an image-splitting prism," Nanophotonics **9**(1), 143–148 (2020).
218. A. Descloux, K. S. Grußmayer, E. Bostan, T. Lukes, A. Bouwens, A. Sharipov, S. Geissbuehler, A.-L. Mahul-Mellier, H. A. Lashuel, M. Leutenegger, and T. Lasser, "Combined multi-plane phase retrieval and super-resolution optical fluctuation imaging for 4D cell microscopy," Nature Photon **12**(3), 165–172 (2018).
219. A. K. Shukla and U. Kumar, "Positron emission tomography: An overview," J Med Phys **31**(1), 13–21 (2006).
220. D. Nguyen, "Optical projection tomography for whole organ imaging," EPFL (2019).
221. V. Ntziachristos, "Going deeper than microscopy: the optical imaging frontier in biology," Nat Methods **7**(8), 603–614 (2010).
222. D. W. Holdsworth and M. M. Thornton, "Micro-CT in small animal and specimen imaging," Trends in Biotechnology **20**(8), S34–S39 (2002).
223. H. Benveniste and S. Blackband, "MR microscopy and high resolution small animal MRI: applications in neuroscience research," Prog Neurobiol **67**(5), 393–420 (2002).
224. M. J. Paulus, S. S. Gleason, S. J. Kennel, P. R. Hunsicker, and D. K. Johnson, "High resolution X-ray computed tomography: an emerging tool for small animal cancer research," Neoplasia **2**(1–2), 62–70 (2000).
225. T. Deffieux, C. Demene, M. Pernot, and M. Tanter, "Functional ultrasound neuroimaging: a review of the preclinical and clinical state of the art," Curr Opin Neurobiol **50**, 128–135 (2018).

226. H.-P. Brecht, R. Su, M. Fronheiser, S. A. Ermilov, A. Conjusteau, and A. A. Oraevsky, "Whole-body three-dimensional optoacoustic tomography system for small animals," J Biomed Opt **14**(6), 064007 (2009).
227. D. Razansky, C. Vinegoni, and V. Ntziachristos, "Imaging of mesoscopic-scale organisms using selective-plane optoacoustic tomography," Phys Med Biol **54**(9), 2769–2777 (2009).
228. C. H. Contag and B. D. Ross, "It's not just about anatomy: In vivo bioluminescence imaging as an eyepiece into biology," Journal of Magnetic Resonance Imaging **16**(4), 378–387 (2002).
229. M. Weber, M. Mickoleit, and J. Huisken, "Chapter 11 - Light sheet microscopy," in *Methods in Cell Biology*, J. C. Waters and T. Wittman, eds., Quantitative Imaging in Cell Biology (Academic Press, 2014), **123**, pp. 193–215.
230. H.-U. Dodt, U. Leischner, A. Schierloh, N. Jährling, C. P. Mauch, K. Deininger, J. M. Deussing, M. Eder, W. Zieglgänsberger, and K. Becker, "Ultramicroscopy: three-dimensional visualization of neuronal networks in the whole mouse brain," Nat Methods **4**(4), 331–336 (2007).
231. R. Menzel, "Ultramicroscopy – Imaging a Whole Animal or a Whole Brain with Micron Resolution," Frontiers in Neuroscience **5**, 11 (2011).
232. P. J. Keller and H.-U. Dodt, "Light sheet microscopy of living or cleared specimens," Current Opinion in Neurobiology **22**(1), 138–143 (2012).
233. M. B. Ahrens, M. B. Orger, D. N. Robson, J. M. Li, and P. J. Keller, "Whole-brain functional imaging at cellular resolution using light-sheet microscopy," Nat Methods **10**(5), 413–420 (2013).
234. P. J. Keller and M. B. Ahrens, "Visualizing Whole-Brain Activity and Development at the Single-Cell Level Using Light-Sheet Microscopy," Neuron **85**(3), 462–483 (2015).
235. A. Kaufmann, M. Mickoleit, M. Weber, and J. Huisken, "Multilayer mounting enables long-term imaging of zebrafish development in a light sheet microscope," Development **139**(17), 3242–3247 (2012).
236. P. J. Keller, A. D. Schmidt, A. Santella, K. Khairy, Z. Bao, J. Wittbrodt, and E. H. K. Stelzer, "Fast, high-contrast imaging of animal development with scanned light sheet–based structured-illumination microscopy," Nat Methods **7**(8), 637–642 (2010).
237. L. Silvestri, A. Bria, L. Sacconi, G. Iannello, and F. S. Pavone, "Confocal light sheet microscopy: micron-scale neuroanatomy of the entire mouse brain," Opt. Express, OE **20**(18), 20582–20598 (2012).
238. N. Jährling, K. Becker, B. M. Wegenast-Braun, S. A. Grathwohl, M. Jucker, and H.-U. Dodt, "Cerebral β-Amyloidosis in Mice Investigated by Ultramicroscopy," PLOS ONE **10**(5), e0125418 (2015).
239. M. Pende, K. Becker, M. Wanis, S. Saghafi, R. Kaur, C. Hahn, N. Pende, M. Foroughipour, T. Hummel, and H.-U. Dodt, "High-resolution ultramicroscopy of the developing and adult nervous system in optically cleared Drosophila melanogaster," Nat Commun **9**(1), 4731 (2018).

240. J. Sharpe, U. Ahlgren, P. Perry, B. Hill, A. Ross, J. Hecksher-Sørensen, R. Baldock, and D. Davidson, "Optical Projection Tomography as a Tool for 3D Microscopy and Gene Expression Studies," Science **296**(5567), 541–545 (2002).
241. A. Bassi, L. Fieramonti, C. D'Andrea, M. Mione, and G. Valentini, "In vivo label-free three-dimensional imaging of zebrafish vasculature with optical projection tomography," J Biomed Opt **16**(10), 100502 (2011).
242. T. Alanentalo, A. Asayesh, H. Morrison, C. E. Lorén, D. Holmberg, J. Sharpe, and U. Ahlgren, "Tomographic molecular imaging and 3D quantification within adult mouse organs," Nat Methods **4**(1), 31–33 (2007).
243. T. Alanentalo, C. E. Lorén, A. Larefalk, J. Sharpe, D. Holmberg, and U. Ahlgren, "High-resolution three-dimensional imaging of islet-infiltrate interactions based on optical projection tomography assessments of the intact adult mouse pancreas," J Biomed Opt **13**(5), 054070 (2008).
244. T. Alanentalo, A. Hörnblad, S. Mayans, A. Karin Nilsson, J. Sharpe, A. Larefalk, U. Ahlgren, and D. Holmberg, "Quantification and three-dimensional imaging of the insulitis-induced destruction of beta-cells in murine type 1 diabetes," Diabetes **59**(7), 1756–1764 (2010).
245. J. A. Gleave, M. D. Wong, J. Dazai, M. Altaf, R. M. Henkelman, J. P. Lerch, and B. J. Nieman, "Neuroanatomical phenotyping of the mouse brain with three-dimensional autofluorescence imaging," Physiol Genomics **44**(15), 778–785 (2012).
246. L. Quintana and J. Sharpe, "Preparation of mouse embryos for optical projection tomography imaging," Cold Spring Harb Protoc **2011**(6), 664–669 (2011).
247. B. W. Lindsey, A. M. Douek, F. Loosli, and J. Kaslin, "A Whole Brain Staining, Embedding, and Clearing Pipeline for Adult Zebrafish to Visualize Cell Proliferation and Morphology in 3-Dimensions," Front Neurosci **11**, 750 (2017).
248. U. J. Birk, A. Darrell, N. Konstantinides, A. Sarasa-Renedo, and J. Ripoll, "Improved reconstructions and generalized filtered back projection for optical projection tomography," Appl. Opt., AO **50**(4), 392–398 (2011).
249. A. K. Trull, J. van der Horst, W. J. Palenstijn, L. J. van Vliet, T. van Leeuwen, and J. Kalkman, "Point spread function based image reconstruction in optical projection tomography," Phys Med Biol **62**(19), 7784–7797 (2017).
250. A. K. Trull, J. van der Horst, L. J. van Vliet, and J. Kalkman, "Comparison of image reconstruction techniques for optical projection tomography," Appl Opt **57**(8), 1874–1882 (2018).
251. D. S. Richardson and J. W. Lichtman, "Clarifying Tissue Clearing," Cell **162**(2), 246–257 (2015).
252. J.-H. Lambert, *J. H. Lambert,... Photometria, sive de Mensura et gradibus luminis, colorum et umbrae* (sumptibus viduae E. Klett, 1760).
253. Rich Radke, *DIP Lecture 18: Reconstruction from Parallel Projections and the Radon Transform* (2015).
254. J. Radon, "On the determination of functions from their integral values along certain manifolds," IEEE Transactions on Medical Imaging **5**(4), 170–176 (1986).

255. D. Farrell, "Radon Transform," https://imagej.nih.gov/ij/plugins/radon-transform.html.
256. R. Bracewell, *Fourier Analysis and Imaging* (Springer US, 2003).
257. G. T. Gullberg, "The reconstruction of fan-beam data by filtering the back-projection," Computer Graphics and Image Processing **10**(1), 30–47 (1979).
258. S. Inoué and K. Spring, *Video Microscopy: The Fundamentals*, 2nd ed. (Springer US, 1997).
259. A. Liu, W. Xiao, R. Li, L. Liu, and L. Chen, "Comparison of optical projection tomography and light-sheet fluorescence microscopy," Journal of Microscopy **275**(1), 3–10 (2019).
260. J. Sharpe, "Optical Projection Tomography," Annual Review of Biomedical Engineering **6**(1), 209–228 (2004).
261. J. R. Walls, J. G. Sled, J. Sharpe, and R. M. Henkelman, "Correction of artefacts in optical projection tomography," Phys. Med. Biol. **50**(19), 4645–4665 (2005).
262. M. Rieckher, U. J. Birk, H. Meyer, J. Ripoll, and N. Tavernarakis, "Microscopic Optical Projection Tomography In Vivo," PLOS ONE **6**(4), e18963 (2011).
263. R. W. Cole and J. N. Turner, "Light-emitting diodes are better illumination sources for biological microscopy than conventional sources," Microsc Microanal **14**(3), 243–250 (2008).
264. Texas Instruments Incorporated, "DLP6500 0.65 1080p MVSP S600 DMD," (2016).
265. S. Shin, D. Kim, K. Kim, and Y. Park, "Super-resolution three-dimensional fluorescence and optical diffraction tomography of live cells using structured illumination generated by a digital micromirror device," Sci Rep **8**(1), 9183 (2018).
266. N. Chakrova, A. S. Canton, C. Danelon, S. Stallinga, and B. Rieger, "Adaptive illumination reduces photobleaching in structured illumination microscopy," Biomed. Opt. Express **7**(10), 4263 (2016).
267. M. Li, Y. Li, W. Liu, A. Lal, S. Jiang, D. Jin, H. Yang, S. Wang, K. Zhanghao, and P. Xi, "Structured illumination microscopy using digital micro-mirror device and coherent light source," Appl. Phys. Lett. **116**(23), 233702 (2020).
268. M. Lei, X. Zhou, D. Dan, J. Qian, and B. Yao, "Fast DMD based super-resolution structured illumination microscopy," in *Frontiers in Optics 2016 (2016), Paper FF3A.5* (Optical Society of America, 2016), p. FF3A.5.
269. Texas Instruments Incorporated, "Using Lasers with DLP® DMD technology," (2008).
270. P. T. Brown, R. Kruithoff, G. J. Seedorf, and D. P. Shepherd, "Multicolor structured illumination microscopy and quantitative control of polychromatic light with a digital micromirror device," Biomed. Opt. Express, BOE **12**(6), 3700–3716 (2021).
271. C.-H. Lee and S.-H. Ma, "Dual-layer blazed grating fabricated by the roll-to-roll microreplication process for chromostereoscopy," Appl. Opt., AO **51**(16), 3614–3621 (2012).

272. N. Chakrova, B. Rieger, and S. Stallinga, "Development of a DMD-based fluorescence microscope," in *Three-Dimensional and Multidimensional Microscopy: Image Acquisition and Processing XXII* (International Society for Optics and Photonics, 2015), **9330**, p. 933008.
273. M. Lachetta, *Biophotonics-Bielefeld/Coherent-Dmd-Sim-Simulator*, GitHub Repository (Biophotonics Bielefeld, 2021).
274. J. Pospíšil, T. Lukeš, J. Bendesky, K. Fliegel, K. Spendier, and G. M. Hagen, "Imaging tissues and cells beyond the diffraction limit with structured illumination microscopy and Bayesian image reconstruction," GigaScience **8**(1), (2019).
275. Y. Yan, M. Grossman, and V. Sarkar, "JCUDA: A Programmer-Friendly Interface for Accelerating Java Programs with CUDA," in *Euro-Par 2009 Parallel Processing*, H. Sips, D. Epema, and H.-X. Lin, eds., Lecture Notes in Computer Science (Springer, 2009), pp. 887–899.
276. R. V. den Eynde, A. Sandmeyer, W. Vandenberg, S. Duwé, W. Hübner, T. Huser, P. Dedecker, and M. Müller, "Quantitative comparison of camera technologies for cost-effective super-resolution optical fluctuation imaging (SOFI)," J. Phys. Photonics **1**(4), 044001 (2019).
277. R. P. J. Nieuwenhuizen, K. A. Lidke, M. Bates, D. L. Puig, D. Grünwald, S. Stallinga, and B. Rieger, "Measuring image resolution in optical nanoscopy," Nature Methods **10**(6), 557–562 (2013).
278. M. van Heel and M. Schatz, "Fourier shell correlation threshold criteria," Journal of Structural Biology **151**(3), 250–262 (2005).
279. Ushio Europe B.V., "633 nm Diodelaser HL63163DG Datasheet," (2021).
280. M. Müller and M. Lachetta, *FairSIM/FastSIM-GratingSearch*, GitHub Repository (fairSIM, 2019).
281. K. O'Holleran and M. Shaw, "Optimized approaches for optical sectioning and resolution enhancement in 2D structured illumination microscopy," Biomedical Optics Express **5**(8), 2580 (2014).
282. M. Shaw, L. Zajiczek, and K. O'Holleran, "High speed structured illumination microscopy in optically thick samples," Methods **88**, 11–19 (2015).
283. R. V. den Eynde, W. Vandenberg, S. Hugelier, A. Bouwens, A. Bouwens, J. Hofkens, J. Hofkens, M. Müller, M. Müller, M. Müller, P. Dedecker, and P. Dedecker, "Self-contained and modular structured illumination microscope," Biomed. Opt. Express, BOE **12**(7), 4414–4422 (2021).
284. A. Edelstein, N. Amodaj, K. Hoover, R. Vale, and N. Stuurman, "Computer Control of Microscopes Using μManager," Current Protocols in Molecular Biology **92**(1), 14.20.1-14.20.17 (2010).
285. A. D. Edelstein, M. A. Tsuchida, N. Amodaj, H. Pinkard, R. D. Vale, and N. Stuurman, "Advanced methods of microscope control using μManager software," Journal of Biological Methods **1**(2), e10–e10 (2014).
286. I. Arganda-Carreras, C. O. S. Sorzano, R. Marabini, J. M. Carazo, C. Ortiz-de-Solorzano, and J. Kybic, "Consistent and Elastic Registration of Histological

Sections Using Vector-Spline Regularization," in *Computer Vision Approaches to Medical Image Analysis*, R. R. Beichel and M. Sonka, eds., Lecture Notes in Computer Science (Springer Berlin Heidelberg, 2006), **4241**, pp. 85–95.
287. Texas Instruments Incorporated, "DLP® LightCrafter™ 6500 and 9000 Evaluation Module (EVM) User's Guide," (2016).
288. Texas Instruments Incorporated, "DLPC900 Programmer's Guide," https://www.ti.com/lit/ug/dlpu018d/dlpu018d.pdf.
289. M. Müller and M. Lachetta, *FairSIM/FairSIM-VIGOR*, GitHub Repository (fairSIM, 2021).
290. A. Arranz, D. Dong, S. Zhu, M. Rudin, C. Tsatsanis, J. Tian, and J. Ripoll, "Helical optical projection tomography," Opt. Express, OE **21**(22), 25912–25925 (2013).
291. "lag-opt.github.io," https://lag-opt.github.io/.
292. P. V. Ramirez, *PedropabloVR/2D_Reconstruction_patched* (2019).
293. P. P. Vallejo Ramirez, J. Zammit, O. Vanderpoorten, F. Riche, F.-X. Blé, X.-H. Zhou, B. Spiridon, C. Valentine, S. E. Spasov, P. W. Oluwasanya, G. Goodfellow, M. J. Fantham, O. Siddiqui, F. Alimagham, M. Robbins, A. Stretton, D. Simatos, O. Hadeler, E. J. Rees, F. Ströhl, R. F. Laine, and C. F. Kaminski, "OptiJ: Open-source optical projection tomography of large organ samples," Sci Rep **9**(1), 15693 (2019).
294. M. Lachetta, *Lachetta-Physics/Opt-Hist-Matching*, GitHub Repository (2020).
295. J. C. Schuerstedt, "Three-dimensional optical tomography of biological samples," (2021).
296. N. Kirschnick, D. Drees, E. Redder, R. Erapaneedi, A. P. da Graca, M. Schäfers, X. Jiang, and F. Kiefer, "Rapid methods for the evaluation of fluorescent reporters in tissue clearing and the segmentation of large vascular structures," iScience **24**(6), (2021).
297. M. Delay, "Practical Aspects of Mirror Usage in Optical Systems for Biology," (2016).

List of Figures

List of Tables

A Additional methods & materials

A.I Detailed setup component lists

Component list of the one-color DMD-SIM microscope

Main optics

Diode laser	QBAIHE 523nm 100mW 12V, 532MD-100-FB-12V-2
DMD	Texas Instruments, DLP6500FYE and DLP LightCrafter 6500 Evaluation Module
Objective	Olympus, UPLSAPO60XO, 1.35 NA
Camera	IDS uEye UI-3060CP-M-GL Rev.2

Lenses

L1	30 mm, 1 inch, biconvex
L2	150 mm, 1 inch, plano-concave
L3	Thorlabs, AC080-020-A-ML
L4	Thorlabs, AC508-200-A-ML with CXY2
L5	Thorlabs, AC508-100-A-ML with CXY2
L6	Thorlabs, AC508-150-A-ML with CXY2
L7	Thorlabs, AC254-250-A-ML with CXY1

Polarization optics

Polymer circular polarizer	Thorlabs, CP1L532 with RSP1/M
Pizza-polarizer	CODIXX, colorPol VIS 038 BC3 CW01 with Thorlabs, K6XS

Other components

ND-filter 10 %	Thorlabs, NE210B
ND-filter 50 %	Thorlabs, NE203B
High-power fiber	OZ Optics, QSMJ-A3HPC 3S-488-3.5/125-3AS
Dichroic mirror	Semrock, Di03-R532-t3-25x36
Sample stage	Newport, M-562-XYZ
DF orange	Semrock, FF01-575/59-25
DF red	Chroma, ET 632/60 M
Micro-controller	ATMEGA328 processor Arduino Uno board

Table 4: Main components of the one-color DMD-SIM microscope (Figure 43)
Table taken from our corresponding publication [8].

Component list of the dual-color DMD-SIM microscope

Blue 473 nm fiber coupling

DPSS laser	Spectra Physics Excelsior 473, 473nm/50mW, 2008
Cleanup filter	Chroma, ZET473/10x
Telescope lens 1	Thorlabs, AC254-030-A-ML
Telescope lens 2	Spindler & Hoyer achromatic 150 mm, 30 mm diameter
Coupling objective	Newport, 10x, 0.25 NA, 16.5 mm in Thorlabs, ST1XY-D/M (xy translation mount)
High power fiber	OZ Optics, QSMJ-A3HPC,3S-488-3.5/125-3AS-3
Collimator	Thorlabs, AC080-020-A-ML

Red 631nm fiber coupling

Power supply with temperature control	MEOS GmbH, LDC-01
Laser diode	Ushio, HL63163DG, 633nm/100mW, AlGaInP Laser Diode
Laser collimator	Thorlabs, C060TMD-A in S1TM09
Coupling lens	Thorlabs, C260TMD-A in S1TM09 in ST1XY-D/M (xy translation mount)
High power fiber	OZ Optics, PMJ-3AHPM3AF-633-4/125-3AS-3-1
Collimator lens	Thorlabs, AC080-020-A-ML

Microscope

DMD	Texas Instruments, DLP6500FYE und DLP LightCrafter 6500 Evaluation Module
Objective	Olympus UPLSAPO60XO, 1.35 NA with Thorlabs, CP1XY (xy mount)
Sample stage	Newport, M-562-XYZ
CMOS camera	IDS uEye UI-3060CP-M-GL Rev.2
λ/4 plate	BVO AQWP3 25.4mm OD 400-900nm BBAR in Thorlabs RSP1/M (rotation mount)
Pizza-polarizer	CODIXX, colorPol VIS 038 BC3 CW01 in Thorlabs RSP1/M (rotation mount)
L1	Thorlabs, AC508-200-A-ML in CXY2 (xy translation mount)
L2	Thorlabs, AC508-100-A-ML in CXY2 (xy translation mount)
L3	Thorlabs, AC508-150-A-ML in CXY2 (xy translation mount)
L4	Thorlabs, AC254-250-A-ML in CXY1 (xy translation mount)
DC1	Semrock, LM01-503-25
DC2 & DC3	Semrock, Di01-R405/488/561/635-25x36
DF 473 nm excitation	Semrock, FF01-525/45-25
DF 631 nm excitation	Chroma, ET685/70m

Table 5: Main components of the dual-color DMD-SIM microscope (Figure 56)
Table taken from our corresponding publication [64].

Component list of the fluorescence OPT Setup

Main components

Motorized xyz stage	3x, Standa, 8MT167-100
Rotating stage	Standa, 8MR190-2
Tip-tilt stage	2x, Newpoort, M-TGN80
Sample cuvette	20 x 20 mm² quartz glass cuvette of an old dye laser (Lambda Physik)
Sample adhesive	Loctite 454
Camera	Tucsen, FL-20BW, 5472 x 3648, 1” CMOS
Filter Cubes	4x, Thorlabs, DFM1/M in CM1-DCH/M (cube holder)

Lenses

L1	Thorlabs, ACL25416U in CXY1 (xy translation mount)
L2	Thorlabs, AC254-150-A-ML CXY1 (xy translation mount)
L3	Thorlabs, AC508-300-A-ML in CXY2 (xy translation mount)
L4	Thorlabs, AC508-150-A-ML in CXY2 (xy translation mount)

LEDs and filters UV channel

LED 405 nm	Thorlabs, M405D2, 1500 mW
EF	Chroma, ET420-40m
DC	Chroma, T455LP
DF	Chroma, AT465LP

LEDs and filters blue channel

LED 470 nm	Thorlabs, M470D3, 760 mW
EF	Chroma, ET480/30m
DC	Chroma, T505LPXR
DF	Chroma, ET535/50m

LEDs and filters green channel

LED 565 nm	Thorlabs, M565D2, 880 mW
EF	Chroma, ET550/60m
DC	Chroma, T588LPXR
DF	Chroma, ET615/40m

LEDs and filters red channel

LED 625 nm	Thorlabs, M625D3, 700 mW
EF	Chroma, HQ625/20M
DC	Semrock, FF650-Di01-25x36
DF	Chroma, ET700/75m

Table 6: Main components of the fluorescence OPT setup (Figure 69)

A.II DMD-SIM additional information

The following two paragraphs "Two dichroic mirrors from the same batch for SIM" and "HL63163DG red laser diode wavelength and mode-hopping" are taken from the supplemental document of our corresponding publication [64].

Two dichroic mirrors from the same batch for SIM

The DMD SIM setup uses a combination of two dichroic mirrors, reflecting in a horizontal and vertical arrangement. This is a typical solution to realize a SIM setup with off-the-shelf dichroic mirrors, as it solved the problem of polarization-dependent phase delay. With a standard dielectric mirror [297], the P- and S-polarized components of light being reflected exhibit different amounts of phase delay. In many applications, this does not cause issues, as either maintaining polarization is not of importance, or light is purely P- or S-polarized (often the case when using fully horizontally or vertically polarized light and reflecting it in the same plane on an optical table). However, in SIM, different polarizations that do not align with P- and S-polarization of the mirror have to be maintained to obtain full pattern contrast in the sample plane, while the different phase delays cause the polarization to become elliptical [210].

An easy solution that does not require custom components is using two dichroic mirrors in an arrangement as described above, so that light that is S-polarized for the first mirrors is seen as P-polarized by the second mirror, and vice versa. Thus, the different phase delay effects cancel out, and the delay becomes independent of polarization state. For this to work, we have found that two completely identical mirrors, ideally produced in the same batch, should be used.

As an additional remark, all conventional mirrors should be checked for polarization effects when they are used in a SIM excitation path. However, when no dichroic properties are needed, using metallic instead of dielectric mirrors typically provides an easy solution to achieve a polarization-maintaining light path.

HL63163DG red laser diode wavelength and mode-hopping

The AlGaInP laser diode (Ushio, HL63163DG) has a typical wavelength of 633 nm with 100 mW output power at 170 mA operating current (single transvers spatial mode).

The wavelength (longitudinal mode) of the laser diode depends on the temperature of the laser diode (approx. 0.2 nm/°C) and on the injection current (approx. 0.05 nm/mA). With fixed current the wavelength of the laser diode can be altered by changing the temperature.

With raising temperature, the refractive index and the length of the laser cavity, and therefore the wavelength, increases. If the (longitudinal) mode no longer fits into the

cavity a neighboring mode oscillates. This course a mode jump of about 0.2.5 nm which can be seen in the curves (see Figure 55b). These mode hops are not reproducible (temperature dependent hysteresis). Sometimes the laser diode is running in two or more longitudinal modes as can be seen in Figure 77.

The laser diode (5.6 mm TO Package) is mounted on an external thermo electric cooling element for controlling the diode temperature together with a thermistor for measuring the case temperature. All parts are in a round housing which fits in the 30 mm cage system (Thorlabs). With the laser diode controller (Meos LDC-01) it is possible to set the temperature in steps of 0.2°C, over a range of 5 to 40°C.

The strongly divergent laser beam is collimated by a aspheric lens (f=9.6 mm, NA=0.3, Thorlabs C060TMD-A) The collimated beam with its elliptic shape than is coupled into the single mode fiber with a further aspheric lens (f=15.29, NA=0.16, Thorlabs C260TMD-A).

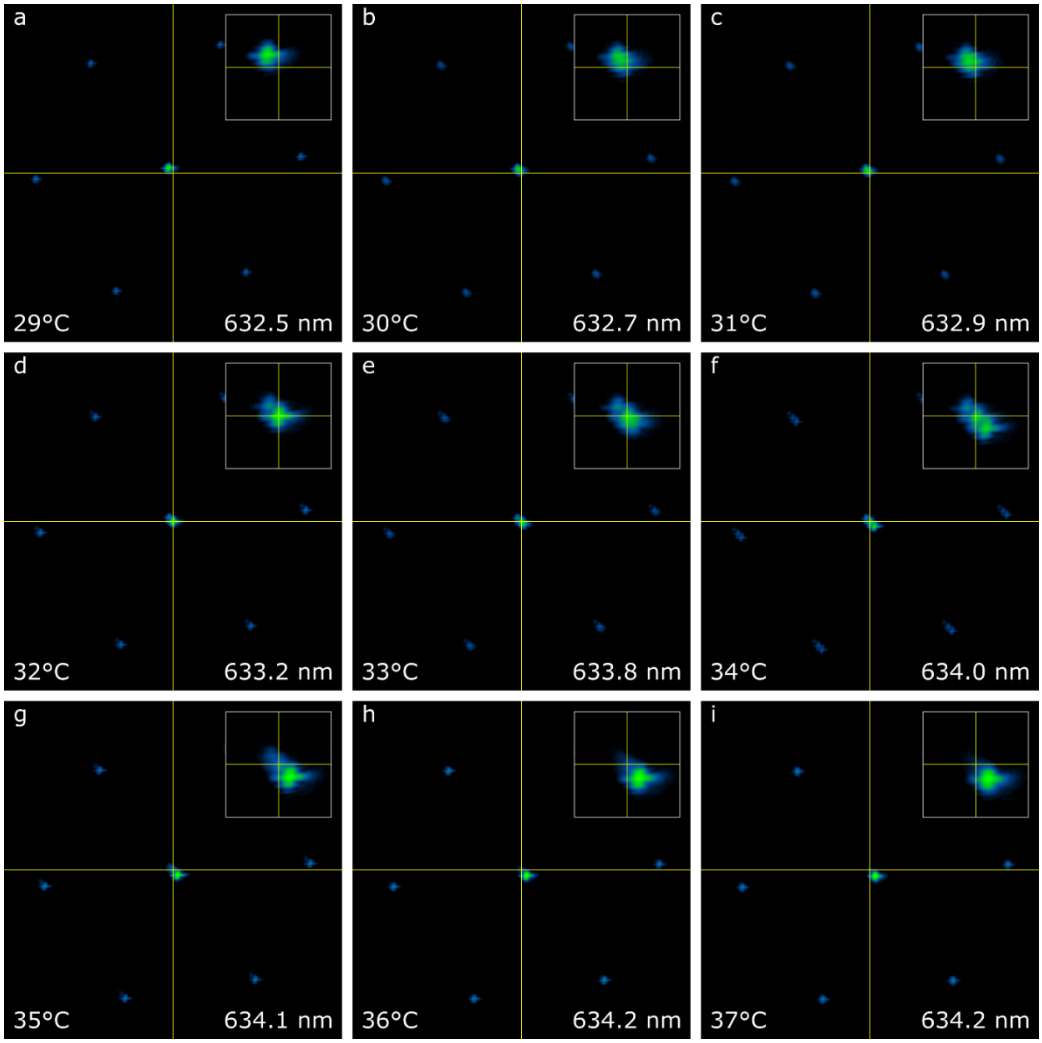

Figure 77: Longitudinal mode hopping in the Fourier plane

Diffraction images (1.3° × 1.3° / 4.5 mm x 4.5 mm) of the DMD at case temperatures of (a) 29° to (i) 37°C (632.5 nm to 634.2 nm) of the diode laser in linear intensity representation, integrated over the three SIM angles. Measured with an IDS uEye UI-3060CP-M-GL Rev.2 in the Fourier plane of the setup (Figure 56). The inlays each show the magnification of the central diffraction order. The yellow crosses in the center serve as a static reference to the moving central diffraction order. With increasing temperature and wavelength, all diffraction orders migrate along the diagonal perpendicular to the tilting axis of the DMD's micromirrors. Several mode jumps with a distance of approx. 82 µm can be seen on the camera chip. This is equivalent to an angular difference of approx. $\Delta\beta = 0.02°$, which in a linear approximation of the native grating diffraction of the DMD corresponds to a mode jump of approx. $\Delta\lambda = 0.5\ nm$ each. This is about twice the mode jumps described in the data sheet of the laser diode. We assume that in our case we can only observe double mode jumps, since the modes in between either hardly oscillate or smaller temperature steps are required to see them. In (f) it is easy to see that sometimes even three modes can be active at the same time. For operation as a SIM microscope, it is desirable that only one mode is active, as can be seen in Figure 58. Figure taken from our corresponding publication [64].

Nonlinearities in the diffraction space of the simulations

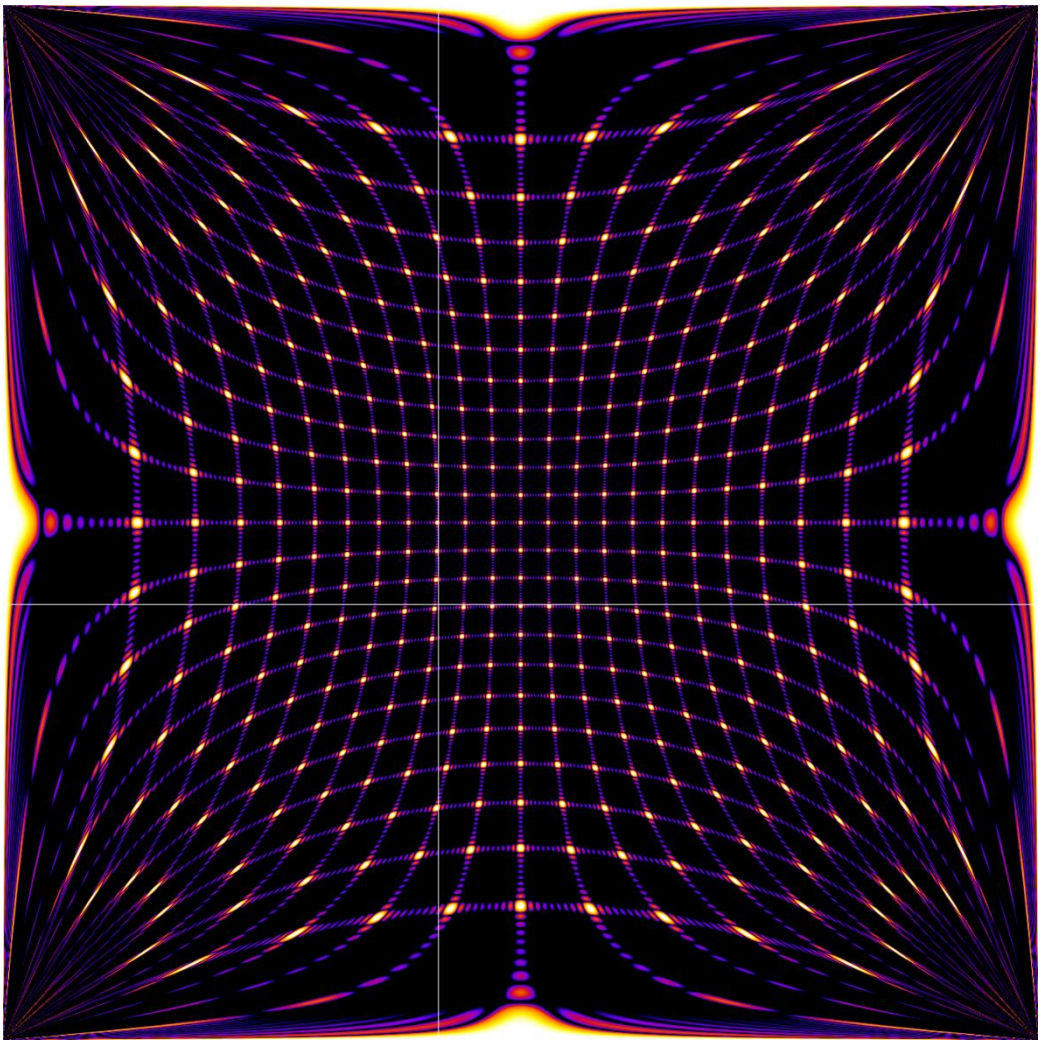

Figure 78: Nonlinearities in the diffraction space of the simulations

Diffraction image (90° x 90°) of the native grating diffraction of a DMD optimized for the logarithmic representation of the nonlinearities in the diffraction space of the simulations. The nonlinearities stem from the use of the tangent function in the coordinate choice of φ and ϑ (see eq. (88)) and exhibit singularities for $\varphi \to \pm 90°$ and $\vartheta \to \pm 90°$. For small angles in particular along the coordinate axes, the angular coordinates φ and ϑ can be assumed to be Euclidean. For larger angles especially along the 45° diagonal, the nonlinearities have an increased effect. The white cross indicates the angle of emergence of $\beta = -19.7°$ and $\varphi = -\vartheta = -14.2°$ respectively (dual-color DMD-SIM microscope, section 3.6). Simulation parameters: 10 x 10 micromirrors, 7.56 µm pixel pitch, $\varphi_a = \vartheta_a = 0°$, $-90° < \varphi_b, \vartheta_b < 90°$, grating approach.

A.III BABB protocol for sample clearing

- Incubate in 50% Methanol in H_2O for 1 h at room temperature
- Incubate in 70% Methanol in H_2O for 1 h at room temperature
- Incubate in 95% Methanol in H_2O for 1 h at room temperature
- Incubate in >99% Methanol (anhydrous) 2x for 1 h at room temperature
- Incubate in 1:1 Methanol:BABB for 24 h at room temperature
    - (1:2 Benzyl alcohol/Benzyl benzoate)
- Incubate in BABB for 24 h at room temperature

B Publications

This thesis is based in major parts on the following publications:

Markwirth, A., Lachetta, M., Mönkemöller, V., Heintzmann, R., Hübner, W., Huser, T., & Müller, M. (2019). Video-rate multi-color structured illumination microscopy with simultaneous real-time reconstruction. Nature communications, 10(1), 1-11.

Author contributions: A.M. constructed the opto-mechanics, control electronics and wrote parts of the paper. M.L. implemented the GUI and the network/control flow software V.M. performed the sample preparation and imaging R.H. provided the opto-mechanical design and details of the SIM image reconstruction process and helped with the project W.H. performed the sample preparation and imaging. T.H. conceived and supervised the research project. M.M. wrote the image reconstruction software, supervised and participated in the construction and implementation of the opto-mechanics and electronics of the microscope and its utilization during image acquisitions and wrote parts of the paper. All authors participated in the reading and editing of the final paper.

Kong, C., Bobe, S., Pilger, C., Lachetta, M., Øie, C. I., Kirschnick, N., Mönkemöller, V., Hübner, W., Förster C., Schüttpelz, M., Kiefer, F., Huser, T., & Schulte am Esch, J. (2021). Multiscale and Multimodal Optical Imaging of the Ultrastructure of Human Liver Biopsies. Frontiers in Physiology, 12, 149.

Author contributions: CK, SB, CP, ML, CØ, VM, and WH acquired data. All authors helped analyze the data. All authors were involved in writing the manuscript. FK, TH, and JS perceived the project and supervised the work.

Sandmeyer, A., Lachetta, M.*, Sandmeyer, H., Hübner, W., Huser, T., & Müller, M. (2021). Cost-Effective Live Cell Structured Illumination Microscopy with Video-Rate Imaging. ACS Photonics 8(6), 1639–1648.*

**These authors contributed equally to this work. A.S. built the DMD-SIM microscope, performed the blazed grating effect and SIM measurements, processed the SIM reconstructions, prepared samples, and wrote the manuscript. M.L. wrote the DMD simulation software, set up electronics and control software of the microscope, and wrote parts of the manuscript. H.S. helped to implemented and crosschecked math and simulation of the blazed grating effect. W.H. prepared the fixed and live-cell samples. T.H. supervised the project and helped write the manuscript. M.M. conceived of and supervised the project, performed FRC analysis, and wrote the manuscript. All authors took part in editing and approving of the manuscript.*

Lachetta, M., Sandmeyer, H., Sandmeyer, A., Schulte am Esch, J., Huser, T., & Müller, M. (2021). Simulating digital micromirror devices for patterning coherent excitation light in structured illumination microscopy. Philosophical Transactions of the Royal Society A, 379(2199), 20200147.

M.L. wrote the DMD simulation software, developed the analytic phase shifting approach, the grating approach, the blaze condition approach, set up electronic and control software of the DMD-SIM microscope and drafted the manuscript. H.S. developed the ray tracing approach and crosschecked math and simulations. A.S. built the DMD-SIM microscope, performed the SIM measurements and processed the SIM reconstructions. T.H. and J.S.a.E. supervised the project and helped write the manuscript. M.M. envisioned the project and wrote the manuscript. All authors read and approved the manuscript.

Lachetta, M., Wiebusch, G., Hübner, W., Schulte am Esch, J., Huser, T. & Müller, M. Dual color DMD-SIM by temperature-controlled laser wavelength matching. Optics Express, accepted, submitted September 2021.

ML developed the DMD simulation software, the dual color DMD-SIM microscope and drafted the manuscript. GW provided technical support, especially with the lasers and the wavelength tuning via temperature. WH prepared the U2OS cells and carried out their measurement with the dual color DMD-SIM Microscope. TH and JSaE supervised the project and helped write the manuscript. MM envisioned the project and wrote the manuscript. All authors read and approved the manuscript.

C Acknowledgments

At this point, I would like to thank all those who have contributed to the success of this thesis through their professional and personal support.

First, I would like to thank my doctoral thesis supervisor, Prof. Dr. Thomas Huser, who made it possible for me to write this thesis. In particular, I would like to thank him for the freedom he gave me in the course of my research, for the trust he placed in me, and for his advice.

Furthermore, I would like to thank Prof. Dr. Andreas Hütten for providing an expert opinion on this thesis. Besides Prof. Dr. Thomas Huser and Prof. Dr. Andreas Hütten, Prof. Dr. Joris Verbiest and Prof. Dr. Thomas Dahm made themselves available as part of the examination committee, for which I would like to express my gratitude to all professors.

Special thanks and respect go to Dr. Marcel Müller, who always supported me with his expertise and suggestions for solutions. Having had such a competent and motivated contact person at my side has contributed significantly to the success of my projects and this PhD Thesis. I very much appreciate the cooperation with him and the discussions beyond that.

I would also like to thank Dr. Gerd Wiebusch, Dr. Christian Pilger and Andreas Markwirth for their support in realizing optical setups. Thanks to their experience, some seemingly hopeless problems could be solved or circumvented with clever tricks and alternatives.

For the joint development of the one-color DMD-SIM microscope, I would like to express my gratitude to Dr. Alice Sandmeyer. I also express my gratitude to Dr. Hauke Sandmeyer, who cross-checked and partially helped develop the programming of the DMD simulations. I thank Dr. Wolfgang Hübner for the preparation and joint measurements of cells. I also thank him for the great photos of the setups shown in this thesis.

It fills me with joy to see how the OPT project I started is being continued successfully and with enthusiasm by Jasmin Schürstedt. I am grateful that I can hand this project over to her with a clear conscience. I wish her a lot of scientific success for her intended doctorate.

Of course, I would like to thank all colleagues in my research group (D3, Biomolecular Photonics) for the pleasant and open working atmosphere, as well as the constructive exchange. I would also like to thank the mechanical and electronic workshop of the faculty of physics for the completion of custom-made components.

At this point I would like to thank Prof. Dr. med. Fritz Mertzlufft and Prof. Dr. med. Jan Schulte am Esch, representing the Protestant Hospital of Bethel Foundation, for funding my research.

I would also like to thank my fellow students Marcel Skaletz and Björn Büker, who accompanied me through my studies and doctorate. In particular, I would like to thank them for the daily coffee rounds and joint preparations for exams.

Finally, I would like to thank my family, whose support made my studies and thus also my doctorate possible.

D Statutory declaration

I hereby certify that the work presented in this PhD Thesis is my original work without the use of anything other than the listed resources. All ideas that are not mine have been fully and properly acknowledged.

Bielefeld, 22.10.2021

Mario Lachetta